Cavitation and Film Formation in Hydrodynamically Lubricated Parallel Sliding Contacts

Von der Fakultät für Maschinenbau

der Gottfried Wilhelm Leibniz Universität Hannover

zur Erlangung des akademischen Grades

Doktor-Ingenieurin (Dr.-Ing.)

genehmigte Dissertation

von

Dilek BULUT, M.Sc. Eng.

2021

1. Referent: Prof.Dr.-Ing. Gerhard Poll

2. Referent: Prof. Noël Brunetière PhD

Vorsitzender: Prof.Dr.-Ing. Friedrich Dinkelacker

Tag der Promotion: 04.10.2021

ABSTRACT

Cavitation and Film Formation in Hydrodynamically Lubricated Parallel Sliding Contacts

Cavitation influences the pressure distribution in hydrodynamically lubricated contacts and therefore also the load carrying capacity. Film formation in parallel sliders is investigated experimentally and numerically by focusing on its relationship with cavitation.

Friction torque, contact temperature and film thickness measurements are conducted on textured and non-textured rectangular face seals. The textured seals have bidirectional structures ('T-shape' structures) on their axial faces. It is found that the textured seals have a better performance. The friction torque and the contact temperatures of the structured seals are lower at high speeds.

Cavitation is observed and film thickness measurements are performed by using the laser induced fluorescence method. Cavitation forms in the divergent zones of the structures for the structured seals. Cavitation is randomly distributed over the seal interfaces of the standard seals and it seems to occur due to macro and micro surface irregularities. The cavitation area ratio increases rapidly with speed in the mixed lubrication regime. In the hydrodynamic regime, the change in cavitation with speed becomes small. Both the film thickness and the cavitation area ratio decrease with increasing sump temperature and pressure. There is a strong correlation between lubricant film thickness and cavitation.

Local contact temperatures over the sealing contact are observed via infrared thermography. The structured seals heat up near cavitation zone. The standard seals warm in patches on their axial faces. It is observed that structuring can generate cooling effect.

Hydrodynamic film formation is modelled based on cavitation by a mass conservative Jakobsson-Floberg-Olsson cavitation model solved using the Fischer-Burmeister-Newton algorithm. The numerical results are validated via the experiments. Influences of structuring, macro surface irregularities, waviness, radial taper, and cavitation pressure are investigated. Experimental and numerical results correlate well in the hydrodynamic regime when realistic contact temperatures and realistic cavitation pressures are taken into account. It is shown that surface structuring can generate a considerable hydrodynamic load support. The manufactured surfaces of the seals influence pressure generation and cavitation. Therefore, it is necessary to consider the manufactured surfaces to predict the cavitation and film formation accurately. For the current application, surface structures are found to be more dominant on film formation than waviness and radial taper. A variation of the cavitation pressure showed that increasing cavitation pressure can result in higher film thicknesses and lower cavitation sizes. Comparison of these results with the results from optical experiments enabled a prediction of a feasible cavitation pressure for the system.

Furthermore, the implementation of the numerical model for other applications is described. Surface structuring of a vane pump is analysed. Here, dimple like structures are investigated. The numerical model is further extended and roughness is considered in the application of nominally flat sliding contacts. Thus, first attempts to understand the influence of roughness on film formation and inter-asperity cavitation are described.

ZUSAMMENFASSUNG

Kavitation und Schmierfilmverhalten in geschmierten hydrodynamischen parallelen Kontakten

Kavitation beeinflusst die Druckverteilung und den Schmierfilmaufbau in hydrodynmaischen geschmierten Kontakten und somit auch das Lasttragvermögen. In der vorliegenden Arbeit wird der Schmierfilmaufbau in nominell parrallelen Gleitkontakten mit dem Schwerpunkt Kavitation experimentell und numerisch untersucht.

Das Reibmoment, die Kontakttemperaturen und die Schmierfilmdicke wurden in strukturierten und unstrukturierten Rechteckdichtungen gemessen. Die strukturierten Dichtungen waren heribei mit T-förmigen Strukturen in der axialen Kontaktfläche versehen. Die Experimente zeigten hierbei, dass die strukturierten Dichtungen niedrigere Reibung lieferten. Hierbei zeigten sich besonders bei höheren Geschwindigkeiten niedrigere Reibmomente und korrelierende niedrigere Kontakttemperaturen im Vergleich zu unstrukturierten Dichtungen. Mithilfe Laser induzierter Fluoreszenz (LIF) wurde die Kavitation optisch betrachtet und die Schmeirfilmdicke gemessen. In strukturierten Dichtkontakten konnte eine Konzentration der Kavitation innerhalb der divergierenden Strukturhälften beobachtet werden. In den unstruktureirten Dichtungen wurde Kavitation in kleinen zufällig verteilten Bereichen auf der Oberfläche erkannt. Hierbei konnten die Orte Unregelmäßigkeiten der Oberfläche, sowohl Makro- und Mikroskopisch, zugeordnet werden. Der Anteil der Kontaktfläche auf der Oberfläche steigt mit steigender Geschwindigkeit im Bereich der Mischreibung an. Im Gebiet der Vollschmierung findet die Ausbreitung nicht mehr mit derselben Geschwindigkeitsabhängigkeit statt. Sowohl Kavitationsausbreitung als auch Schmierfilmdicke sind hierbei von der Schmierstofftemperatur abhänging und nehmen mit steigender Temperatur ab. Die Schmierfilmdicke korreliert hierbei mit dem Kavitationsanteil auf der Oberfläche der Dichtungen. Weiterhin wurden zur Beobachtung der lokalen Effekte Messungen mittels Inrarotthermografie durchgeführt. Somit wurde die Entstehung und räumliche Verteilung der Erwärmungen im Kontakt ermittelt. Hierbei zeigte sich in den strukturierten Dichtungen eine Erwärmung im Bereich, der dem Auftreten der Kavition entspricht. Unstrukturierte Dichtungen erwärmten sich in Flecken, die über den gesamten Kontaktbereich verteilt waren.

Eine numerische Modellierung der Kontakte wurde durchgeführt. Hierzu wurde die Reynoldsgleichung mit dem masseerhaltendenden Kavitationsmodell von Jakobsson-Floberg-Olsson genutzt, welches mittels Fischer-Burmeister-Newton Algorithmus gelöst wurde. Die Ergebnisse wurden mit den Experimentellen Ergebnissen abgeglichen und validiert. Anschließend wurden Effekte und Einflüsse einzeln und detaillierter betrachtet. Es wurden die Einflüsse der Strukturierung, makroskopischer Oberflächeneigenschaften, Welligkeit, Verkippen der Dichtung und Kavitationsdruck untersucht. Bei Einbeziehung der gemessenen Kontakttemperaturen konnten die gemessenen Schmierfilmdicken gut abgebildet werden. Es konnte gezeigt werden, dass die Strukturierung einen hydrodynmaischen Druckaufbau begünstigt. Weiterhin konnte gezeigt werden, dass makroskopische Oberflächenabweichungen die Kavitationsbildung und damit den Druckaufbau deutlich beeinflussen. Es ist zur genaueren Vorhersage der Schmierfilmbildung in derartigen Systemen notwendig diese Makroabweichungen zu berücksichtigen. In den untersuchten strukturierten Dichtungen überwiegen die Effekte der Strukturen über den durch Welligkeit und Verkippung der Dichtung erzeugtem Druckaufbau. Aus der Studie des Kavitationsdruckes konnten in Verbindung mit den Experimenten realistische Werte ermittelt werden. Es wurde die Beeinflussung des Schmierfilmaufbaus gezeigt durch den Kavitationsdruck gezeigt.

Die Anwendung des numerischen Modells auf weitere technische System wurde erarbeitet. Hierbei wurde der Einfluss von Strukturen bei einer Flügelzellenpumpe gezeigt. In der Anwendung einer nominell parallelen Gleitpaarung wurde eine Erweiterung zur Berücksichtung der Rauheiten erstellt. Hierbei werden die Wechselwirkungen zwischen Rauheit und Kavitation sowie deren Beitrag zur Schmierfilmbildung herausgearbeitet.

PUBLICATIONS

The main findings of this dissertation have been reported in the following publications and conferences:

Journal Papers

1. Bulut, D., Bader, N., Poll, G., 2021, "Cavitation and film formation in hydrodynamically lubricated parallel sliders," Tribology International, vol 162, 107113, https://doi.org/10.1016/j.triboint.2021.107113

Conference Papers

1. Bulut, D., Poll, G., 2018, "The measurement of lubricant film thickness in rectangular seal rings by using fluorescence method," ICETAT 2018 International Conference on engineering tribology and applied technology, Taiwan, 16 Nov 2018 - 18 Nov 2018.

2. Bulut, D., Poll, G., 2019, "Film formation and temperature development in textured rectangular face seals," 46th Leeds-Lyon Symposium on Tribology, Lyon, France, September 2-4, 2019.

3. Bulut, D., Bader, N., Wennehorst, B., 2020, "Evaluation of cavitation in structured face seals, 25th International Conference on Fluid Sealing," Manchester, 4th – 5th March 2020.

The following publications are not included in this dissertation:

Journal Papers

1. Bulut, D., Temiz, V., Parlar, Z., 2015, "The Effect of Interference on the Friction Torque Characteristics of TPU Based Rotary Lip Seals," Tribology in Industry 37(3):346-353.

2. Bulut, D., Girista, V., Temiz, V., Parlar, Z., 2016, "The Effect of Lubricant Type on the Friction Torque Characteristics of Rotary Lip Seals," International Journal of Science and Engineering Investigations, vol. 5, no. 50.

3. Bulut, D., Krups, T., Poll, G., Giese, U., 2019, "Lubricant compatibility of FKM seals in synthetic oils," Industrial Lubrication and Tribology, vol. 72, no. 5, pp. 557-565. doi.org/10.1108/ILT-02-2019-0065

Conference Papers

1. Bulut, D., Seibel, T., Poll, G., Giese, U 2017, "Dichtungsbeständigkeit in synthetischen Ölen," 22. Tagung der Bezirksgruppe DKG Nord, Germany, 11 May 2017 - 12 May 2017.

2. Bulut, D., Seibel, T., Poll, G., Giese, U., 2018, "Radial lip seal aging in synthetic oil," in Proceedings. pp. 33-34, 21st International Colloquium Tribology, TAE, 9 Jan 2018.

ACKNOWLEDGMENTS

CONTENTS

iii

List of Figures

List of Tables

NOMENCLATURE

A	m^2	Area
A	m	Wave peak amplitude (in the context of waviness)
a	m	Width of the structures
b	m	Width
B, B^+, B^-		Global coefficient of transmission (+, - are direction of propagation)
c	m/s	Speed of light
c	mol/m^3	molar concentration (in the context of fluorescence)
C		Radiometric coefficients
D	m	Diameter
E	J	Photon energy (in the context of thermography)
E	Pa	Elastic modulus (in the context of numerical calculations)
E^+, E^-		Global coefficient of emission (+, - are direction of propagation)
F	N	Force
F_{el}	N	Elastic forces
F_L	N	Lifting force
F_f	N	Friction force
F_N, F_n	N	Normal force
F_{shear}	N	Shear force
F_z	N	Centrifugal force
f		Coefficient of friction
g		Switch function
h	µm	Film thickness
h	J·s	Planck's constant (in the context of thermography)
H, h_F	m	Height
h_D	µm	dimple depth
h_{dyn}	µm	Hydrodynamic film thickness / min. film thickness
h_f	µm	land film thickness
h_{min}	µm	Minimum gap height
I	W/m^2	Intensity (in the context of fluorescence)
I_o	W/m^2	Incident light intensity (in the context of fluorescence)
I_f	W/m^2	Fluorescence intensity collected by a CCD pixel (in the context of fluorescence)
I_{fluo}		Fluorescence intensity as a gray value collected by a CCD camera
I	W/m^2	Radiant intensity (in the context of thermography)
I_{amb}	W/m^2	Radiative intensity of the radiation from surrounding
I_{cam}	W/m^2	Radiative intensity collected by an IR camera
I_0	W/m^2	Radiative intensity of the radiation from black body
I_1	W/m^2	Radiative intensity of the radiation from sapphire disc

I_2	W/m^2	Radiative intensity of the radiation from lubricant
I_3	W/m^2	Radiative intensity of the radiation from atmosphere
k		Balance ratio (in the context of seal forces)
k	J·K^{-1}	Boltzmann constant (in the context of thermography)
K		Pressure gradient factor
L, l	m	Length
L_c	m	Characteristic linear dimension
M	Nm	Friction torque
M	W/m^2	Radiant exitance (in the context of thermography)
M_λ, M_v	W/m^3, W·m^{-2}·Hz^{-1}	Spectral exitance (in the context of thermography)
$\vec{n}$		Normal unit vector
n		Refraction index
n_{air}		Air refraction index
n_1		Sapphire refraction index
n_2		Oil refraction index
P, p	Pa	Pressure
P_{cav}, p_{cav}	Pa	Cavitation pressure
$P_{gas\ sat}$	Pa	Gas saturation pressure
P_{sat}	Pa	Vapour pressure
Q	g/min	Leakage rate
r	m	Radius
R		Cavitation area ratio
R^+, R^-		Global coefficient of reflection (+, - are direction of propagation)
Re		Reynolds number
S		Energy levels of a molecule
S_k	µm	Core height
S_{ku}		Kurtosis
S_{pk}	µm	Reduced peak height
S_q	µm	Root mean square height
S_{sk}		Skewness
S_{vk}	µm	Reduced valley depth
t	s	Time
T	°C or K	Temperature
T_f	Nm	Friction torque
T_g	°C	Glass transition temperature
T_n	°C	Near-contact temperature
TM_1, TM_2	°C	Axial contact temperatures
T_0	°C	Test head temperature

T_1, T_2	°C	Near-circumferential contact temperatures (in the context of friction tests)
T_3	°C	Lubricant temperature
T_1, T_3	K	Mean temperature of sapphire, and mean temperature of a seal (in the context of thermography)
U, u, u_s, V	m/s	Velocity, sliding velocity
U_1, U_2	m/s	Speeds of the surfaces in the x direction
V_1, V_2	m/s	Speeds of the surfaces in the y direction
V_n	m/s	Velocity vector
W_1, W_2	m/s	Speeds of the surfaces in the z direction
w	N	Normal load
α	Radian	Angle (in the context of simulations)
α		Absorptivity (in the context of thermography)
β	Pa	Bulk modulus of fluid
$\dot{\gamma}$	s^{-1}	Shear rate
$\epsilon(\lambda_{ex})$		Molar absorption coefficient
ε		Emissivity
$\varepsilon_1, \varepsilon_3$		Emissivity of sapphire, emissivity of seal
ϵ		Cavity fraction stabilization coefficient
ζ		A constant related with the efficiency of the monitoring
θ_n, θ		Fractional film content / cavity fraction
λ		Lambda ratio
λ	m	Wavelength (in the context of fluorescence and thermography)
λ_{as}		Texture aspect ratio
μ	Pa·s	Dynamic viscosity
ν		Poisson's ratios
ν	Hz	Frequency (in the context of fluorescence and thermography)
ρ	kg/m^3	Density of the fluid
$\rho, \rho_{air,1}, \rho_{1,2}$		Reflectivity (in the context of thermography), reflectivity of the interfaces environment/sapphire and sapphire/oil
ρ_{cav}	kg/m^3	Fluid density at cavitation pressure
ρ_0	kg/m^3	Reference lubricant density at a given temperature and atmospheric pressure
ρ_{avg}	kg/m^3	Average density of mixture of lubricant and gas
σ	W/m^{2}K^4	Stefan-Boltzmann constant
$\sigma^*, \sigma_1, \sigma_2$	μm	Composite surface roughness, surface roughness of the friction pairs
τ		Transmissivity (in the context of thermography)
τ	Pa	Shear stress
φ	Radian	Angle
Φ		Quantum efficiency (in the context of fluorescence)
ϕ_0	Watt	Radiant flux (in the context of thermography)
ϕ_0	Watt	Radiant flux striking to an object (in the context of thermography)

$\phi_{\mathrm{amb}}, \phi_{\mathrm{atm}}$	Watt	Ambient radiant flux, atmosphere flux
ϕ_{det}	Watt	Detected radiant flux by IR camera
ϕ_{K}	Watt	Camera specific calibration curve flux
$\phi_{\mathrm{object}}^{\mathrm{BB}}$	Watt	Equivalent flux of a black body at an object's temperature
$\phi_{\mathrm{R}}, \phi_{\mathrm{T}}, \phi_{\mathrm{A}}$	Watt	Reflected, transmitted, and absorbed radiant flux
ω	1/s	Rotational speed

SUBSCRIPTS

ab	Absorption
amb	Ambient / surrounding
atm	Atmosphere
C	Circumference
cam	Camera
cav	Cavitation
cont	Contact
dyn	Dynamic
d	Dimple
em	Emission
ex	excitation
F	Face
Fr	Friction
G	Gap
Gr	Groove
max	Maximum
i, in	Inside
o, out	Outside
s	Shaft
T	Tangential stress
targ	Target

ABREVIATIONS

BC	Boundary condition
CW	Clockwise
CCW	Counterclockwise
cof	Coefficient of friction
EHL	Elastohydrodynamic lubrication
Eq.	Equation
FBN	Fischer Burmeister Newton algorithm

Inc. sur.	Inclined surfaces of a structure
I.D.	Inner diameter
IR	Infrared
HL	Hydrodynamic lubrication
JFO	Jakobsson-Floberg-Olsson cavitation model
LIF	Laser induced fluorescence method
Pcav	Cavitation pressure
PEEK	Polyetheretherketone
O.D.	Outer diameter

1   INTRODUCTION

The largest quantities of energy are used by industry (29 %) and in transportation (27 %) [184]. In passenger cars, one-third of the fuel energy is used to overcome friction in the engine, transmission, tires, and brakes [185]. Energy losses due to friction and wear could potentially be reduced by 40% in the long term (15 years) and by 18% in the short term (8 years) via reducing friction losses and wear [186]. In order to reduce friction and wear, classically, the mating surfaces of the machine elements are often lubricated.

The contact between the machine elements can vary depending on its geometry. This will also influence the behaviour of the lubricant in the contact. Basically, when a viscous fluid is flowing in a wedge like gap, pressure can occur within the lubricant due the gap geometry and viscosity property of the lubricant. This pressure can be so strong that the mating surfaces can be separated by the lubricant. Consequently, friction and wear will decrease.

The contact between macroscopically flat surfaces is called 'parallel sliding contact'. This type of contact is very common in industry and will also be important in future developments of rotating machinery. Film formation in parallel sliding contacts has been an interesting subject since decades. The reason is these contacts do not have the prior feature to generate a lubricant film: 'gap height variations'. Different theories have been suggested to explain the hydrodynamic pressure generation in such contacts. Basically, the pressure generation is attributed to the other surface features such as roughness and surface deviations. While explaining the working mechanism of these features, the role of cavitation is pointed out. Cavitation is simply occurrence of gas/vapour bubbles within the lubricant when the pressure is decreased to cavitation pressure. Although cavitation has been studied for a long time, there are still open questions. Modelling cavitation is complex. In the literature, there are different cavitation models. The validation of these models is generally performed via observing surfaces with dimples. The detailed observation of cavitation is limited in literature. A detailed work about cavitation and the influences of different contact features on cavitation would still contribute substantially the numerical modelling world.

On the other hand, some surface optimization methods such as surface texturing have recently become popular to decrease friction and wear. Surface texturing has shown efficient impact in friction reduction. Features of the surface textures depend on the application. In order to design the optimum structure, it is important to understand the working mechanism of the structures. There are different theories to explain this mechanism. The most outstanding one is cavitation theory. Both the physical understanding of the lubrication mechanism and numerical modelling may help to enable a further optimisation of such contacts. This would allow for a friction reduction in the applications of such mechanical elements as well as open the possibility of developing novel solutions for sliding contact problems. Therefore, a detailed experimental and numerical investigation of surface structuring by considering cavitation mechanism is presented in this work.

2   STATE of the ART

2.1   CONFORMAL and NON-CONFORMAL CONTACTS

Tribological contacts can be categorized as conformal or non-conformal contact (Figure 2.1). When the mating surfaces fit relatively well into each other geometrically, the contact between those surface is categorized as a conformal contact. In these contacts, the load is supported by a large area compared to the lubricant film thickness [1]. Mating convex and concave surfaces generally result in a conformal contact. A classical example of this case is journal bearings (Figure 2.3). The radial clearance between the bearing and the journal is about one-thousandth of the journal diameter. The load is carried over the length of the bearing and approximately half of the circumference [2]. As the load is increases, the load supporting area does not change significantly. For these contacts, coefficients of friction are in order of 10^{-2}.
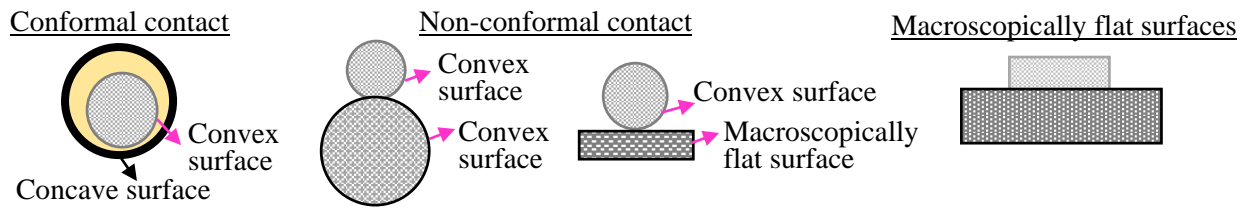
Figure 2.1: Conformal, non-conformal contacts and macroscopically flat surfaces.

In non-conformal contacts, the mating surfaces do not conform each other. This usually happens between two convex surfaces. The load is carried by a small lubricated area. This contact area increases with the load. Typically, the pressure generated in the contact area ranges from 0.5 to over 3 GPa with a friction coefficient in order of 10^{-2} to 10^{-1} [2]. Such high pressures in small contact area are capable to deform the surfaces elastically. In addition, the high pressures in the contact lead to an increase of several orders of magnitude in the lubricant viscosity.

The contact between two nominally flat surfaces can be classified as a conformal contact in geometry. However, elasticity may cause local non-conformal behaviour.

2.2   FRICTION

Friction is the force which is resisting the relative motion of objects. When dry contacts are considered, friction can be static or kinetic friction. Static friction occurs between stationary objects while kinetic friction occurs when the objects are moving relative to each other. Friction is a phenomenon takes place a lot in daily life from simple to complex issues. While walking, the foot pushes on the ground. If there would not be any static friction, the foot would slide backwards such as in walking on ice. However, static friction force resists sliding backwards and forward motion becomes possible. On the other hand, while pulling an object over the ground, kinetic friction occurs between the surfaces and additional, useless effort is required.

Friction is investigated since early times. The friction occurring in tribological contacts can be classified by the contact pairs and mechanisms involved [3]. Basically, friction can be divided into four categories: dry friction, which occurs between sliding bodies without additional layers or lubricants; boundary friction (i.e., friction between boundary layers or ultra-thin lubricant films) and, mixed and fluid film lubrication where friction originates partially (mixed lubrication) or fully (fluid film lubrication) within a fluid film separating friction pairs [3,4].

In dry friction, friction is the result of adhesive forces and deformations [3]. The laws of dry friction were suggested by Amontons (1663-1705) and Coulomb (1736-1806):

- The friction force (F_f) is directly proportional to the applied normal load (w).
- The friction force is independent of the apparent sliding contact (A).
- The kinetic friction force is independent of the sliding velocity (u_s).

According to these laws, the friction force in dry contacts can be calculated as:

$$F_f = fw \tag{2.1}$$

Here, f is the coefficient of friction. However, these laws are a rough approximation. In contrast to Amontons, Coulomb differentiated between material couples, where the dry friction laws are a good approximation, and other, where there are significant deviations from the dry friction laws [5]. Overall, the classical laws are useful for engineers to deal with dry sliding contacts. However, the generalized laws of friction, including the dependencies on different factors such as normal force and the shape, remain hot topics in modern tribology [5,6].

In industry, friction is useful for the systems such as brakes, tyres, etc. However, friction has also negative effects such as energy losses. One-fourth of the global energy and material losses result from friction and wear [7]. Lubrication is used as an effective method to reduce friction and wear.

2.3 FRICTION IN LUBRICATED CONTACTS

There are three basic friction regimes in lubricated contact bodies [3,4]:

- Boundary friction: This type of friction occurs when the lubricant film thickness is smaller than 10 atomic layers or two rubbing surfaces separated by a lubricant layer interact with each other due to asperities. There is no load carrying hydrodynamic lubricant film. Therefore, the friction is governed by mechanical interaction between the boundary layers and possibly the shearing of ultra-thin lubricant films between asperities.
- Mixed friction: A hydrodynamic film starts to form. However, there are still some asperities in contact. The load is carried both by the asperities and the lubricant film. Therefore, friction is the result of mechanical interactions of the asperities and shearing losses in the lubricant.
- Fluid friction (full film friction): The rubbing bodies are fully separated by a lubricant. The friction occurs only due to the shearing of the lubricant.

The behavior of the friction in lubricated contacts including these friction regimes was described by Stribeck around 120 years ago [8]. Today, the dependency between the coefficient of friction as a function of speed, contact pressure and viscosity is known as Stribeck curve [9,10]. Figure 2.2 shows a Stribeck curve which is obtained by plotting the coefficient of friction with respect to Hersey number. Hersey number is a dimensionless number which is the dynamic viscosity of the fluid (μ) times the entrainment speed of the fluid (u), divided by the normal load per length of the contact (P). At low Hersey numbers, the coefficient of friction is high and boundary friction occurs due to low film thickness. With increasing Hersey number, the coefficient of friction decreases as the lubricant film builds up. The lubrication regime becomes mixed lubrication regime. The minimum coefficient of friction occurs in mixed lubrication. Later on, the lubricant film becomes thick enough to separate the friction surfaces completely and full film lubrication occurs. The coefficient of friction increases again as the film thickness increases. It should be noted that, when Stribeck curve is plotted for a lubricated perfectly smooth plain surface with a wedge shaped geometry, the coefficient of friction would start from zero and increase rapidly with increasing Hersey number. In such a contact, the entrainment of the lubricant separates the surfaces directly since there are no asperities and dry contact does not occur. Therefore, the coefficient of friction curve becomes as so called 'smooth surface assumption curve' in Figure 2.2. This curve and the classical Stribeck curve coincide in the hydrodynamic zone.
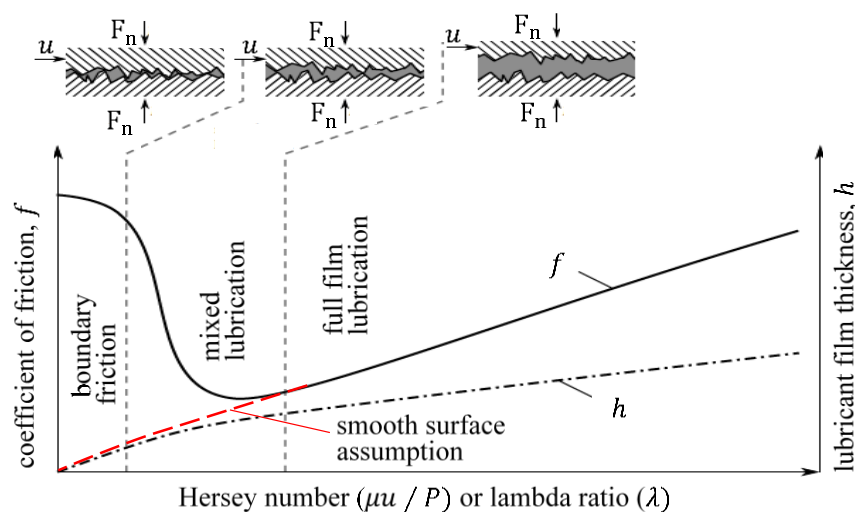
Figure 2.2: Schematic of Stribeck curve [3].

While Hersey [11] showed that hydrodynamic friction is a function of $\mu u / P$, the situation in non-conforming contacts, such as are present in rolling element bearings and gears is different [12,13]. The machine elements with a non-conforming contact operate in the elastohydrodynamic regime at moderate to high speeds. In this region, the coefficient of friction tends to be independent of viscosity and reaches a constant limiting value [12]. In addition, the film thickness varies only marginally with load [12]. Therefore, researchers suggested lambda ratio (λ) which is the ratio of film thickness (h) to composite surface roughness (σ^*):

$$\lambda = \frac{h}{\sigma^*} = \frac{h}{\sqrt{\sigma_1^2 + \sigma_2^2}} \tag{2.2}$$

Here, σ_1 and σ_2 are the surface roughness of the friction pairs. The lubrication in sliding contacts can be characterized via λ. Classically, $\lambda \geq 3$ indicates full film lubrication; $1 < \lambda < 3$ indicates mixed lubrication; $\lambda \leq 1$ indicates boundary lubrication. However, λ is not suitable as well to determine the lubrication regime under some circumstances (non-Newtonian fluid, consideration of thermal effects, etc.) [14]. It is shown that surface roughness deforms under very high pressure and this deformation depends on the operating conditions [15]. Because of such reasons, researchers continue to investigate different parameters to identify the lubrication regimes [13,16].

2.4 FULL FILM LUBRICATION

Full film lubrication can be divided into hydrodynamic and elastohydrodynamic lubrication. Hydrodynamic lubrication (HL) generally occurs in conformal contacts. In this lubrication, viscosity of the lubricant, relative motion and the geometry of the surfaces lead to separation of the surfaces by a lubricant film. Basically, if the gap between the surfaces is converging in the sliding direction, the fluid adhering to the moving surface will be dragged into the narrowing clearance space, thus building up a pressure sufficient to carry the load [17]. The operation of a lot of machines and vehicles relies on the HL mechanism (Figure 2.3).
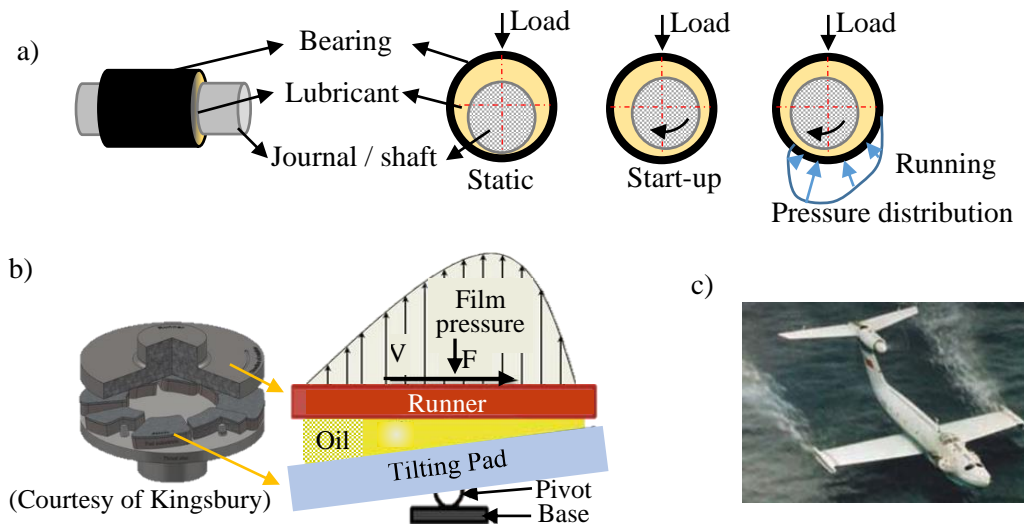
Figure 2.3: Machine elements and vehicles operating based on HL principle: a) journal bearing, b) tilting pad thrust bearing [19], c) ground effect aircraft / SM-6 [20].

Elastohydrodynamic lubrication (EHL) often occurs in non-conformal contacts. The small contact area results in a high contact pressure which is about 1000 times more than the lubricant film pressure of HL [10, 18]. Therefore, the elastic deformation of the surfaces cannot be neglected. This elastic deformation is often significantly greater than the minimum film thickness. The contact area increases as a result of the elastic deformation. Consequently, a gap occurs for the lubricant to pass through. In addition, the increase in the lubricant viscosity due to high pressures leads to an increase in the load carrying capacity

and keeps the lubricant from flowing out of the contact [1]. Proper functioning of rolling element bearings, gears and human joints etc. relies on EHL.

2.5 HYDRODYNAMIC LUBRICATION MODELLING

The thin fluid film flow between two solids was first described mathematically by Reynolds in 1886 [21]. Now, his equation which is so called Reynolds equation is the basis of lubrication theory. Reynolds equation can be derived from the momentum equations and the continuity equation. Momentum equations are known as Navier-Stokes equations and are based on the principle of conservation of momentum. Continuity equation is based on the principle of conservation of mass [22].

2.5.1 REYNOLDS EQUATION

The following assumptions are made to derive Reynolds equation:

1) The fluid is Newtonian.
2) There is no slip on the interface between fluid and solid surfaces. Therefore, the lubricant velocity is equal to the velocity of the solid surface on the interface.
3) The fluid inertia is negligible.
4) The lubricant flow is laminar. This assumption is related to the thin film characteristic of lubricated contacts, which yields flows with very small Reynolds numbers (Re), i.e. the inertia effects are negligible in comparison with viscous behaviour [23]:

$$\text{Re} = \frac{\rho \, u \, L_c}{\mu}$$

(2.3)

5) Body forces such as gravity and magnetic forces are negligible.
6) The film is thin. The pressure variations across the film are negligible ($\frac{\partial p}{\partial z} = 0$).
7) Viscosity remains the same across the lubricant film thickness. This assumption is for mathematical convenience [22].
8) The film thickness is negligible compared to the radius of the bearing surface. Therefore, curvature effects are negligible.
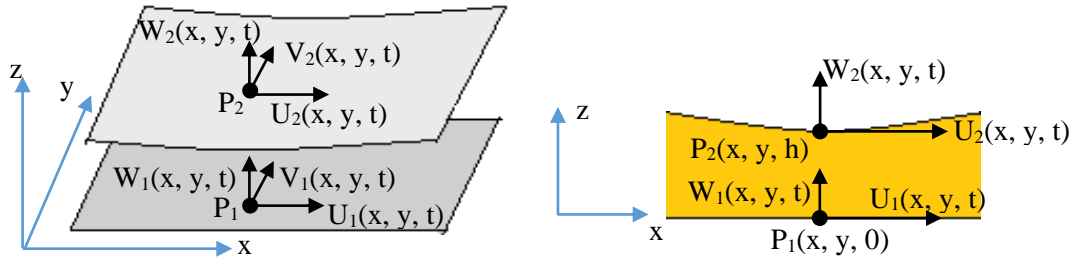
Figure 2.4: Thin fluid film bounded by the surfaces and the kinematic variables.

For the thin film shown in Figure 2.4, the generalized Reynolds equation can be written as:

$$\underbrace{\frac{\partial}{\partial x}\left(\frac{\rho}{12\mu}h^3\frac{\partial p}{\partial x}\right) + \frac{\partial}{\partial y}\left(\frac{\rho}{12\mu}h^3\frac{\partial p}{\partial y}\right)}_{\text{Poiseuille term}} = \underbrace{\frac{\partial}{\partial x}\left(\frac{\rho h(U_1+U_2)}{2}\right) + \frac{\partial}{\partial y}\left(\frac{\rho h(V_1+V_2)}{2}\right)}_{\text{Couette term}} \dots$$

(2.4)

$$\dots + \underbrace{\rho(W_2-W_1)}_{\substack{\text{Normal squeeze} \\ \text{term}}} - \underbrace{\rho U_2\frac{\partial h}{\partial x} - \rho V_2\frac{\partial h}{\partial y}}_{\substack{\text{Translation squeeze} \\ \text{term}}} + \underbrace{h\frac{\partial \rho}{\partial t}}_{\substack{\text{Local expansion} \\ \text{term}}}$$

Eq. (2.4) can be rewritten by neglecting the side leakage term $\left(\frac{\partial}{\partial y}\right)$ and with the detailed Couette term [24]:

$$\underbrace{\frac{\partial}{\partial x}\left(\frac{\rho}{12\mu}h^3\frac{\partial p}{\partial x}\right)}_{\text{Poiseuille term}} = \underbrace{\underbrace{\frac{h(U_1 + U_2)}{2}\frac{\partial \rho}{\partial x}}_{\text{Density wedge}} + \underbrace{\frac{\rho h}{2}\frac{\partial(U_1 + U_2)}{\partial x}}_{\text{Stretch}} + \underbrace{\frac{\rho(U_1 + U_2)}{2}\frac{\partial h}{\partial x}}_{\text{Physical wedge}} \cdots}_{\text{Couette term}}$$

(2.5)

$$\cdots + \underbrace{\rho(W_2 - W_1)}_{\substack{\text{Normal} \\ \text{squeeze term}}} - \underbrace{\rho U_2 \frac{\partial h}{\partial x}}_{\substack{\text{Translation} \\ \text{squeeze} \\ \text{term}}} + \underbrace{h\frac{\partial \rho}{\partial t}}_{\substack{\text{Local} \\ \text{expansion} \\ \text{term}}}$$

Poiseuille term (pressure flow): This is the lubricant flow induced by the pressure gradients within the lubricant.

Couette term: This is the lubricant flow induced by the surface velocities. It can be subdivided as [24]:

- Density wedge: This term considers the flow rate at which the lubricant density changes in the sliding direction. The decrease of the density in the sliding direction can generate positive pressure. This effect can be obtained by increasing the temperature of the lubricant as it passes through the gap. This term is called thermal wedge as well. This mechanism is not important for most of the systems. It has been suggested that it might be important for the macroscopically parallel surfaces, where the major pressure generating actions are absent.
- Stretch: This term considers the flow rate at which surface velocities change in the sliding direction. This effect occurs when the surfaces are elastic and the extent to which the surfaces are stretched varies through the bearing. This term is negligible for conventional plain bearings.
- Physical wedge: This is the main term for pressure generation. When the surface geometries result in a wedge like gap, there would be different Couette flow rate at each section due to variable h along the gap. Flow continuity can be achieved only if a balancing Poiseuille flow is superimposed. If the lubricant film decreases in the sliding direction, a positive load carrying capacity can be obtained.

Normal squeeze term: This is a term as important as the physical wedge term for lubrication. It results from the difference in normal velocities $(W_2 - W_1)$. This term generates a fluid cushioning effect when the surfaces tend to be pressed together.

Translation squeeze term: This occurs due to the translation of inclined bearing surfaces.

Local expansion term: Lubricant flow is induced with the effects related with the lubricant compressibility [23]. In this term, the pressure generating mechanism can be simply described as the thermal expansion of the lubricant between the stationary surfaces.

Reynolds equation shows that kinematic and geometric features and, lubricant properties (μ, ρ) are important for hydrodynamic lubrication.

2.5.2 HYDRODYNAMIC CAVITATION in FLUID FILMS

The hydrodynamic pressures which are calculated via the Reynolds equation may reach negative values (relative pressures). Sommerfeld solved the Reynolds equation for a journal bearing and obtained the pressure distribution along the bearing circumference. He assumed that the bearing is long (L/D >> 1, L= axial length, D= diameter) hence, the film pressure is constant in the axial direction. In addition, he assumed that the whole bearing clearance is full of lubricant [25]. His method is known as Sommerfeld full film condition. This method leads to negative pressures in the divergent gap (Figure 2.5). The positive and the negative pressures are symmetrical hence, there is no net positive lubricant lifting force for a non curved contact surface. In addition, the negative pressures mean that the lubricant is subjected to high tensile stresses. However, it is not very likely that the liquids can sustain large tensile stresses.

When the pressure becomes very low, the lubricant film ruptures and this results in cavities filled with a mixture of liquid and gasses/vapours. This phenomenon is called cavitation. Cavitation can be categorized as [26]:

Gaseous cavitation: Many liquids contain dissolved gasses. As the liquid pressure falls below the gas saturation pressure ($P_{gas\ sat}$), the dissolved gasses escape out and diffuse into gaseous bubbles. This type of cavitation shows a stable behaviour. It is predominant in the systems operating under steady state or low transient conditions [23].

Pseudo cavitation: it is a form of gaseous cavitation during which the gas bubble expands due to its surrounding depressurization without further gas mass diffusion from liquid to gas phase.

Vaporous cavitation: It is the result of a thermodynamic non-equilibrium event when the pressure drops below the vapour pressure (P_{sat}) of the liquid at a given temperature. This type of cavitation bubble is mostly filled by vapour of the liquid. It mostly occurs in systems operating at highly transient conditions. It is not as stable as gaseous cavitation due to its thermodynamic nature. The forming process of vaporous cavitation is generally followed by the growth and implosion of the bubble. During the implosion, shockwaves, noise etc. can occur. Therefore, vaporous cavitation can damage the surfaces.
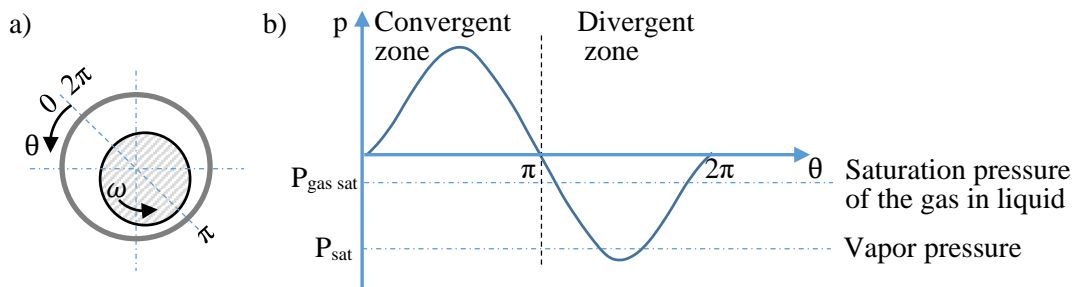
Figure 2.5: a) A journal bearing under a load, b) full Sommerfeld pressure distribution along the journal bearing circumference [26].

Cavitation influences the pressure distribution in the lubricant and thus, the load carrying capacity. In addition, it might lead to severe damages in the lubricated systems as mentioned above. Many researchers described the fundamentals of the cavitation mechanism and showed that cavitation plays an important role in hydrodynamic lubrication [21,27-31].

Some recent works also investigated cavitation and the film buildup in parallel sliders by taking micro and macro surface features into account. Harp *et al.* [32] investigated the effects of inter-asperity and global cavitation on the lubricant film of lip and mechanical face seals. It is found that the inter-asperity cavitation is important for small ratios of film thickness and RMS roughness. It leads to a higher load support prediction in the numerical models for hydrodynamic lubrication with global cavitation. Brunetière *et al.* [33] worked on textured mechanical face seals. They showed that it is important to consider cavitation to model hydrodynamic lift. Liu *et al.* [34] also analysed textured face seals numerically and found that cavitation enhances hydrodynamic pressure generation. Hirayama *et al.* [35] investigated the influence of cavitation on the static bearing characteristics of a spiral grooved journal bearing. They reported that the numerically calculated load carrying capacity and pressure distribution of the model with cavitation is significantly different from the one without cavitation. The numerical results fit better to the experimental results when cavitation is considered. Yagi *et al.* [36] calculated the load carrying capacity of a textured surface in hydrodynamic lubrication numerically by considering cavitation. Influences of boundary conditions were investigated.

2.5.3   THEORETICAL MODELLING of CAVITATION

The cavitation bubble interface generates a discontinuity in the lubricant film and creates a challenge in the solution of the Reynolds equation [26]. Therefore, different mathematical models have been suggested by the researchers. In this section, basic cavitation models are described.

2.5.3.1   HALF SOMMERFELD MODEL (GÜMBEL'S MODEL)

The rupture of the lubricant film was first taken into account by Gümbel [37]. His approach is a very simplistic way to deal with cavitation while solving the Reynolds equation. In this approach, a limit cavitation pressure (p_{cav}) is defined for cavitation. This limit can be equal to the vapour pressure of the liquid or the gas saturation pressure of the dissolved gasses. The pressures equal to or lower than p_{cav} are set equal to p_{cav}. In this theory, it is assumed that the cavitation occurs in the immediate vicinity of the film's minimum clearance and cavitation pressure (p_{cav}) prevails within the divergent zone (Figure 2.6).

Gümbel's model does not consider the reformation of the lubricant film. It does not satisfy the mass conservation principle of the lubricant flow on the cavitation boundaries. Because the method allows only the positive pressures [26]. In addition, limiting the pressures with a cut-off like approach violates the original conservative nature of Reynolds equation [23].
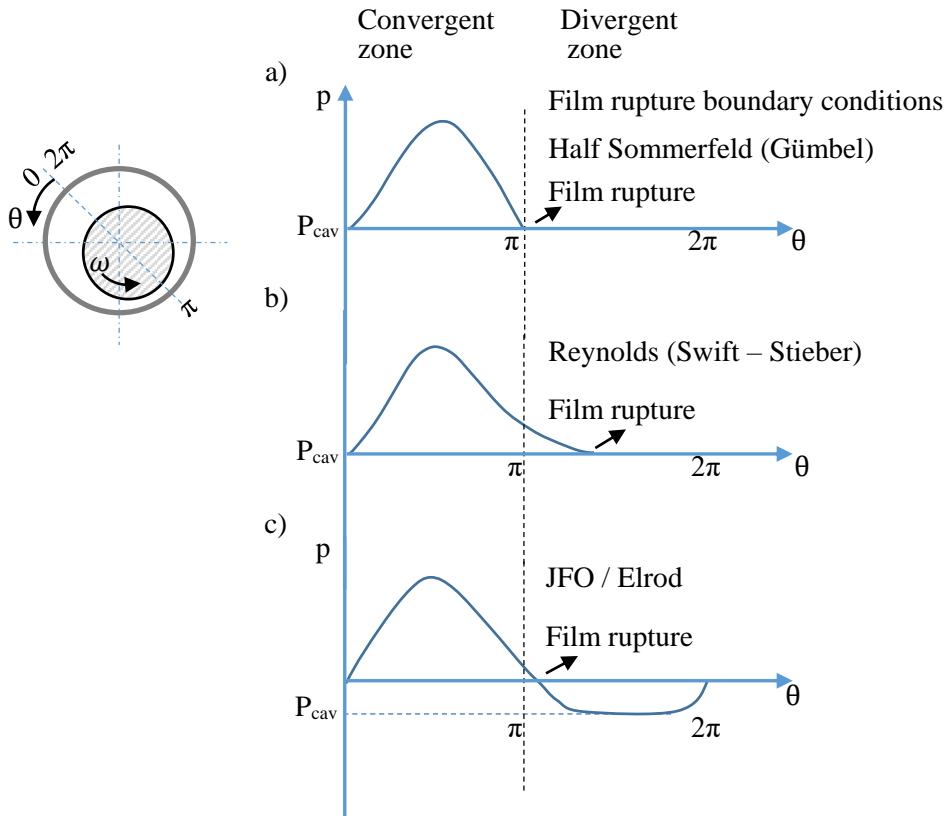
Figure 2.6: Hydrodynamic pressure distribution along a journal bearing circumference based on different cavitation models [23,26].

2.5.3.2   REYNOLDS MODEL (SWIFT-STIEBER MODEL)

Swift [39] and Stieber [38] independently suggested another approach for the film rupture. They assumed the pressure gradients as zero on the cavitation boundaries (Figure 2.6). In addition, cavitation pressure is constant within the cavitation zone. Reynolds boundary conditions can be written as (according to the coordinates shown in Figure 2.7):

$$p = p_{cav} \text{ (in the cavitation zone)} \qquad \frac{\partial p}{\partial \vec{n}} = 0 \qquad (2.6)$$

Here, $\vec{n}$ is the direction normal to the cavitated boundary. According to this model, the Poiseuille flow is zero in the axial and the circumferential direction within the cavitation region and the lubricant is carried through the streamers via the Couette flow (Figure 2.7). Reynolds boundary conditions work well at moderate loads [26, 40]. However, they only predict the rupture boundary of the film and not the reformation boundary. While the mass conservation principle is satisfied on the rupture boundary, it is

not fully enforced on the reformation boundary in this method. Reformation boundary occurs as the pressure increases in the convergent zone. Also, it does not provide good results for dynamically loaded bearings [26,41,42].

2.5.3.3 JAKOBSSON-FLOBERG-OLSSON (JFO) CAVITATION MODEL

Jakobbson, Floberg [43] and Olsson [44] proposed the most widely accepted cavitation model. It assumes that the lubricant is carried through the streamers within the cavitation region as in the Swift-Stieber model (Figure 2.7). However, this model enforces the mass conservation through the entire cavitation zone together with the rupture and reformation boundaries. In this model, it is assumed that the pressure within the cavitation zone is constant and equal to p_{cav}. The film rupture starts when the pressure derivative with respect to the normal direction is zero. These conditions can be written as [45]:

$$p = p_{cav} \text{ (in the cavitation zone)}, \qquad \frac{\partial p}{\partial \vec{n}} = 0 \text{ (on the rupture front at steady state)} \qquad (2.7)$$

In addition, the boundary condition at the film reformation front is defined as [45]:

$$\frac{h^2}{12\mu}\frac{\partial p}{\partial \vec{n}} = \frac{V_n}{2}(1 - \theta_n) \qquad (2.8)$$

Here, V_n is the velocity vector (m/s) and θ_n is the fractional film content (see next section). JFO cavitation model provides realistic prediction of cavitation zones [46,47]. However, it is not easy to implement JFO boundary conditions since cavitation is unknown a-priori (moving boundary problem). Elrod and Adams [48,49] developed one of the first and the most widely used algorithms to implement the JFO cavitation model developed. They incorporated the JFO model into a single Reynolds equation. This method is a mass conservative algorithm and known as Elrod-Adams cavitation algorithm or $p - \theta$ model.
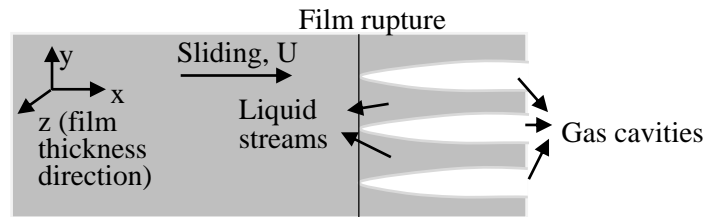
Figure 2.7: Cavities and liquid streams according to Swift – Stieber and JFO boundary conditions [26].

2.5.3.4 $p - \theta$ FORMULATION of the REYNOLDS EQUATION

Elrod [48,49] defines a variable which is so called fractional film content (θ):

$$\theta = \frac{\rho}{\rho_{cav}} \qquad (2.9)$$

Here, ρ_{cav} is the fluid density at the cavitation pressure. The fluid density is denoted by ρ. A cavitation index (g) is defined from a knowledge of θ:

$$\begin{aligned} g = 0; \ \theta < 1 \\ g = 1; \ \theta \geq 1 \end{aligned} \qquad (2.10)$$

This means that the cavitation index is zero within the cavitation zone, and unity elsewhere. The fluid is slightly compressible. The relationship between the density and the pressure is described with the fluid's bulk modulus $\beta = \rho\partial p/\partial\rho$. Reynolds equation can be reformulated with the help of mass conservation equations [50]:

$$\frac{\partial}{\partial x}\left(\frac{\rho_{cav}}{12\mu}h^3 g\beta\frac{\partial\theta}{\partial x}\right) + \frac{\partial}{\partial y}\left(\frac{\rho_{cav}}{12\mu}h^3 g\beta\frac{\partial\theta}{\partial y}\right) = \rho_{cav}\frac{U}{2}\frac{\partial(\theta h)}{\partial x} + \rho_{cav}\frac{\partial(\theta h)}{\partial t} \qquad (2.11)$$

The detailed derivation of eq. (2.11) can be found in [50]. Elrod's method handles both cavitated and non-cavitated zones with the help of g and θ variables.

Many researchers have utilized Elrod's method while dealing with cavitation. Some of them suggested refinements and some developed new approaches based on Elrod's concept [51-53]. Giacopini et al. [54] presented a mass-conserving complementarity formulation of the one dimensional Reynolds equation for the solution of cavitation problems with incompressible fluids. They assumed that the density of the fluid is constant and equal to ρ_0 in the non-cavitated region. In the cavitated region, the fluid cavitates by forming vapor and gas with a density $\rho(x, t)$, which is always lower than or equal to ρ_0 and which varies in both space and time. They defined the complementary variables $p - \theta$ as:

$$\theta = 1 - \rho/\rho_0$$
$$p \geq 0, \quad \theta \geq 0, \quad p\theta = 0$$

(2.12)

In the active region (non-cavitated), the pressure p is greater than or equal to zero and θ is equal to zero while in the non-active region (cavitated), the pressure p is equal to zero and θ is greater than or equal to zero. The one dimensional Reynolds equation is obtained as:

$$\frac{\partial}{\partial x}\left(\frac{h^3}{\mu}\frac{\partial p}{\partial x}\right) = 6U\frac{\partial h}{\partial x} + 12\frac{\partial h}{\partial t} - 6U\frac{\partial(\theta h)}{\partial x} - 12\frac{\partial(\theta h)}{\partial t}$$

(2.13)

This method looks similar to the Elrod's method but there are important differences:

- In contrast to Elrod's method, the variables in eq. (2.12) are complementary through the whole domain. It should be noted that the θ is defined in Elrod's method as mass fraction. However, here it is defined as the void fraction (cavity fraction).
- In Elrod's work the relation between p and θ is obtained via a switch function. Therefore, an *if* statement has to be used in the numerical work. In Giacopini's method, the relationship between p and θ is expressed in terms of complementarity as in eq. (2.12), which holds both in the lubricated zone and in its cavitated counterpart. This eliminates the non-continuous problems and allows for a more efficient solution without application of boundary conditions at the transition from lubricated to cavitated region.
- The formulation of Giacopini results in a standard linear complementarity problem. This implies that the problem is expressed in a form suitable for solution using readily available numerical methods.

Bertocchi et al. [55] extended the method to two dimensional problems. Biancofiore et al. [56] developed a model by using the complementarity formulation in the former references [54,55] to predict the behavior of bearings in which both cavitation and slip at the wall occur. Woloszynski et al. [57] developed an efficient algorithm based on the Fischer-Burmeister-Newton (FBN) method to solve the complementarity formulation of the Reynolds equation. They showed that this algorithm reduces the computational time. This method makes the transient analysis and the optimization of the contacts with complex shapes computationally feasible. Based on this work, Biboulet et al. [58] developed an efficient global grid refinement solver for the iso-viscous-rigid Reynolds equation with cavitation. In the references [59-62], more works about the implementation of FBN based algorithms can be found.

In the current work, the cavitation problem is handled with complementarity variables and FBN algorithm based on the works of Giacopini and Woloszynski [54,57].

2.6 PARALLEL SLIDERS
Parallel sliding contacts are common for machine elements such as face seals, lip seals, and thrust bearings. The sliding surfaces may be macroscopically plain with a random micro geometry (e.g. roughness or pores) or structured in a deterministic manner in order to improve the film formation of either liquid media or liquid lubricants.

According to the classical lubrication theory, the macroscopically plain parallel sliders have no load carrying capacity unless there is squeeze motion. This is basically due to the lack of height variations in the sliding direction. However, in parallel sliding contacts, it is possible to observe a Stribeck-type transition from boundary to mixed lubrication and eventually to full film lubrication [63-65]. In order to explain this, different explanations are suggested which can be categorized as: geometrical imperfections of the surfaces, variation of the lubricant viscosity and, thermal and mechanical deformations of the surfaces [66]. In the next section, some explanations are described.

2.7 LUBRICATION MECHANISMS of the PARALLEL SLIDING CONTACTS

2.7.1.1 DENSITY WEDGE

This mechanism is described in Chapter 2.5.1. It occurs due to temperature increase in the lubricant as it passes a gap between two surfaces. The lubricant heats up due to viscous friction. As a result of heating, the lubricant density decreases. Due to continuity, the mass flow rate must be constant therefore, the volume flow rate must increase. This can cause a load carrying pressure. However, it is stated that this pressure is not sufficient to reach the load carrying capacities which are observed in the experiments [67,68]

2.7.1.2 VISCOSITY WEDGE

Viscosity wedge occurs due to temperature variations in the same way as the density wedge since lubricant viscosity is related to the temperature. Therefore, the viscosity wedge often accompanies the density wedge [68]. Cameron [69] investigated the viscosity wedge. He assumed that one surface which is stationary has a constant temperature and the other surface, which is sliding, is colder at the inlet than it is at the outlet. This will cause a variable viscosity across the film. Consequently, a greater volume of fluid will attempt to enter than will attempt to exit [70]. This will generate a load carrying pressure. An opposite configuration can lead to negative effects. A viscosity wedge can influence the load carrying capacity more significantly than the density wedge since viscosity is more sensitive to temperature.

2.7.1.3 MICRO SURFACE FEATURES (SURFACE ROUGHNESS)

Lebeck [70] explained the influence of micro surface features on hydrodynamic lift as considering each of them as a step bearing. According to this, pressure increases as the fluid flow approaches to an asperity. After the flow reaches the asperity, the pressure decreases. For a symmetrical asperity, the increase and the decrease in pressure would be anti-symmetrical and there would have been no hydrodynamic lift. However, cavitation formation limits the pressure decrease as described earlier. Since there is no such limit for the pressure increase, micro surface features can generate a hydrodynamic lift.

Orcutt *et al.* [72] observed cavitation streamers within the lubricant film and stated that they might be related with surface roughness. Naduvinamani *et al.* [73] investigated the effect of surface roughness on the hydrodynamic lubrication of porous step slider bearings. It is stated that the appropriate surface roughness pattern can increase the load carrying capacity. Similarly, Sahlin [74] worked on micro dimples and showed that pressure generation in a fluid can be enhanced via surface roughness. Minet *et al.* [75] showed that the hydrodynamic lift generated by the surface roughness is sufficient to separate the surfaces.

Brunetière *et al.* [76] modelled the influence of surface roughness by using a very fine mesh. It is stated that the influence of surface roughness can only be fully simulated by capturing the roughness in a realistic way. The hydrodynamic pressure is generated due to the height variations which result from the roughness. The asperities do not act as an independent slider bearing. They show a collective effect on the pressure distribution. Wennehorst *et al.* [77] investigated rough 'soft' elastic solid bodies. In such bodies, elastic deformation cannot be neglected. Elastic deformation may allow a thin film to form between the asperities. Based on this, they modelled the lubricated contact without considering a solid contact Coulomb-like friction law. It was stated that even though the pressure generation by asperities may not be sufficient to separate the surfaces completely, it can decrease the friction significantly in mixed lubrication regime.

2.7.1.4   *SQUEEZE FILM*

This mechanism is described in Chapter 2.5.1. When two lubricated surfaces move towards each other in the normal direction (for instance due to vibrations), the viscous fluid between the surfaces cannot be instantaneously squeezed out [78]. Therefore, a positive pressure can occur in the contact. This can provide cushioning effect and support the load. Lebeck [70] stated that for a sufficient hydrodynamic pressure generation, a higher excitation frequency is necessary than the expected frequencies for mechanical face seals.

2.7.1.5   *DEVIATIONS from PARALLEL*

It has been suggested that true parallel sliding is an ideal which is hard to achieve in the experiments [70]. The surfaces have generally some deviations from parallel due to manufacturing, thermal distortions, etc. Such deviations can generate hydrodynamic load support. It is stated that this mechanism is stronger than the other mechanisms [70]. For the valve part of a swash-plate type axial piston pump, Shin *et al.* [79] calculated significant decreases in the power loss due to enhanced lubrication via deviations from flatness. Face seals can have radial taper or waviness which is described in Section 2.8.

2.8   RECTANGULAR FACE SEALS

2.8.1   RECTANGULAR FACE SEAL DESIGN

Rectangular face seals are commonly used in rotary connections of automatic automotive transmissions, which transmit pressurized oil to the actuators (Figure 2.8a). They are similar to mechanical face seals but they have rather a simple design. Figure 2.8b shows a cross-sectional view of a rectangular face seal in operation. The seal is placed in a groove on a shaft with a loose fit. The pressurized oil pushes the seals to the counterface and the housing and thus, the sealing function is realized. It should be noted that a small portion of the seal face is not in contact with the counterface. The seal can move relative to the housing and the counterface. Either the housing can be stationary while the counterface is rotating or vice versa. In such sealing systems, the area of interest is generally the contact between the seal and the counterface (axial sealing interface). The influence of the contact between the seal and the housing (circumferential sealing interface) is negligible since the relative motion between the seal and the housing was observed to be small [80,81].
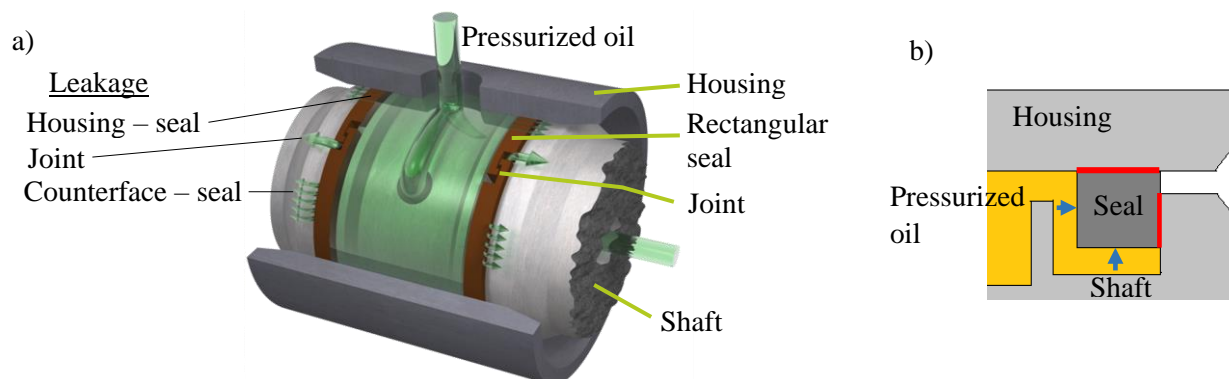
Figure 2.8: a) Rotary joint with rectangular face seals [80] b) Cross sectional view of a face seal in operation. Red lines represent the contacts seal – housing and seal – counterface.

Rectangular face seals have a joint for an easy assembly (Figure 2.9). This joint is the main leakage source and can result in high leakage amounts. However, high leakage is tolerable in rectangular face seals since the leaked oil stays in the transmission system. In order to decrease the leakage through the joint, different joint designs are developed [82]. In addition to the joint, the leakage can occur from the axial and the circumferential sealing faces.

Grey cast iron is used commonly as a rectangular face seal material. However, thermoplastics such as polyether ether ketone (PEEK) have started to become popular because of their attractive properties like high temperature resistance.
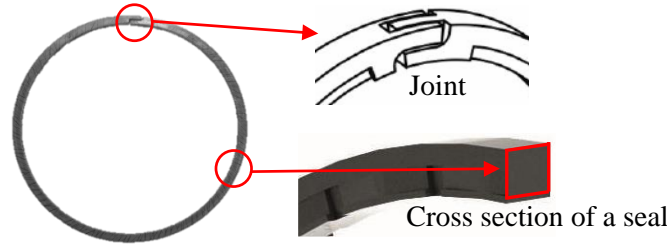
Figure 2.9: Rectangular face seal.

2.8.2 KINEMATICS and FRICTION TORQUE

It is not predetermined whether the seal slides at the axial face or the circumferential face. Depending on the sliding motion, friction losses can occur at the axial face or at the circumferential face or at both faces simultaneously. In case the friction losses occur at both faces, the seal rotates at a speed lower than the speed of the shaft. This is due to the balance of the forces acting on the seal. For a stationary housing and the rotating counterface, the friction forces are acting at the opposite directions on the seal as seen in Figure 2.10. The friction force (F_F) acting on the axial face tries to make the seal rotate in CCW direction while the friction force (F_C) between the seal and the housing counteracts to F_F. When the friction forces F_F and F_C balances each other, the seal rotates neither with acceleration nor deceleration.
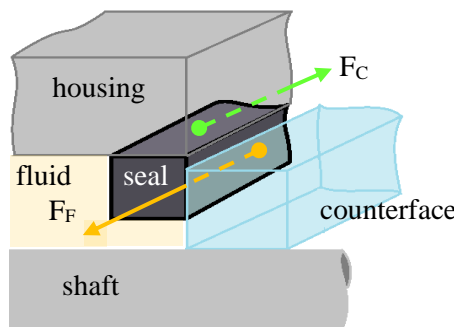
Figure 2.10: Forces acting on a rectangular face seal. The counterface is rotating in CCW direction while the housing is stationary.
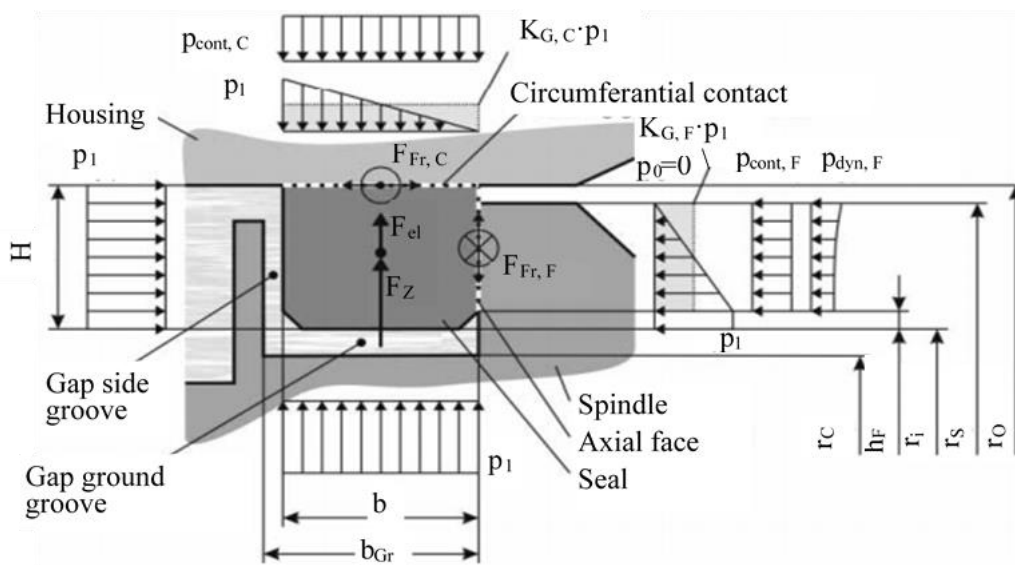
Figure 2.11: Forces acting on a rectangular face seal [83].

A simple model is shown in Figure 2.11 with the forces acting on a seal [83]. The maximum friction torques occurring at the axial and the circumferential faces are $M_{Fr,F}$ and $M_{Fr,C}$, respectively. They can be determined via a force balance. In the axial direction, the hydraulic force resulting from the pressure p_1 is acting. Against this force, the forces resulting from the median contact pressure ($p_{cont,F}$) and the hydraulic pressure in the gap are acting. Hydraulic pressure in the gap between the counterface and the housing has a static portion ($p_{cont,F}$) caused by the pressure profile in the gap and a dynamic portion ($p_{dyn,F}$), as consequence of the tangential fluid flow. Similarly, the forces occurring in the gap between the housing and the counterface can be analysed. It should be noted that no force caused by the dynamic portion of the hydraulic pressure occurs in the circumferential gap.

The force ratio between both circumferential and axial surfaces can be obtained from the balance ratio (hydraulic loading area divided by the area of the seal face):

$$k_F = \frac{A_1}{A} = \frac{r_O^2 - (r_i + h_F)^2}{r_S^2 - (r_i + h_F)^2} \tag{2.14}$$

The fluid pressure resulting from the dropping pressure profile in the axial gap is proportional to the sealed pressure ($K_{G,F} \cdot p_1$). When the gap is parallel, the pressure profile is almost linear. Therefore, the pressure gradient factor $K_{G,F}$ becomes 0.5. When the gap is convergent, pressurized oil can penetrate further in the gap so the load at the axial contact face decreases ($K_{G,F} \rightarrow 1$). Vice versa happens when the gap is divergent ($K_{G,F} \rightarrow 0$). Here, a convergent gap is the gap where the gap height increases towards pressurized oil; the opposite means a divergent gap.

The contact pressure and the friction torque at the axial face can be determined as:

$$p_{cont,F} = p_1(k_F - K_{G,F}) - p_{dyn,F} \tag{2.15}$$

$$M_{Fr,F} = f_F \int_{r_i+h_f}^{r_s} \int_0^{2\pi} p_{cont,F} \cdot r^2 \, d\varphi \, dr \tag{2.16}$$

$$M_{Fr,F} = \frac{2}{3}\pi \cdot f_F \cdot (r_s^3 - (r_i + h_F)^3) \cdot p_{cont,F} \tag{2.17}$$

Here, f_F represents the coefficient of friction at the axial contact. Similarly, the contact pressure and the friction torque at the circumferential face is:

$$k_C = \frac{b \cdot r_i + b_F \cdot h_F}{b \cdot r_o} \tag{2.18}$$

$$p_{cont,C} = p_1(k_C - K_{G,C}) - p_{dyn,C} + \frac{F_z + F_{el}}{2 \cdot \pi \cdot b \cdot r_o} \tag{2.19}$$

$$M_{Fr,C} = f_C \int_0^b \int_0^{2\pi} p_{cont,C} r^2 \, d\varphi \, db \tag{2.20}$$

$$M_{Fr,C} = 2\pi \cdot f_C \cdot r_o^2 \cdot b \cdot p_{cont,C} \tag{2.21}$$

Here, F_z and F_{el} are the centrifugal and the elastic forces, respectively. f_C is the coefficient of friction at the circumferential contact. If f_C is assumed to be equal to f_F, the seal rotation would only depend on the geometry of the shaft and the seal and, the gap geometry.

The axial face of the seal has a tendency to generate a converging gap. This provides a better cooling by the fluid. Therefore, it is generally preferred to have the sliding motion of the seal at the axial face surface of the seal.

2.8.3 HYDROSTATIC LUBRICATION of RECTANGULAR FACE SEALS

As described in the previous section, face seals have a pressure gradient across the face. There is pressurized oil at the inner diameter and ambient pressure at the outer diameter. This pressure difference generates a fluid flow across the gap. Since this pressure generates a force counteracting to the hydraulic force acting on the seal, a hydrostatic pressure relief can be achieved. The pressure profile in the gap depends on the gap shape (Figure 2.12). For a parallel gap, hydrostatic pressure increases as the gap becomes convergent while it decreases as the gap becomes divergent. On the other hand, the convergent gap would increase the leakage while the divergent gap can lead to wear of the seal surface.
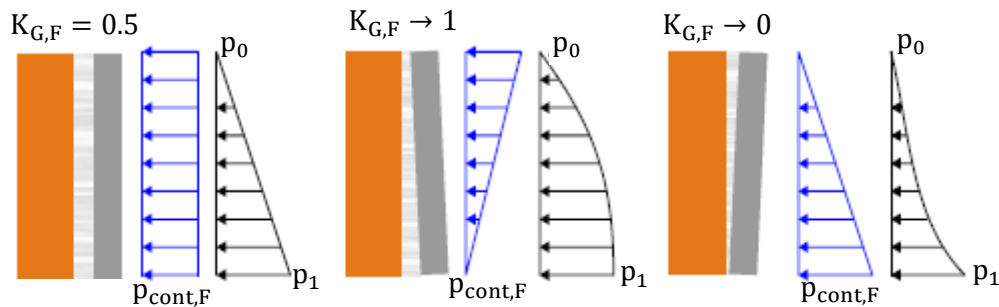
Figure 2.12: Influence of the gap form on pressure distribution [80].

The deviation from parallel in the radial direction is called as radial taper / tilt. It can occur due to the axial temperature gradient and pressure distribution. Gronitzki *et al.* [80] investigated pressure and temperature induced deformations of a rectangular face seal and the groove in which the face seal is placed. Because of the groove geometry in which the seal is placed (see Figure 2.13a), the cross section of the seal rotates at CW when the pressurize oil is introduced. Therefore, the axial gap becomes convergent (Figure 2.13a). On the other hand, pressure induced deformations of the shaft are negligible, unless it would be a hollow shaft with a thin wall.
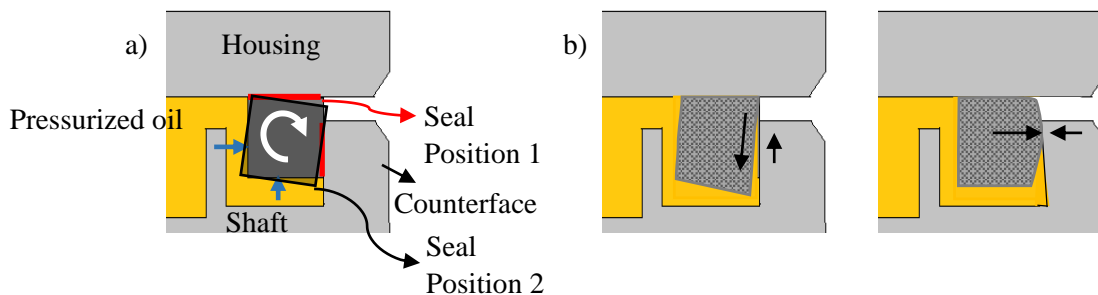
Figure 2.13: (a) Pressure and (b) temperature induced deformation of a rectangular face seal [80].

The temperature increase on the axial face of the shaft leads to the expansion of the seal in both axial and radial direction (Figure 2.13b). The final deflection of the seal ring is the combination of the temperature and pressure induced deflections. Different researchers have worked on the effects of the radial taper [84,85]. Etsion [86] showed that hydrostatic effects are as important as hydrodynamic effects for a proper sealing operation.

2.8.4 HYDRODYNAMIC LUBRICATION of RECTANGULAR FACE SEALS

The mechanisms described in Chapter 2.7 have been considered to generate hydrodynamic pressure in face seals. However, except surface deviations, the influence of other mechanisms on pressure generation are negligible or low. Deviations from the parallel in circumferential direction such as waviness are found to generate the most considerable hydrodynamic pressures (Figure 2.14). The influence of waviness is investigated commonly for mechanical face seals. It is suggested if a mechanical face seal operates at a film thickness of 1 μm, a variation of the order of 0.1 μm would be sufficient to generate a hydrodynamic lift [84].
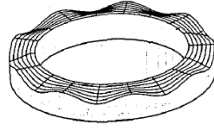
Figure 2.14: A wavy seal surface [87].

Waviness can be present on the face seal surface due to manufacturing or non-axisymmetric heating during the operation. Minet et. al. [88] provided some statistics about the waviness of mechanical face seals. It is reported that the waviness is up to 1 μm with two peaks in face seals. Many researchers investigated the influence of waviness numerically and experimentally and showed the contribution of the waviness [89-93].

2.8.5   OPTIMIZATION of RECTANGULAR FACE SEALS

Rectangular face seals are subjected to high pressures, high sliding speeds, and thermal stresses. Minimizing the friction losses is priority. The friction torque (M_F) at a given speed results from the integral of tangential stresses acting in the dynamic sealing face, both from solid contact and fluid shear. Mostly, the friction torque from solid contact will prevail [83]:

$$M_F = \int_{F_T} r \, dF_T = \int_A r \cdot f \cdot p_{cont} \, dA \qquad (2.22)$$

The friction torque depends on the effective radius (r) of the contact area, coefficient of friction for boundary or solid contact (f), the contact pressure (p_{cont}) and the contact area (A). Friction torque can be decreased by decreasing the normal contact force ($p_{cont} \cdot$dA) via hydrostatic and hydrodynamic load reduction. Another method can be reducing apparent coefficient of friction by macroscopic or microscopic features, which enhance micro-elastohydrodynamics and reduce boundary lubrication contribution [83].

2.8.5.1   HYDROSTATIC LOAD REDUCTION

The easiest method to reduce the normal contact force ($p_{cont} \cdot$dA) is to the decrease the contact area. This can be done by manufacturing hydrostatic pockets and chamfers which are open to the pressurized fluid (Figure 2.15). With hydrostatic surface features, friction torque and consequently, the contact temperature can be reduced significantly.

Figure 2.15: Hydrostatic load reduction via chamfers (left) and pockets (right) [83].

2.8.5.2   HYDRODYNAMIC LOAD REDUCTION

Surface waviness and texturing / structuring can enhance the hydrodynamic pressure generation and thus lubricant film formation. Waviness can be machined in to the surface initially. In the last decade, surface texturing became quite popular and it is applied to different machine elements. Etsion *et al.* [94] investigated mechanical face seals with structures theoretically and experimentally. It was reported that the seal performance can be improved via surface texturing. Other researchers also reported that textured seals and thrust bearings showed a better performance [95-99].

Structures can trigger cavitation. Pressure decreases in the divergent zone of structures whilst it increases in the convergent zone. Cavitation may occur in the divergent zone and would limit the pressure drop. Thus, a positive net lifting force can be obtained. In contrast to some researchers, Brunetière *et al.* [33] reported that the structures can only generate a significant hydrodynamic lift when they are combined with roughness.

Some other mechanisms are also suggested to explain the enhanced lubricant film after surface texturing. According to Tønder [100], lubricant is trapped in the contact due to textures and this sustains the lubricant film. Fowell *et al.* suggested [101] a mechanism which is so called 'inlet suction'. In this mechanism, when a lubricant enters to the divergent zone of a structure a large decrease in the lubricant pressure occurs. This pressure gradient has the effect of sucking lubricant into the contact. When the enhanced flow reaches the convergent zone of the structure a greater peak pressure is induced than would otherwise be the case. Vladescu *et al.* [102] also showed that the cavitation formation can enhance the lubricant entrainment.

Some researchers suggested that inertia effects are responsible for load carrying capacity in textured surfaces [166]. Therefore, they solved the full Navier-Stokes equations for the textured surfaces since the Reynolds and the Stokes equations do not consider the inertia effects. Sahlin [167] suggested that the inertia effects are the dominant mechanism for pressure generation in textured surfaces. However, Dobrica et al. [168] found contradicting results. It is suggested that the inertia effects can be positive or negative depending on the local flow conditions [169]. Asymmetric features (steps and wedges) do not need cavitation. However, symmetrical structures need cavitation to generate lift.

Etsion's [170] and Tønder [171] proposed that the mechanism of the surface texturing is based on the collective texture effect. Therefore, partially textured surfaces can often be more efficient than the fully textured surfaces [172]. According to this concept, the textured inlet has a larger mean film thickness than the non-textured outlet. Therefore, a partially textured contact behaves similarly to a Rayleigh step [166]. This can lead to a considerable load carrying support, even if cavitation does not occur at all.

Overall, surface texturing is an attractive method to decrease friction by producing hydrodynamic effects. The favourable features and the influences of the textures depends on the application.

3   AIMS AND SCOPE

Parallel sliding contacts are common for face seals, lip seals and plain thrust bearings. The sliding surfaces may be macroscopically plain with a random micro geometry (roughness, pores) or structured in a deterministic manner in order to improve film formation either by liquid media or by liquid lubricants. In both cases it is possible to observe a Stribeck type transition from boundary to mixed lubrication and eventually to full film lubrication. The existence of local films and a net lifting force coincides with local cavitation on a microscopic respectively macroscopic scale. Many researchers showed that cavitation plays an important role in hydrodynamic film build up. In this work film formation mechanisms in parallel sliding contacts are investigated via textured rectangular face seals experimentally and numerically by focusing on the relationship between cavitation and film formation. The work presented here selects a textured seal as the main object for the ease of cavitation observation and cavitation area calculation. Secondary aim of the work is to show the influence of structures on friction and film formation. For this reason, a non-textured rectangular face seal is also investigated. Firstly, a group of experiments are realized and then the axial sealing contact is modelled. Friction torque, contact temperature and film thickness measurements are conducted on textured and non-textured rectangular face seals. Thus, the seal performances are investigated. Secondly, film thickness measurements are performed at an optical test rig by using a laser induced fluorescence method. Besides, cavitation is observed and evaluated at the axial seal interface. The selected texture type is a bidirectional structure and applied to the axial face of the seals. This type of texture allows to realize direct observation of concentrated cavitation within texture at the seal interface. Thus, validation of numerical results is possible in terms of cavitation form and size in addition to film thickness. This was not possible with non-textured seals since there; the cavitation was randomly distributed. Thirdly, thermographic measurements are performed at the optical test rig to observe local temperature increments at the axial sealing interface during operation. For this reason, a thermal camera is used. The measured maximum and the minimum temperatures are recorded. Also it is determined that where the seals are starting to heat up during operation. This is important to understand thermal deformations of a seal and also viscosity effect in the contact.

Later on, textured sealing contacts are numerically modelled. Reynolds equation is solved by using a mass conservative algorithm based on JFO cavitation theory to predict pressure build-up and cavitation in textured rectangular face seals for full film hydrodynamic lubrication conditions. For the simulation three different models are implemented; a purely smooth surface, a surface with macro irregularities and a rough surface. To get real macro irregularities and roughness, seal surface is scanned via a laser microscope. The numerical results are validated by comparison with experimental results in terms of cavitation area ratio, film thickness and friction force. Influence of temperature thus, viscosity is shown by applying different viscosities to the models. Influences of tilting and waviness of the seal gap on cavitation and film formation are shown by changing gap forms. Furthermore, different cavitation pressures are selected and used in simulations to investigate how cavitation pressure changes the cavitation and film formation behaviour. In addition, the work also shows besides the effect of texturing, the effect of surface irregularities and roughness as well.

The work presented here allows an understanding of film formation by focusing on cavitation occurrence in axial contacts and shows consideration of cavitation is an important parameter to model film formation. Besides, it contributes to the surface texturing field. Some researchers showed that structures alone do not generate hydrodynamic lift. However, many of these works were done for dimple type structures. The current work presented here focuses on relatively large structure form which is a "T shape". It could be shown that macro irregularities change film formation noticeably by influencing pressure build up and cavitation formation. Because many simulations focus on idealized geometries the influence of macro deviations needs to be considered. The results show that the numerical and the experimental approaches, implemented in the current work applicable to the other parallel sliding contact applications.

4   EXPERIMENTAL METHODS

4.1   TEST SAMPLES

Test seals are made of PEEK (Table 4.1). The sealing material contains glass bubbles which has a density lower than 1 g/cm^3 and therefore they are used to produce low-weight compounds (Table 4.2). The structured seals are injection molded. After this, the surfaces are ground to decrease the burrs. However, the burrs are significant in the structure zones even after grinding as the tool is less capable to remove the burrs in these zones. The glass bubbles are persisting only in the subsurface zone due to grinding.

Table 4.1: Properties of PEEK.

Glass transition (T_g)	~145°C – 150°C
Melting point	~343 °C

Each structured seal has 28 bidirectional structures on its axial face and a joint for an easy assembly (Figure 4.1). One structure consists of inclined surfaces to generate hydrodynamic effects and a deep, rectangular area between the inclined planes for feeding oil. The deep area is open to the pressurized oil. There is a small, plain, unstructured area between the structures.

The non-textured seals are called as standard seals in this work. They are completely mechanically processed. The surfaces of the standard seals have randomly distributed micro-pores (Figure 4.2a). These features are due to glass bubbles. They explode during the manufacturing process. The diameter of the glass bubbles varies from 30 µm to 90 µm. The depth of the micro pores is generally up to 10 µm. However, the depth of a few pores reaches up to 50 µm. Furthermore, some of the glass bubbles do not generate pores. They are at the same height with the main surface but there are dents around them in which they are located. The standard seals have a step with a depth of 300 µm (Figure 4.2b). The width of the faces of the standard seals are slightly larger than those of the structured seals. However, the contacting areas of the structured seals are not smaller in total since these seals have plain, unstructured areas between the structures.
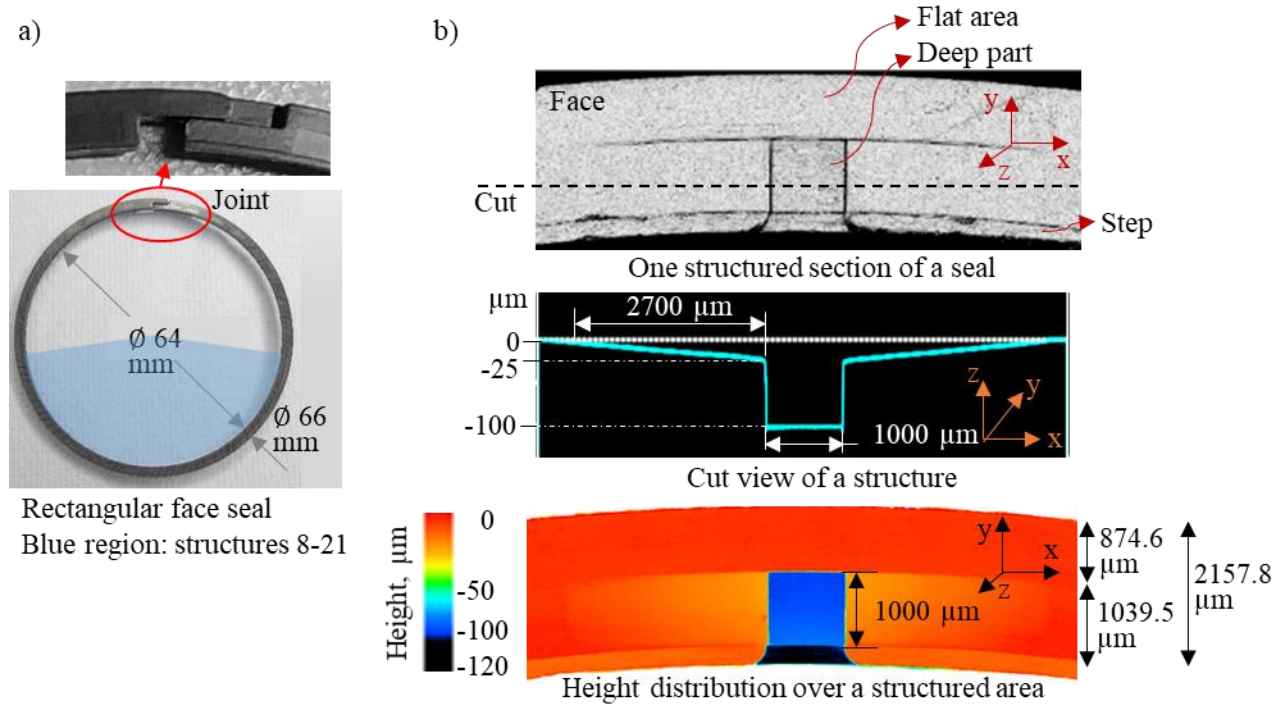
Figure 4.1: a) Structured seal b) Geometry of a structure.
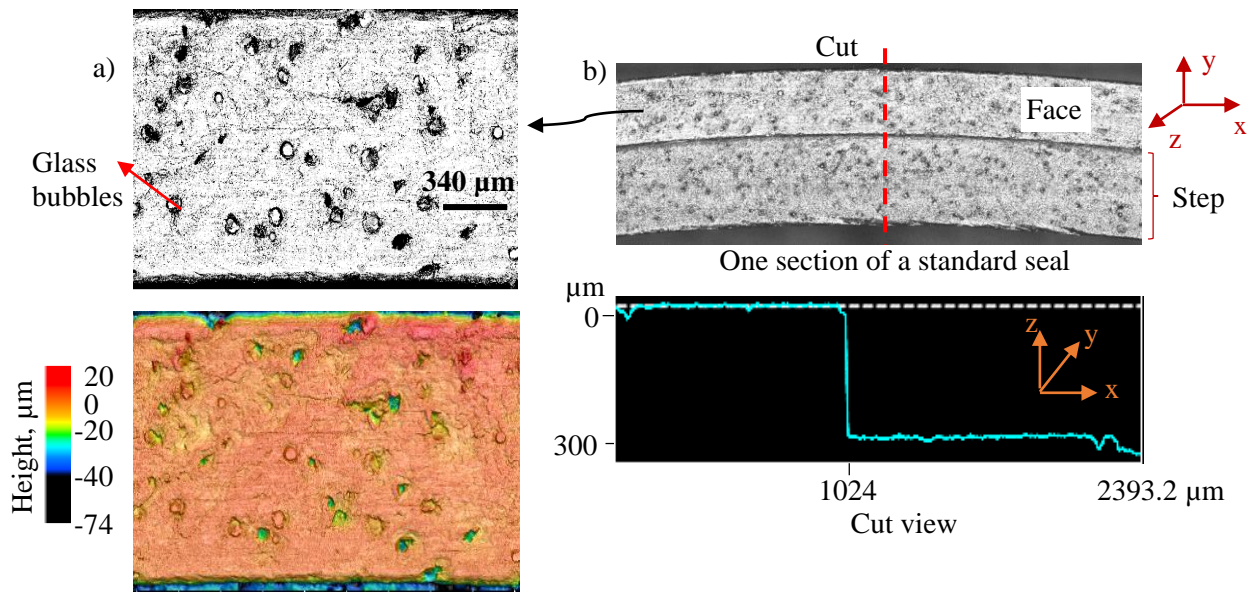
Figure 4.2: a) Randomly distributed glass bubbles over the standard seal surface b) Standard seal geometry

During the experiments, ATF M-1375.4 which is a transmission oil is used. The properties of this lubricant are shown in Table 4.3.

Table 4.2: Properties of the test seals.

	Structured seal	**Standard seal**
Outer diameter	66 mm	66 mm
Production method	Injection moulding	Mechanical
Basic polymer	PEEK	
Filler	10 % Glass bubbles, 40 % anorganic / mineral fillers	

Table 4.3: Properties of the lubricant ATF M-1375.4.

Dynamic viscosity	51.3 mPa·s at 20 °C
Boiling point	> 280 °C (estimated value(s))
Vapour pressure	< 0.5 Pa at 20 °C (estimated value(s))

4.2   FRICTION, TEMPERATURE and LEAKAGE TESTS

4.2.1   UNIVERSAL TEST RIG

Gronitzki [80] developed a universal test rig by using standardized measurement methods in order to measure friction torque, sealing contact temperature and leakage of the seals. It has been improved by Schüller [81]. This test rig is based on a rotary connection (Figure 4.3). It is driven by a direct current motor with the power of 6 kW via a belt. The maximum operating speed is 15000 min^{-1} and reached via different transmission ratios. An inductive torque sensor is placed between counter shaft and the main shaft to measure friction torque and rotational speed. A telemetry is placed to measure the sealing contact temperatures. The modular test head design allows to test different rotary connection systems. In the current work, a common rotary connection design with a stationary housing and a rotary shaft is used.
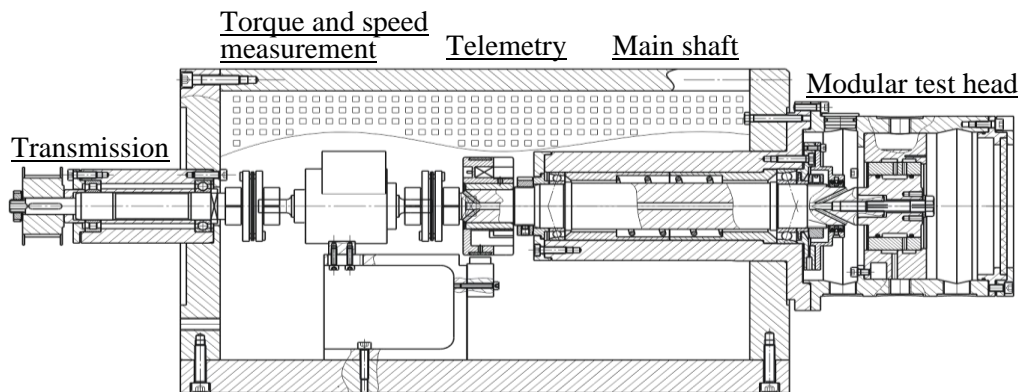
Figure 4.3: Universal test rig [80].

Figure 4.4 shows a cross sectional view of the modular test head with the pressure chamber used in the experiments. The pressure chamber is sealed with two rectangular seals and it consists of the test shaft, the test sleeve and the outer adapter. The test head has some bores to supply pressurized and warm oil. The warm oil enters the system through the bore (9) and reaches a radial channel in the outer adapter. It warms up the test head and leaves the system through a bore at the back of the test head. The housing, the outer adapter and the test sleeve are sealed via interference fits which provide acceptable sealing up to 7 MPa.

Pressurized oil enters the system through the bore (10). It reaches the radial channel between the test sleeve and the test shaft via the outer adapter / housing and the test sleeve. Rectangular seals are responsible to seal left and right sides of the channel. Pressurized oil can only leave the system as leakage through the leakage path between the test sleeve and the test shaft as much as the rectangular seals allow.

The leaking oil from the seals exits the test head via the bores (11). It is first collected separately by leakage weighing cups which can be opened and closed by means of solenoid valves. During the leakage measurements, leaking oil accumulates in the closed weighing cups and measured via the load cells. When the measurement is completed, the cups are open and the oil rejoins into the oil circuit.

The test rig has thermocouples at different points (Figure 4.5). The temperature of the test head (T_0) is measured by placing a thermocouple through the outer adapter. Another group of thermocouples are placed through the test sleeve to measure the oil temperature (T_3) and the temperatures near the sealing contacts between the seals and the test sleeve (T_1, T_2). In addition, two thermocouples are placed through the counterface of each seal to measure the temperatures between the seals and the counterfaces (TM_1 and TM_2). It should be noted that contact temperatures TM_1 and TM_2 are average values and they do

not show the local temperatures. The bores where the thermocouples were placed in were made as small as possible (around $0.5 - 0.6$ mm) to minimize their influences on the axial sealing contacts. For the sake of assembling the thermocouples, the test shaft was manufactured as multi piece (Figure 4.5). Therefore, the counterfaces of the rectangular face seals were manufactured as separate discs and assembled to the main shaft via screws. Isolated thermocouples were assembled as their tips were slightly higher than the counterface surfaces by using a two component epoxy adhesive. After assembly of the thermocouples, the counterfaces were ground to obtain an even counterface surface. For the technical details of temperature measurements see Ref. [80].

1) a- Shaft
   b- Counterfaces
2) Seal1
3) Seal 2
4) Test sleeve
5) Outer adapter
6) Main shaft
7) Screw
8) Housing
9) Warm oil
10) Pressurized oil
11) Leakage bores
12) Thermocouple T_0
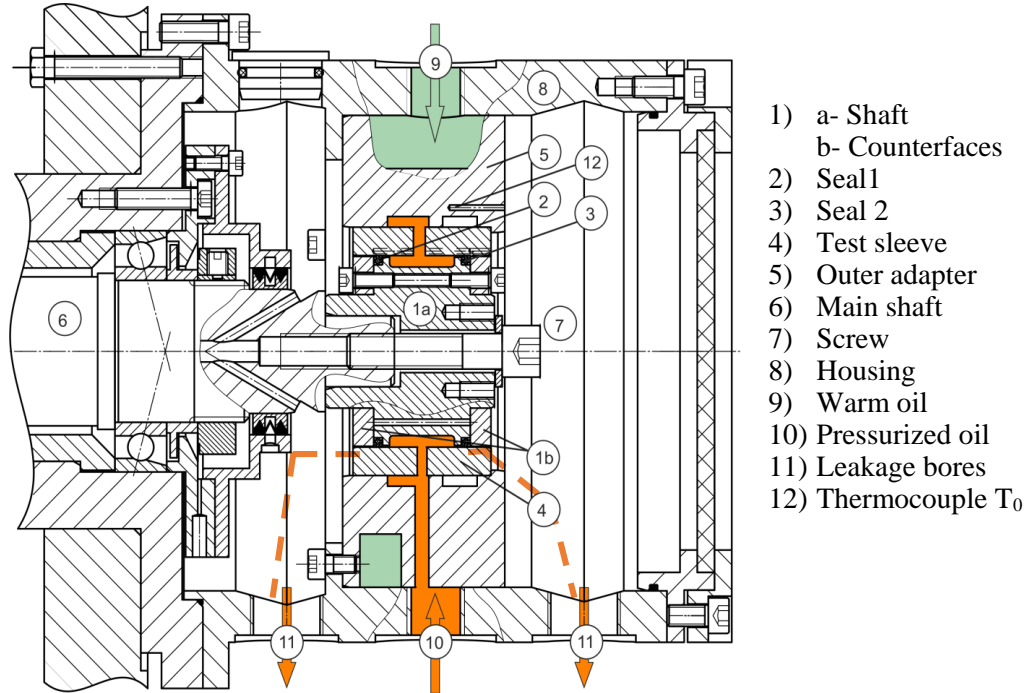
Figure 4.4: Modular test head [80,81].

The sump oil is temperature pre-conditioned via heating elements. During operation, friction losses in the sealing contact can warm up the test head rapidly. Therefore, a cooling system is available to keep the test head temperature at the desired sump temperature.
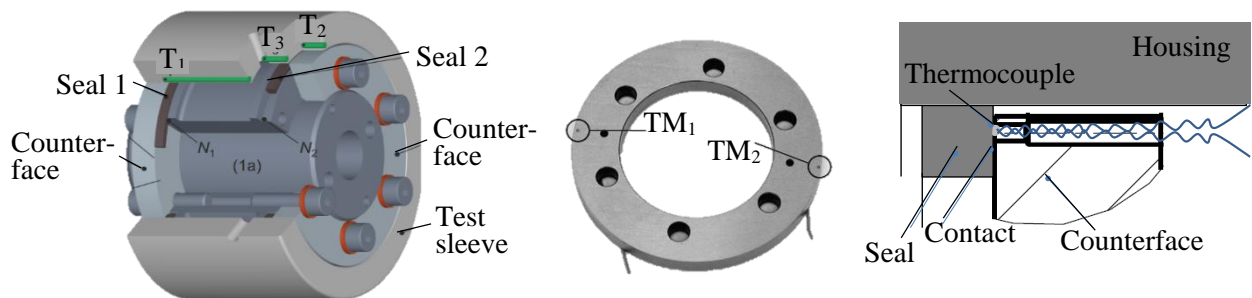
Figure 4.5: Multi piece test shaft (left), a counterface with thermocouples (middle) and the contact temperature measurement (right) [80,81].

4.2.2 TEST PROGRAM

The test program consists of three stages:

1) Idle running: The test rig is run without the rectangular face seals, test shaft and oil to determine friction torque in the main shaft which arise from the bearings and the labyrinth seals. Friction torque is measured at different speeds after 120 s rotation at each speed to provide uniform temperature distribution in the bearings. A curve showing the behaviour of friction torque with respect to speed

is obtained. Thus, it can be subtracted from the measured friction torque during the experiments to find the friction torque arises only from the seal rings.

2) Function test: Sealing performance is investigated at different pressures and speeds by measuring friction torque, leakage and temperatures (T_0, T_1, T_2, T_3, TM_1 and TM_2). Figure 4.6 shows pressure and speed steps which are used in the function tests. The rotational speed increases from 0 to 6400 rpm and the pressure increases from 0 to 2 MPa for each speed. Each pressure-speed step is held for 270 s for the system stabilization. The functional test is carried out before and after the long term test in order to investigate the influence of wear.
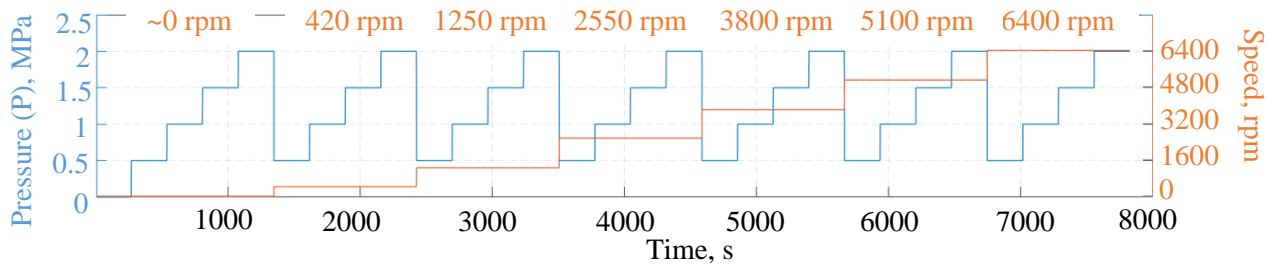
Figure 4.6: Pressure and speed steps in the function test.

3) Long term test: The seals run under continuous load as in a real transmission whilst changing gears. This test consists of load cycles with the duration of 240 s. The load cycle, which is shown in Figure 4.7, is repeated over a period of 18 h. In one cycle, the rotational speed is 850 rpm for 55 seconds and 6400 rpm for 160 seconds. In parallel, the pressure is increased to 2 MPa and reduced three times to 0 MPa for a total of three seconds. The aim of the long term test is to observe influence of the running in process on seal performance and wear behaviour of the seals. Therefore, speeds and pressures are selected to achieve the aging of the rectangular seals within the test duration.
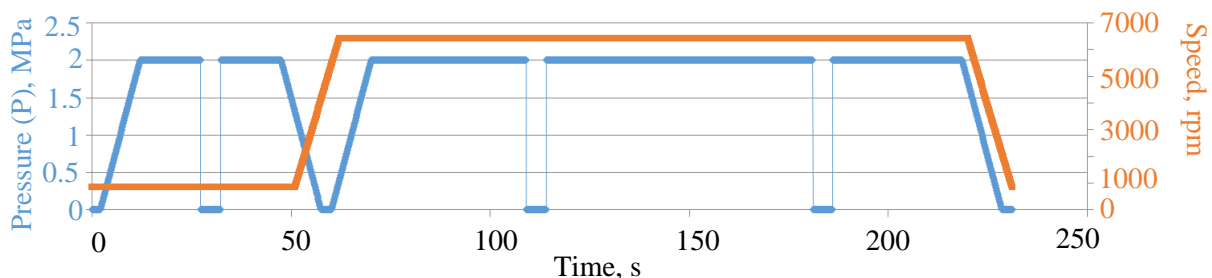
Figure 4.7: One cycle of the long term test

Four seals from each seal type and four counterfaces were tested in the universal test rig (Figure 4.8). For each test, two seals and two counterfaces were combined in pairs. Surface profile and roughness of the seals and the counterfaces were investigated via laser microscope before and after tests. The sump and the test head temperature was selected as $T_0 = 90\ °C$ (see Figure 4.4).
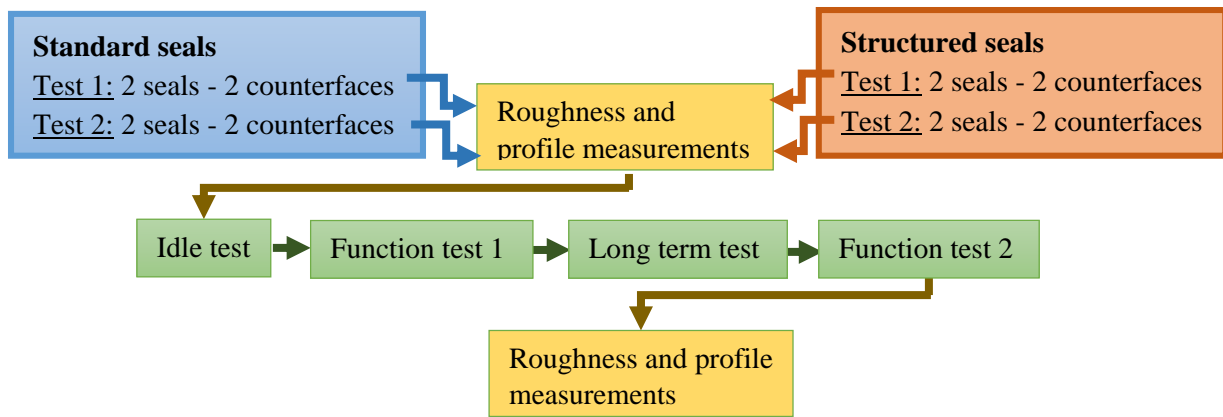
Figure 4.8: Test method.

4.3 OPTICAL TESTS

The optical tests fulfil two main tasks; determination of the lubricant film thickness including the observation of the cavitation morphology and detecting the local contact temperatures. There are various methods to realize these aims. These methods are described in the following chapters. Later on, the optical test rig and the fundamentals of the selected methods are explained.

4.3.1 FILM THICKNESS and TEMPERATURE MEASUREMENT METHODS

In the following, different lubricant film thickness determination methods and local contact temperature monitoring techniques are described. Depending on the advantages and the disadvantages of the described methods, the reasons of the selected methods are explained in the conclusion.

4.3.1.1 FILM THICKNESS MEASUREMENT METHODS

Lubricant film thickness measurement methods can be divided into two groups; electrical and optical methods (Table 4.4) [103,104]. Electrical methods are based on the fact that many machine elements are metallic and the lubricant film which is separating those elements behaves as an electrical insulator. Therefore, the film can be assumed as an electrical resistance or capacitance. Electrical resistance method [105-107] struggles to determine the absolute film thickness since it gives different results depending on the measurement location due to asperities. Most important, it is shown that the resistivity of the lubricant changes with temperature. Therefore, the results can change with increasing contact temperatures [108]. This method is suitable for light loads, very slow speeds and linear geometries (contact length is necessary to calculate the lubricant resistance) and it is successful to detect the film rupture [109,110].

The electrical capacitance method implements the electrical capacitance theory to determine the film thickness which separates two machine elements. It assumes the surfaces of the machine elements to be parallel to each other; thus the system becomes a parallel plate capacitor. This assumption leads to a direct relationship between the quantity of the capacitance and the lubricant film thickness. In addition to being often used for roller bearings [111-114], it is also used to measure the film thickness in thrust bearings [115,116], internal combustion engine piston rings [117,118], cams [119,120] and gears [121]. This method has some drawbacks such as the sensors which should be assembled in the lubricant film. The film can be disrupted at the locations of the sensors. Also, this method is more sensitive for thin films hence, measuring the film thickness distribution is hard and the film thickness can be underestimated. Besides, the capacitance of the lubricant can change during the operation due to contamination, air entrainment [122], shear rate and temperature [123, 124].

Inductive methods [125-127] determine the lubricant film thickness by using the change in magnetic flux across the contact. They are based on the fact that in case an alternating current flows through a coil, it will generate eddy currents in a magnetic material which is located close to the coil and these eddy currents will decrease with increasing film thickness since the film separates the coil and the

surface. This method can generate problems since some transducers should be used in the contact as in the film capacitance method. Furthermore, contact temperatures may influence the results.

Table 4.4: Film thickness measurement methods.

Film thickness measurement methods		
Electrical methods	Optical methods	Others
• Electrical resistance • Film capacitance • Inductive	• Optical interferometry • Fluorescence	• Ultrasound

Optical methods allow the direct observation of the lubricant film and they are powerful methods. These methods consist of techniques such as optical interferometry, x-ray transmission and fluorescence. Optical interferometry is based on the interference of the two light waves. The lubricant film thickness can be measured via two techniques by using an optical interferometry. Fringe colour technique [128,129] is quite similar to the Michelson Interferometry [130]. A light can be split and transmitted to a reference mirror and a machine element. The lubricant film at the interface of a machine element generates a delay in the light which is reflecting from the machine element. When this light is recombined with the light reflected from the mirror, interference patterns can be obtained and used to analyse the lubricant film. This method is mostly suitable for EHL contacts since it can measure thin films (up to around 1 μm since the coherence of the light decreases as the film increases).

In dark band fringe technique [131], a white light is used to produce a group of reflected beams at different wavelengths. Later on, all the reflected beams are collected with a fixed angle thus a circular fringe is obtained. The fringe pattern which consists of black and white circles results from the combination of the beams with different angles. This technique allows the measurement of thick films.

Fluorescence methods utilize the properties of the fluorescent substances to measure the lubricant film thickness. Fluorescent substances emit light at longer wavelengths when they are excited by a light source. The emitted light is the amount of fluorescent substance in the area of interest. After the calibration of the system, a relationship between the fluorescence intensity and the lubricant film thickness can be obtained. A broad range of film thicknesses (from thick films to the fluorescence emission from one molecule depending on the visualization equipment) can be measured via the fluorescence method [132]. Fowell et al. [133] mapped the whole contact areas of the elastomeric seal materials via laser induced fluorescence method and they measured a very wide span of thicknesses (50 nm to 100 μm). Similarly, Necas et al. [134] used the fluorescence method for lubricant film mapping. They used a mercury lamp to induce the fluorescent substance instead of laser. Petrova et. all [135] managed to transition between the lubricant regimes via fluorescent method. Drawbacks of the fluorescent method are the reflectivity of the objects, requirement of a reliable calibration and the fluorescence quenching. Some researchers improved the method to solve the reflectivity problem by using two different fluorescent substances [136]. Calibration and fluorescence quenching are described in the next chapters. Overall, the optical methods require optically translucent machine elements which might be costly or difficult to manufacture.

In addition to electrical and optical methods, some other techniques are also available such the ultrasound method. In the ultrasound method, a transducer is placed at the back of a machine element and it transmits ultrasound through the machine element. The transmitted ultrasound penetrates to the lubricant film at the interface of the machine element where it is partially reflected back. The proportion of the reflected ultrasound can be used to determine the reflection coefficient. Thus, the lubricant film thickness can be calculated via an   ultrasonic spring model which contains the reflection coefficient [137]. Being comparatively new, the ultrasound method has been used to investigate the film thickness in different machine elements such as roller bearings, journal bearings and mechanical face seals [124, 138-141]. Redyhoff et al. [141] stated some drawbacks of the ultrasound method. Materials of high attenuation do not let the ultrasound pass efficiently. The sensitivity of the measurement can be

influenced by the impedance mismatch of the surfaces of the interested machine elements. Also, the sensors which are used in this method are sensitive to temperature. Moreover, large air bubbles or voids in the lubricant film will directly reflect the ultrasound and generate spikes in the determined film thickness while the small air bubbles will reduce the speed of sound and lead to overestimation of the film thickness.

4.3.1.2 LOCAL CONTACT TEMPERATURES MONITORING METHODS

Local contact temperatures monitoring can be performed via direct and indirect methods. The direct method is based on the classical use of thermocouples. These thermocouples can be placed as close as possible to the lubricant film as in the universal test rig (Chapter 4.2). If the thermocouples are not placed directly into the contact and the material in which they are embedded has a low thermal conductivity, this type of measurement is not suitable. In addition, temperature mapping is also not easy.

With the indirect method, the temperature of the sealing contact can be determined by using an infrared thermal camera [142-144]. This camera measures the radiated infrared by the objects and converts this radiation to temperature according to Planck's law. This method provides high thermal resolution and makes possible to detect transient variations. However, the thermal camera detects the radiation both from the friction surfaces and the lubricant film. Therefore, if the aim is just to determine the temperature distribution within the lubricant, some different methods such as coatings are necessary to filter the radiation from the machine elements [145]. If the aim is to determine the temperature distribution over the seal surface, it can be extracted via equations [150]. One of the problematic issues in infrared thermography is that the thermal camera is sensitive to the reflections and the radiation from the surrounding [3].

As a non-intrusive method, some researchers have been using the laser induced fluorescence method for temperature mapping of the lubricants [146-148]. It is based on the effect that the fluorescence emission depends on temperature. However, to determine the temperature correctly, the lubricant should be illuminated uniformly and the optical conditions should be constant during the measurements. Noise (in the optical images) can influence the calibration. At large temperature gradients, fluid density thus refractive index changes. This leads to a change in laser intensity locally which influences the local fluorescence intensity hence, the local temperature [149]. Furthermore, this method only allows the temperature mapping of the lubricant. Fluorescent particles are mixed with the lubricant in this method and this mixture might not be distributed sufficiently over the sealing contact under boundary and mixed lubrication conditions. Therefore, this method is more suitable for hydrodynamic regime.

4.3.1.3 CONCLUSION

In the preceding section, different film thickness and local temperature measurement methods are examined. The film thickness measurement methods such as electrical, interferometry and ultrasound do not fully fulfil the requirements of the current work. Electrical methods generally measure the minimum film thickness and require machine elements with good electrical conductivity. However, the sealing material in the current work is PEEK which has a bad electrical conductivity.

Optical interferometry requires reflective surfaces and the reflectivity of the current seal surfaces is not sufficient. Ultrasound method can be performed by placing a transducer to the back of the machine element. In the current work, both the seals and the counterfaces are rotating. Placing a transducer to the back face of the rotating seal can lead to problems. Also the transducers are sensitive to temperature changes. In addition, ultrasound overestimates the film thickness in case of cavitation occurrence. This means that the film thickness can be calculated incorrectly at many points since it is the aim to investigate a hydrodynamically lubricated contact with occurrence of cavitation.

Fluorescence method is the best solution for the current work. It determines the film thickness reliably when the calibration is performed diligently and, the suitable light source and the fluorescent substance are selected. It is not influenced by cavitation. Moreover, using an optically translucent object to realize

this method allows to observe the complete contact area. Therefore, cavitation formation can be observed directly which is one of the aims of the experiments.

The local contact temperatures cannot be detected by using thermocouples since the seal rotates relative to the counterface. Laser induced fluorescence temperature measurement and infrared thermography are advantageous since they allow the visualization of the sealing contact. Laser induced fluorescence method is remarkable but it needs an elaborate measurement set-up and calibration. For reliable results, selection of the sensitive fluorescent dyes is necessary. Also, it determines only the temperature of the lubricant.

Infrared thermography provides a simple set-up. If it is necessary, radiations which arises from different components can be filtered and the temperature over the seal surface can be found. However, even without filtering, this method can show high friction areas and give an insight for the sealing deformation. Also, it is shown that the elastic deformations of the seals influence the lubricant film more significantly than the thermal wedge effect which arises from the temperature gradients within the lubricant [70].

As a result, a fluorescence method and infrared thermography are selected to measure film thickness and the local contact temperatures at the axial sealing interface.

4.3.2 The OPTICAL TEST RIG

The optical test set-up (Figure 4.9) is based on the work of Schüller [81] and has been modified. The fundamentals of the test rig are similar to the universal test rig. This test rig has a chamber which consists consists of a shaft, counterfaces, and a housing. Two seal rings seal the chamber. One of the counterfaces of the seals is replaced with a sapphire disc to enable the optical investigation of the contact. Sapphire has a similar thermal conductivity to steel and therefore, the thermal behavior of the system is kept similar to that of a real application. The sapphire disc is coated matt black except the sealing contact to prevent the reflection from the surrounding materials. The roughness of the sapphire disc is within the suggested parameters. The contact area is illuminated and observed via a light microscope and a CCD camera.

a) Optical test rig   b) Cross sectional view of the optical test rig
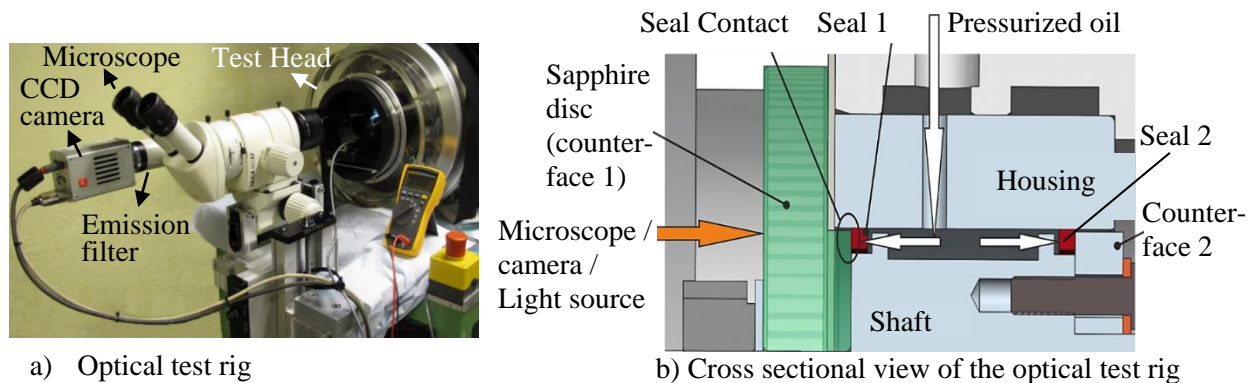
Figure 4.9: Optical test rig [81].

4.3.2.1 CAVITATION OBSERVATION

In order to observe cavitation formation, the contact area is illuminated with a white light source. The joint may influence the film behavior and cavitation. The highest film thickness is expected to occur in the region at the opposite of the joint. Therefore, only cavitation occurring within the structures 8 and 21 (see Figure 4.1a) is considered. Cavitation area ratio (the ratio of the cavitation area to the total area of one structured section) is calculated within these structures and used for a quantitative comparison.

In the optical tests, the friction torque and the average near-contact temperature are also measured. The friction torque is measured via a torque sensor. A thermocouple is placed through the housing, near the sealing contact, to measure the near-contact temperature.

4.3.3 LASER INDUCED FLUOROESCENCE METHOD

In this chapter, the basics of fluorescence phenomenon and its implementation to measure the lubricant film thickness are described.

4.3.3.1 PRINCIPLES of FLUORESCENCE

Fluorescence is a type of photoluminescence which is emission of light by a substance as a result of absorption of photons. Hence, the emission of light in the fluorescence is not a result of heat. To understand the fluorescence phenomenon, some basic properties of light should be examined first. Therefore, both wave and particle (photon) approaches for light will be used.

Light is a form of electromagnetic radiation. It has an oscillating electrical field and an oscillating magnetic field perpendicular to it. The oscillating magnetic field acts as waves travelling at the speed of light, c [151]. Light has also a wavelength (λ) and frequency (v) as properties which have the relationship with each other as:

$$v = \frac{c}{\lambda} \tag{4.1}$$

Planck defined a relationship between light and energy which is relevant for fluorescence since the molecules absorb and emit one photon of energy. If E is the photon energy and h is Planck constant ($6.626 \cdot 10^{-34}$ J·s), this relationship is represented with the photon frequency v as below [152,153]:

$$E = hv \tag{4.2}$$

Molecules have energy levels and the state of their energy can make a transition from one level to another when they absorb photons. These energy levels can be illustrated via the Jablonski diagram (Figure 4.10). When a fluorescent molecule (fluorophore) absorbs a photon, its energy level (usually the lower level which is the so called ground state (S_o)) changes to a higher level (higher level singlets such as S_1, S_2, etc.) and it becomes unstable. This energy change contains also a vibrational energy change which is arising from the molecule itself. After the absorption, the molecule has excess electronic and vibrational energy. First, the vibrational energy is dissipated very quickly in the form of heat as a result of the molecule interaction with the surrounding [151]. As a result, the molecule reaches the relaxed energy state S_1 and then goes back to its ground state by emitting fluorescence. The whole excited state of the fluorophore is $1 \cdot 10^{-9}$ s to $10 \cdot 10^{-9}$ s (the lifetime of the fluorescence). Some of the molecules can lose their energy with collisional quenching (collisions with other molecules) [159] instead of emitting fluorescence before returning to the ground state.
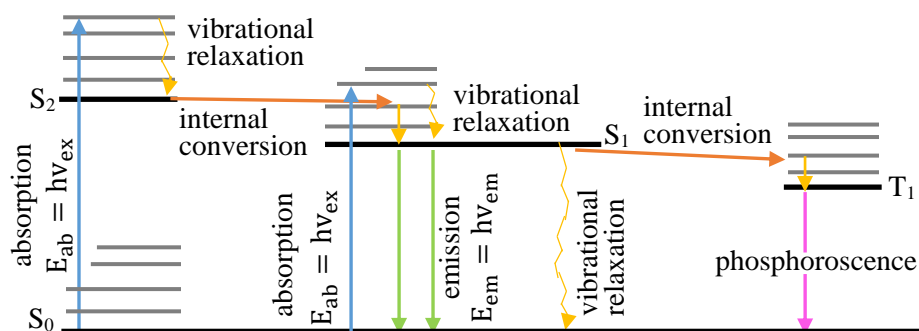
Figure 4.10: Jablonski diagram showing the absorption and fluorescence processes. E_{ab}= absorption energy, v_{ex}= excitation frequency, E_{em}= emission energy, v_{em}= emission frequency.

Molecules can also change their spin state from singlet to triplet as a result of internal conversion. From this state the molecules can return to the ground state by emitting photophosphorescence, which is very weak. The excitation time in photophosphorence is much longer (10^{-4} s to 10 s). The emission continues longer (even after the removal of exciting radiation) since the triplet state has a longer lifetime.

In fluorescence, emission energy (thus the frequency and the wavelength of the emission) is always lower than the absorption energy. This phenomenon is so called Stokes shift. As a result of this shift, lubricant film thickness can be measured by using the filters only allows the emission radiation to pass.

4.3.3.2   LUBRICANT FILM THICKNESS MEASUREMENT with FLUORESCENCE

In order to measure a lubricant film thickness via the fluorescence method, the fluorescence response of an excited lubricant – fluorophore mixture should be examined. The total fluorescence which is emitted from a rectangular differential volume with the cross sectional area *A* and the length *dx* irradiated by light (normal to the area) with uniform intensity I_{ex} can be expressed as [136,146,153]:

$$F = I_{ex}\epsilon(\lambda_{ex})c\Phi A\Delta x \tag{4.3}$$

The fluorescent intensity depends on;

- $I_{ex}=$ excitation light intensity. It generates molecular transitions to excited levels,
- $\epsilon(\lambda_{ex}) =$ molar absorption coefficient. It determines how much of the incident light per molecule produces molecular transitions,
- $c=$ dye concentration. It is the measure of the number of molecules present,
- $\Phi=$ the quantum efficiency. It is the ratio of the emitted photons to the absorbed photons.
- $A\cdot \Delta x=$ the volume of the element. Excitation and fluorescence occur within this control volume.

The fluorescent intensity can be obtained by dividing the eq. (4.3) with the area *A*. If the area *A* is assumed to be the projected area of a single pixel, the fluorescence intensity collected by a CCD pixel from the differential fluorescent element is determined as below [136,146,153]:

$$I_f = I_{ex}\zeta\epsilon(\lambda_{ex})c\Phi\Delta x \tag{4.4}$$

ζ is a constant which is related with the efficiency of the monitoring [153]. It arises due to the fact that the emitted fluorescence is pointed at every direction and only a fraction of the total emitted fluorescent radiation is collected by the detector. ζ is between 0 and 1 over the whole thickness of the sample when the thickness and the sample half-width over which fluorescence is occurring are significantly smaller than the distance from the detector. Eq. (4.4) is accurate for thin films. A more accurate representation can be obtained for both thin and thick films by using the Beer – Lambert Law [155,156] which describes the absorption of the excitation light by the finite fluid through which it travels [136,146,153]:

$$I_{ex}(x) = I_0 e^{-\epsilon(\lambda_{ex})cx} \tag{4.5}$$

I_o represents the incident light intensity in eq. (4.5). If a differential element is considered within a finite film thickness, the fluorescent intensity collected by the detector is:

$$dI_f = I_{ex}\zeta\epsilon(\lambda_{ex})c\Phi dx \tag{4.6}$$

Here, I_{ex} can be replaced by the eq. (4.5):

$$dI_f = I_0 e^{-\epsilon(\lambda_{ex})cx} \zeta\epsilon(\lambda_{ex})c\Phi dx \tag{4.7}$$

Thus, the total intensity recorded by the detector for a defined film thickness *h* is:

$$I_f(h) = \int_0^h I_0 e^{-\epsilon(\lambda_{ex})cx} \zeta\epsilon(\lambda_{ex})c\Phi dx = I_0\zeta\Phi\left(1 - e^{-\epsilon(\lambda_{ex})ch}\right) \tag{4.8}$$

If *h* is small (thin film) eq. (4.8) becomes:

$$I_f(h) \approx I_0 \zeta\epsilon(\lambda_{ex})c\Phi h \tag{4.9}$$

Here, categorizing a lubricant film as optically thin or optically thick depends on the product $\epsilon(\lambda_{ex})c$ [136, 146]. When the fluorescence intensity is plotted with respect to the film thickness, a curve with

three regions is obtained (Figure 4.11) . These regions were examined in detail by Poll *et al.* [157]. The first region is quasi linear. In this region, almost all of the fluorescence particles are excited. The incident light intensity is more than can be absorbed and it is transferred into fluorescence. The fluorescence intensity mostly depends on the amount of the fluorescent particles thus, on the film thickness and the fluorescent dye concentration.

The second region is the transition region where the fluorescence intensity changes with the film thickness non-linearly. The film thickness reaches values where some fluorescence particles are not excited. Fluorescence intensity depends on both fluorescent particles and light intensity.

In the third region which is the so called 'saturation region', all the incident light is used for fluorescence or transformed into heat at a distance shorter than the total film thickness. The fluorescence intensity versus film thickness curve becomes a plateau. In this region, fluorescence intensity depends on the light intensity. However, in practice, there is a small influence of the florescent dye concentration as well but it is weak compared to that in the linear and the transition regions. Poll *et al.* [157] explained this as that the mean travelling distance of the incident light and the fluorescent radiation decreases with fluorescence concentration for a given incident light intensity. Thus, it becomes less probable that the light is lost by absorption or transformation into other energy forms rather than fluorescence.
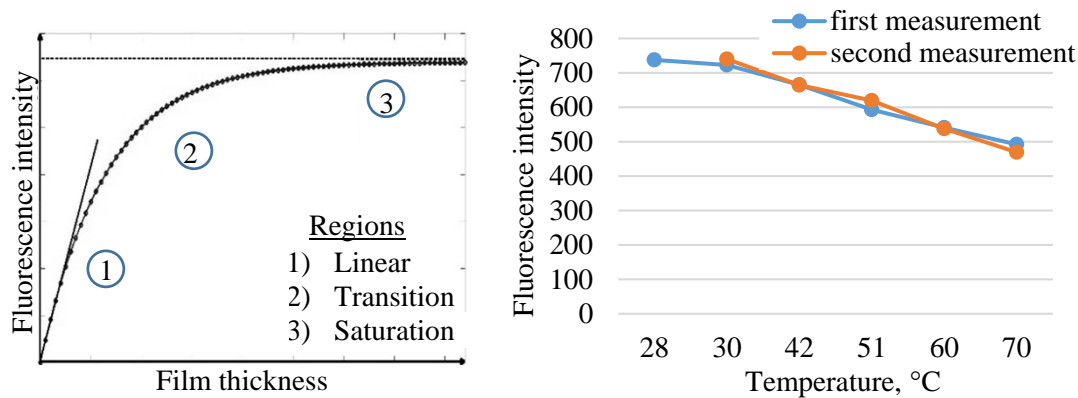
Figure 4.11: Left: The relationship between fluorescence intensity and film thickness. Right: Temperature dependency of fluorescent yellow in ATF M-1375.4 (concentration: 2000 ppm). Fluorescence intensity is measured in the flat area of the structured seal at 0 rpm and 5 bar. Therefore, the lubricant film thickness is low (around 0.6 μm).

High fluorescence particle concentrations can have a negative effect on the fluorescence process. Fluorescent radiation might hit other particles and may be transformed into heat. This is a type of fluorescence quenching (a process that leads to decrease in fluorescence intensity). After this, these particles cannot radiate fluorescence.

4.3.3.3   LASER INDUCED FLUORESCENCE IMPLEMENTATION
4.3.3.3.1   SELECTION of the INSTRUMENTS
To implement the fluorescence method, some important factors such as the fluorescent dye, light source and the detector should be selected carefully. In this section, the selection of the important materials is described:

Fluorescent dye:
For the selection of the fluorescent particles, solubility of the dye in the main lubricant, the temperature dependency and the excitation/emission wavelength of the dye should be considered. Besides, the hazardous effects of the dye should be low. Polarity of the fluids shows the solubility of a material. The main lubricant ATF M-1375.4 used in the work is a mineral oil and highly non-polar. Thus the fluorescent should be non-polar too. The temperature dependency of the lubricant should also be quite low. The excitation/emission wavelength of the dye should be within the visible range.

Concentration of the fluorescent dye:
As described in Chapter 4.3.3.2, fluorescence emission increases as the dye concentration increases until the saturation concentration. Low dye concentrations extend the linear region of the fluorescence intensity – film thickness curve beyond the interested film thickness range and decrease the sensitivity. High concentrations can shorten the linear behaviour of the fluorescence intensity and the film thickness than the necessary film ranges. Fluorescence dyes have also suggested concentration limits (2500 ppm for fluorescent yellow). Beyond this limit, dyes might influence the properties of the main lubricant.

Temperature dependency of fluorescence intensity:
Fluorescence intensity generally decreases as the temperature increases [179, 180]. The influence of the temperature should be kept as minimum as possible. Figure 4.11 shows the dependency of the fluorescent yellow dye which is used in the experiments. Although the intensity decreases with temperature, it is acceptable up to 50 °C in the current work since the change in fluorescence intensity would result in an error below 0.5 µm.

Light source:
Light should have an appropriate wavelength and be strong enough to illuminate the area of interest sufficiently. In addition, the incident light ideally should be distributed over the sealing contact uniformly. Generally, light from a point source has a Gaussian spatial intensity distribution, however, this can be corrected via appropriate lenses such as Powell lenses. These lenses can also be used to avoid speckles which occur in lasers. However, it should be noted that the lenses might decrease the intensity of the excitation light. Besides, intensity of the incident light should not change with time. Generally, lasers provide a more stable intensity. However, it should be noted that lasers provide intensive excitation light which can lead to photo bleaching which means the deactivation of the fluorescence feature of a fluorophore.

Detector:
One of the most important features of the detector set-up is the exposure time. In the current work the seals rotate slowly and their speed increases with increasing shaft speed. If the exposure time of the detector is too long, recorded photographs will be blurred. As a result, the film thickness cannot be determined correctly. High speed cameras can record the sealing contact for short durations but this means illumination of the sealing contact should be more powerful. In case of the weak illumination, CCD cameras which provide longer exposure time need to be used. Another important point is the microscope which is used to visualize the sealing contact in detail. When the magnification of the microscope is increased, the resolution of the recorded data increases. However, the collected light by the camera sensors decreases according to the aperture.

In the current work, Fluorescent Yellow (FY131SC) is selected as the fluorescent dye and mixed with the transmission oil ATF M-1375.4 (Table 4.3). Fluorescent yellow dissolves in the oil and it does not influence the bulk behaviour of the oil. The concentration of the fluorescent dye is selected as 2000 ppm. The magnification of the optical light microscope is set as 5x. The objective of the microscope is plan 1.0x. The working distance of the microscope is 55 mm. The numerical aperture 0.4137. A narrow band pass filter which allows emitted light to pass in the range from 570 to 600 nm is used in the optical path from the object to the camera (see Figure 4.9). A Nd:YAG laser with a wavelength of 532 nm is used to illuminate the contact. The laser beam is spread to 12 mm diameter via a lens system. The intensity of the laser is measured before the experiments and found to be stable. A set of preventive measures are performed against the reflection from the contact and the surrounding. The sapphire disc is coated opaquely, except for the area of the axial sealing contact. The test rig is covered and the measurement area is darkened.

4.3.3.3.2   CALIBRATION of FLUORESCENCE INTENSITY

The recorded data from the sealing contact are evaluated with a software so called 'Image J'. In this software, the intensity of the fluorescence is represented as grey values from the monochrome sealing

contact photos. Figure 4.12a shows the fluorescence photograph of one structured section of the structured seal. The speed and the lubricant pressure is 500 rpm and 5 bar, respectively. Rotation of the seal is CCW. Within the right half of the structure, cavitation is visible. Cavitation consists of dark areas and thin light areas. Dark areas correspond to gas regions while the thin bright areas correspond to liquid streamers.

The cross section of Figure 4.12a is represented via fluorescence intensity in Figure 4.12b. Fluorescence intensity becomes low in the cavitation zone. At some regions, fluorescence intensity fluctuates and the structure geometry deviates from its original shape (Figure 4.12c). Here, the seal is non-stationary; however, these fluctuations partly occur when the system is stationary, too. The fluctuations are particularly visible in the deepest part of the structure. These fluctuations can be due to the speckles in the laser light. It should be noted that fluorescence intensity depends on the excitation light intensity at high film thicknesses as described earlier. Therefore, the fluctuations might be occurring more in the deep regions of the structures. It should be noted that the microscope is not adjusted to detect the roughness due to loss of collected radiation from the sealing contact. Thus only the macro surface features are captured by the fluorescence measurements described here.
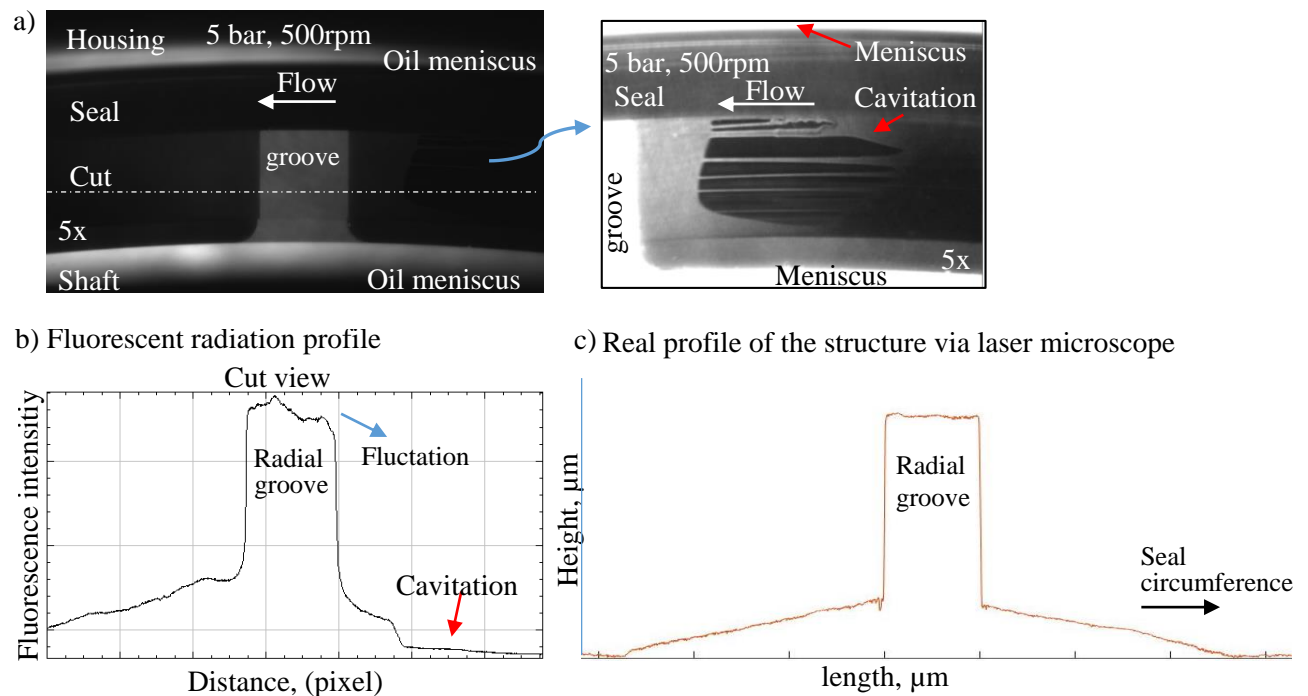
Figure 4.12: a) Fluorescence emission of one structured seal section with cavitation (to make it more easily visible the photo contrast is adjusted) b) Depiction of the structure via fluorescence intensity c) The real surface profile of the structure determined via laser microscope.

In order to translate the fluorescence intensity into the film thickness, an elaborate calibration is necessary. External calibration can be useful at the selection stage of a fluorescent dye and of its concentration. However, in-situ calibration can provide more reliable results since it takes into account the influencing parameters from the surrounding and the test set-up. The fundamentals of the in-situ calibration are described by Poll *et al.* in detail [154,157,158]. Structured seals are particularly suitable to implement this method. Therefore, calibration is performed with the structured seals.

The fluorescent dye – oil mixture is pumped into the system when the system is stationary. The emitted light from a structured section is recorded. The fluorescence emission from the structure at 0 rpm correlates with the profile of the structure. The inclined surfaces of the structure are used to determine the fluorescence intensity for different oil thicknesses (Figure 4.13). Consequently, the calibration curve is obtained (Appendix A, Figure A-1).

Film thickness is measured at different speeds. The same structured section which is used for the calibration is recorded to measure the film thickness to minimize the error in the measurement results. This structured section is in the region at the opposite of the joint. Film thickness is determined at the flat surface over the structure (Figure 4.13). The measurement area is 0.13 x 2.83 mm^2. This area is near the calibration area to eliminate the influence of a possibly inhomogeneous light distribution. The calibrated film thickness results include the initial profile of the seal. Therefore, the fluorescence emission at zero rpm is subtracted from the film thickness measurements to obtain only the film thickness due to hydrodynamic lift. It should be noted that a hydrostatic part might still be taking place in the results due to elastic deformation of the seal during operation.
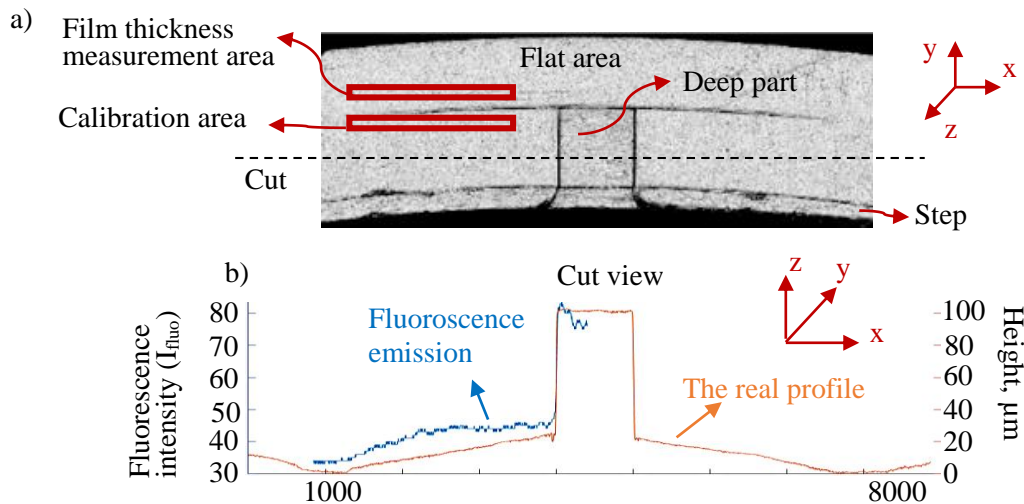
Figure 4.13: a) Calibration and the film thickness measurement areas b) Obtaining the calibration curve by using the inclined planes of a structure.

For the calibration of the standard seals, the calibration curve which is obtained for the structured seals is used since the standard seals do not have any surface feature to generate a calibration curve. Thus the error in the film thickness measurements of the standard seals might be higher.

The reproducibility of the measurements was checked as well (see Appendix A). For this, a group of measurements were repeated after some time. Similar results were found; thus, under the same conditions the results are reproducible. To prevent the influence of any change in the system after the calibration, the measurements are performed shortly after the calibration.

4.3.4 INFRARED THERMOGRAPHY

4.3.4.1 PRINCIPLES of INFRARED THERMOGRAPHY

To measure the local contact temperatures, a microscope and a CCD camera are replaced with a thermal camera (Figure 4.14). To exclude the radiation from the surrounding the test rig is covered with an infrared (IR) opaque material (in this case it is aluminium which is a strong IR reflector). As the measurements are influenced by the ambient temperature, a thermocouple is used to measure the ambient temperature which is kept as 20 °C during the experiments.

Figure 4.14: Infrared thermography set-up.

All physical bodies radiate energy which depends on the body temperature. Based on Planck's law, the total radiant power into the hemisphere of a black body at a temperature T in the wavelength interval λ, $\lambda+d\lambda$ can be expressed as [3,160]:

$$M_\lambda(T)\,d\lambda = \frac{2\pi hc^2}{\lambda^5}\left(e^{\frac{hc}{\lambda kT}} - 1\right)^{-1} d\lambda \tag{4.10}$$

h is Planck's constant ($6.626 \cdot 10^{-34}$ J·s), c is the speed of light in vacuum ($2.998 \cdot 10^8$ m/s), λ is the wavelength of the radiation, k is Boltzmann constant (1.380649×10^{-23} J·K^{-1}), and T is the absolute temperature (in K). The radiant exitance of a black body, according to the Stefan–Boltzmann law is:

$$M(T) = \int_0^\infty M_\lambda(T)\,d\lambda = \int_0^\infty M_\nu(T)\,d\nu = \sigma T^4 \tag{4.11}$$

Here, σ is the Stefan-Boltzmann constant ($5.67 \cdot 10^{-12}$ W/m^{2}K^4). As IR imaging only detects a predefined spectral range of $\lambda_1 \rightarrow \lambda_2$, the black body radiation (Figure 4.15) is compared to the total emission [3]:

$$F_{(\lambda_1 \rightarrow \lambda_2)} = \frac{\int_0^\lambda M_\lambda\,d\lambda}{\int_0^\infty M_\lambda\,d\lambda} \tag{4.12}$$

This equation is described for 500 °C with the hatched areas in Figure 4.15. This can be used to obtain the portion of black body radiation and excitation for the limited band detected by the IR sensor.
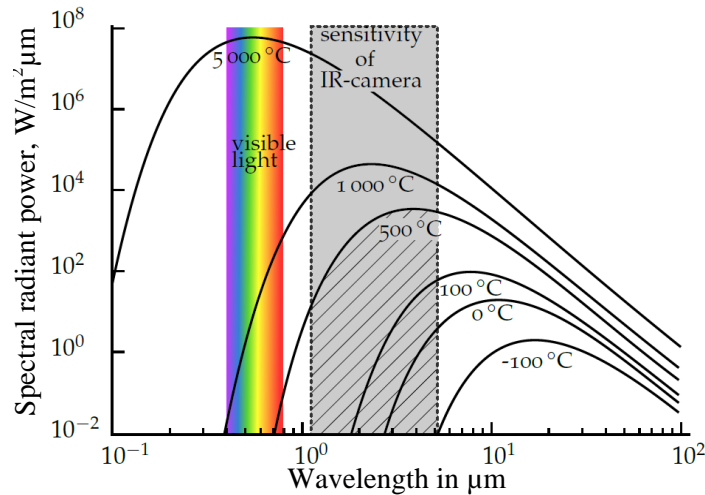
Figure 4.15: Spectral radiant power of Planck's black body [3] with respect to wavelength for different temperatures.

In nature, the objects are not ideal black bodies but rather grey bodies. The grey bodies only absorb and emit the incident radiation partially. Therefore, some terms such as emissivity should be defined to understand the heat transfer of the grey bodies. Emissivity (ε) shows how much thermal radiation an object emits to its environment. It is the ratio of the thermal radiation emitted by a grey body to the thermal radiation emitted by a black body at the same temperature. It is between 0 and 1 for grey bodies. Similarly, absorptivity (α) and reflectivity (ρ) are the measure of how much thermal radiation is absorbed and reflected, respectively. Lastly transmissivity (τ) is the measure of how much thermal radiation passes through an object. The values of these terms can change with wavelength. Also, according to Kirchhoff law, for a body emitting and absorbing thermal radiation in thermodynamic equilibrium, the emissivity is equal to the absorptivity:

$$\alpha = \varepsilon \tag{4.13}$$

A radiation (ϕ_0) which is striking an object can be reflected (ϕ_R), transmitted (ϕ_T), or absorbed (ϕ_A) by this object [3]:

$$\phi_R + \phi_T + \phi_A = \phi_0 \qquad (4.14)$$

For a given temperature (T) and a wavelength (λ), absorptivity, transmissivity and reflectivity can be written as:

$$\alpha(\lambda, T) = \frac{\phi_{\lambda,\alpha}}{\phi_{\lambda,0}} \quad \tau(\lambda, T) = \frac{\phi_{\lambda,\tau}}{\phi_{\lambda,0}} \quad \rho(\lambda, T) = \frac{\phi_{\lambda,\rho}}{\phi_{\lambda,0}} \qquad (4.15)$$

By using the equations (4.14) and (4.15), it is obtained that the sum of the absorptivity, reflectivity and the transmissivity of an object for a given wavelength is:

$$\rho + \tau + \alpha = 1 \qquad (4.16)$$

By considering eq. (4.13), emissivity is directly related to reflectivity $\varepsilon = 1 - \rho$ for IR nontransparent bodies. Measurements of the thermal cameras depends on the emissivity of the objects and this factor is influenced by the material, surface roughness, viewing angle and temperature in addition to wavelength. Metals and polished surfaces have low emissivity.
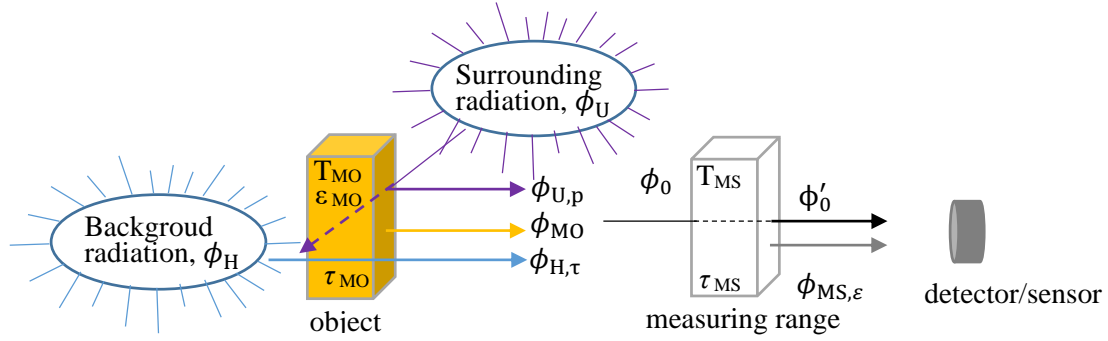
Figure 4.16: The radiometric chain [3,161].

The measured radiation from an object can be converted to the temperature with the help of the radiometric chain (Figure 4.16) [3,161]. In this chain, the interested object is assumed to have the temperature T_{MO} and it emits the radiation ϕ_{MO}, reflects $\phi_{U,\rho}$ and transmits $\phi_{H,\tau}$. In addition, the radiant power which is detected by the detector is influenced by the radiation from the measuring range ϕ_{MS} (this is due to the bodies between the detector and the interested object such as a thermal camera lens). The detected radiant power ϕ_{det} can be obtained as [3]:

$$\phi_{det} = \tau_{atm}\varepsilon\phi_{object}^{BB}(T_{object}) + \tau_{amb}(1-\varepsilon)\phi_{amb}(T_{amb}) + (1-\tau_{atm})\phi_{atm}(T_{atm}) \qquad (4.17)$$

Here, $\varepsilon\phi_{object}^{BB}(T_{object})$ is the radiant power of the object which is reduced by the transmittance τ_{atm} of the atmosphere. $\tau_{amb}(1-\varepsilon)\phi_{amb}(T_{amb}) = r\phi_{amb}(T_{amb})$ is the reflected radiation from the surrounding. $(1-\tau_{atm})\phi_{atm}(T_{atm})$ is the radiant power which is emitted by the atmosphere. Thus the radiant power of the object can be determined as (note; it is assumed that $\tau_{atm} = \tau_{abm}$ and $T_{atm} = T_{abm}$):

$$\phi_{object}^{BB}(T_{object}) = \frac{\phi_{det}}{\tau_{atm}\varepsilon} - \frac{(1-\varepsilon)}{\varepsilon}\phi_{amb}(T_{amb}) - \frac{(1-\tau_{atm})}{\tau_{atm}\varepsilon}\phi_{atm}(T_{atm}) \qquad (4.18)$$

By using a camera specific calibration curve ϕ_K instead of the black body radiant power, the temperature of the object T_{object} can be obtained:

$$T_{object} = \phi_K^{-1}\varepsilon^{-1}\left(\frac{\phi_{det} - (1-\tau_{atm})\phi_{atm}(T_{atm})}{\tau_{atm}} - (1-\varepsilon)\phi_{amb}(T_{amb})\right) \qquad (4.19)$$

Here, it is necessary to know the emissivity ε of the of the object, surrounding temperature T_{amb}, the atmospheric temperature T_{atm} and the atmospheric transmittance τ_{atm}. The thermal camera which is used in the current work calculates the atmospheric transmittance τ_{atm} via a software using the LOWTRAN model [71]. For this calculation, the atmospheric temperature T_{atm}, the relative humidity and the measurement distance should be defined in the the software.

4.3.4.2 *IMPLEMENTATION of INFRARED THERMOGRAPHY*

In the current work, the aim is to determine the local temperatures of the seal surface based on the work of Tournerie [150] and Adjemout [163]. Figure 4.17 shows the radiation from the sealing contact. The thermal camera collects radiative intensity I_{cam} which is the sum of the radiations from the contact. The surrounding emits the radiation with radiative intensity I_{amb} which strikes the contact and is reflected by the sapphire disc, the lubricant film and the seal. The sapphire disc emits radiation (I_1) as well since it is not fully IR transparent. I_1 is reflected by the lubricant film and the seal.

Tournerie *et al.* [150] measured the transmissivity of an oil sample which is 1 mm thick (Figure 4.17 right). It is found that the transmissivity is higher than 0.9 except for the absorption band 3.3 to 3.6 μm. Therefore, they assumed that the transmissivity is 1 and, the emissivity is negligible for the lubricant film. Since the lubricant film is also thinner than 1 mm in the current work, the same assumptions can be made (see also transmittance analysis of an ATF oil in Appendix B, Figure B-1). This leads to elimination of the lubricant film radiation (I_2).

The seal ring emits the radiation (I_3). From the atmosphere, radiation (I_{atm}) is received by the camera. The camera is placed at a distance 0.2 m from the seal interface. Therefore, the atmosphere transmissivity τ_{atm} is assumed to be 1 while the emissivity ε_{atm} can be neglected [150, 162]. I_{cam} can be written as [150,162,163]:

$$I_{cam} = C_{amb}\, I_{amb} + C_1\, I_1 + C_3\, I_3 \tag{4.20}$$

Here, C_i are radiometric coefficients which depend on the properties of the media:

$$I_{cam} = \left(R^- + \frac{B^2\rho_3}{1 - \rho_3 R^+}\right) I_{amb} + \left(E^- + \frac{E^+ B \rho_3}{1 - \rho_3 R^+}\right) I_1 + \left(\frac{\varepsilon_3 B}{1 - \rho_3 R^+}\right) I_3 \tag{4.21}$$

Optical coefficients B, R^+, R^-, E^+, E^- are given in Appendix B.
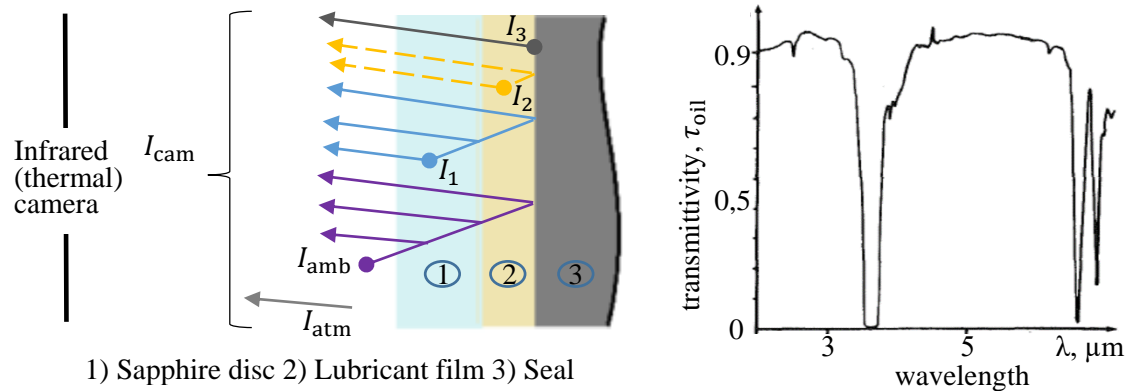
Figure 4.17: Left: Analysis of radiation components of the sealing contact. Right: Oil transmittivity for a tickness of 1 mm [150].

I_i in eq. (4.21) can be expressed with the radiative intensity (I_0) of the black body at the same temperature [163]:

$$I_{amb} = I_0(T_{amb}), \qquad I_1 = I_0\left(T_1 = \frac{T_{targ} + T_3}{2}\right), \qquad I_3 = I_0(T_3) \tag{4.22}$$

Here, T_{amb}, T_1 and T_3 repreresent the ambient temperature, the mean temperature of the sapphire, and the temperature of the seal, respectively. The temperature of the sapphire T_1 is assumed to be the mean of the seal temperature T_3 and the external surface temperature of the sapphire disc T_{targ}. To find the surface temperature of the sapphire disc a target which behaves as a black body can be stuck on to the surface of the disc. In the current work, a coated region near the sealing contact is used. To check whether the coating acts approximately as a black body, the sapphire disc is heated and its temperature is measured via a thermocouple. The radiation from the coating is determined via thermal camera. Since the coating is black and matt, it is found that it practically acts like a black body.

5 EXPERIMENTAL RESULTS

5.1 FRICTION TORQUE MEASUREMENTS INCLUDING LEAKAGE and TEMPERATURE

In this chapter, the results of the experiments which were performed at the universal test rig are described. It should be noted that the friction torque graphs show the friction torque resulted from two seals since two seals were tested in each test. On the other hand, the temperature and the leakage results are shown for individual seals. It should be noted that the temperatures are mean temperatures. In addition, the error indicators in the graphs represent the maximum and the minimum values.

5.1.1 STRUCTURED SEALS

5.1.1.1 TEST A

5.1.1.1.1 FUNCTION TEST 1 (BEFORE the LONG TERM TEST)

The graphs shown below consists of the results of both the function test 1 and 2. Here, the function test 1 is discussed. The curves which are named as 'before' and 'after' represent the results of the function test 1 and 2, respectively.

In the function test 1, extra leakage occurred at the side of the seal 2 which results from one of the screws of the counterface. Therefore, leakage rates of seal 2 are not considered. It should be noted that this extra leakage started directly at the beginning of the test and continued until the very end. The screw which generated extra leakage was located more in the inner diameter direction of the counterface and it was not close to the seal contact. The near-circumference contact temperatures (T_1 and T_2) and the axial contact temperatures (TM_1 and TM_2) are similar for both seal 1 and 2 (Figure 5.2-Figure 5.4). Only at high pressures and high speeds, TM_2 becomes considerably lower than TM_1. However, such difference occurs in other tests as well. In addition, T_2 is higher than T_1 at high pressures and speeds. These results show that the contacts are largely dominated by conditions in the contact area, while the surrounding conditions, e.g., additional flow do not change the behaviour.
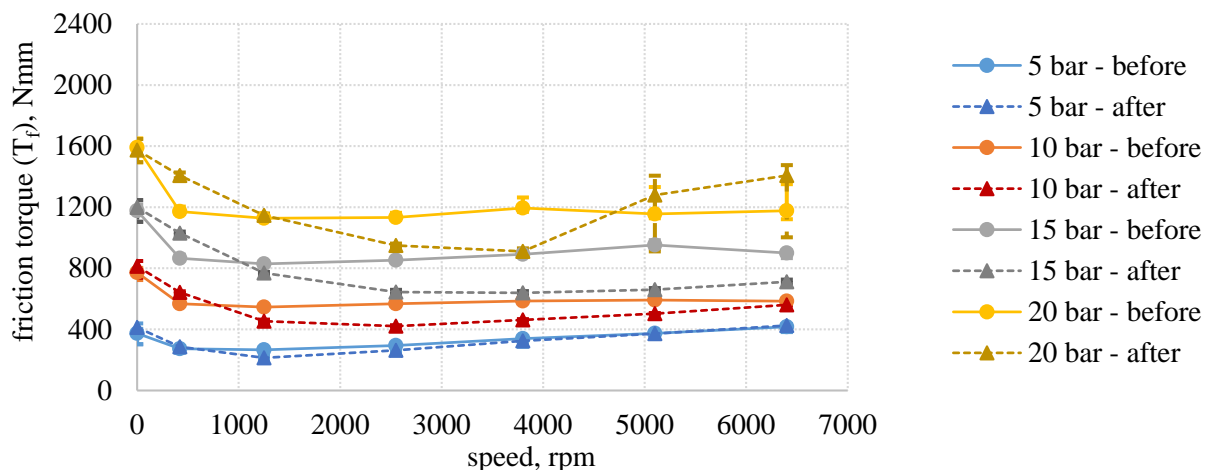
Figure 5.1: Friction torque (resulting from two structured seals) in Test A. 'before' and 'after' represent the function tests 1 and 2, respectively.

The highest friction torque occurs at almost 0 rpm for each pressure (Figure 5.1). At this speed, the friction torque is proportional to the applied fluid pressure as suggested by Coulomb's law. With increasing speed, the friction torque decreases and reaches a minimum value around 1250 rpm for each pressure. After this, the friction torque increases again. For 20 bar, the difference between the minimum and the maximum values of the friction torque becomes more distinct. Because, the friction torque is quite high at the beginning of these speed-pressure steps (Figure 5.5) and it decreases immediately. This behaviour occurs in other speed-pressure steps as well but it is not as significant as in the high speed and high pressure combinations. It seems to occur due to running–in process of the seals.
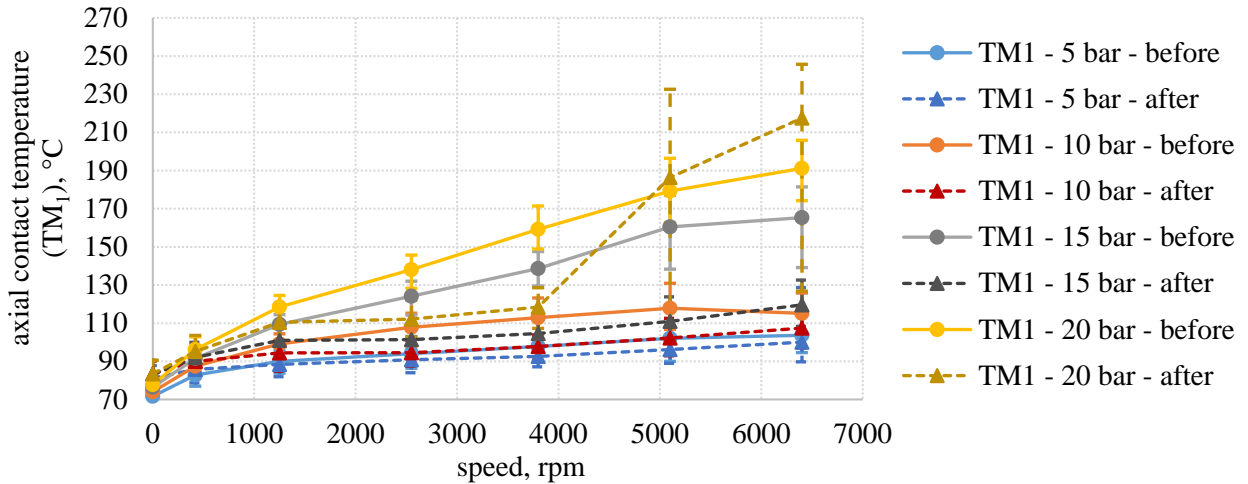
Figure 5.2: Axial contact temperatures for the structured seal 1 in Test A. 'before' and 'after' represent the function tests 1 and 2, respectively.

The axial contact temperatures (TM_1 and TM_2) increase with increasing speed as the friction torque (Figure 5.2 Figure 5.3). This increase is particularly dramatic at high speeds and high pressures. Both TM_1 and TM_2 reach and exceed glass transition temperature of the seal material (also allowable temperature for these seals). Figure 5.5 shows the behaviour of TM_1 and TM_2 during the whole experiments. As the friction torque, TM_2 shows significant peaks at the beginning of high speed and high pressure steps. This indicates that there is a strong correlation between the friction torque and the contact temperatures.
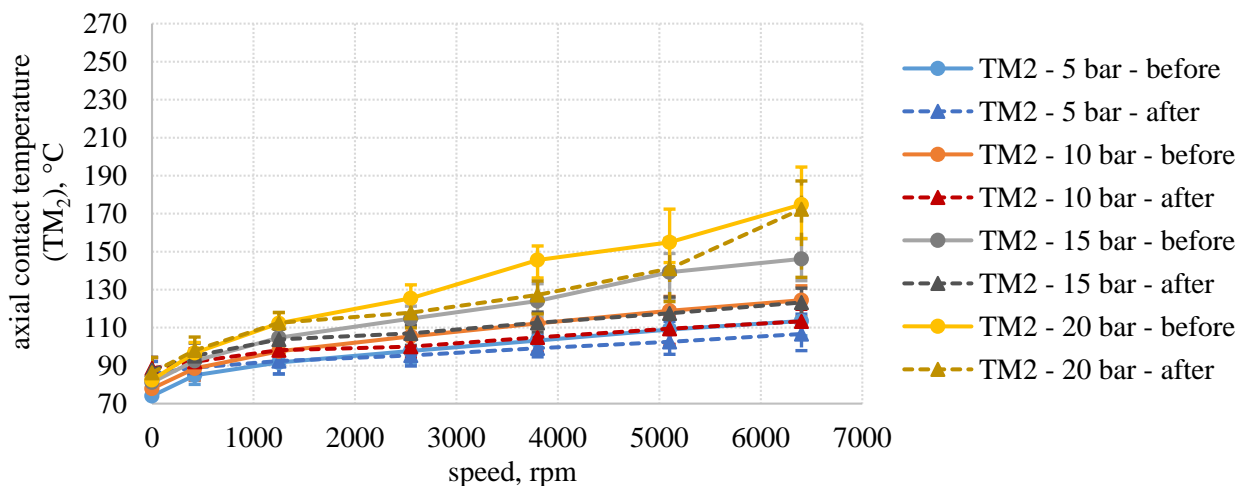
Figure 5.3: Axial contact temperatures for the structured seal 2. 'before' and 'after' represent the function tests 1 and 2, respectively.

a)

b)
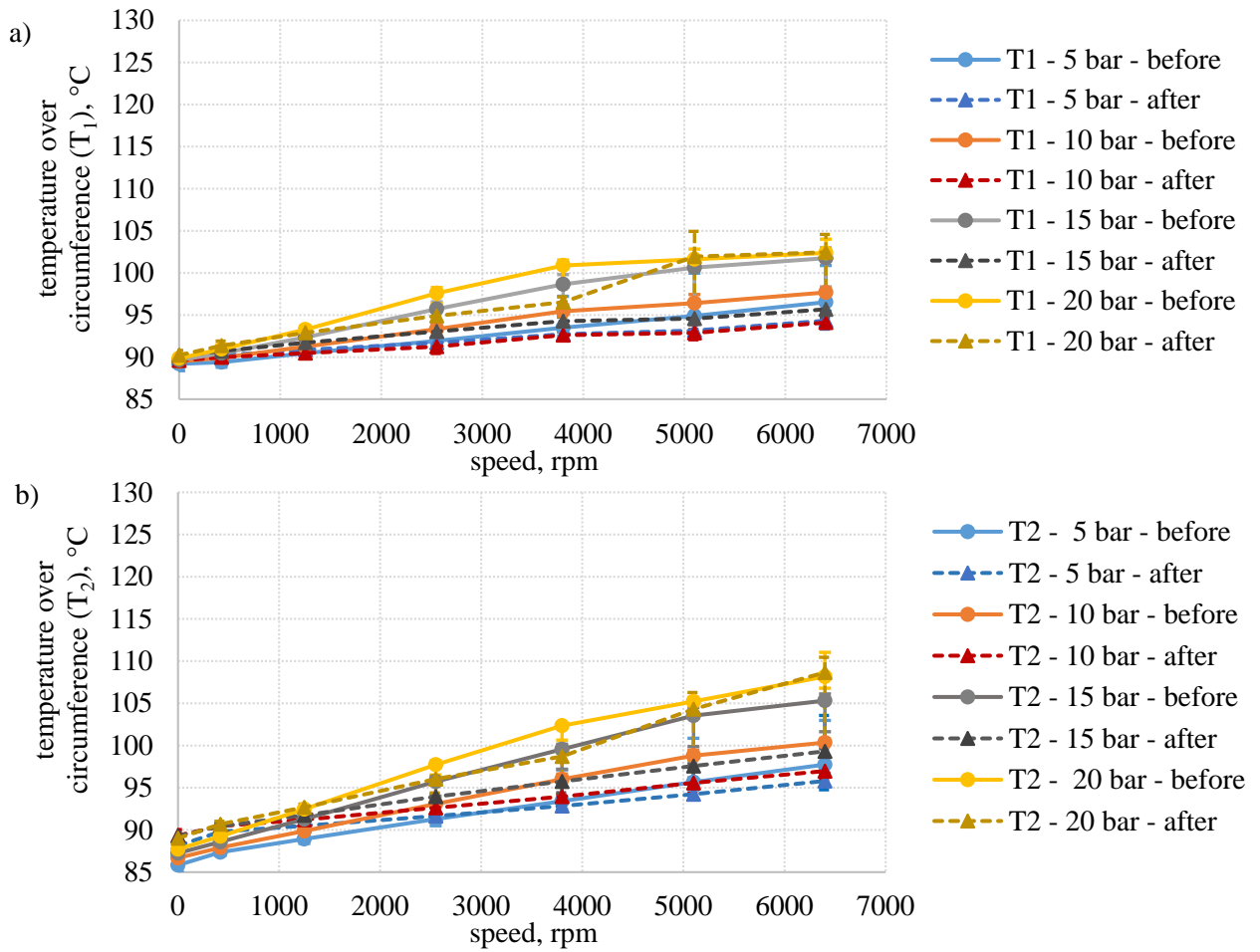
Figure 5.4: Temperatures over the circumferences of (a) structured seal 1 and (b) structured seal 2. 'before' and 'after' represent the function tests 1 and 2, respectively.

a)

b)
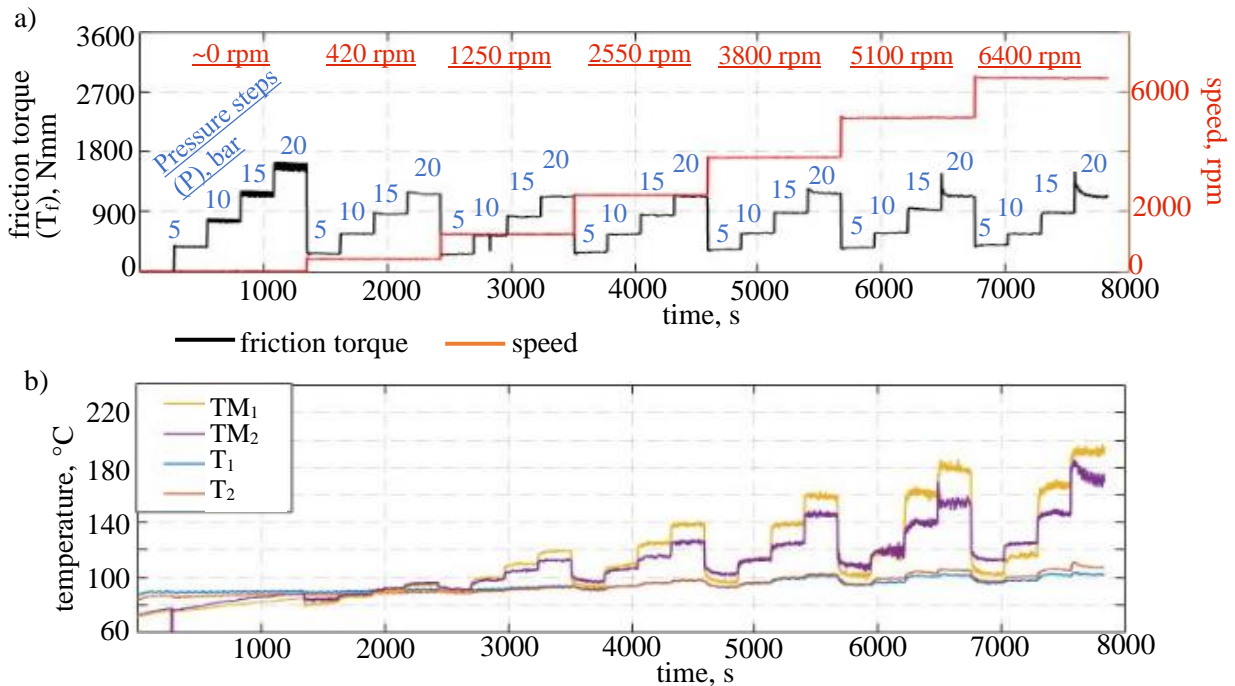
Figure 5.5: Friction torque and the temperature behaviour for the structured seals during the whole function test 1.

Figure 5.4 shows the near-circumference contact temperatures (T_1 and T_2). It should be noted that the scales of these graphs are different than that of the (TM_1 and TM_2) to show more details. For a direct comparison of T_1, T_2 and TM_1 and TM_2, the results of T_1 and T_2 are shown with the scale of TM_1 and TM_2 in Appendix C (Figure C-1). The near-circumference contact temperatures (T_1 and T_2) increases with speed as well. However, this increase is not as significant as in the axial contact temperatures. This indicates that the axial contact is more dominant on the sealing performance than the circumferential sealing contact.
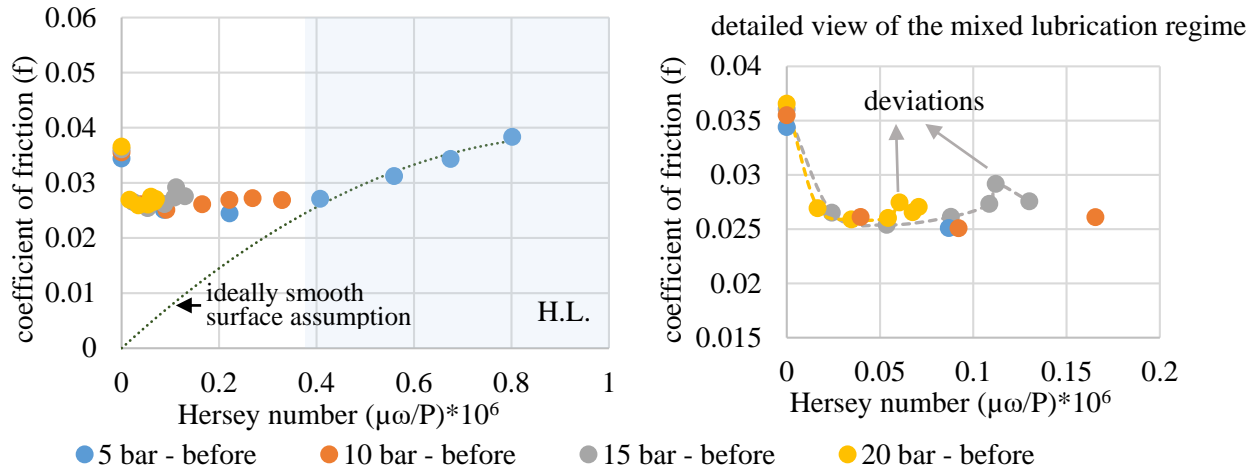
Figure 5.6: Coefficient of friction values for the structured seals. H.L.: possible pure fluid friction region. 'before' represents the function test 1.

Figure 5.6 shows the coefficient of friction with plotted over the Hersey number (coefficient of friction vs. speed graph is shown in Appendix C, Figure 3). The friction of two seals in the system is assumed to be equal. The coefficient of friction is calculated by using the friction torque shown in Figure 5.1 and, the normal force acting on the axial sealing contact. The Hersey number is calculated as viscosity (Pa·s) times speed (1/s) divided by pressure (Pa). The viscosity is determined as the mean of TM_1 and TM_2. Consequently, a Stribeck like curve is obtained. The curve has some deviations at low Hersey numbers. This can be because that the classical Hersey number is not sufficient for mixed lubrication or the gap form changes at high pressures. Another reason can be that the contact heats up dramatically at some locations and this leads to significantly thinned film regions. Consequently, dramatic local increases in the coefficient of friction might be occurring.
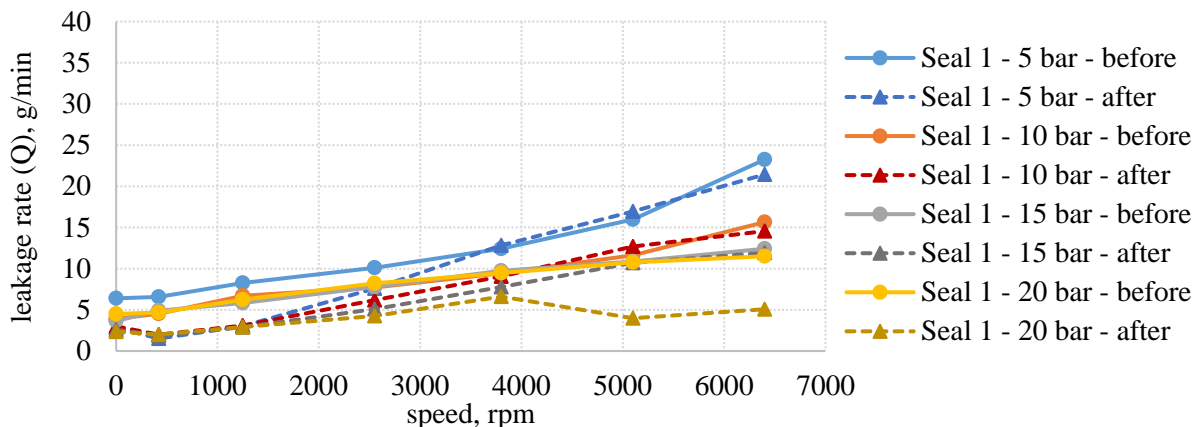
 Figure 5.7: Leakage rates for the structured seal 1 in Test A. 'before' and 'after' represent the function tests 1 and 2, respectively.

The mixed lubrication regime does not exhibit a clear minimum. Instead, the curve is more plateau like for a broad region in the mixed lubrication. This indicates that solid-solid contact might still be occurring

until high Hersey numbers. As the Hersey number increases further, the system seems to operate fully in hydrodynamic lubrication.

Leakage rates of seal 1 increases with respect to speed (Figure 5.7). This can be due to the film formation in the contact. Although the axial contact warms up (therefore, viscosity decreases), axial sealing gap seems to get thicker with increasing speed. The leakage values are higher at 5 bar but interestingly, they are similar at 10 bar, 15 bar and 20 bar except for 6400 rpm. This observation is even valid at 0 rpm. This means that the surface irregularities and the peaks which can generate leakage paths were pushed more with increasing pressure. The effect of the pressure seems to be balanced from 10 bar on. At higher speeds than 0 rpm, the leakage might be lower for high pressures due to high contact temperatures and other factors such as elastic deformations of the seal and cavitation formation.

5.1.1.1.2   FUNCTION TEST 2 (AFTER the LONG TERM TEST)

Here, the seal performance after the long term test is described. At 0 rpm, the friction torque values in the function test 2 are similar to those for the function test 1 (Figure 5.1). This shows that the normal force acting on the sealing contact is not notably changed. At 5 bar, the friction torque continues to be similar to that in the function test 1 with increasing speed as well. This behaviour is valid for the temperatures too although the seals are worn. Brunetière *et al.* [33] showed that the surface texturing can reduce the dependency of friction on surface roughness. However, the current results cannot be explained just with this phenomenon since it is not observed at other pressures.
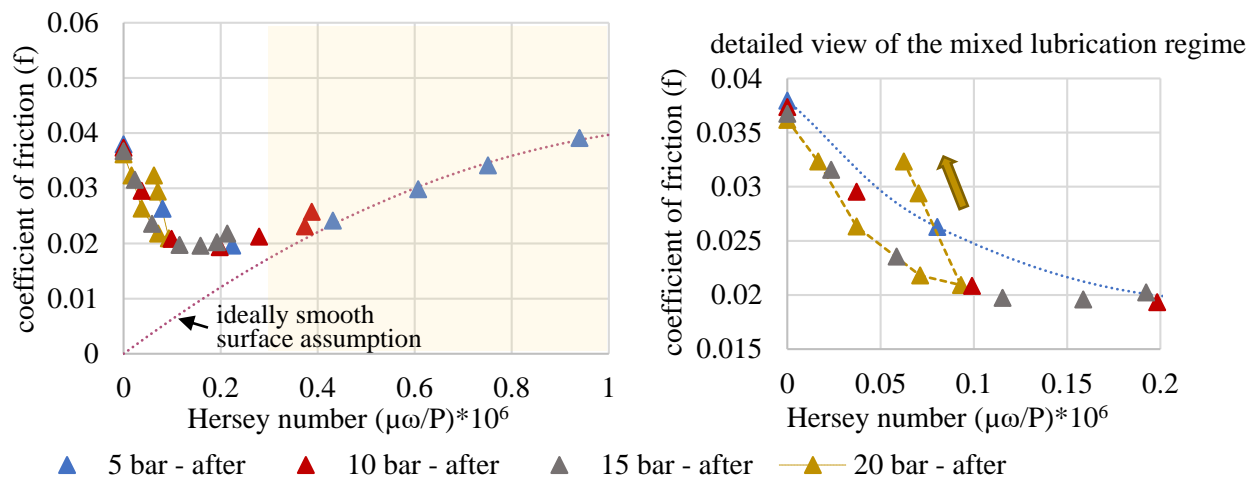
Figure 5.8: Coefficient of friction values for the structured seals. H.L.: possible pure fluid friction region. 'after' represents the function test 2.

At 10 bar and 15 bar, the minimum torque occurs at higher speeds than in the function test 1. This does not seem to be due to the contact temperatures since they are lower in the function test 2. At 20 bar, hydrodynamic regime does not seem to occur. The friction torque decreases until 3800 rpm and it increases sharply after this speed. However, this increase is not due to film formation. Excessive contact temperatures indicate that the seals were about to fail (Figure 5.2Figure 5.3). Figure 5.9a shows that the rapid increase in the torque occurs at the beginning of high speed and high pressure steps and the friction torque stabilization takes longer. The temperature at the axial interface of seal 1 (TM_1) shows a rapid increase similar to the friction torque (Figure 5.9b). TM_1 exceeds the glass transition temperature and reaches to the critical values. Obviously, the mean friction torque and the mean axial contact temperature behaviour is the result of the influences of each other.

Figure 5.8 shows the coefficient of friction plotted versus the Hersey number. Due to the excessive contact temperatures, the coefficient of friction increases drastically at 20 bar. The influence of the temperature is so dominant that even the Hersey number starts to decrease although the speed increases. Other than this, no significant deviation is visible in the curve. This can be because that the peaks are worn and they do not influence the sealing gap significantly.
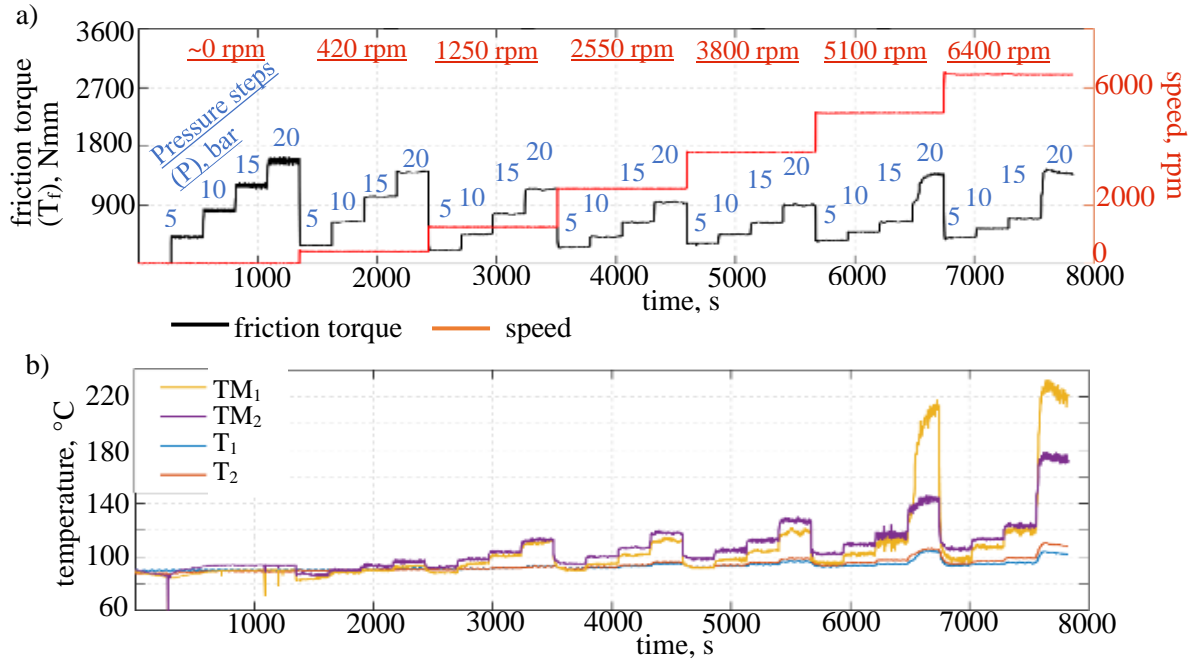
Figure 5.9: Friction torque and temperature behaviour for the structured seals during the whole function test 2.

The leakage rates are lower in the function test 2 for low speeds (Figure 5.7). With increasing speed, the leakage rates start to reach the leakage levels of the function test 1 except for 20 bar. This might be an indication for the similar gap heights and full film lubrication both in the function tests 1 and 2. However, the friction torque results are not same for both of the tests at high pressures and high speeds. It might be that there are high peaks and macro surface irregularities resulting thin films and a different gap form in the function test 1. This might lead to higher friction. However, the leakage amount can still be similar to that in the function test 2. In addition, Brunetière *et al.* [33] states that the leakage is controlled by different parameters:

- Pressure flow due to pressure difference at the seal gap and leakage paths influences leakage.
- Cavitation zones at the contact prevents leakage due to no pressure gradient within the cavitation.
- Roughness and speed can generate either an inward or outward pumping effect.

In the current work, it is known that the surface of the seals changed at macro and micro level but, it is unknown how this influences the pressure distribution and cavitation. However, it is possible to say that the leakage paths are changed since the leakage is lower at 0 rpm in the function test 2.

At 20 bar, the leakage rates are low at high speeds as well. This might be because of that the excessive contact temperatures resulted a kind of relaxation in the seal material. As a result of this, the leakage paths might be partially blocked.

5.1.1.1.3   TEST A – COMPARISON of the FUNCTION TESTS 1 and 2
Figure 5.10 shows the comparison of the coefficient of friction values for the function test 1 and 2. Around 0 rpm, the coefficient of friction values for both of the seals are similar. With increasing Hersey number, coefficient of friction becomes lower for the function test 2. In addition, the coefficient of friction reaches to a minimum value and starts to increase earlier. There is no clear minimum value for the function test 1. Instead, there is a broad mixed lubrication region. In the function test 2, the solid-solid contact seems to end earlier. The lower contact temperatures in the function test 2 can be an indication for less solid contact (Figure 5.2 and Figure 5.3).

Hydrodynamic lubrication occurs earlier in the second function test. Classically, the reduction of the roughness or the temperature can shift the transition from mixed to hydrodynamic lubrication to lower

Hersey numbers. As stated, the temperatures are lower in the function test 2. However, the roughness of the seal surfaces increases (Figure 5.13). On the other hand, macro surface features such as manufacturing errors are worn after the long term test. This might be resulting a more favourable gap. In addition, the curves of the tests are very similar in the hydrodynamic regime but they do not coincide completely. This indicates that the gap has changed slightly in the function test 2.
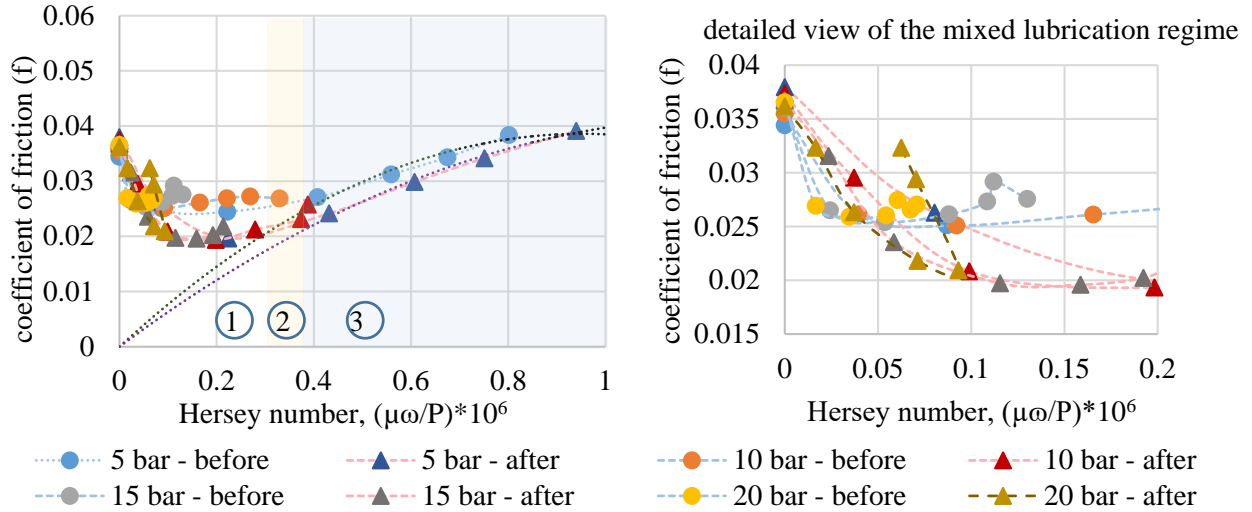
Figure 5.10: Comparison of the coefficient of friction values for the function tests 1 and 2 of the structured seals. Region 1 is mixed lubrication for both tests. Region 2 is the hydrodynamic lubrication for the function test 2 while it is mixed lubrication for the function test 1. Region 3 is mixed lubrication for the function test 1. 'before' and 'after' represent the function tests 1 and 2, respectively.
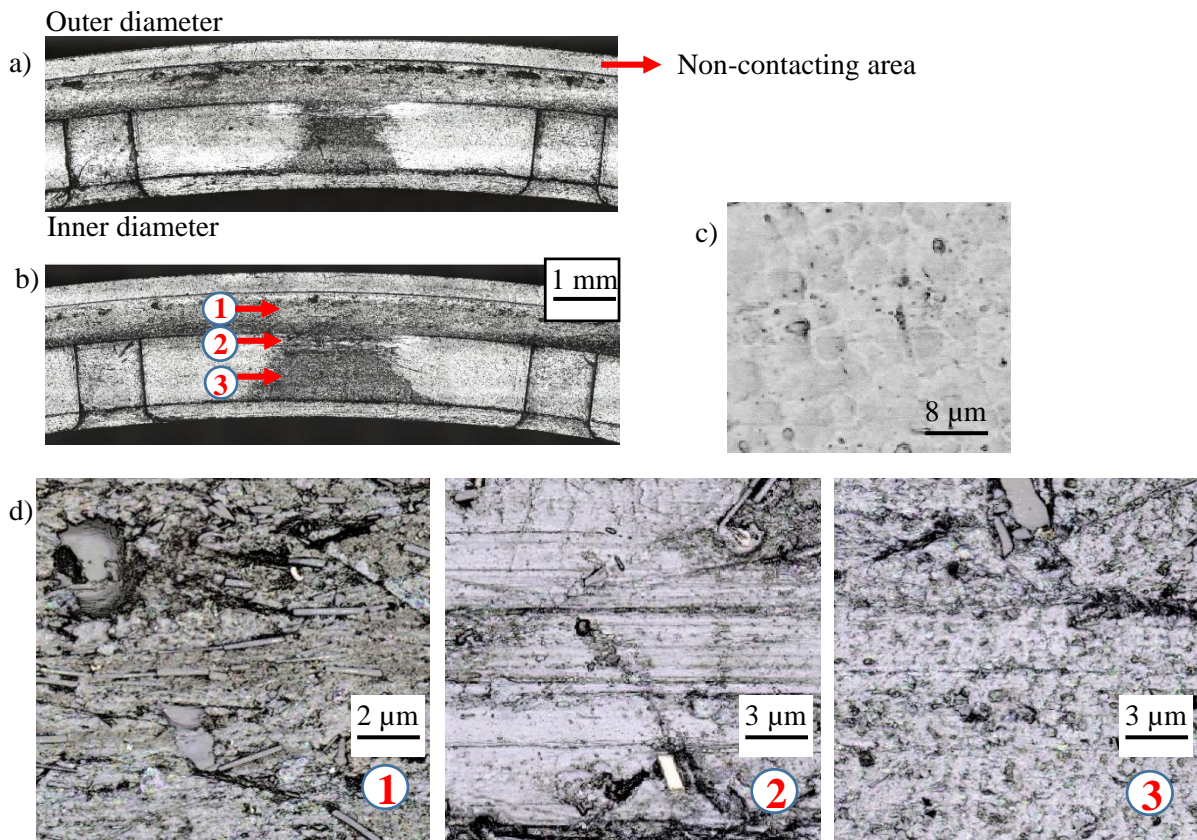
Figure 5.11: Wear behaviour of the structured seal 1. Flow is in the CW direction. a) The wear pattern between the structures 4 and 5 (10x). b) The wear pattern between the structures 14 and 15 (10x). c) The seal surface before the tests (100x) d) The detailed view of the wear (100x).

5.1.1.1.4   TEST A – WEAR BEHAVIOUR of the SEALS and the COUNTERFACES

Figure 5.11 shows that the seals are worn significantly after the tests. As a positive result of this, the surface imperfections such as the burrs mostly disappeared which can be a reason of lower friction in the function test 2. The wear occurs on the unstructured surfaces. The wear pattern changes depending on the location. This can be due to non-uniform distribution of the lubricant film and the temperature because of elastic deformations of the seals or the non-uniform initial surface heights. The unstructured surface over the structures (1) has many short scratch-like patterns and grooves. It seems like high temperature locations occurred on this area. The unstructured areas between the structures (3) became broader due to wear particularly in the region at the opposite of the joint. On these areas, there are a lot of grooves. These grooves can be due to the glass bubbles in the sealing material. Although the glass bubbles are embedded 50 – 60 μm under the surface, some of them might be reaching to the surface and be destroyed. The transition area (2) between the areas (1) and (3) looks smooth with a few scratches.
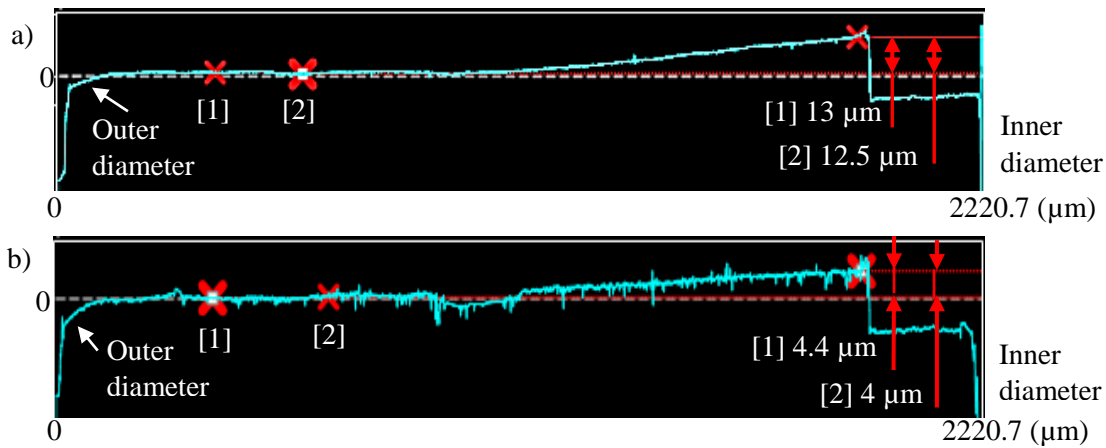
Figure 5.12: The radial surface profile between the two structures of seal 1: a) before the tests, b) after the tests.

Overall, the structures kept their initial profile. However, they became slightly shorter since the flat areas between the structures became broader. In addition, the geometry of the right and the left edges are changed. The profiles of the seals are changed as well in the radial and the circumferential direction. The manufacturing errors between the structures are flattened (Figure 5.12). This can influence the film formation since it influences the gap form. These manufacturing errors were resulting a divergent form. When they disappeared, the gap form might become more convergent with the pressure. Therefore, the hydrostatic load reduction might have been higher in the function test 2.
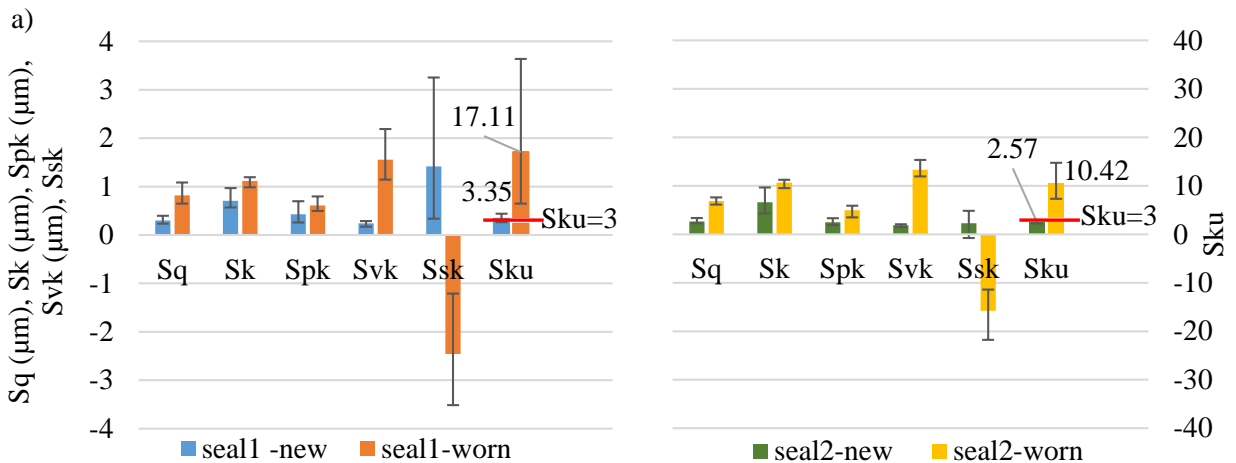
Figure 5.13: Surface roughness parameters of structured seal 1 and 2 before and after the tests.

The roughness parameters S_q, S_k, S_{pk}, S_{vk} increase after the tests (Figure 5.13). Particularly, S_{vk} increased significantly. This indicates that the deeper valleys took place on the sealing surface after the tests. Also, skewness S_{sk} becomes negative. This shows that the peaks are mostly removed and the deep scratches or valleys are dominant on the seal surfaces. Kurtosis also increased after the tests.
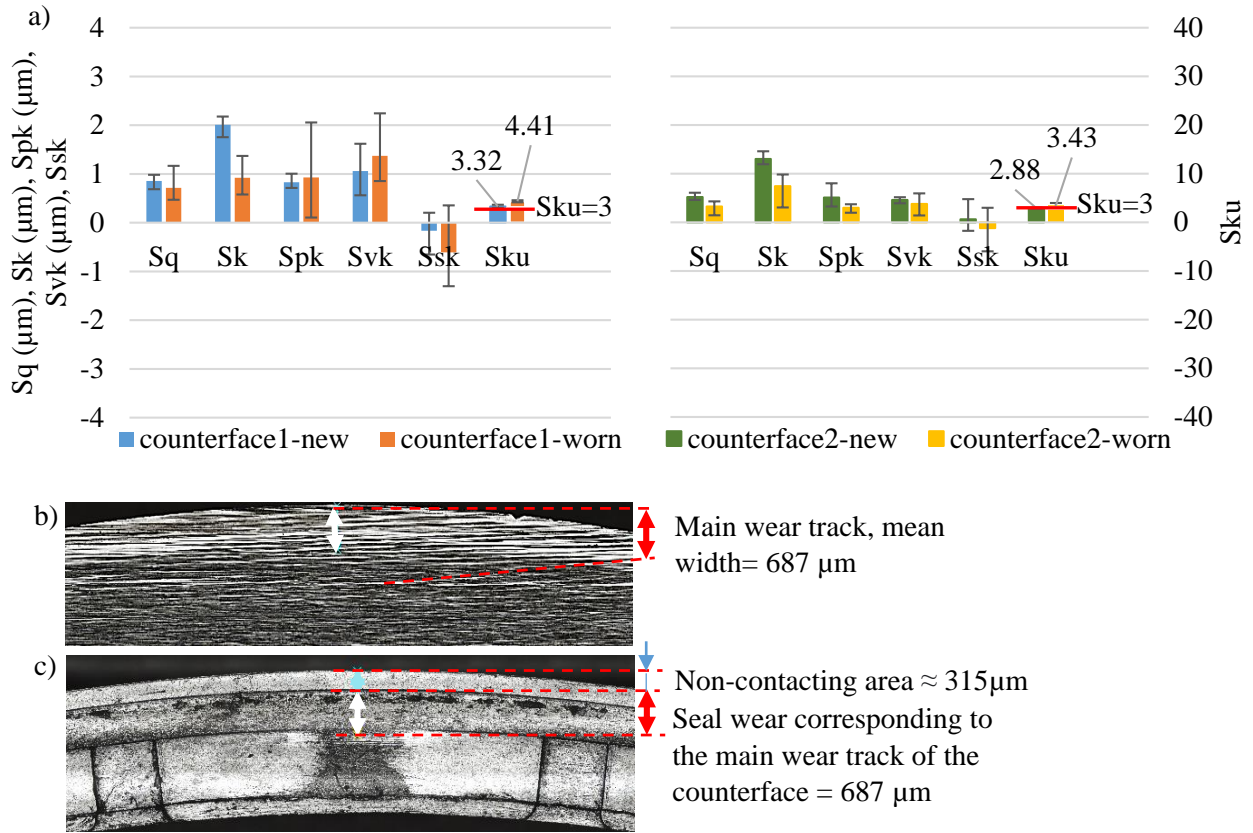
Figure 5.14: a) Surface roughness parameters of the counterfaces 1 and 2 before and after the tests. b) The wear track on counterface 1. c) The wear track on the structured seal 1.

It has been suggested that negative skewness and high kurtosis values lead to lower friction in mixed lubrication regime [164,165]. Sedlaček et al. [164] introduced micro-dimples on a surface. This surface is characterized by a wide spacing between the dimples and the small dimple depths which yields a high kurtosis and a negative skewness. In the current case, the kurtosis, skewness and the depth of the valleys might have become favourable after the long term test. This might be one of the reasons for the lower friction and temperatures in function test 2. It should be noted that the roughness and the profile measurements are made after all of the tests but not directly after the long term test (therefore, not before function test 2). During the function test 2, the seal surfaces might have been still changed due to the high contact temperatures.

In contrast to the seals, the counterfaces are polished after the tests. The roughness parameters S_q, S_k, S_{pk} and S_{vk} decreases (Figure 5.14a). The peaks and the valleys of the counterface 2 become shorter and shallower, respectively due to the decrease in S_{pk} and S_{vk}. While the skewness values (S_{sk}) becomes more negative, the kurtosis S_{ku} does not change significantly. The wear track on the counterfaces corresponds to the wear band over the structures on the seals (Figure 5.14b, c). The unstructured areas between the structures do not generate any visible wear track on the counterfaces since they are small.

5.1.1.2 TEST B
The results of Test B are shown in Appendix C (Figures C-3-10). Overall, the performance of the seals is very similar to those in Test A. However, the friction torque and the axial contact temperatures TM_1 and TM_2 rises dramatically at high speeds and 20 bar in the function test 1 of Test B. At these test steps,

the leakage is also high. Despite of this, the seals manage to function during the long term and the function test 2.

In the tests, the surfaces of the seals damaged severely. Due to the wear, the height difference between the worn surface and the non-contacting surface at the outer diameter of the seal reached at tenth of microns. The sealing material started to melt and flow into the structures. Structures are worn as well. The divergent halves of the structures are worn more than the convergent halves. This can be attributed to the cavitation formation in the divergent zones.

5.1.1.3   COMPARISON of TEST A and TEST B

Figure 5.15 shows the comparison of the function tests of Test A and Test B. The behaviours of the seals are very similar at high Hersey numbers (i.e. hydrodynamic regime). It seems that the features leading to the hydrodynamic regime do not change from one test group to another significantly. This indicates that the structures might be the dominant surface features on lubrication.
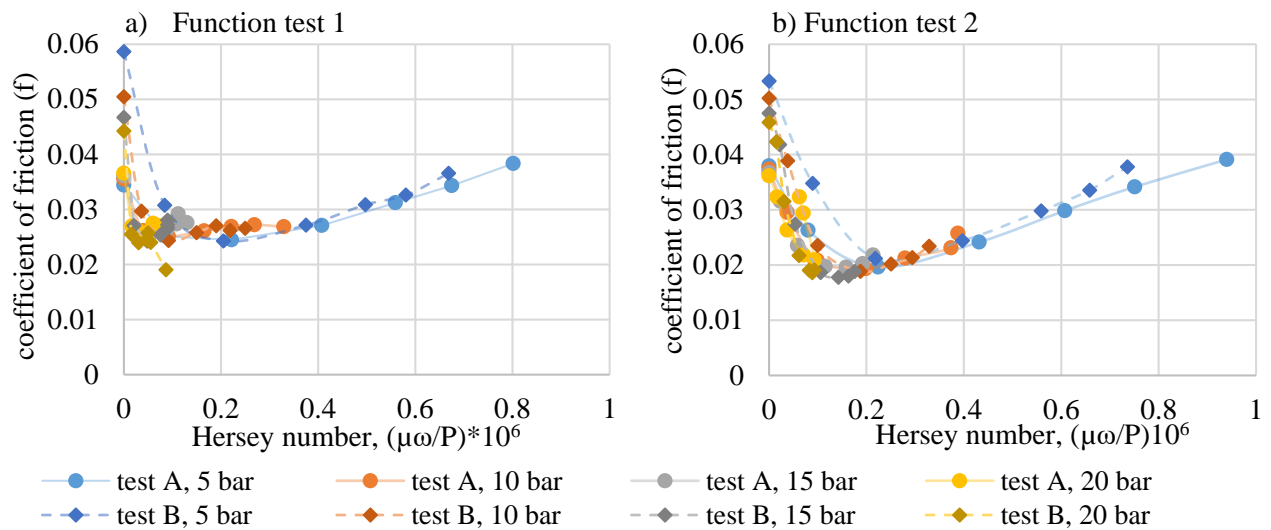
Figure 5.15: Comparison of the friction tests of the structured seals.

5.1.1.4   CONCLUSION

The results below can be drawn from the friction tests of the structured seals:

- It is demonstrated that the friction torque behaviour is directly related with the axial contact temperatures. The results show that the lubrication is dominated by the axial contact temperatures instead of the sump temperatures.
- At high pressures and temperatures, the seals seem to operate mostly in mixed lubrication.
- Combination of high speeds and 20 bar seems to be critical for the structured seals. Under these conditions, high friction torque and high contact temperatures are observed. Some seals started to melt. Therefore, the seal operation limits might be lower than suggested.
- High temperature seems to occur in the outer diameter direction. The unstructured surfaces over the structures are the most worn surfaces. The structures are not changed dramatically after the tests. They became slightly shorter. The divergent halves of the structures wear more probably due to cavitation formation.
- After the long term tests, the separation of the seal and the counterface surfaces seem to occur earlier. This probably due to the wear of the manufacturing errors and the burrs.
- Both for the function tests 1 and 2, the behaviour of the seals is not very different in hydrodynamic lubrication. This shows that the structures might be the dominant surface features on lubrication.

5.1.2   STANDARD SEALS

5.1.2.1   TEST C

5.1.2.1.1   FUNCTION TEST 1 (BEFORE the LONG TERM TEST)

In test C of the standard seals, extra leakage occurred at the side of the seal 1 which results from one of the screws of the counterface. Therefore, leakage rates of seal 1 are not considered. This extra leakage does not influence the contact temperatures since the contact temperatures of seal 1 is not notably different than those of seal 2 (Figure 5.18 and Figure 5.19).
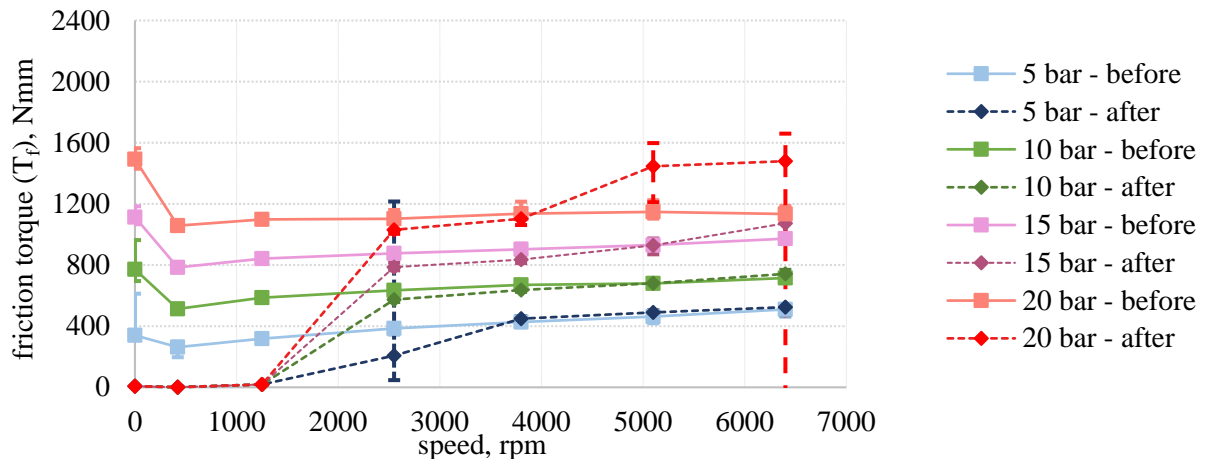
Figure 5.16: Friction torque (resulted from two standard seals) in Test C. 'before' and 'after' represent the function tests 1 and 2, respectively.

In the first function test, friction torque decreases until 420 rpm and then it increases slightly (Figure 5.16). As in the structured seals, the torque is higher at the beginning of each speed – pressure step probably due to the running-in process (Figure 5.17a). The behaviour of the friction torque is very similar to that of the axial contact temperatures (Figure 5.17b).
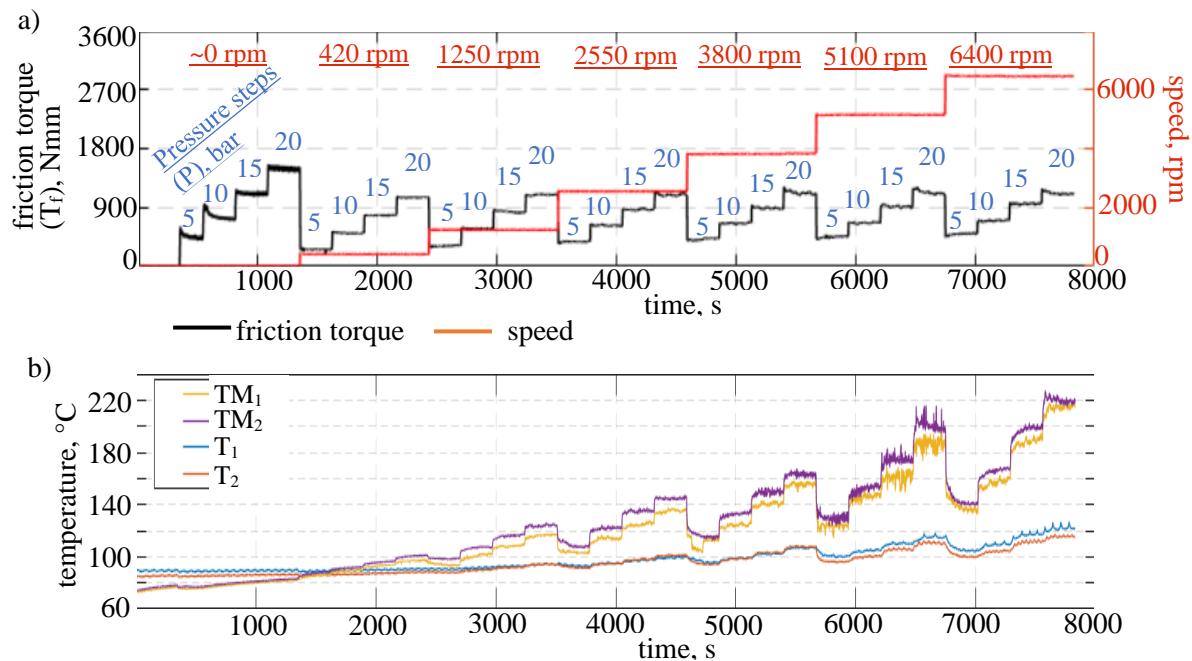
Figure 5.17: Friction torque and temperature behaviour during the whole function test 1 of the standard seals.
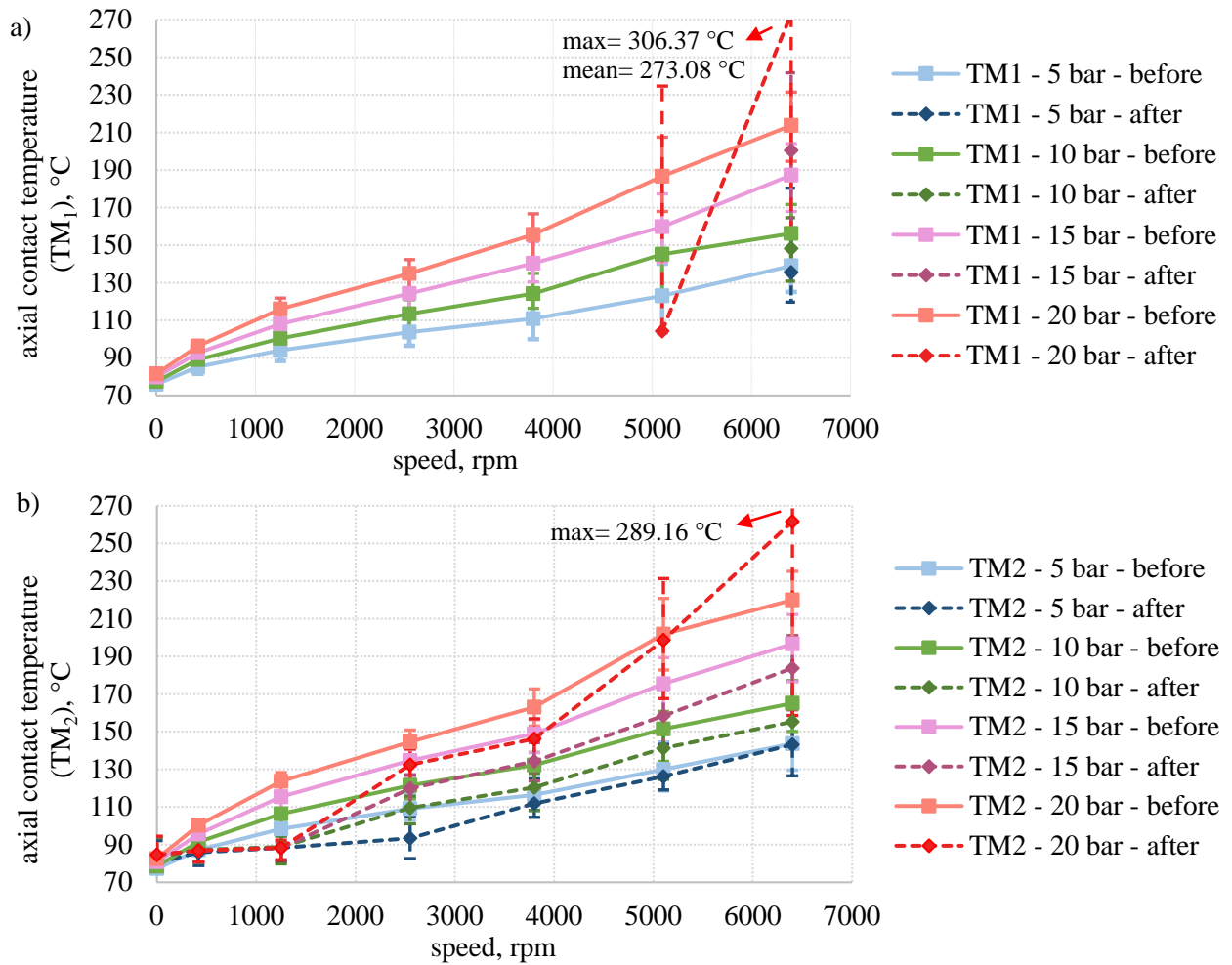
Figure 5.18: Axial contact temperatures for (a) standard seal 1 and (b) standard seal 2 in Test C. 'before' and 'after' represent the function tests 1 and 2, respectively.

The axial and the circumferential contact temperatures increase with pressure and speed (Figure 5.18 and Figure 5.19). The axial contact temperatures (TM_1 and TM_2) reach to glass transition temperature earlier than the structured seals. The near-circumferential contact temperatures (T_1 and T_2) are also high. They almost reach to the glass transition temperature as well. It should be noted that the scales of the graphs of T_1 and T_2 are different than that of the (TM_1 and TM_2). For a direct comparison of T_1, T_2 and TM_1 and TM_2, the results of T_1 and T_2 are shown with the scale of TM_1 and TM_2 in Appendix C (Figure C-11).

Figure 5.20 shows the coefficient of friction with plotted over the Hersey number. It should be noted that the steps of the standard seals are not subtracted from the contact area while calculating the coefficient of friction. This is for the comparison with the numerical results in the future work. The coefficient of friction decreases at the beginning. After reaching a minimum, it starts to increase. At high Hersey numbers, the lubrication regime might be hydrodynamic lubrication. However, the coefficient of friction curve is quite steep in this region. Therefore, the lubricant film might be thin. Consequently, the contact temperatures can increase fast and the lubricant film might be rupturing at some point again. In addition, the coefficient of friction increases almost vertically at some Hersey numbers. This shows that the contact temperatures become too high and more dominant than the speed.
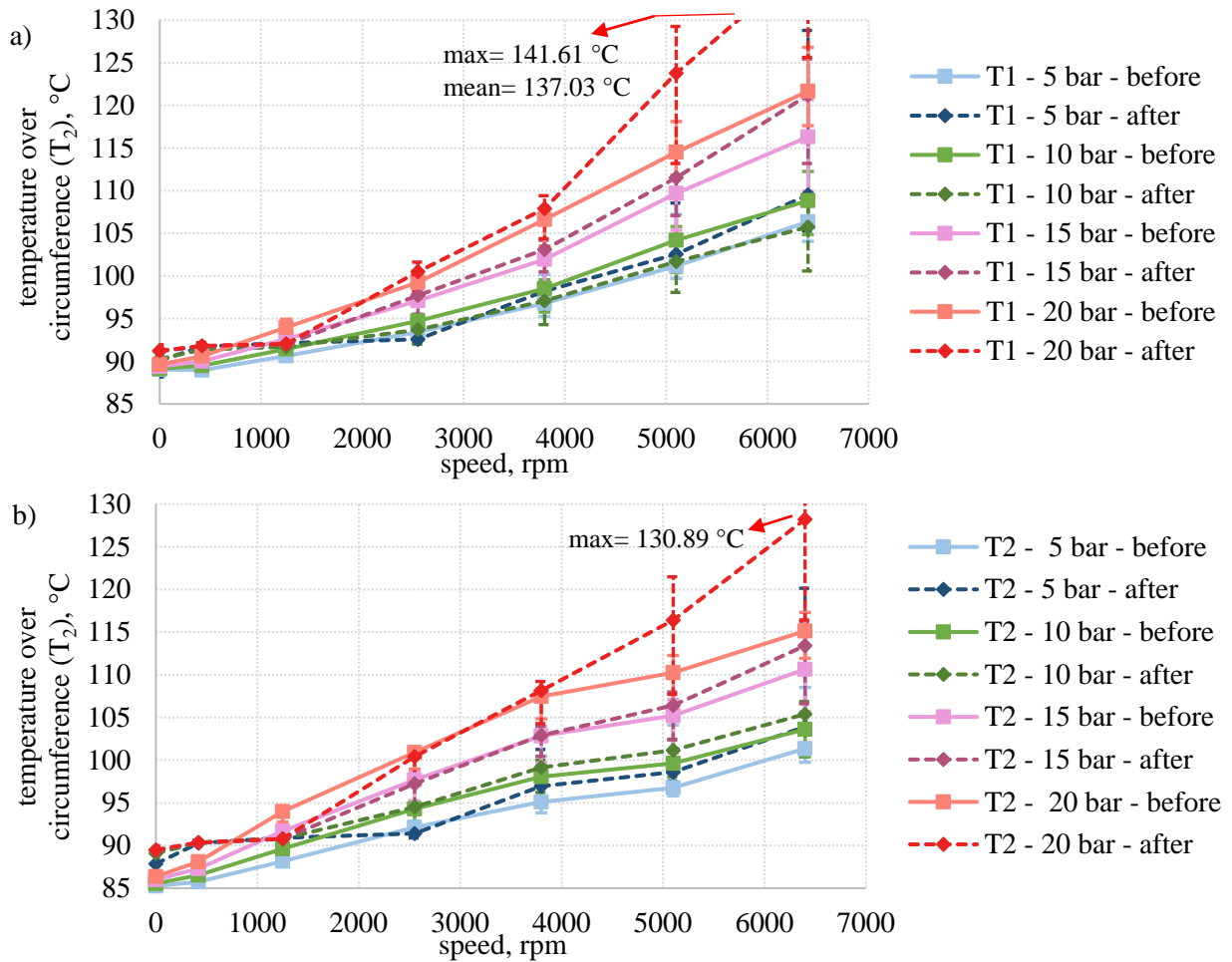
Figure 5.19: Temperatures over the circumferences of (a) standard seal 1 and (b) standard seal 2. 'before' and 'after' represent the function tests 1 and 2, respectively.
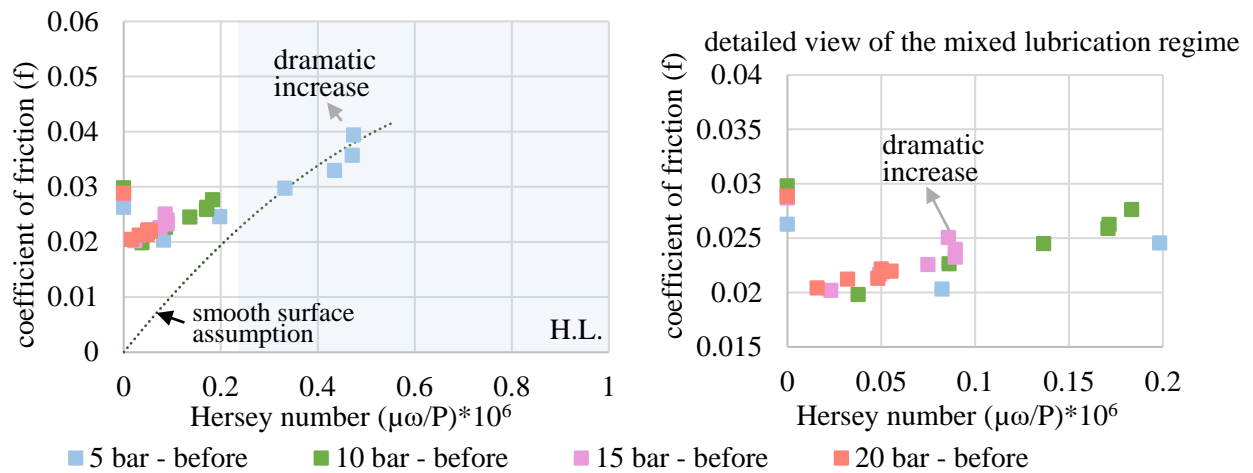
Figure 5.20: Coefficient of friction values for the standard seals. H.L.: possible pure fluid friction region. 'before' represents the function test 1.

The leakage rates of the seals do not change significantly with speed. They increase slightly with increasing pressure (Figure 5.21). This can be because that the lubricant film thickness at the axial sealing contact does not change. It might even be that the seals do not even run in full hydrodynamic regime at during the experiments. Another reason can be that the leakage paths are initially big (like joint) and the leakage which is resulted from these paths are much higher than that of the lubricant film.
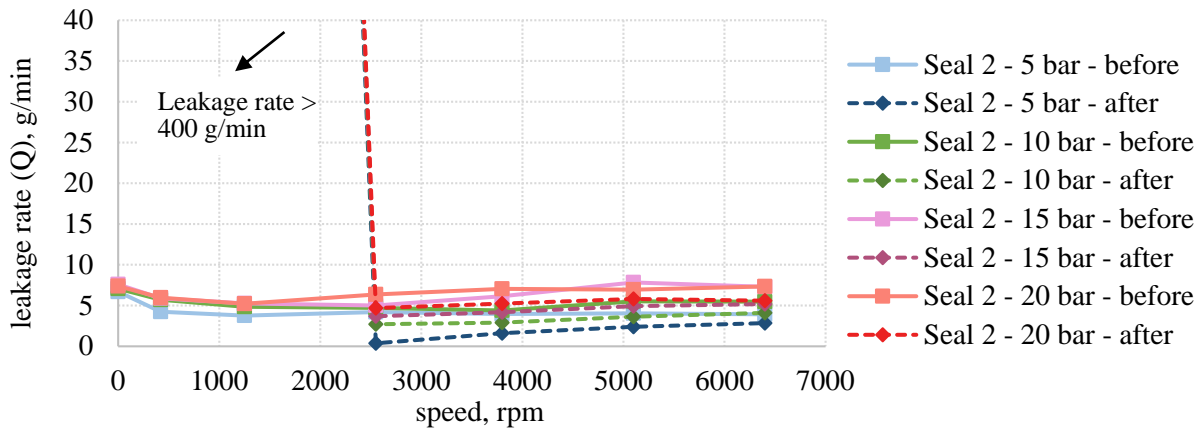
Figure 5.21: Leakage rates for the standard seal 2. 'before' and 'after' represent the function tests 1 and 2, respectively.

5.1.2.1.2   FUNCTION TEST 2 (AFTER the LONG TERM TEST)

In function test 2, the seals did not hold the pressure until 2550 rpm (Figure 5.16). When the seals held the pressure again, the generated friction torques are very similar to those in the first function test except for the high pressure and high speed combinations. The friction torque and the contact temperatures are significantly high at high pressures and high speeds. Under these conditions, the maximum axial contact temperatures are around 300 °C which is close to the melting temperature of the seal material. The behaviour of the axial contact temperatures (TM_1 and TM_2) correlate with the behaviour of the friction torque as in the other tests (Figure 5.23). It should be noted that TM_1 mostly could not be measured due to the signal loss.
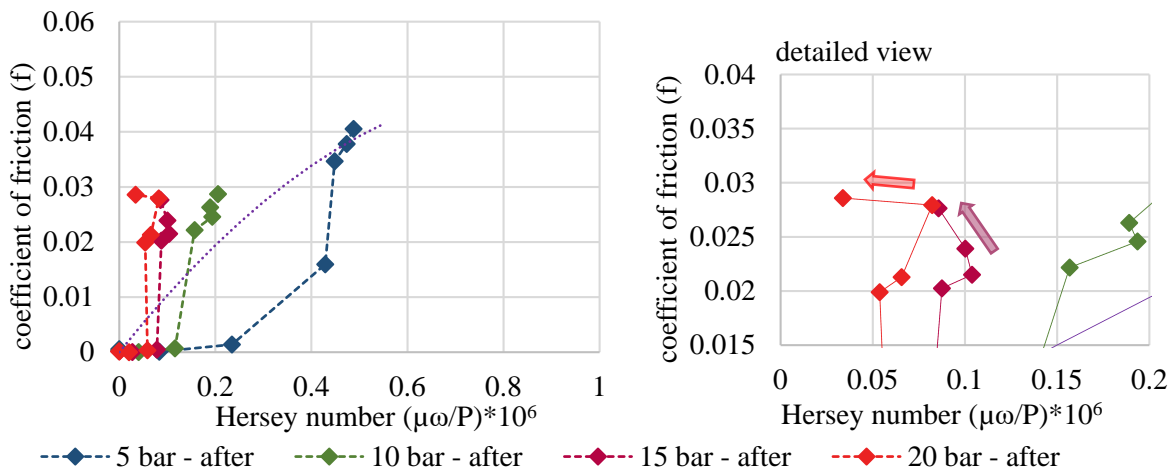
Figure 5.22: Coefficient of friction values for the standard seals. 'after' represents the function test 2.

Figure 5.22 shows the calculated coefficient of friction values. Many points are zero due to the loss of pressure during the experiment. On the other hand, the calculated points indicate that the contact temperatures were very high during the experiment. These high temperatures result so low viscosities that the Hersey number decreases while the speed and the coefficient of friction are increasing. Consequently, the coefficient of friction curves change their direction.
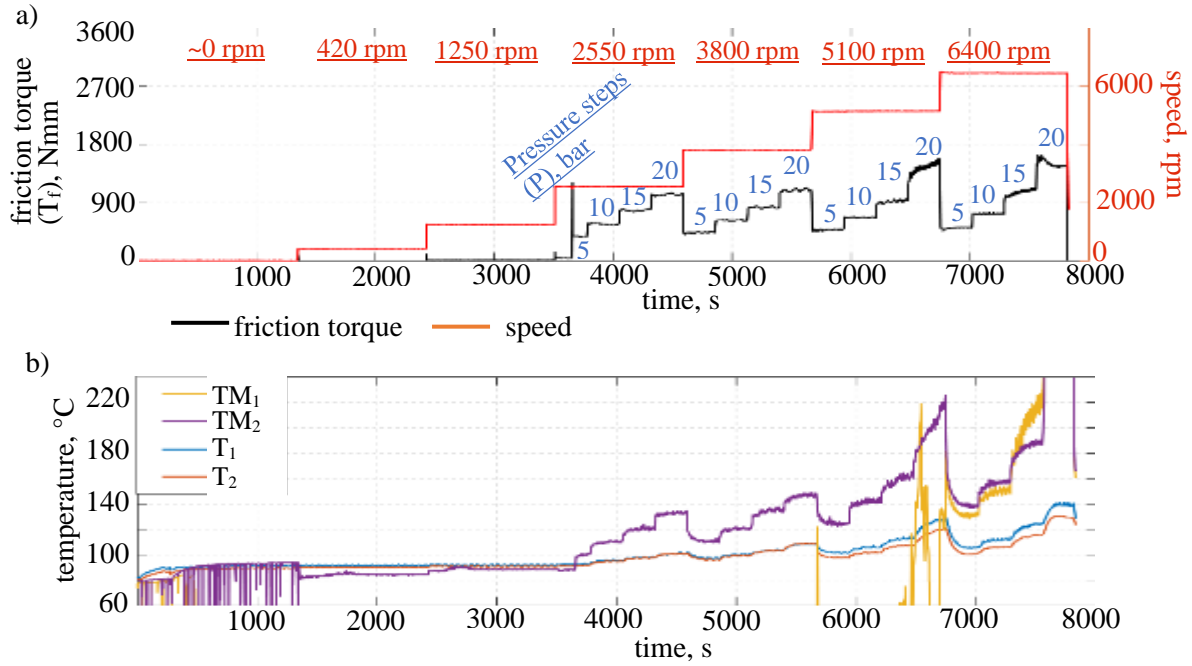
Figure 5.23: Friction torque and temperature behaviour during the whole function test 2 of the standard seals.

The leakage rates (Figure 5.21) are very high at the beginning of function test 2 due to the loss of pressure. When the seals held the pressure, leakage decreases and it is lower than that in the first function test. Leakage rates increases with increasing pressure. On the other hand, the influence of speed on leakage is quite low.

5.1.2.1.3 TEST C – COMPARISON of the FUNCTION TESTS 1 and 2

Due to the loss of pressure in the function test 2, it is not possible to make a reliable comparison of the function tests 1 and 2. However, the measured coefficient of friction for both of the tests are similar at 5 bar (Figure 5.24). For higher pressures, the seal surface warms up critically in the function test 2.
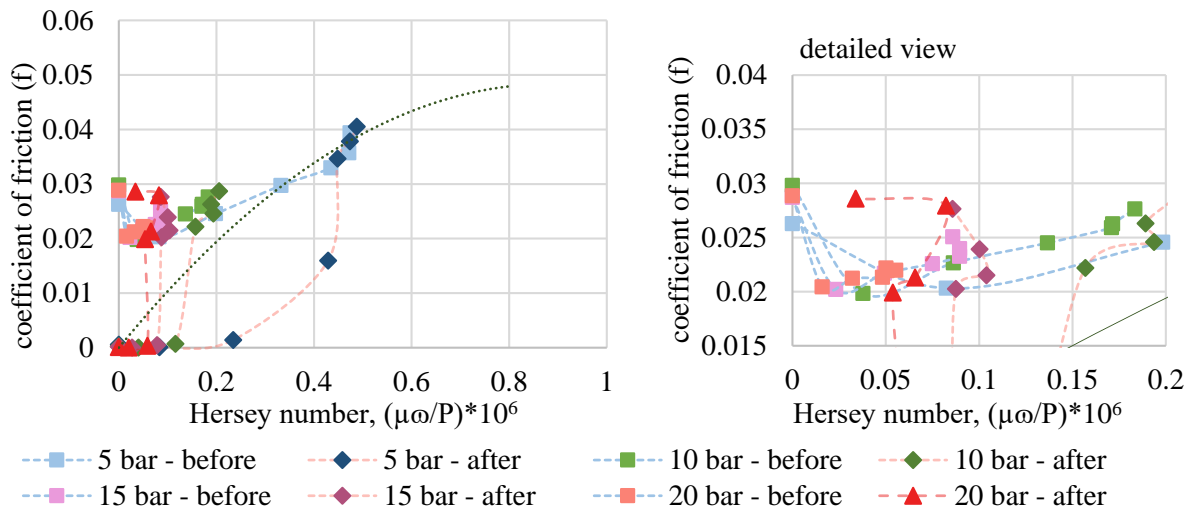
Figure 5.24: Comparison of the coefficient of friction values for the function tests 1 and 2. 'before' and 'after' represent the function tests 1 and 2, respectively.

5.1.2.1.4 TEST C – WEAR BEHAVIOUR of the SEALS and the COUNTERFACES

The seals worn severely after the tests (Figure 5.25). The height difference between the non-contacting seal surface and the seal surface in contact with the counterface is tenth of micrometeres (Figure 5.25c).

Due to the wear, the pores are dissappeared. The glass bubbles which were at subsurface started to stick out of the surface (Figure 5.25b). Some of the measured glass bubbles protrude up to 16 µm which can rupture the lubricant film.

After the tests, the non-contacting area seems to become shorter (it is 300 µm when the system is stationary and the seal is untilt). This is probably due to the melting of the seal material. The seals seem to heat more at the outer diameter of the counterface. Consequently, the material melts and generates a ridge at that region (Figure 5.25c). Also, some patches looks like burned areas are visible on the seal surface at that region (Figure 5.25e, area 1). These patches are randomly distributed. At area 2, less patches are visible. On the other hand, there is no damaged patches at area 3. The surface looks rather polished in the inner diameter direction.
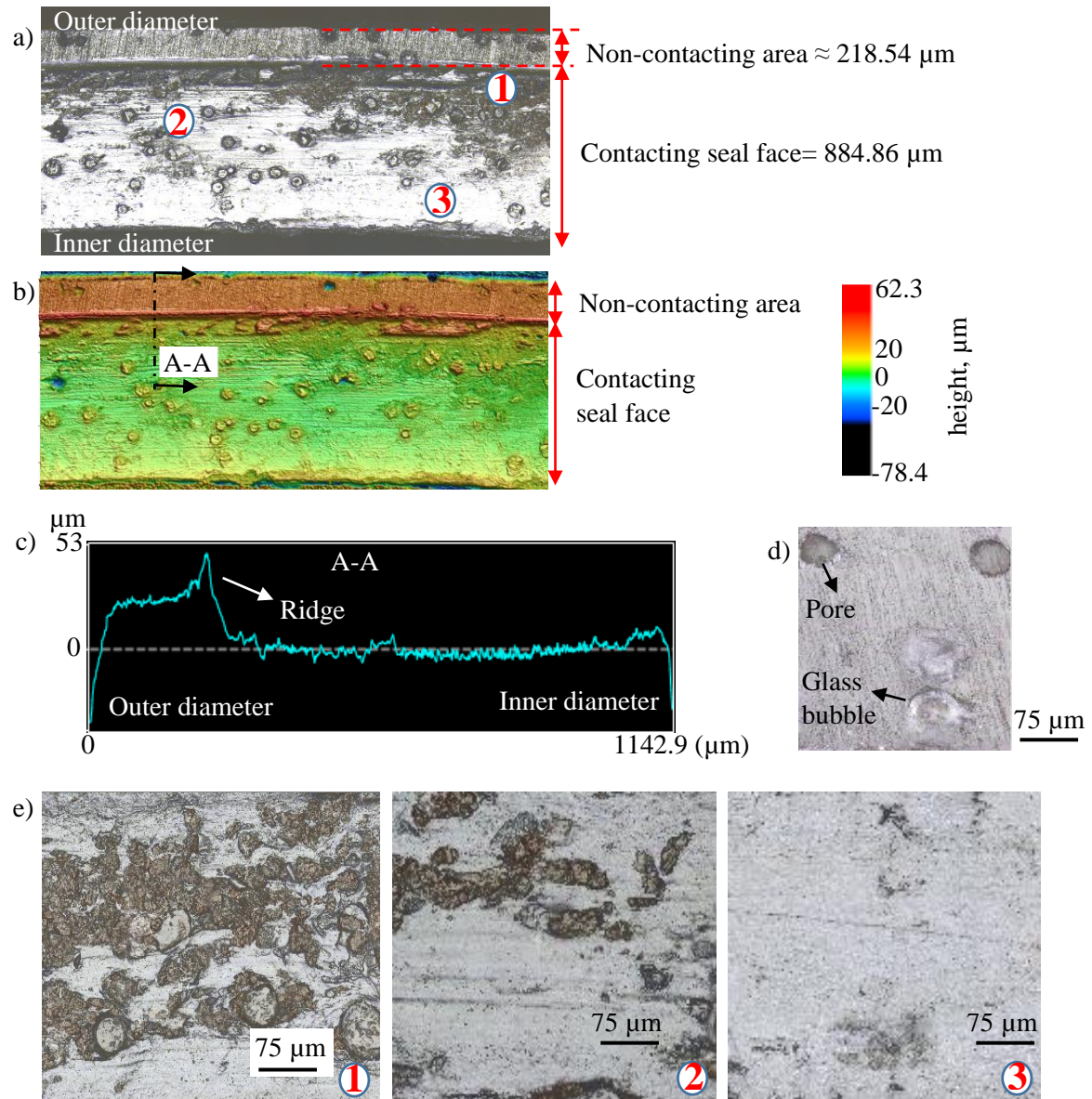
Figure 5.25: a) Wear behaviour of the standard seal 1 (10x). Flow: CW. b) Height distribution of (a). c) Radial profile of seal 1 after the tests. d) Seal surface before the tests (100x) e) Detailed view of the worn seal surface (100x); 1) severe damage 2) medium damage 3) polished, less damaged surface.

Figure 5.26 shows the change in the roughness parameters of the seals and the counterfaces after the tests. To measure these roughness parameters of the seals, the areas without the glass bubbles are selected. Overall, the roughness parameters of the standard seals are not very different than those of the structured seals. This is also valid for the counterfaces.

After the tests, S_q and S_k of the standard seals decrease slightly. On the other hand, skewness does not show a common behaviour. While it indicates that the surface of seal 1 has more peaks after the tests, the second seal surface is dominated by the grooves.

According to the friction results, the surface features of the standard seals seem to be not sufficient to generate an optimum lubricant film. The depth of some micro pores on the unworn seals are very deep this might lead to film rupture. Similarly, some glass bubbles which stick out the surface and are very high can influence the film negatively. They might be the reason of high contact temperatures.
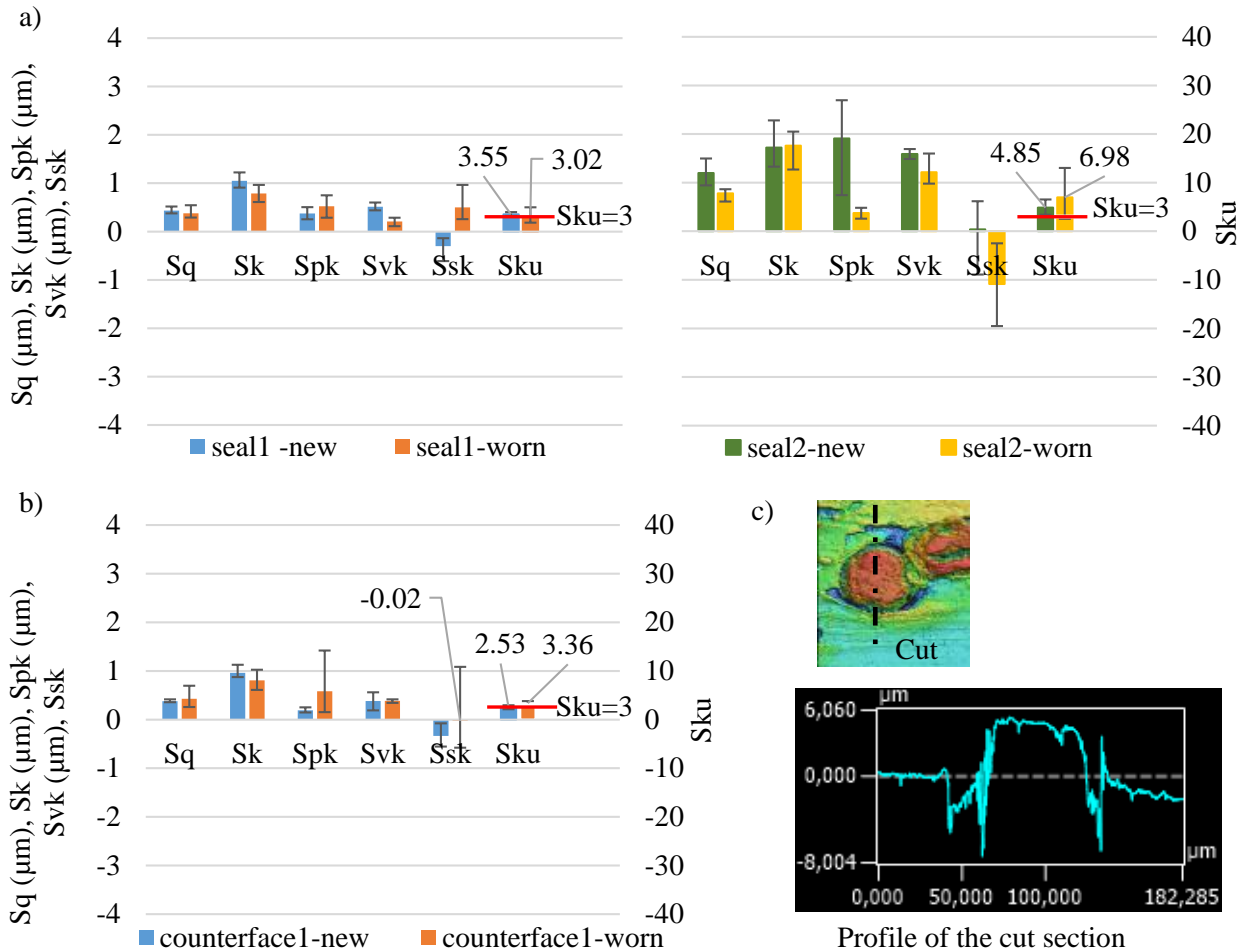
Figure 5.26: Surface roughness parameters of (a) the standard seals 1 and 2 and, (b) the counterfaces 1 and 2 before and after the tests. c) Profile of a glass bubble sticking out the seal surface.

5.1.2.2 TEST D

In test D, the standard seals failed at the end of the function test 1. They melted due to the high contact temperatures hence, the second function test could not be performed. The results of the function test 1 is shown in Appendix C (Figures 13-20). The friction torque and the contact temperatures increase dramatically at 6400 rpm and 20 bar. The seals seem to fail at this step. On the other hand, the leakage rates are not very high. The melted seal material seems to block the leakage paths.

5.1.2.3 COMPARISON of TEST C and TEST D

Since the seals in test D melted after the function test 1, test C and test D is only compared via the function test 1 (Figure 5.27). In general, the coefficient of friction values and the contact temperatures are higher in test D. Therefore, probably the lubricant film is thinner.

The coefficient of friction curves of the tests C and D do not coincide when they are plotted over Hersey numbers. This indicates that the contact features are not similar in these tests. The roughness parameters of the seals in test D are higher. Furthermore, the seals might be warming up in a different manner which

can result different gaps in the tests. These might be the reason of the offset between the coefficient of friction curves.

The coefficient of friction curves reach the minimum value at the same Hersey number for both tests. After the minimum, the curves increase with a very steep slope. Therefore, the lubricant film seems to be very thin in both tests.
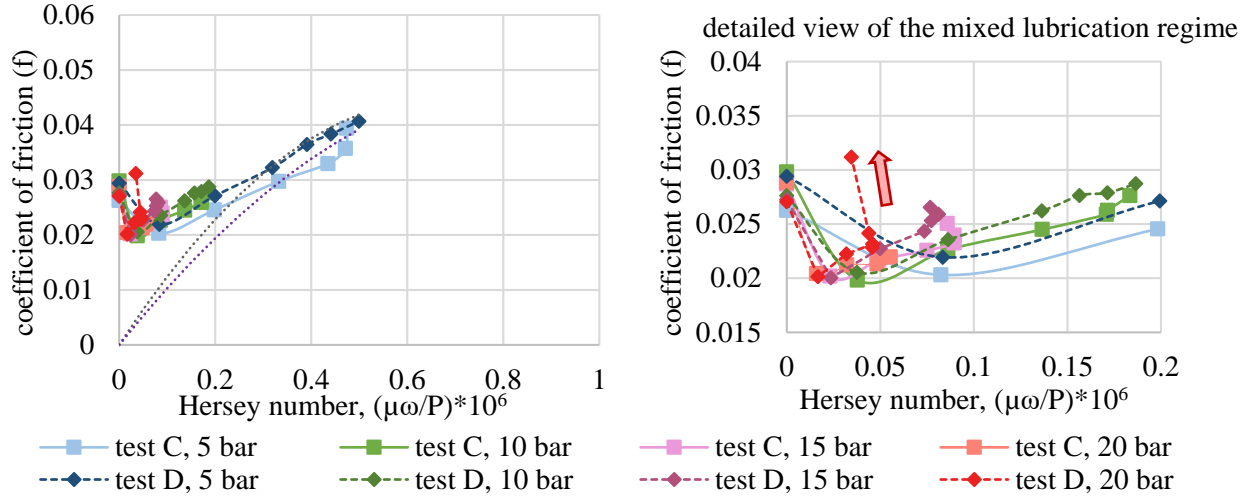
Figure 5.27: Comparison of the coefficient of friction values for the function tests 1 of the standard seals. 'before' represents the function test 1.

5.1.2.4 CONCLUSION

The results below can be drawn from the friction tests of the standard seals:

- As in the structured seals, the friction torque behaviour is directly related with the axial contact temperatures. Understanding the axial contact temperatures are essential to understand the lubrication conditions.
- Standard seals warm up significantly and they reach to critical temperatures quickly. High contact temperatures occur in the warm patches in the outer diameter direction of the seals.
- Combination of high speeds and high pressures is critical for the standard seals. Many of the test seals melted under these conditions. The operational limits of the standard seals seem to be lower.
- The surfaces of the standard seals wear severely. As a results, some glass bubbles starts to stick out the surface. These glass bubbles are quite high, Therefore, they can rupture the lubricant film.
- The coefficient of friction curves indicates that the lubricant film is thin for the standard seals. This seems to lead to high contact temperatures and consequently, the rupture of the film. Therefore, the micro pores on the seal surfaces seems to be not sufficient to generate a lubricant film.
- The leakage rates are almost constant with increasing speed for the standard seals. Therefore, the film thickness probably does not increase with increasing speed and the film thickness seems to be quite low. Hence, the leakage from the axial seal contact might be very low compared to that from the joint.

5.1.3 COMPARISON of the STRUCTURED and the STANDARD SEALS

Figure 5.28 shows the comparison of the friction coefficient curves of the standard and the structured seals. In the function test 1, the standard seals have slightly lower coefficient of friction than the structured seals in mixed lubrication. In addition, the coefficient of friction of the standard seals reach to a minimum value earlier. This might be because of the steps on the surfaces of the standard seals. These steps are much deeper than the structures of the structured seals. Therefore, the steps can provide a higher reduction in the shear force (and thus the friction) within the lubricant film. On the other hand, the coefficient of friction values become higher after reaching the minimum for the standard seals. The increase in the coefficient of friction is quite sharp with increasing Hersey number. It seems like the

standard seals have a thinner lubricant film. The hydrodynmic effects seems to be not suffcient to provide an optimum film.
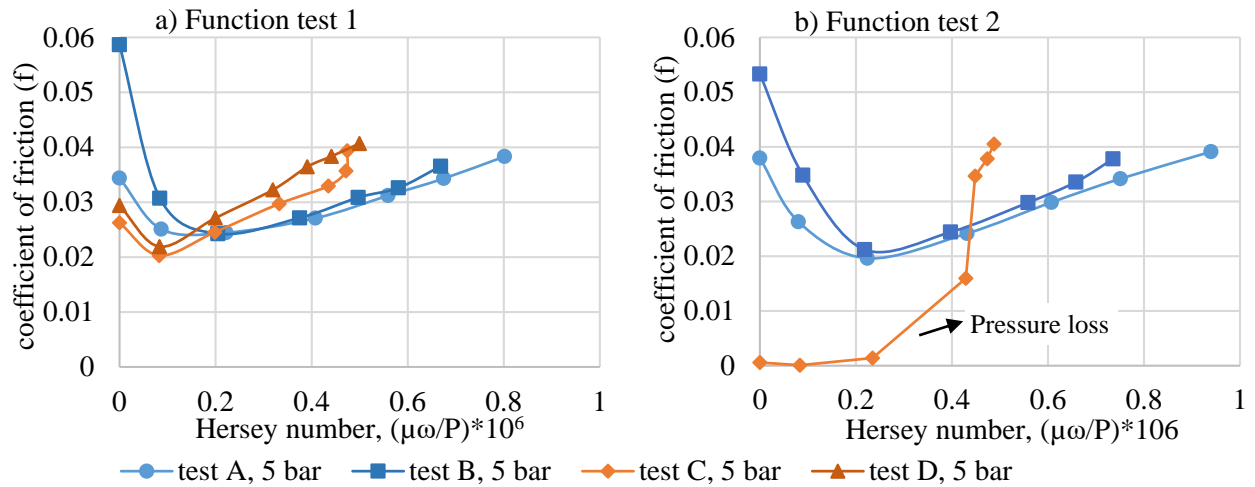
Figure 5.28: Comparison of the structured and the standard seals. The friction tests of the structured seals are the tests A and B. The friction tests of the standard seals are the tests C and D.

In the function test 1, the structured seals have a broader mixed lubrication but they provide a reduction in the coefficient of friction up to 25 % in the possible hydrodynamic regime. The reduction in the coefficient of friction seems to be the result of the hydrodynamic load reduction of the structures. Furthermore, the structured seals have coinciding curves in hydrodynamic regime. On contrary, the standard seals result different coefficient of friction curves when they are plotted over Hersey number. This indicates that the structures dominates the lubricant behaviour in hydrodynamic regime. In the function test 2, a suffcent data is not available for the standard seals but they seem to have higher coefficient of friction values at high Hersey numbers.
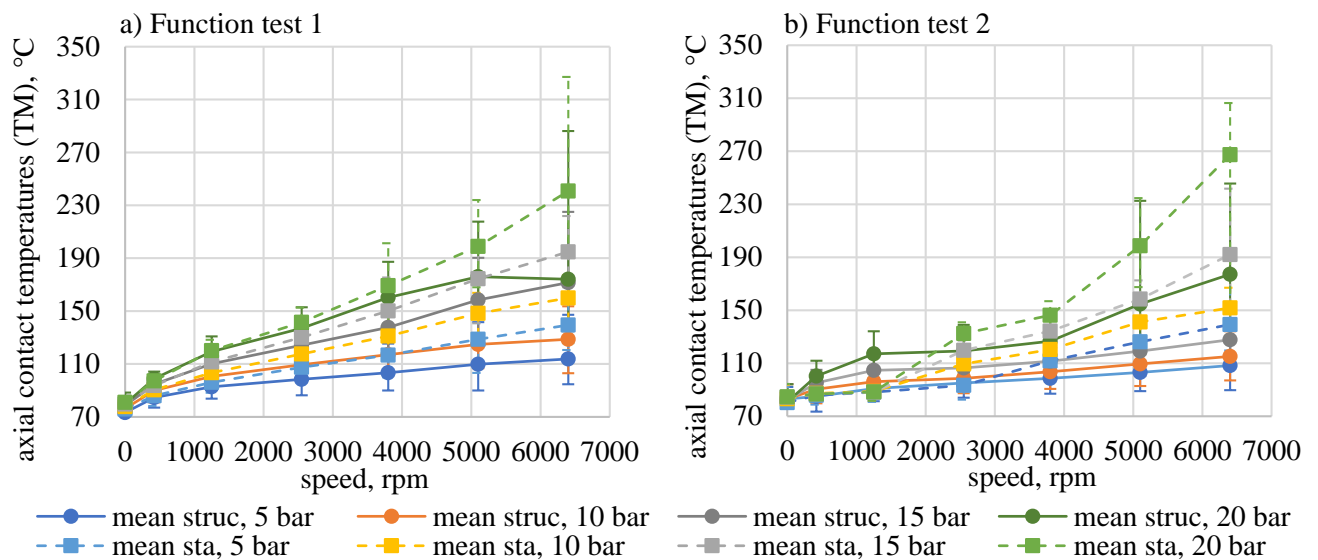
Figure 5.29: Comparison of the axial contact temperatures of the structured and the standard seals. 'mean struc' and 'mean sta' represent the mean temperatures for the structured and the standard seals, respectively.

Comparison of the axial contact temperatures and the leakages of the structured and the standard seals are shown in Figure 5.29-Figure 5.30. These graphs are not shown per tests. They are the mean of the tests A and B for the structured seals and, the mean of the tests C and D for the standard seals. It should be noted that the contact temperatures of the standard seals should not be considered up to 2550 rpm in

the function test 2 due the pressure loss. The contact temperatures are higher in the standard seals. As mentioned earlier, this probably leads to a thinner film in the standard seals. As a result, the standard seals wear severely. On the other hand, both the structured and the standard seals suffer from high contact temperatures at high speeds and 20 bar. Particularly, the standard seals cannot operate under these conditions.
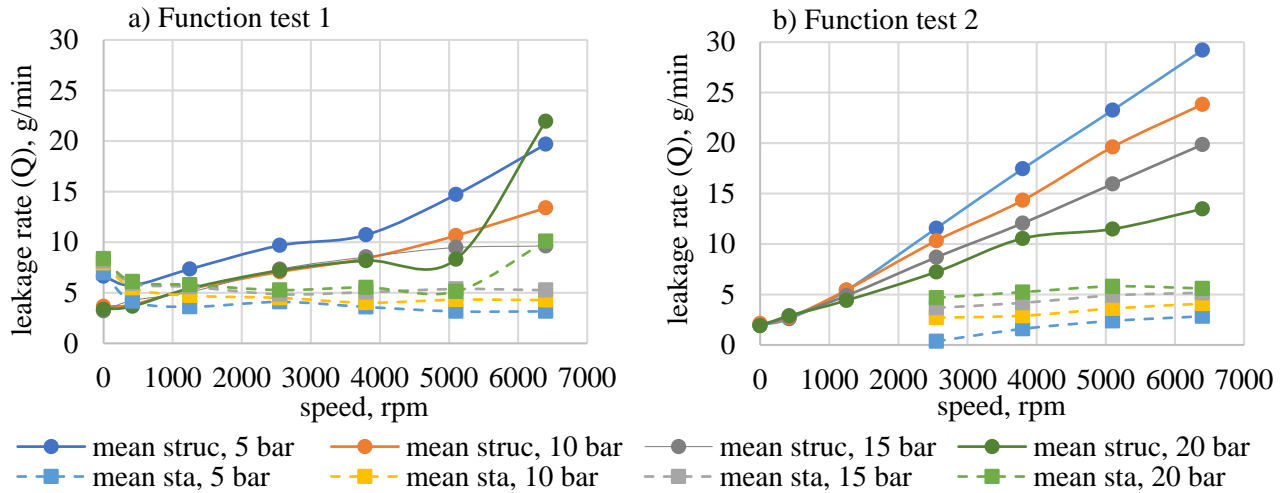
Figure 5.30: Comparison of the leakage rates of the structured and the standard seals. 'mean struc' and 'mean sta' represent the mean leakages for the structured and the standard seals, respectively.

The leakage rates of the structured seals are higher due to the surface structuring. Their leakage rates increase with increasing speed. This might be because of that the structured seals might be operating in hydrodynamic regime at high speeds. Consequently, the lubricant film thickness might be increasing with increasing speed. On the other hand, this is not valid for the standard seals. This indicates either there is no real hydrodynamic lubrication or the film is very thin thus, the leakage is low compared to the leakage of the joint.

5.2 RESULTS of the OPTICAL EXPERIMENTS

5.2.1 CAVITATION FORMATION

5.2.1.1 STRUCTURED SEALS

Figure 5.31a shows the cavitation formation at 500 rpm, 20 °C and 5 bar. The rotation direction is CCW and this configuration is kept identical during all of the experiments. In the divergent zone of the structure (area 3a), pressure decreases and the lubricant film ruptures. Consequently, cavitation forms within the structure. Cavitation consists of gas regions and liquid streamers. This fits to the film rupture boundary conditions of Swift-Stieber and JFO cavitation theories. These theories assume Poiseuille flow is zero in the axial and the circumferential direction within the cavitation region and the lubricant is carried through the streamers via the Couette flow [26,38,39,43,44].

Figure 5.31b shows a seal ring with numbers which represent the structure positions on the axial seal face. The cavitation formation between the positions 1 and 28 is shown in Figure 5.31c-m for 1250 rpm, 20 °C and 5 bar. Overall, the cavitation region has a curvy shape at the rupture boundary. This is probably due to the shape of the seal surface. Cavitation is inclined at the reformation boundaries. The cavitation region expands at the bottom. This may be due to the radial tilt of the seal. Cavitation is pushed towards the outer diameter at the reformation boundary side (Figure 5.31f, position 7). This seems to be because pressurized oil enters to the contact via the deep part of the structure and pushes the cavitation outwards.
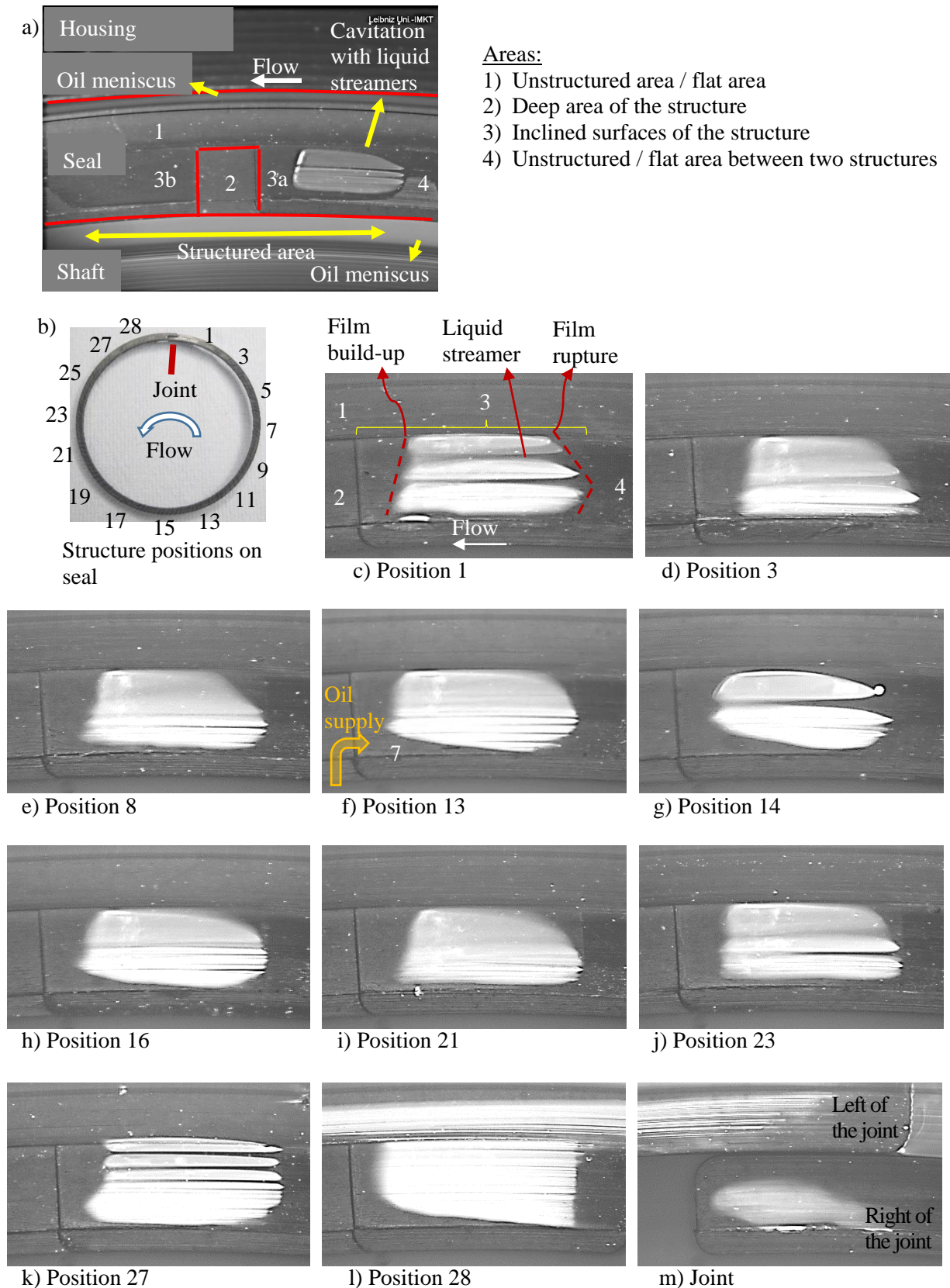
Figure 5.31: Cavitation formation within the structures a) at 500 rpm, 20 ºC (sump temperature) and 5 bar b-m) at 1250 rpm. The flow direction is CCW.

Depending on the position, some differences are visible in the size and morphology of cavitation. Particularly, cavitation is pushed towards the outer diameter direction less between the position 21 and 8. Surface irregularities and non-uniform film distribution may be the reasons for the differences in

cavitation. These position are also close to the joint where the lower film thickness is expected. Around the joint, there are also extra cavitated areas in the unstructured zones. This can be an indication for the lower film thickness. Micro-surface features might be generating inter-asperity cavitation at low film thicknesses. At position 28, the cavitation form is quite different. This is due to the seal surface is different at this position. The edge of the structure is straight.

5.2.1.2 CAVITATION AREA RATIO and the FILM THICKNESS DISTRIBUTION over the SEAL SURFACE

Figure 5.32a shows the cavitation area ratio with respect to the structure position over the sealing interface at different speeds and sump temperatures. At 70 °C, cavitation area ratio increases with increasing speed. On the contrary, it does not change significantly with speed at 20 °C. With increasing temperature, cavitation becomes smaller due to a decrease in the lubricant viscosity.

Cavitation is bigger at positions 27, and 28 which are near the joint. At 70 °C, cavitation becomes smaller between the positions 8 and 21. This might be because of the thermal deformation of the seal which can lead to a non-uniform film distribution. Cavitation do not show this trend clearly at 20 °C since there are some deviation at the positions 13, 15 and 16.
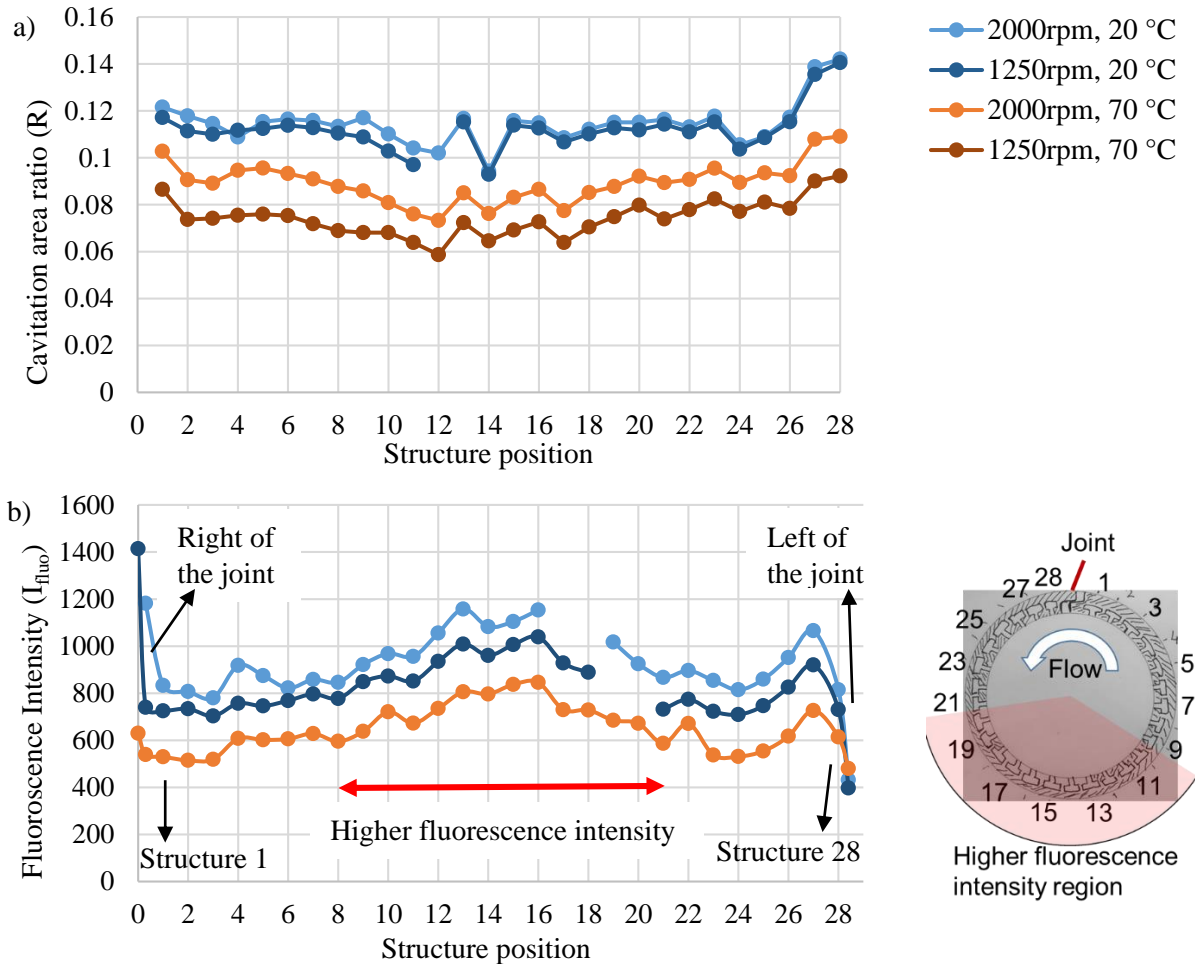
Figure 5.32: a) Cavitation area ratio and b) fluorescence intensity over the seal circumference. P= 5 bar. Flow is CCW.

The average fluorescence intensity of each structured section is determined at the unstructured surface of the seal (Figure 5.31, area 1) to obtain the film distribution. Figure 5.32b shows the results. It should be noted that the fluorescence intensities at 20 °C and 70 °C cannot be compared without calibration since the fluorescent intensity depends on temperature. The fluorescence intensity is higher in the region between the structures 8 and 21. This shows that the film distribution is non-uniform and the film is thicker in the region at the opposite of the joint. It seems like there is a waviness with one peak over the

seal circumference. Also, the fluorescence intensity decreases significantly at the left half of the joint while it is increasing at the right half. This indicates that the cross section of the seal might be twisted at the joint.

The film thickness curve seems to show opposite behaviour of the cavitation curve. These results indicate that the cavitation has a correlation with the film thickness. For a given speed and pressure, cavitation area ratio seems to decrease with increasing film thickness.

5.2.1.3   STANDARD SEALS

Figure 5.33 shows the cavitation formation at the different locations of a standard seal interface. The step of the seal face is filled with pressurized lubricant. Cavitation occurs at the seal face which is in contact with the counterface. It is randomly distributed (Figure 5.33a). It should be noted that there are some big size non-exploded glass bubbles on the seal surface (Figure 5.33b-2). These glass bubbles are very seldom but they reflect the light. Therefore, they should not be confused with cavitation. Furthermore, these bubbles should not be taken into account during the film thickness measurements.
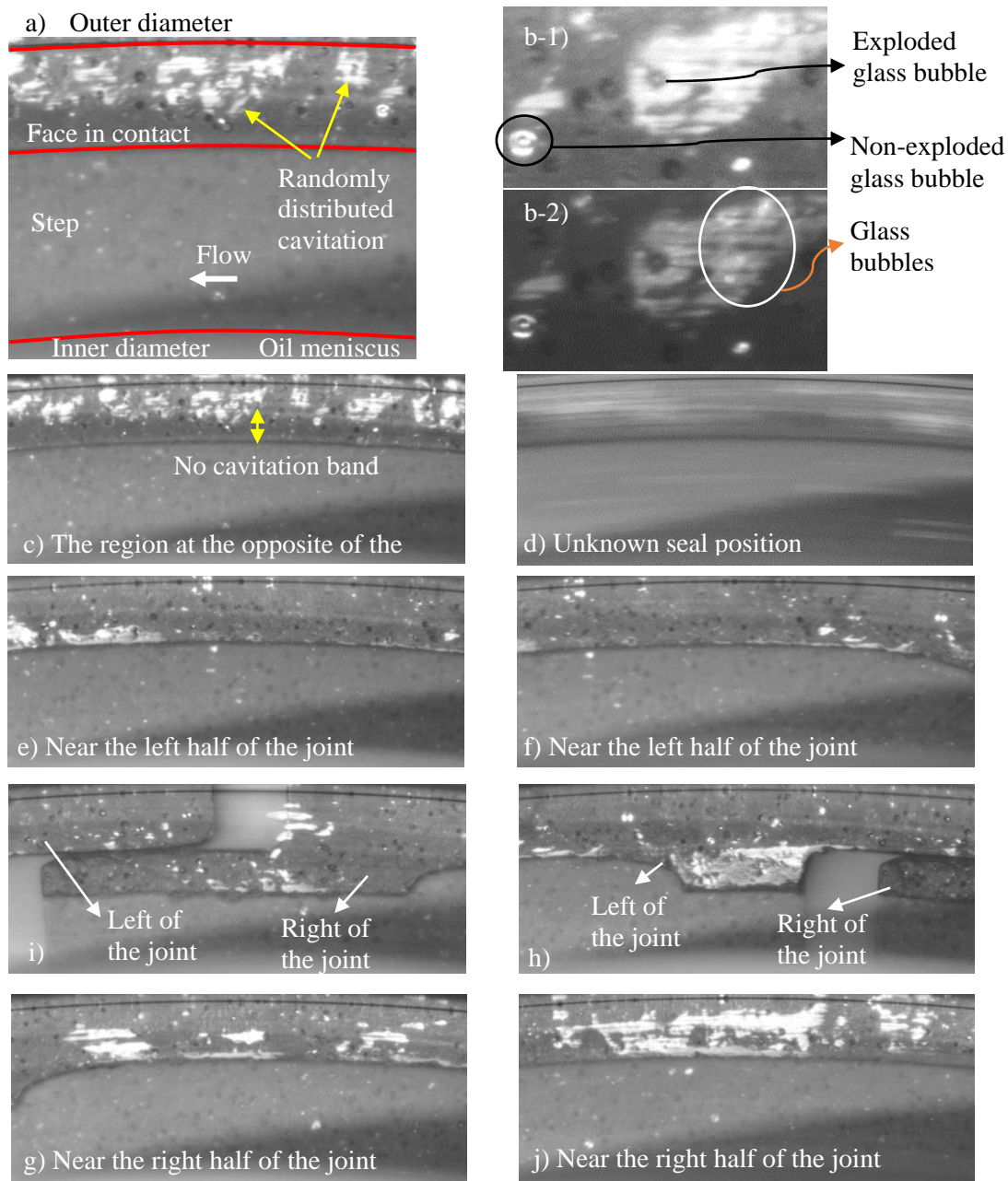
Figure 5.33: Randomly distributed cavitation at the different locations of the standard seal interface at 100 rpm, 20 ºC (sump temperature) and 5 bar. Rotation direction is CCW.

Cavitation seems to occur mostly around the micro-pores but not within the pores (Figure 5.33b-1). It is distributed to a larger zone than the visible pores. When the contrast of the photos is adjusted (Figure 5.33b-2), it is visible that there are smaller micro-pores in the cavitation zone in addition to the bigger pores. Therefore, cavitation seems to occur due to the surface irregularities which are caused by the fillers. There are also cavitation zones without any visible pores. Surface asperities might be resulting in inter-asperity cavitation.

In the region at the opposite of the joint, cavitation forms more in the outer diameter direction. There is no significant cavitation in the inner diameter direction (Figure 5.33c). It can be because of that the seal ring tilts and generates a converging gap. This can enable more pressurized oil to enter the contact. As a result, cavitation might be pushed outwards. The wear behaviour of the seals (see Chapter 5.1.2.1.4) also correlates with the cavitation formation and indicates that there might be a radial tilt.

Around the joint, the number of the cavitation zones decreases. Furthermore, cavitation mostly occurs in the inner diameter direction (Figure 5.33e-f). This can because the film thickness decreases around the joint. The film thickness might only be sufficient to form cavitation in the inner diameter direction due to the penetrating pressurized oil. The change in the cavitation formation around the seal circumference shows that the standard seals might be deforming circumferentially and radially during the operation.

The rotation of the standard seals sometimes accelerates. Figure 5.33d shows a photo of the contact while the seal is accelerating. The cavitation is extended and looks as dull white lines. This seems to occur due to the exposure time of the CCD camera. The rotation of the seal depends on the force balance (Chapter 2.8.2). Therefore, the acceleration can be due the lubricant starvation in the axial gap. This can result in a high friction force between the seal and the counterface.

The change in the cavitation formation around the joint shows that the standard seal might be deforming circumferentially during the operation in addition to the radial tilting as in the structured seals and the radial tilt is changing over the seal interface.

Overall, the standard seals seem to operate under unbalanced conditions. Cavitation seems to occur due to the macro and micro surface irregularities. Inter-asperity cavitation indicates that the lubricant film is thin even at high speeds.
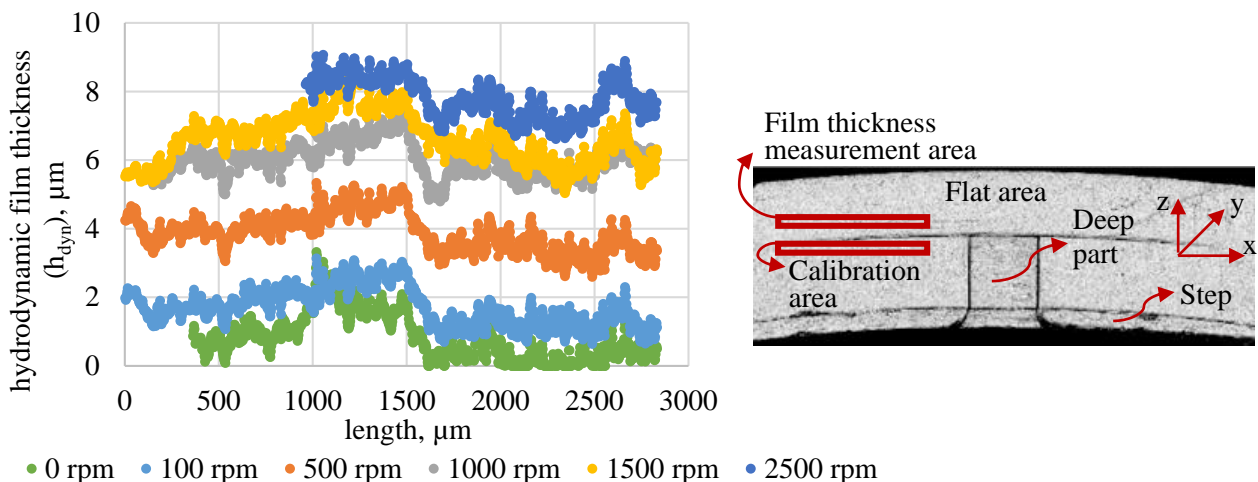
Figure 5.34: Hydrodynamic film thickness distribution within the calibration area at different speeds for the structured seals. The sump temperature is 20 °C. Pressure is 5 bar.

5.2.2 FILM THICKNESS MEASUREMENTS

Figure 5.34 shows the hydrodynamic film distribution within the calibration area for a structured seal at 20 °C and 5 bar. The lubricant film thicknesses fluctuate. This is due to the error in the calibration. The calibration is performed at 0 rpm and there were some laser speckles. However, when the counterface rotates, micro surface features of the sapphire disc rotate as well and they refract the laser at different directions. This results in a more uniform distribution of the laser over the contact. Another error is that

the position of the measurement area is not completely the same with the calibration area due to rotation. In addition, surface irregularities in the laser microscope measurements could be included in the calibration. Furthermore, the elastic deformations of the seal during the operation can generate deviations in the results since they are not considered in the calibration.

The hydrodynamic film thickness increases as speed increases. This increase is higher for the low speeds. Normally, film thickness would increase with speed in a degressive non-linear way at a constant temperature and pressure (see Chapter 6.2.1.4.3). However, the film thickness shown here is almost constant and even has a tendency to decrease after 1000 rpm. This is probably due to the high contact temperatures thus the lower viscosity.

Figure 5.35 shows the average hydrodynamic film thicknesses for the structured and the standard seals. These film thicknesses are measured within the film thickness measurement area in Figure 5.34. In Appendix A (Figure A-2), the film thicknesses which are measured in the measurement and the calibration areas are compared. The results seem to be similar for both measurement and calibration areas. This shows that the LIF method provides consistent results.

At 100 rpm, the average hydrodynamic film thicknesses are similar for both seal type (Figure 5.35). Later on, it increases rapidly for the structured seal and becomes almost constant at high speeds. On the other hand, the average hydrodynamic film thickness decreases with increasing speed for the standard seal. This can be due to the high contact temperatures which are observed in the friction tests of the standard seals. It should be noted that, it was problematic to capture the photos of the standard seal contacts at high speeds as they rotate fast and sometimes accelerate. Therefore, the error in the film thickness measurements of the standard seals might be higher than that in the structured seals.
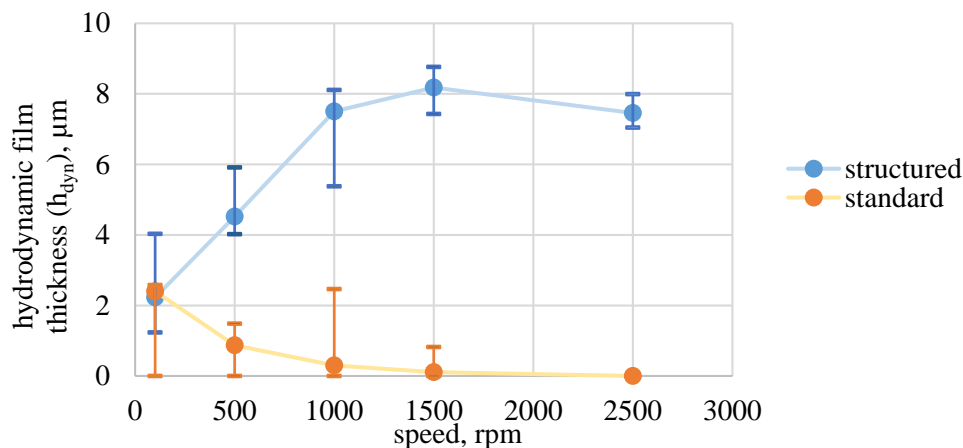
Figure 5.35: The average hydrodynamic film thicknesses at 20 °C and 5 bar for the structured and the standard seals. The measurement area is the film thickness measurement area shown in Figure 5.34. Error bars show the maximum and the minimum film thickness.

5.2.2.1 RELATIONSHIP between FILM THICKNESS, COEFFICENT of FRICTION and CAVITATION AREA RATIO

In this chapter, the lubricant film thickness, coefficient of friction and the cavitation area ratios are compared for the structured seals. This comparison is not performed for the standard seals since the cavitation is randomly distributed.

Figure 5.36a shows the coefficient of friction with plotted over the Hersey number. This coefficient of friction is calculated via the friction torques which are measured in the optical test rig. The lubricant viscosity is determined according to the near-contact temperature Figure 5.36c. The coefficient of friction curves for 20 °C and 70 °C do not coincide. This may be because of thermally induced elastic deformation of the seal which can lead to a different gap. Hydrodynamic lubrication seems to start

around a Hersey number of $0.35 \cdot 10^{-6}$. This corresponds to 250 – 300 rpm for 20 °C and 1250 rpm for 70 °C under 5 bar pressure.

Film thickness and cavitation area ratio are plotted with respect to speed in Figure 5.36b. Although the film thickness and the cavitation area ratio are measured locally (in the region at the opposite of the joint), their behaviour can be correlated with the coefficient of friction. At 100 rpm, 20 °C and 5 bar, the film thickness is around 2 μm. However, the seal does not seem to be fully in the hydrodynamic lubrication regime according to the coefficient of friction measurements. The film thickness is not measured for 70 °C due to the fluorescence quenching with temperature.
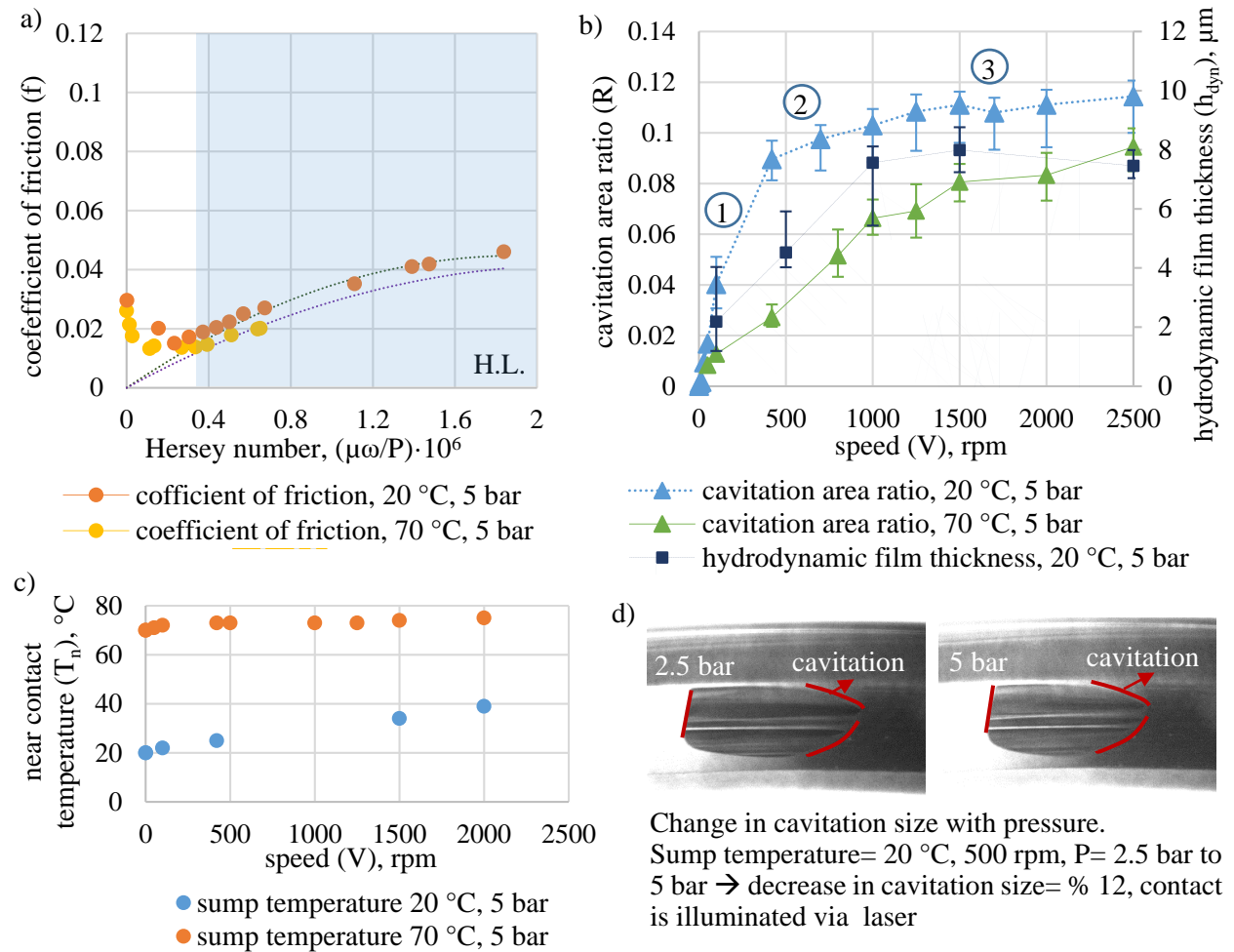
Figure 5.36: a) Coefficient of friction. b) Cavitation area ratio and hydrodynamic film thickness. c) Near contact temperature. d) Influence of pressure on cavitation. H.L.: hydrodynamic lubrication.

For 20 °C, both the film thickness and the cavitation area ratio increase rapidly at the initial speeds. The increase is not significant at high speeds. The trend of the cavitation area ratio may be divided into three sections in relation with film thickness; (1) linear, (2) transition, and (3) saturation. In the linear region, cavitation area ratio increases almost proportional to speed. This region corresponds to mixed lubrication and hydrodynamic lubrication with a thin film. In the transition region, the increase in the cavitation area ratio becomes lower. The seal is in the hydrodynamic regime. Finally, the cavitation area ratio is nearly constant in the saturation region. The film is quite thick. The reasons for the transition and the saturation regions could be contact temperature and film thickness. An increase in the contact temperature leads to a lower viscosity. At thick films, the contribution of the structures to the pressure generation becomes lower. The design of the divergent zone of the structure also somehow restricts the increase in cavitation size (see Chapter 6).

At 70 °C, cavitation starts to occur at higher speeds and is smaller due to a lower viscosity. Linear and transition regions are visible as in 20 °C. The saturation region seems to occur at higher speeds.

The influence of pressure on cavitation is shown in Figure 5.36d. A higher pressure leads to smaller cavitation for a given speed in this system. Because the increased sump pressure leads to a higher overall pressure. The results indicate that there is a strong correlation between lubricant film thickness and cavitation.

5.2.2.2 DETERMINING ELASTIC DEFORMATIONS of the SEALS via LIF METHOD

Pressure and temperature induced deformations of the seals can be determined via the film thickness distribution over the seal interfaces. These deformations can be global as well as local. In this chapter, only the elastic deformations of the structured seals are investigated. Because it is easier to record the same locations on the structured seal faces at different speeds thanks to structures.
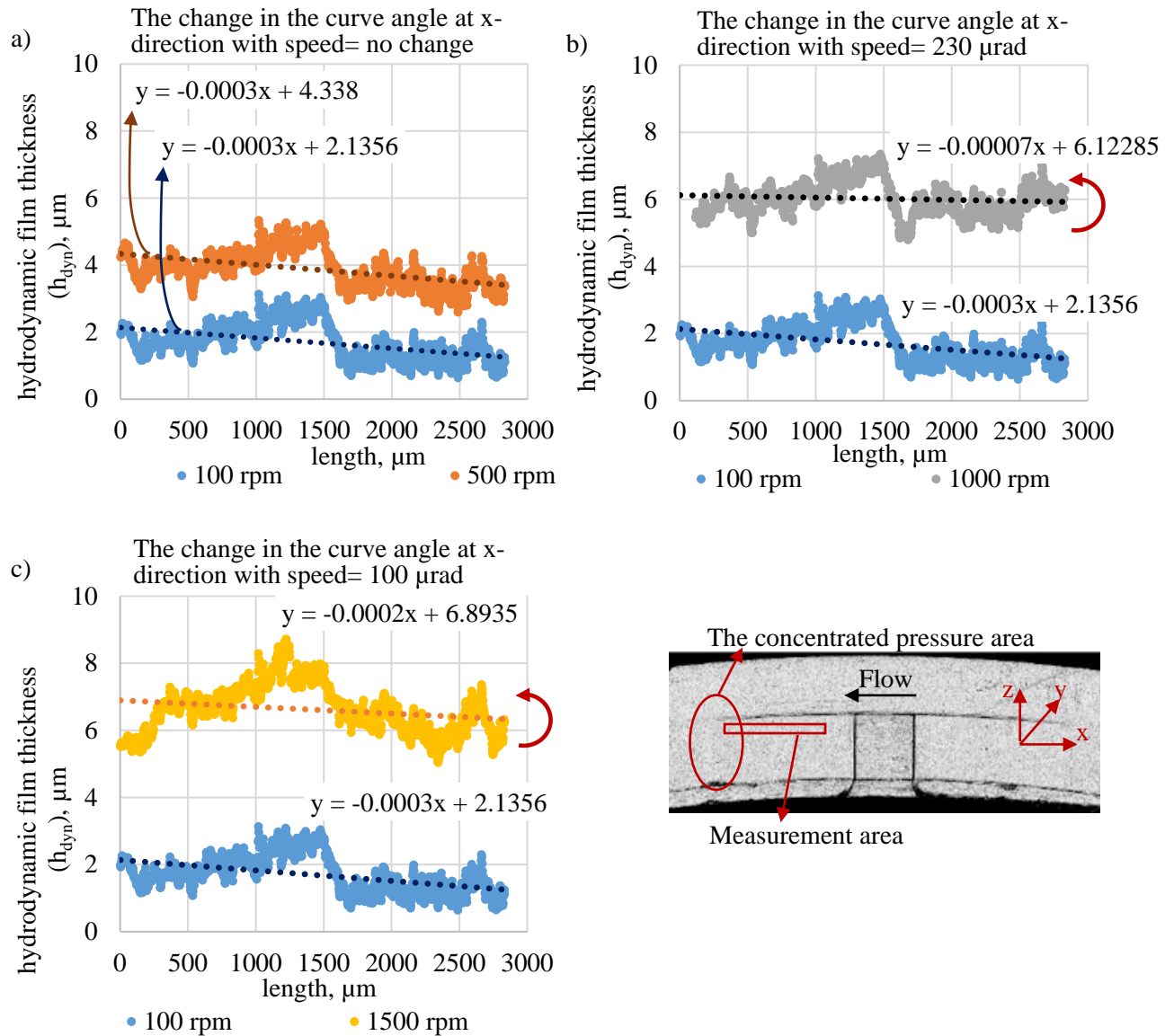
Figure 5.37: Left: The change in the inclination of the converging plane of structure 16 with increasing speed. Sump temperature and pressure are 20 °C and 5 bar, respectively. Right: Structure 16 with the concentrated pressure and the film thickness measurement areas.

The fluorescence intensity distribution over the structured seal interface is already discussed in Chapter 5.2.1.2. It is concluded that the film thickness is lower at the joint. The gap has a waviness with one peak. In addition, the cross section of the seal might be twisted. Here, the local deformations are also

investigated. For this, the inclination of the convergent half of a structure is investigated. Because the lubricant pressure is expected to concentrate within the convergent gap. This can deform the convergent half of the structure.

The inclination of the convergent plane is detected by fitting a first degree polynomial curve to the film thickness profiles as shown in Figure 5.37. The change in the inclination with increasing speed is an indication of the elastic deformation. There is no detectable change in the inclination of the structure when the speed is increased when accelerating from 100 rpm to 500 rpm. However, the inclination of the structure seems to decrease by 230 μrad when the speed is increased from 100 rpm to 1000 rpm. On the other hand, the decrease in the inclination is 100 μm when the speed is increased from 100 rpm to 1500 rpm.
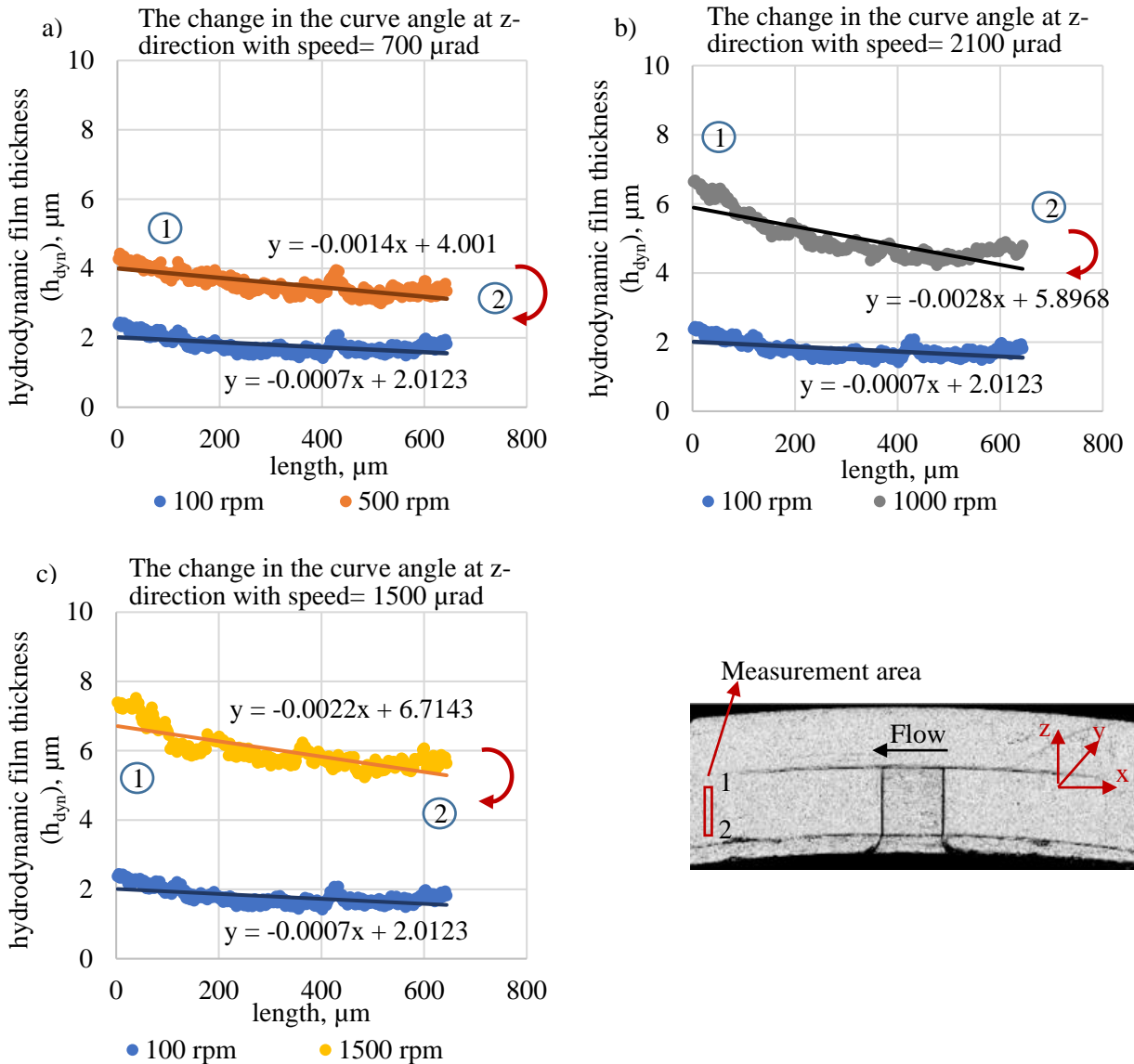
Figure 5.38: Left: The radial tilt of the structure 16. Sump temperature and pressure are 20 °C and 5 bar, respectively. Right: Structure 16 with the fluorescence intensity measurement area.

The results show that the structure does not deform significantly at low speeds in the circumferential direction. With increasing speed, the inclination of the left half of the structure, where the pressure generation occurs, starts to decrease. This decrease is lower at 1500 rpm than that at 1000 rpm. However, the magnitude of the change in the inclination of the structure is same. It should be noted that the deformations are investigated only for one structure. In order to predict the average change in inclination of the structures, other structures should also be investigated. Furthermore, increasing contact

temperatures can lead to fluorescence quenching, which can manipulate the lubricant film thickness distribution. As a result, elastic deformations may be determined inaccurately. Here, the near-contact temperature increases up to 34 °C at 1500 rpm (Figure 5.36). Therefore, no significant decrease in fluorescence intensity due to temperature is expected. Also, the convergent half of the structure heats up locally from left to right. If the fluorescence intensity was decreasing locally due to temperature, the film thickness would have decreased from right to left (opposite direction of fresh oil supply). However, when the fluorescence film thickness values between the positions 1000 μm and 2500 μm are examined, it is visible that the film thickness values have slightly declined in the direction of the fresh oil supply (from left to right) when accelerating from 100 rpm to 1500 rpm (Figure 5.37). Therefore, the slopes of the film thickness curves do not seem to change due to fluorescence quenching.

Similarly, the radial tilt is also investigated in the radial direction (Figure 5.38). The radial distribution of the film thickness represents a divergent gap. This can be attributed to deviations from flatness between the structures. These deviations from flatness might not be disappear completely when the pressurized oil is supplied. By fitting a first order polynomial curve to the film thickness values, it is found that the seal section becomes more divergent in the measurement area. This can be because the areas deviating from flatness heats up and expands (see Chapter 5.2.3). When accelerating from 100 rpm to 1500 rpm, the gap tilts at the order of thousand μrad. This magnitude seems to be reasonable for the current application.

To conclude, laser induced fluorescence method can be used to detect elastic deformations of the seals. However, a comprehensive calibration is necessary for reliability. The current calibration is developed for a small area. However, the fluorescence intensity distributions can be used to have an opinion about the elastic deformations without calibration.

5.2.3   RESULTS of the INFRARED THERMOGRAPHY

5.2.3.1   *STRUCTURED SEALS*

Figure 5.39 shows the local temperatures at the face of a structured seal at 2500 rpm, 20 °C and 5 bar. These temperatures are calibrated (see Chapter 4.3.4) and thus, the heating up of the seal is obtained. The temperature photographs were made at different structure positions after the start of the rotation. Hence, the temperature was not balanced. Each photo shows a structured section with the deep part (groove) and the inclined planes of the structure and the flat surfaces.

Figure 5.39b shows the structure 16 after 82 seconds from the start of the rotation. The temperature is the lowest within the deep part of the structure. The convergent zone of the structure has low temperature as well. Within the divergent zone of the structure, the cavitation zone with the liquid streamers is visible. It looks as if it is not warm. However, this might be due to the low emissivity of the cavitation zone or different refraction index of gas. Furthermore, the gas has a different heat dissipation behavior.

The seal is warmer at the unstructured surfaces. Particularly, the unstructured surface near the cavitation zone heats up (Figure 5.39d). The warm area over the cavitation extends until the middle of the convergent zone of the structure. A small portion of the unstructured surface over the left half of the structure (convergent gap) is colder. This can be attributed to two properties of the structures; elastic deformations and the fresh oil distribution. The pressure generation in the convergent zone of the structure might cause an elastic deformation (Chapter 5.2.2.2). Thus the lubricant film thickness might be slightly higher at that region. However, further investigation is necessary to correlate the local temperature development with the elastic deformations.

Currently, the fresh oil distribution over the seal contact seems to be a more reliable explanation for the local temperatures. The fresh oil enters to the seal interface through the deep part of the structures which are open to the pressurized oil. From the convergent gap, the fresh oil can be supplied to the flat surface over the left half of the structure due to the pressure gradient. On the contrary, cavitation forms within the divergent gap and generates a low pressure zone. This zone can attract more fresh oil from the inner diameter. However, this oil cannot be transferred efficiently through the cavitation to the flat area over

the structure. Also, the cavitation can only attract air from the outer diameter. Therefore, the flat area over the right half of the structure seems to be warmer due to insufficient fresh oil supply. On the other hand, the high temperatures at the unstructured surfaces between the structures seem to be due to the deviations from flatness. Because of these deviations, the film thickness might be lower.

a) The scanned surface

Inc. sur. = Inclined surfaces

b) Structure 16, time after start: 82 seconds

c) Cavitation formation

d) Structure 18, time after start: 142 seconds

e) Structure 23, time after start: 284 seconds

f) Joint, time after start: 474 second
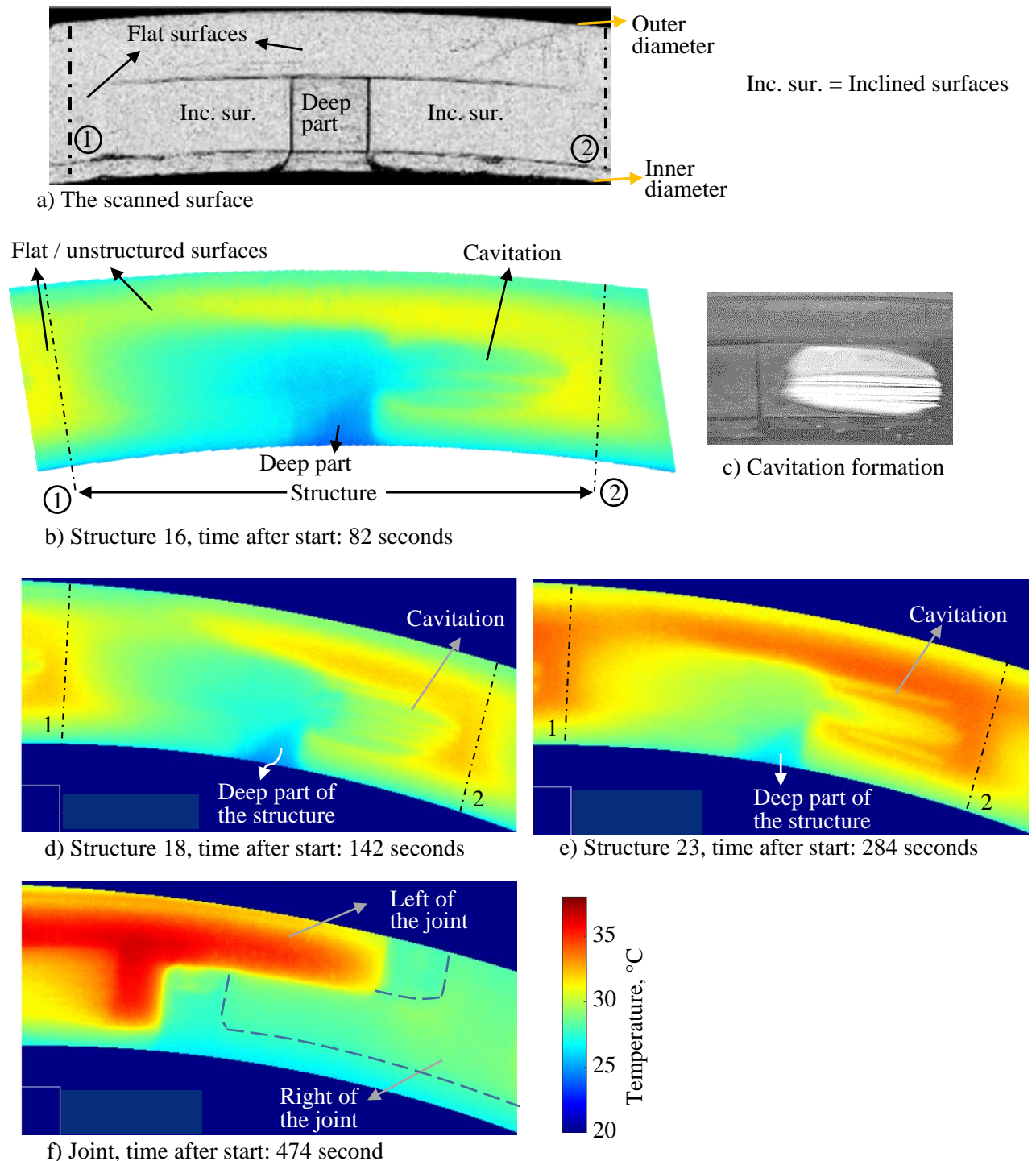
Figure 5.39: Temperature development at the interface of a structured seal at 2500 rpm, 20 °C (sump temperature) and 5 bar. Flow direction is CCW.

Figure 5.39e shows how the flat surfaces continue to heat up further with increasing running time. The temperature increase within the structure except the cavitation is slower. This is due to the higher film thickness within the structure which results lower shear stresses. In addition, the structures are open to the fresh pressurized oil. Therefore, the structures result a cooling effect in addition to enhance lubricant

film. After 5 minutes running, the area near cavitation zone is around 6 °C warmer than the convergent half of the structure (left half). Figure 5.39f shows the joint after 474 seconds running. The left part of the joint is much warmer than the right part of the joint. This supports the fluorescence measurement results which show that the film thickness is lower at the left of the joint (Chapter 5.2.1.2).

5.2.3.2   STANDARD SEALS

Figure 5.40 shows the local temperatures at the interface of a standard seal at 1500 rpm, 20 °C and 5 bar. These temperatures are calibrated (see Chapter 4.3.4) and thus, the heating up of the seal is obtained. There are randomly distributed warm patches at the face of the standard seal. This might be due to the cavitation zones. They look cooler due to their emissivities. Because of this, there are some cooler areas (cavitation zones) and warm patches over the seal face. In reality, the whole face must be heating up and probably, there is no significant cooler zones. The step of the seal is cooler due to the fresh oil entrainment. After the start of the running, a few circular areas heat up quickly (Figure 5.40b). These areas might be the glass bubbles which did not explode during the manufacturing. In addition, the glass bubbles under the surface can change the elastic behavior of the seal material locally. The areas which has glass bubbles close to the surface might not deform as much as the main seal material. Therefore, the seal material with the glass bubble underneath can warm up faster.

It is hard to detect any waviness of the standard seal via the temperature measurements. Since the warm patches seem to be randomly distributed over the seal circumference. The left of the joint is warmer than the half of it (Figure 5.40g-h). However, this behavior seems to be localized at the joint and does not continue for a significant portion of the seal ring.

5.3   CONCLUSION of the EXPERIMENTAL RESULTS

The friction tests described the general behaviour of the seals in terms of friction, temperature and leakage. The optical tests provided quite a detailed observation of the sealing contacts. Cavitation morphology, cavitation area ratio, film thickness and local temperatures are obtained. The most important findings from the experiments can be drawn as below:

- In mixed lubrication regime, standard seals generate lower friction values. However, structured seals provide lower coefficient of friction values in hydrodynamic lubrication regime. This seems to be due to the hydrodynamic load reduction rather than the hydrostatic load reduction.
- In contrast to the standard seals, the structured seals show similar performances in the tests. This can be interpreted as the structures are dominant feature on the seal behaviour.
- As a result of structuring, leakage is higher in the standard seals while the contact temperature is lower. The lower contact temperature is probably due to the enhanced lubricant pressure and the cooling effect of the structures which is explained in the thermography measurements.
- Cavitation occurs within the divergent zones of the structures at the structured seal interface. Its size and morphology changes over the seal circumference. This is probably due to the non-uniform film distribution and the surface irregularities.
- Cavitation forms as randomly distributed patches at the face of the standard seals. It occurs probably due to the macro and micro surface features which indicates that the lubricant film is thin.
- Cavitation decreases with increasing temperature. This is due to a decrease in lubricant viscosity. Cavitation decreases with increasing pressure as well. This seems to be due to a lower film thickness under high loads.
- Structures lead to higher film thicknesses. There is no full film separation in standard seals.
- There is a strong correlation between coefficient of friction, lubricant film thickness and cavitation. Both cavitation area ratio and film thickness increase rapidly at low speeds. They become almost constant at high speeds.
- The elastic deformations of the structured seals are predicted via the fluorescence measurements. The structured seals seem to make a one peak wave at the circumferential direction and a slightly divergent gap at the radial direction.

- The local contact temperatures are observed via the thermal camera. The structures result a cooling effect due to lower shear stresses within the structures. Also, they supply fresh oil to the contact.

a) The scanned surface

b) time after start: 46 seconds

c) Cavitation

d) time after start: 56 seconds

e) time after start: 60 seconds

f) time after start: 70 seconds

g) time after start: ~86 seconds

h) time after start: 86 seconds

i) time after start: 88 seconds
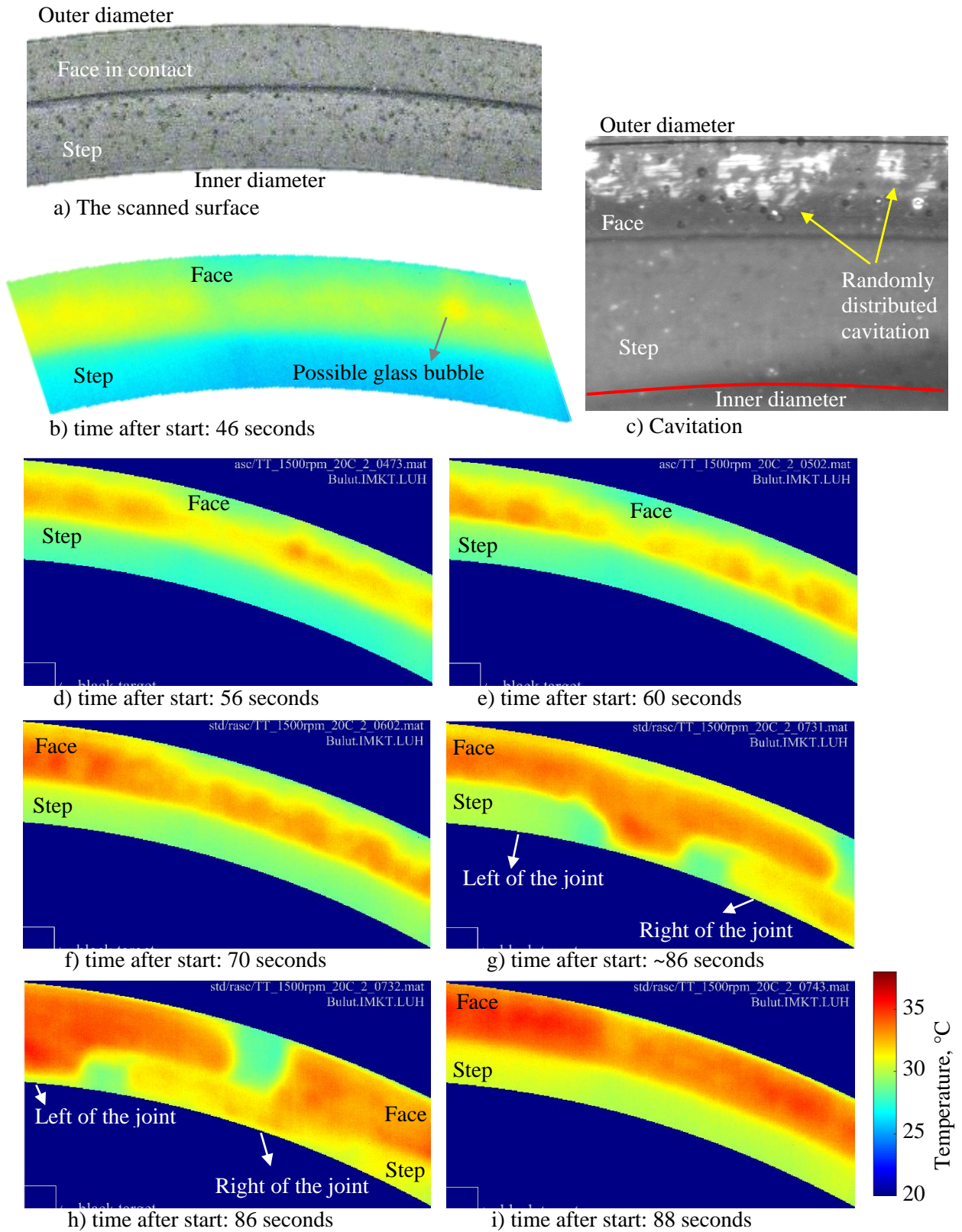
Figure 5.40: Temperature development at the interface of a standard seal at different positions at 1500 rpm, 20 °C (sump temperature) and 5 bar. Flow direction is CCW.

6 NUMERICAL MODELLING of FILM FORMATION

6.1 NUMERICAL MODEL

The numerical model is developed to simulate the hydrodynamic lubrication by considering cavitation. In this chapter, the fundamentals of the model are described. The validation of the model is realized by comparing the numerical and the experimental results.

6.1.1 GOVERNING EQUATIONS

The two dimensional, steady state Reynolds Equation is solved on the fluid structure interface by using the open source finite element software Elmer. Elmer Solver calculates the pressure field at the seal interface as a result of Couette and Poiseuille flow by using iterative methods [181,182]. The mass conservative JFO cavitation theory is implemented by using FBN algorithm to predict cavitation. The following assumptions are made to solve the problem [57]:

- No inertial flow
- No pressure change across the lubricant film in z (height) direction
- No slip on the boundaries between the surfaces and the lubricant

The Reynolds equation is derived from the Navier Stokes equation (Appendix D) and is written as [49,54,55,57,173]:

$$\frac{\partial}{\partial x}\left(\frac{\rho}{\mu} h^3 \frac{\partial p}{\partial x}\right) + \frac{\partial}{\partial y}\left(\frac{\rho}{\mu} h^3 \frac{\partial p}{\partial y}\right) = 6U \frac{\partial[(1-\theta)\rho h]}{\partial x} \tag{6.1}$$

The Reynolds equation was solved in partially non-dimensional form, using a dimensionless density $\rho = \exp(p\beta)$ for the bulk modulus β of the lubricant, viscosity in units of MPa·s, and all length units in μm. This results in pressure units of MPa and a dimensionless cavitation variable θ. The rescaling was done so that the pressure and cavitation variables have the same order of magnitude, which is necessary for the FBN algorithm to yield accurate results.

The JFO model predicts the cavitation by: (1) conserving the mass on the boundaries between full film and cavitation zone which is unknown a-priori; (2) setting a cavitation pressure p_{cav} which is assumed to be uniform and constant within the cavitation zone. These conditions can be formulated as a complementarity constraint [49,54,55,57];

$$(p - p_{cav})\theta = 0, \quad p - p_{cav} \geq 0, \quad \theta = 1 - \rho_{avg}/\rho \geq 0 \tag{6.2}$$

$$\theta = 0, \quad p > p_{cav} \rightarrow \text{no cavitation}$$

$$\theta > 0, \quad p = p_{cav} \rightarrow \text{cavitation}$$

Here, θ is the cavity fraction and ρ_{avg} is the density of mixture of lubricant and gas. In the model, the lubricant is assumed to be 'weakly compressible'. It is time-consuming to solve the eq. (6.1) under the constraint provided by eq. (6.2) [59]. FBN method suggested by Woloszynski *et al.* [57] is adopted to decrease the computational time. The constraint described by eq. (6.2) is reformulated as:

$$p - p_{cav} + \theta \cdot (1 + \epsilon) - \sqrt{(p - p_{cav})^2 + \theta^2} = 0 \tag{6.3}$$

Here, ϵ is a regularization parameter that smoothens this equation to avoid the corner at $(p - p_{cav})$ and $\theta = 0$. The regularization parameter should be chosen small as it allows deviations from the conditions listed in eq. (6.2). The pressure may be non-dimensionalized by using a reference pressure which is 1 MPa in the current model. With the reformulation, the model is changed into an unconstrained system of nonlinear differential-algebraic equations. The calculation can benefit from a direct solution [59,60].

The numerical model is isothermal. In addition to pressure and cavitation, the film thickness is also calculated via the force balance method. In the force balance method, the gap height is changed in the program until the closing and the lifting forces are equal. Here, the closing force is the force which tries

to close the gap between the seal and the counterface. The lifting force is the force generated by the pressure in the lubricant film.

6.1.2 GEOMETRY

Only one structured section of the seal is modelled since the structures are evenly distributed over the seal surface. The modelling of the structured seal geometry is done with two different methods:

Ideal geometry: One section of the structured seal is modelled as a rectangular zone by using MATLAB (Figure 6.3). The modelled seal surface is purely smooth and includes only the structure. No surface irregularities such as roughness and manufacturing errors are included. As described before, there is a circumferential non-contacting area at the outer diameter of the seals. This non-contacting area is subtracted from the model. Here, the term "ideal" represents only the geometry without deviations from the design, however should not be understood to be related to the lubrication.

Real geometry: In practice, the seal surface is not manufactured 100 % according to the design parameters. The flat area between two structures (area 4) is deviating from the flatness up to 8 µm (Figure 6.1a). Both the right and the left edges of the structure are curvy. The global surface deviations such as waviness are also investigated (Figure 6.1b). No significant global irregularity is detected. To include the local deviations and macro surface irregularities in the model, one section of the structured seal is scanned via laser microscope. The magnification of the microscope is selected as 10x. This magnification allows the detection of macro surface irregularities but not roughness. The scanned data is prepared for meshing via MATLAB. The preparation process consists of straightening the circumferential shape of the structured section into a rectangular zone and positioning the surface in relation to the counterface.

a)

Areas:
1) Unstructured /flat area
2) Deep area of the structure
3) Inclined surfaces of the structure
4) Unstructured / flat area between two structures

b)

c)
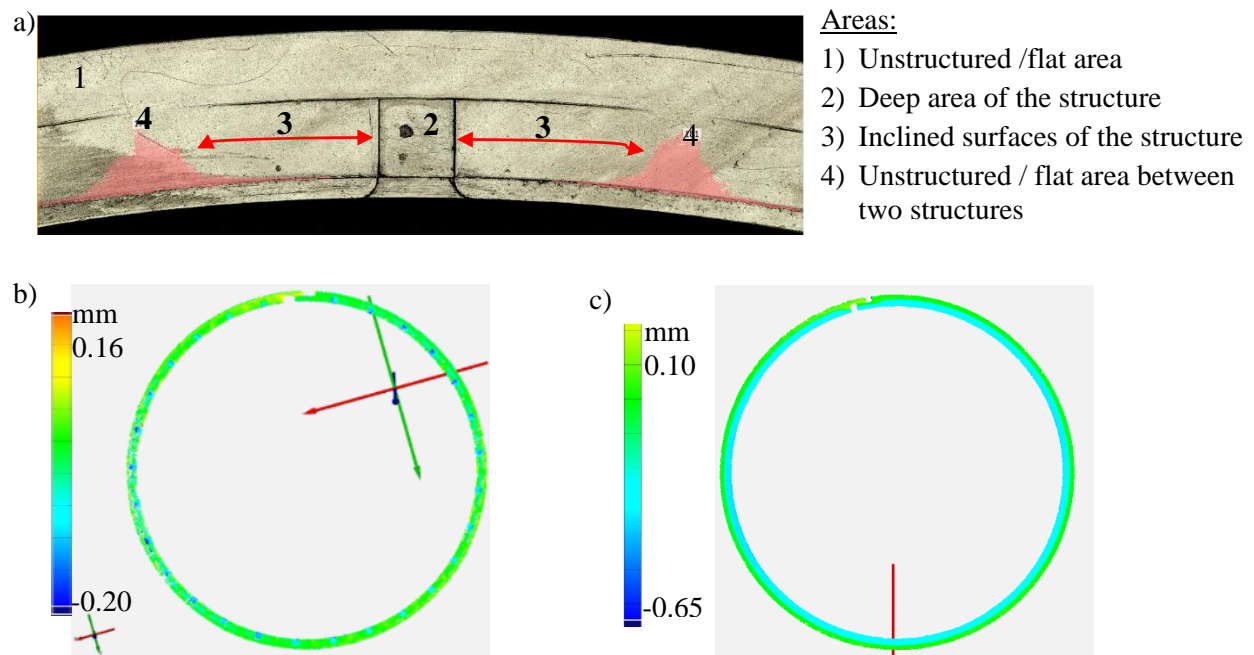
Figure 6.1: a) Macro surface irregularities on a structured seal b) Initial waviness of a structured seal c) Initial waviness of a standard seal.

Positioning the seal surface is necessary since the laser microscope can result an artificial tilt. In addition, the surfaces of the structured seals deviate from the parallel. It can be assumed that the highest peak touches to the counterface at 0 rpm. In this case the contact gap will be as in Figure 6.2a. This gap is not very realistic since the seal does not make any contact with the counterface in the outer diameter direction. The wear behaviour of the seals indicates that the seal is in contact in the outer diameter direction as well. Therefore, it is assumed that the deviation from the flatness and the outer diameter region of the seal is in contact with the counterface. Consequently, a gap similar to that in Figure 6.2b

is obtained. It should be noted that the gap during the experiments is not exactly known. Therefore, there might be some differences between the predicted gap and the gap in the experiments.
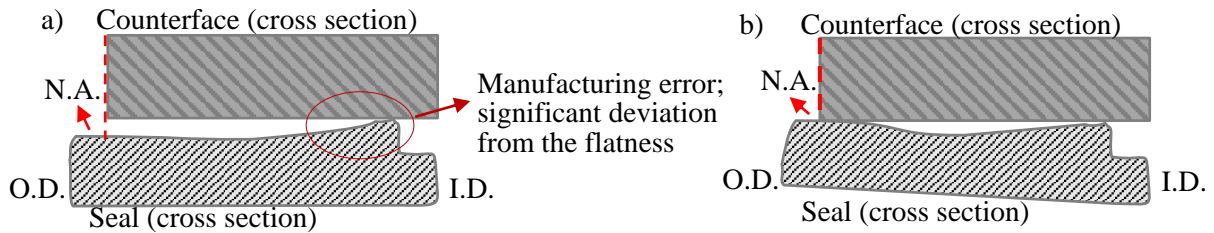
Figure 6.2: Positioning the structured seal in relation to the counterface for the numerical model when the elastic deformations are not included. O.D.= outer diameter, I.D.= inner diameter, N.A.= non-contacting seal area.

In order to model the standard seals, the method described in the section 'real geometry' is used. These seals do not have any significant global waviness (Figure 6.1c). Therefore, only one section of the standard seal can be modelled. The aim is to show the influence of the micro-pores and the glass bubbles on cavitation and film formation. Therefore, the model should capture these features sufficiently. The micro surface irregularities are not considered.

6.1.3 BOUNDARY CONDITIONS

The numerical model has 4 boundary conditions (Figure 6.3). Inlet and outlet pressure is set as lubricant and ambient pressure, respectively. It should be noted that, in the model, absolute pressure is used. In the circumferential direction, boundary conditions are set as periodic boundary conditions. The flow velocity is given as a velocity profile in the radial (y) direction corresponding to the different speeds caused by the radius differences between inner (BC 1 in the figure below) and outer boundary (BC 2 below).
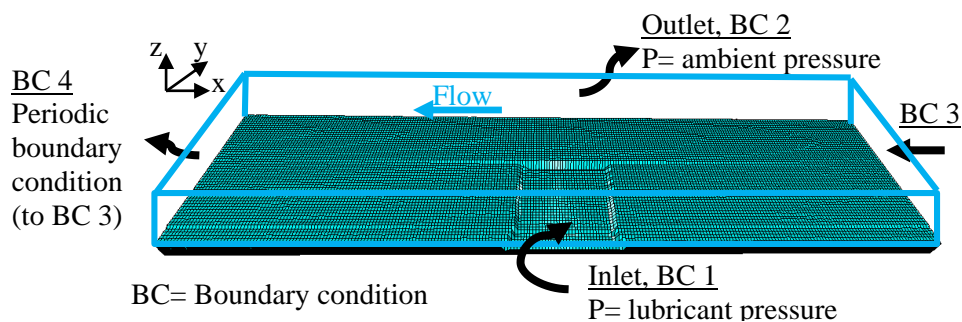
Figure 6.3: Analytical model.

6.1.4 MESH PROCEDURE

The mesh process is performed by using ElmerGrid [174]. The mesh properties were selected after a mesh study. Three dimensional hexahedral mesh is used and the Reynolds equation is solved on one of the surfaces (i.e., mesh of the Reynolds equation is solved in 2-D domain). The number of mesh points is kept constant per geometry (Table 6.1). The results are mesh independent (Appendix E, Figure E-1).

Table 6.1: The number of mesh points.

Seal	Model	Mesh density
Structured seal	Ideal geometry	50x200
Structured seal from the optical tests (unworn)	Real geometry	70x250
Structured seal from the friction tests (worn)	Real geometry	47x243
Standard seal (unworn)	Real geometry	51x245

6.1.5   INCLUDING ROUGHNESS

Influences of roughness is investigated by modelling a structured seal. To include the roughness into the numerical model, one section of the structured seal which is used in the optical tests is scanned via the laser microscope with the magnification of 100x. At this magnification, the laser microscope is not capable to scan the whole structured section. Therefore, only one half of the structured section is scanned. This area is sufficient to capture the roughness. Later on, the scanned data is mirrored to get a full structured seal section and meshed via ElmerGrid.

The models which include roughness generally might require mesh partitioning due to high number of grid elements. In the mesh partitioning technique, the mesh is divided into separate domains which are solved by single processors. The communication between the processors is realized via the nodes that lie on the boundaries of the partitions and are shared by more than one processor [174,175]. The final results are obtained as usual for the whole seal section. In the first attempt of including roughness to the model, mesh partitioning is not used. The resolution is decreased to 5µm laterally. The number of mesh points of the model with roughness is shown in Table 6.2.

Table 6.2: The simulation models and the mesh densities.

Seal	Model	Mesh density
Structured seal from the optical tests (unworn)	Real geometry + roughness	1300x280

6.2   NUMERICAL RESULTS

6.2.1   STRUCTURED SEALS

In this section, comparison of the numerical and the experimental results of the structured seals are described. Later on, influences of macro surface irregularities, cavitation pressure, radial taper, waviness, roughness are shown.

6.2.1.1   *COMPARISON of the NUMERICAL RESULTS and the RESULTS of the OPTICAL EXPERIMENTS*

In order to validate the numerical model, experimental conditions are simulated for the real geometry. Figure 6.4 shows the comparison of numerical and experimental results. Here, the minimum film thickness is equivalent to the hydrodynamic film thickness. In the simulation, the near-contact temperature is used instead of the sump temperature. The cavitation pressure (Pcav) is set as 0 kPa, 50 kPa, and 90 kPa, respectively. In the graphs, the hydrodynamic region which is detected in the optical experiments is shown.

At 20 °C and 5 bar, both the numerically calculated cavitation area ratio and film thickness show similar trends to those in experiments in hydrodynamic lubrication for all the selected cavitation pressures. In the experiments, the film thickness shows a more significant decrease at 2500 rpm in contrast to the simulation. This may be because the real contact temperature is higher than the measured one. Furthermore, the fluorescence measurement may have a higher error at this speed due to the exposure time of the CCD camera used.

The similarity between the trends shows that the consideration of the manufactured surface as well as the contact temperature is important for accurate modelling. A more precise trend can be obtained by determining the contact temperature instead of the near-contact temperature.

For cavitation pressure of 50 kPa, the values of the numerical and the experimental results are similar too, in addition to showing a similar trend. This magnitude of cavitation pressure also agrees with expected values for hydrocarbons from literature (e.g. [26]). Influence of cavitation pressure on film thickness and cavitation is described in Chapter 6.2.1.5 in detail.
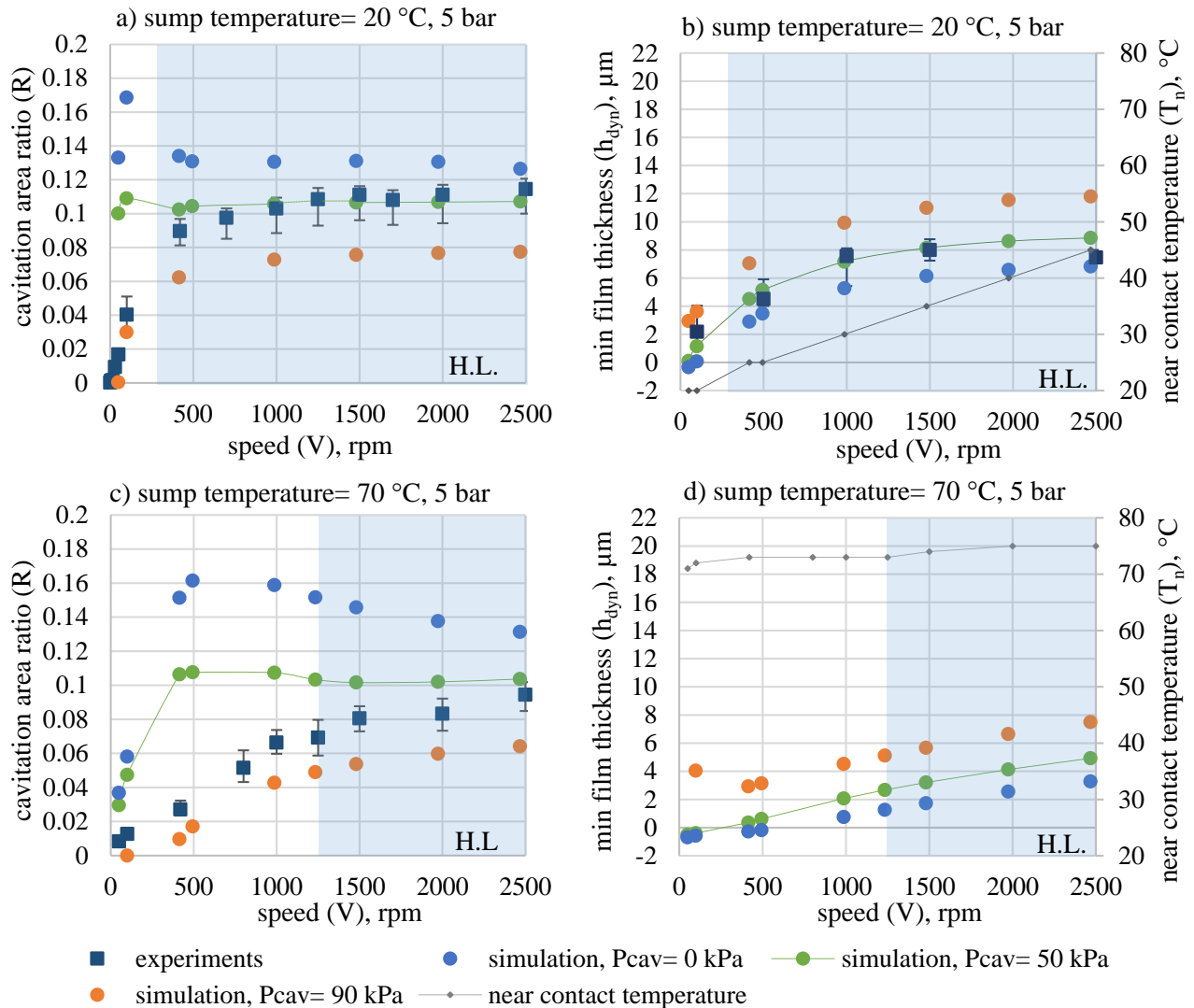
Figure 6.4: Comparison of the numerical and the experimental results. Numerical geometry= real geometry of a structured seal, Pcav= cavitation pressure, H.L.= Hydrodynamic lubrication detected in the experiments.

At 70 °C and 5 bar, additional cavitation at the unstructured surface of the seal occurs until high speeds for low cavitation pressure values. This phenomenon is examined in Chapter 6.2.1.4.3 and it is related to the film thickness. As a result of this phenomenon, the trend of cavitation area ratio is not similar for the numerical and the experimental results at 0 kPa and 50 kPa. However, the trend becomes similar for cavitation pressure higher than 50 kPa. Therefore, the cavitation pressure seems to be different than in 20 °C. Setting the cavitation pressure slightly higher than 50 kPa would result in a good agreement between the numerical results and experiments. This change in cavitation pressure with temperature can be expected since temperature influences the quantity of dissolved gas [26].

6.2.1.2 *COMPARISON of the NUMERICAL RESULTS and the RESULTS of the FRICTION EXPERIMENTS*

In this section, the correlation between the friction tests of the structured seals and the simulations are discussed. The lubrication regimes detected in the function tests 1 and 2 correlated with the simulated film thicknesses. For the function test 1, an unworn seal surface is modelled. For the function test 2, the worn seal from test A (Chapter 5.1.1.1) is modelled. In the simulations, the viscosities are set according to the measured average contact temperatures. Since in Chapter 6.2.1.1 it is shown that the cavitation pressure is slightly higher than 50 kPa at high temperatures, cavitation pressure is set as 60 kPa.

6.2.1.2.1 FUNCTION TEST 1 (BEFORE the LONG TERM TEST)

Figure 6.5 shows the coefficient of friction which is obtained from the tests and the numerically calculated minimum film thicknesses (hydrodynamic film thickness). In the hydrodynamic lubrication (full film) regime, the minimum film thickness is high. It decreases with decreasing Hersey number. At transition from mixed to hydrodynamic regime, the calculated film thickness is around 3.5 µm. Even though this film thickness is higher than the surface roughness, the measured CoF indicate that over the seal circumference some regions of thin film exist. This can be the joint as observed in the optical tests. In addition, there are some burrs on the seal surfaces.
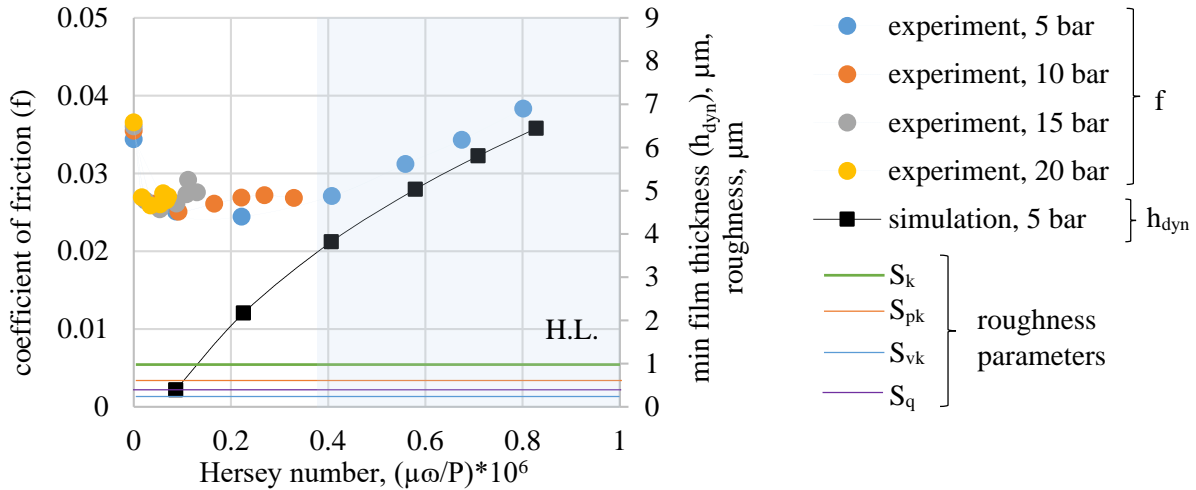
Figure 6.5: Comparison of the simulated film thicknesses and the coefficient of friction values which are obtained from test A – function test 1. Cavitation pressure is set as 60 kPa in the simulation. Numerical geometry= real geometry of a structured seal. H.L.= possible pure fluid friction region.

At minimum coefficient of friction, the calculated film thickness is only around 2 µm. This thickness is still higher than the roughness parameters. However, it might be not sufficient to separate the burrs and the some very high peaks which are randomly distributed over the seal surface. At low Hersey numbers where the seal is fully in mixed lubrication, the hydrodynamic film thickness is only 0.39 µm. This thickness is already at the level of the roughness. This shows that there can be some solid contact in this region.

Although, only one section of the seal is simulated, the numerical results fit to the experimental results. The performance of the seal can be predicted just by modelling a small section when the results are evaluated by considering the surface features deliberately. This can save computational time. However, a comprehensive modelling is necessary to calculate the coefficient of friction in the numerical models quantitatively.

6.2.1.2.2 FUNCTION TEST 2 (AFTER the LONG TERM TEST)

In function test 2, mixed lubrication regime is not as broad as in the function test 1 (Figure 6.6). The full hydrodynamic lubrication starts earlier. The calculated film thickness is quite low for the low Hersey numbers. No full separation is detected for the Hersey numbers lower than $0.2 \cdot 10^{-6}$. For these Hersey numbers, the coefficient of friction curve also indicates the presence of solid contact.

The numerically calculated hydrodynamic film thickness is around 2 µm at the transition from mixed to hydrodynamic lubrication regime. This film thickness is lower than that in the function test 1. This can be expected because the burrs and the high peaks removed after the long term test. Although, it is found that the seal surface is rougher after the tests, the absence of the burrs can lead to earlier transition to full film lubrication. Also, the surface seems to be rougher not because there are more peaks but there are more valleys. Furthermore, the deviations from the flatness wears away as well. This might lead to a more favourable gap form.
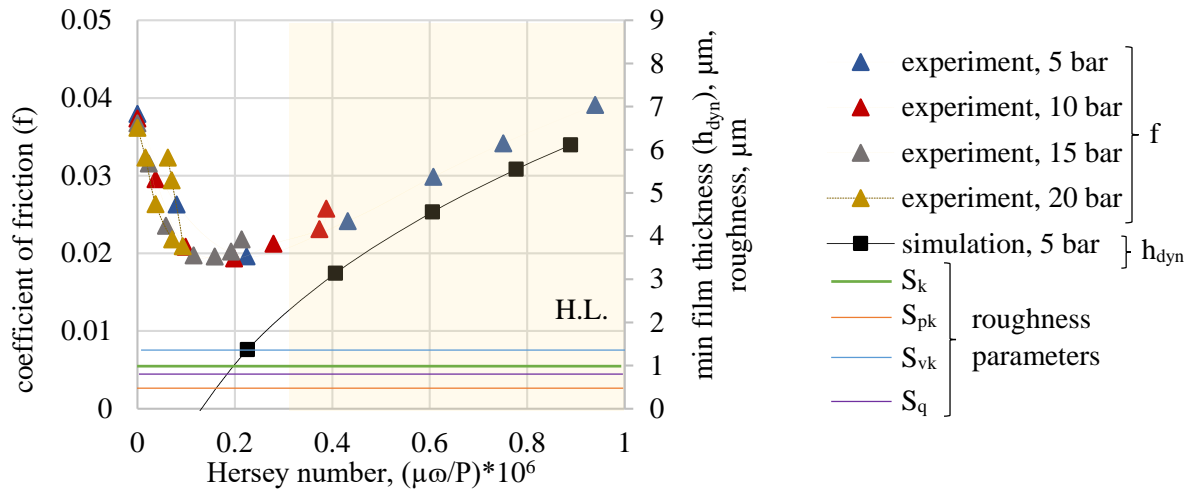
Figure 6.6: Comparison of the simulated film thicknesses and the coefficient of friction values which are obtained from test A – function test 2. Cavitation pressure is set as 60 kPa in the simulation. Numerical geometry= real geometry of a structured seal. H.L.= possible pure fluid friction region.

Interestingly, in the hydrodynamic regime, the calculated film thicknesses for the function tests 1 and 2 are similar for the same coefficient of friction values (Figure 6.7). If the seal would have been in mixed lubrication, different coefficient of friction results would have been expected for the same film thicknesses. Because the surface of the seal changes after the long term test. Therefore, the seal seems to be fully separated from the counterface both in the first and the second function tests at high Hersey numbers. The predicted hydrodynamic regime seems to be reasonable.
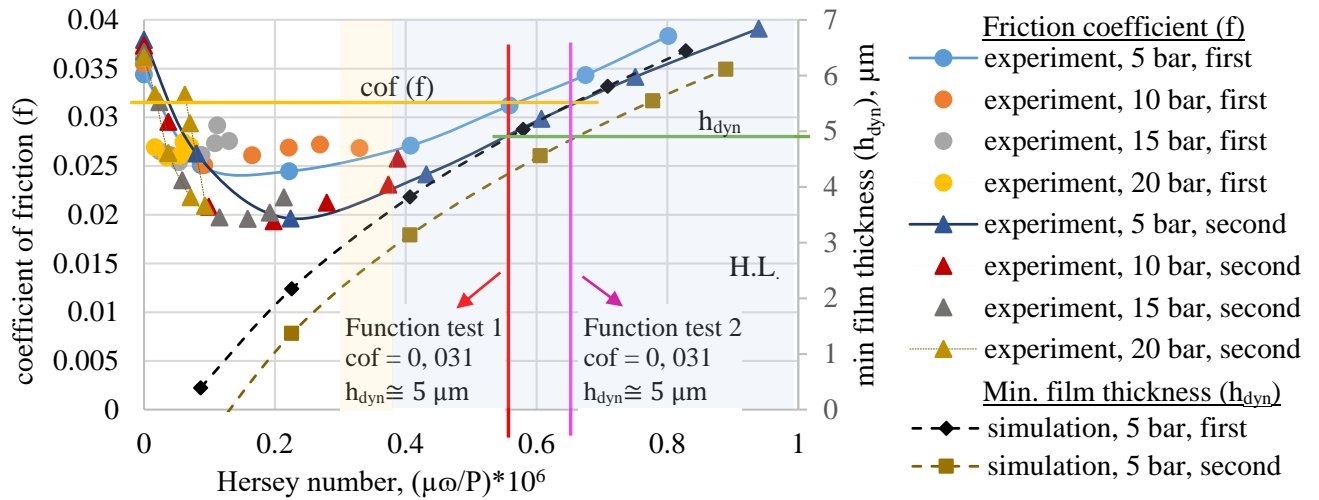
Figure 6.7: Comparison of the simulated film thickness and the coefficient of friction values which are obtained from the first and the second function tests of the friction experiments. Cavitation pressure is set as 60 kPa in the simulation. Numerical geometry= real geometries of structured seals. H.L.= possible pure fluid friction region. 'first' and 'second' represent the function test 1 and 2, respectively.

6.2.1.3   COMPARISON of the COEFFICIENT of FRICTION VALUES from the SIMULATIONS and the EXPERIMENTS

The numerical tool calculates the shear and the nominal forces for the modelled seal section. Thus, the coefficient of friction can be calculated for the numerical results via:

$$f = \frac{F_{shear}}{F_N} \tag{6.4}$$

In Appendix F, the validation of the numerically calculated shear force is investigated for the full film lubrication. For this, the numerically and the analytically calculated shear forces for a parallel and ideally smooth gap are compared. It is shown that the numerical model calculates the shear forces accurately when the friction only arises from the lubricant shear.
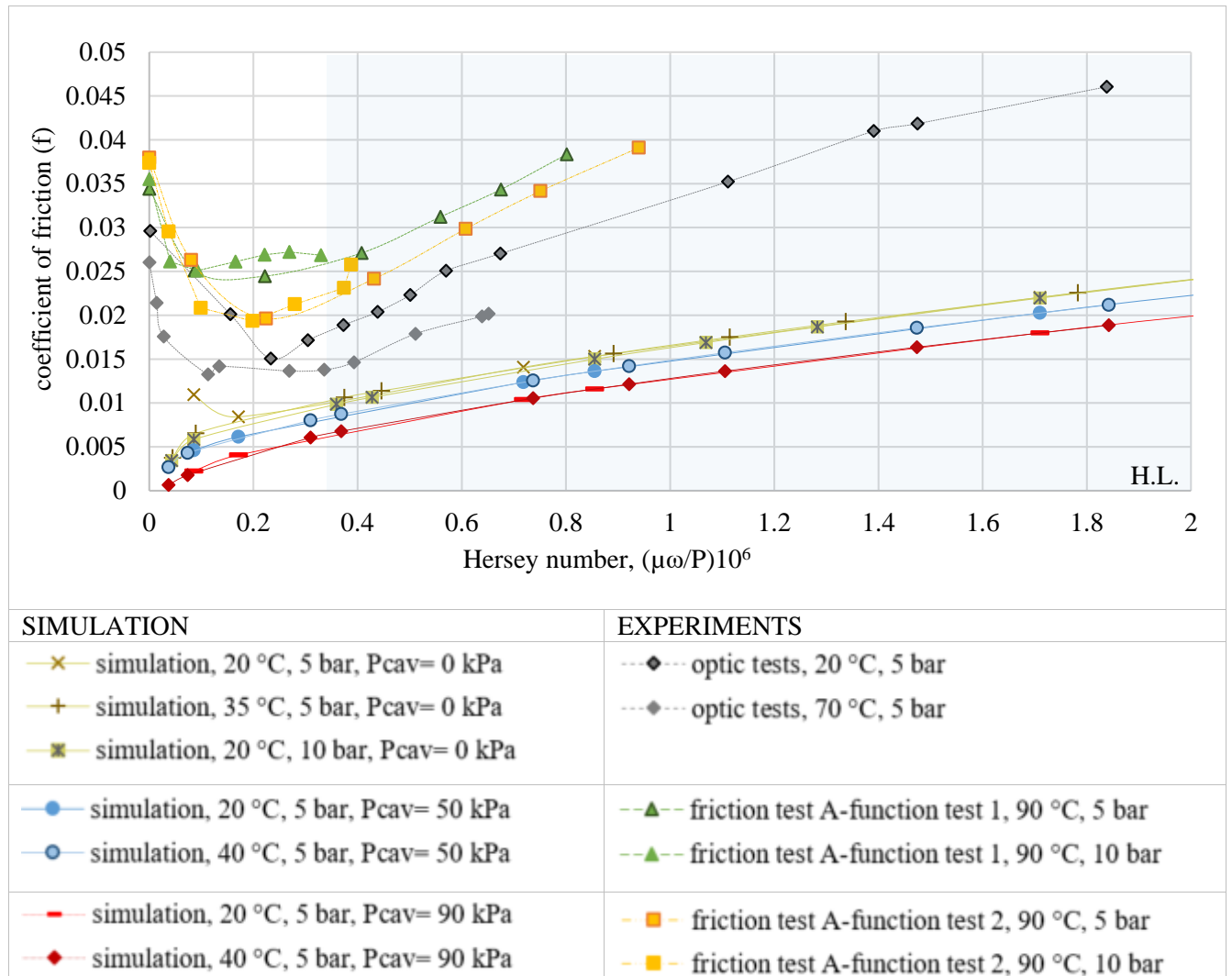
Figure 6.8: Comparison of the numerically and experimentally calculated coefficient of friction values. Numerical geometry= real geometry of a structured seal. H.L.= possible pure fluid friction region. Pcav= cavitation pressure.

Figure 6.8 shows the calculated coefficient of friction values from the simulations and the experiments plotted over the Hersey number. The numerical results should only be considered for the hydrodynamic regime. Because the numerical model does not consider the boundary and the mixed lubrication conditions.

For the same cavitation pressure (Pcav), the numerically calculated coefficient of friction curves coincide for different temperatures and ambient pressures. This agrees with the aim of Hersey number (Coefficient of friction curves of various temperatures, speeds and load should coincide when they are plotted with over the Hersey number for similar gap features.). Also, it shows that the numerical tolerances are quite tight.

With increasing cavitation pressure, the numerically calculated coefficient of friction decreases, because, the film thickness increases (see Chapter 6.2.1.5). Consequently, the shear stress and the force within the lubricant film decreases due to the relationship between the film thickness and the shear force:

$$\dot{\gamma} = \frac{V}{h} \qquad \tau = \eta \cdot \dot{\gamma} \quad F_{shear} = \tau \cdot A \tag{6.5}$$

Here, $\dot{\gamma}$ is the shear rate and, τ is the shear stress. The contact area is denoted with 'A'. This formula also shows that the structures provide a decrease in the shear stress within the structures due to a higher film thickness.

The numerically calculated coefficient of friction values are much lower than the values which are obtained via the experiments. This can be due to the non-uniform film thickness over the seal face. The fluorescence measurements, cavitation distribution and the temperature measurements indicate that the film is thinner around the joint. This can lead to a higher friction force in that section. In addition, very high peaks (5 µm) are removed from the surface in the numerical model since they would lead to an initially high gap. In practice, these high peaks would result locally thin film and high friction.

The deep parts of the structures and the structure might furthermore, lead to turbulent flow. Turbulent flow regime might increase the friction [187]. The current numerical model assumes that the flow is only laminar.

Furthermore, the lubricant which is churning in the test chamber can contribute to the measured friction as well. This would lead to an increased experimental result not directly related to the friction generated by the contact.

The results show that the modelling of only one section of the seal may be insufficient to predict the coefficient of friction. It might be necessary to model the whole seal ring with elastic deformations and solid contacts for an accurate friction calculation in the simulations.

6.2.1.4   INFLUENCE of MACRO SURFACE IRREGULARITIES

6.2.1.4.1   IDEAL GEOMETRY

Figure 6.9a and c shows the calculated pressure generation and cavitation at 1250 rpm, 20 °C and 5 bar for the ideal geometry. Cavitation pressure is set as 0 kPa. Cavitation forms in the divergent zone of the structure as in the experiments. It should be noted that for a robust (i.e., ignoring numerical spikes) differentiation of cavitated and non-cavitated regions a threshold of 0.17 of the cavitation fraction was used. Pressure concentrates at the edge of the convergent zone of the structure.

Pressure and cavitation is shown graphically in Figure 6.9d. Pressure decreases to cavitation pressure within the cavitated area. At the deep part of the structure, the pressure value is around the oil pressure value since this zone is open to the pressurized oil. In the convergent zone of the structure, pressure increases rapidly.

The morphology of the simulated cavitation is different than the experimentally observed one (Figure 6.9b). The rupture boundary is straight. The inclination of reformation boundary is in the opposite direction. The entire cavitation region is pushed to the direction of the outer diameter. These differences can be due to surface irregularities and elastic deformation in the experiments.

6.2.1.4.2   REAL GEOMETRY

Figure 6.10 shows the pressure generation and cavitation at 1250 rpm, 20 °C and 5 bar for the real geometry. It should be noted that the real geometry is slightly shorter than the ideal geometry due to straightening of the seal section. Both cavitation and pressure distribution are different than those for the ideal geometry. The pressure concentrates more in the inner diameter direction. Cavitation morphology is similar to the observed morphology. The rupture boundary is curvy. This proves that the surface irregularities shown in Figure 6.1a lead to the curvy shape of the cavitation region. The reformation boundary is more realistic too but still not as inclined as in the experiments. This may be because the seal deforms during the operation and, as a result, the contact gap is different from the simulated gap.

a) Ideal geometry – cavitation

b) Structure 16

c) Ideal geometry – pressure buildup with isobars

d) Cut view of c – pressure buildup and cavitation

Figure 6.9: Cavitation formation and pressure generation for the ideal geometry of a structured seal at 1250 rpm, 20°C and 5 bar. The cavitation pressure is 0 kPa.

a) Real geometry – cavitation

b) Structure 16

c) Real geometry – pressure buildup with isobars

d) Cut view of c – pressure buildup and cavitation

Figure 6.10: Cavitation formation and pressure generation for the real geometry of a structured at 1250 rpm, 20°C, and 5 bar. The cavitation pressure is 0 kPa.

6.2.1.4.3 COMPARISON of IDEAL and REAL GEOMETRIES and INFLUENCE of OPERATING PARAMETERS

Figure 6.11 shows the numerically calculated cavitation area ratio and the minimum film thickness at various speeds, temperatures, and ambient pressures for the ideal and the real geometries. The cavitation pressure is set as 0 kPa for the sake of comparison as it results in minimal lift contribution of the cavitation area. For the ideal geometry, the film thickness increases with increasing speed. This shows that the structures are capable of generating hydrodynamic lift without additional surface features such as waviness and roughness. For a given speed, the film thickness decreases with increasing temperature and pressure as in experiments.

For the ideal geometry, the cavitation area ratio increases with speed until 1000 rpm. After this, it is nearly constant due to the geometry of the structure. Cavitation already covers a big portion of the divergent gap at high speeds hence, it does not change significantly with speed.

For the real geometry, film thickness is lower than that for the ideal geometry. This is because macro surface irregularities change the gap shape slightly. The film thickness has negative values at low speeds. (Note: negative film thickness means, that the external force is larger than the force generated by the fluid, thus causing a decay of the film thickness until it reaches a numerical value below 0.). This indicates that some surface peaks should be in contact and subsequently deform. However, the model is not developed for mixed and boundary lubrication.

For the real geometry, the cavitation area ratio increases sharply with speed and decreases until high speeds are reached. This behaviour occurs when the predicted minimum film thickness (h_{dyn}) is low or zero. This is because macro surface irregularities become relevant for lubrication when the film is thin. Hence, additional cavitation occurs at the unstructured surface of the seal as in Figure 6.12. With increasing film thickness, this additional cavitation disappears. The cavitation area ratio becomes nearly constant at high speeds as in the ideal geometry. In the experiments, additional cavitation is observed near the joint. This is an indication of non-uniform distribution of film over the seal face.
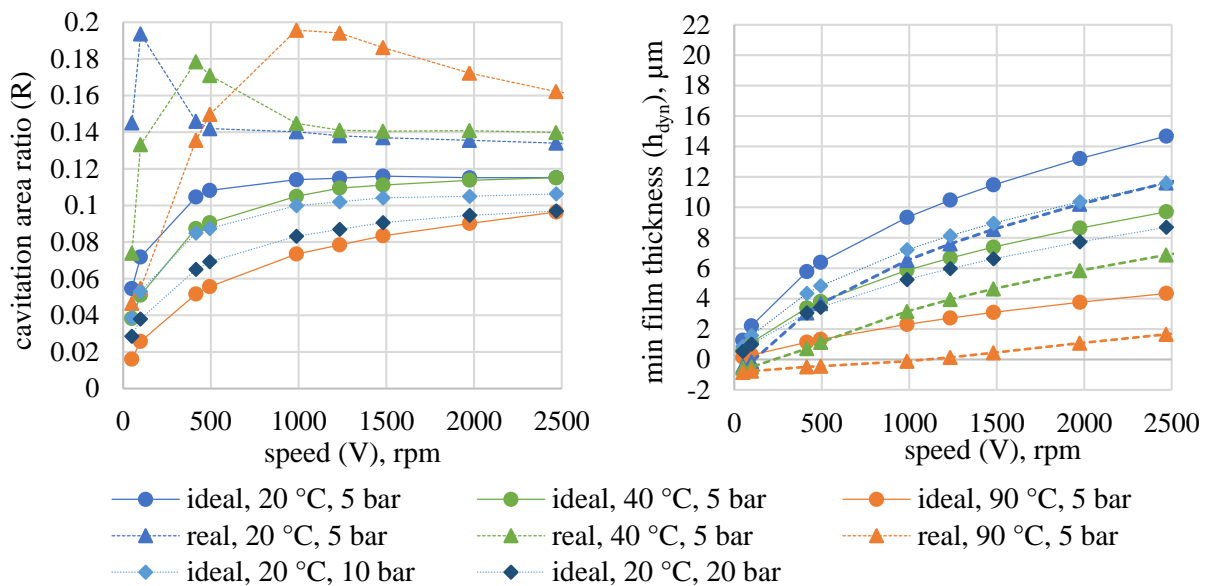
Figure 6.11: Film thickness and cavitation area ratio at different speeds, temperatures and pressures. Ideal: ideal geometry of a structured seal, Real: real geometry of a structured seal. Cavitation pressure is set as 0 kPa.

a) Real geometry – cavitation, 100 rpm, 20 °C, 5 bar, cavitation pressure = 0kPa

b) Structure 23, 100 rpm, 20 °C, 5 bar.
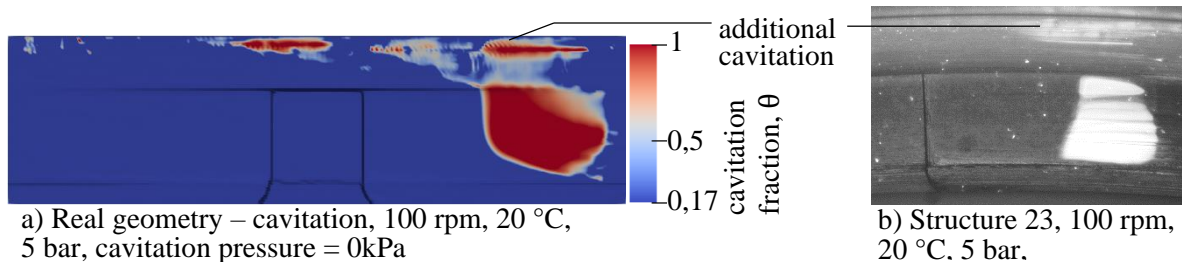
Figure 6.12: Additional cavitation formation: a) in simulation, b) in the experiments.

6.2.1.5 INFLUENCE of CAVITATION PRESSURE

It is unrealistic that gaseous cavitation occurs when the lubricant pressure drops to 0 kPa, which would be vacuum. Figure 6.13a shows the influence of cavitation pressure on the cavitation area ratio for the ideal geometry at 500 rpm, 20 °C, and 5 bar. The minimum gap height is set as 8.5 µm. The cavitation area ratio increases with increasing cavitation pressure.
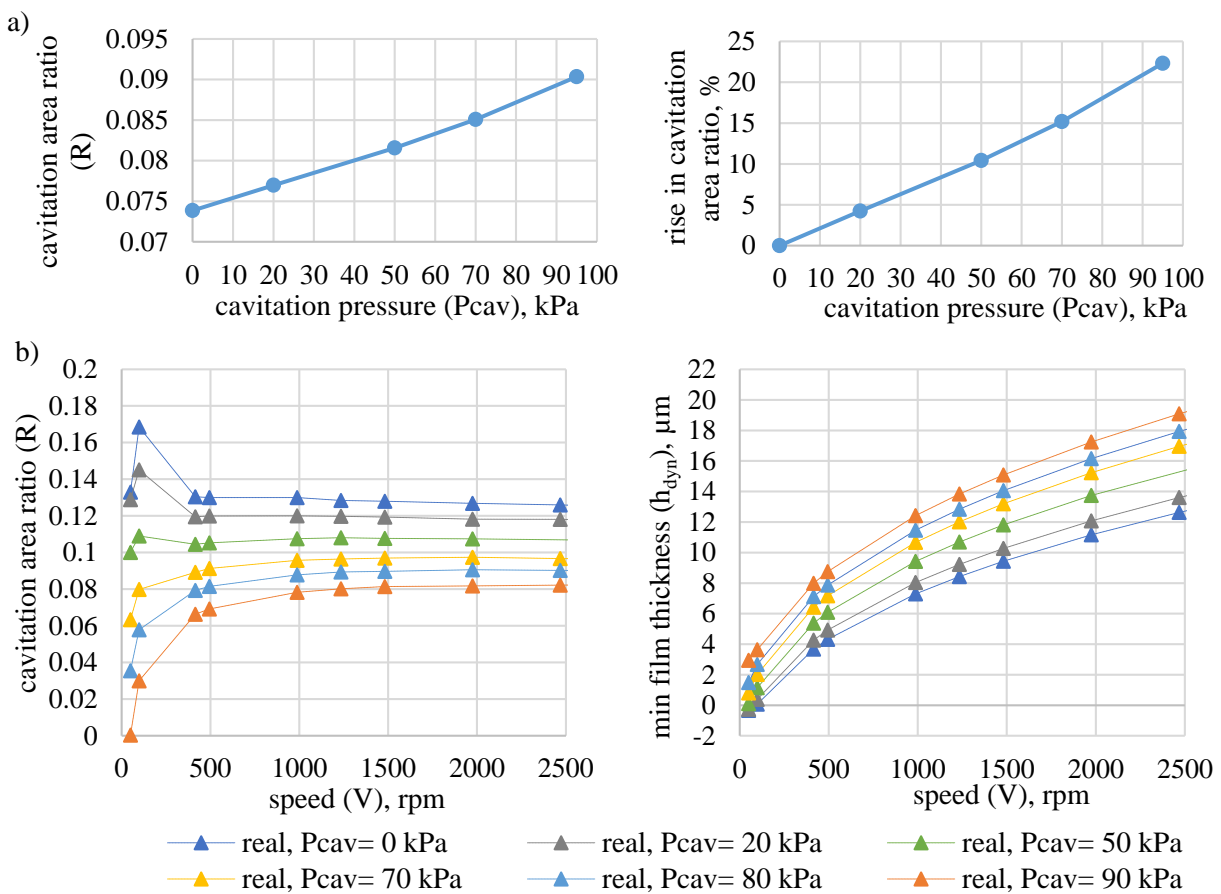
Figure 6.13: Influence of cavitation pressure: a) Ideal geometry of a structured seal, 500 rpm, 20 °C, 5 bar, min. gap height= 8.5 µm. b) Calculated cavitation area ratio and film thickness at 20 °C, 5 bar for the real geometry of a structured seal.

Figure 6.13b shows the calculated min. film thickness and the corresponding cavitation area ratio for different speeds and cavitation pressures. Temperature and pressure are set as 20 °C and 5 bar, respectively. The results are shown for the real geometry but they are similar for the ideal geometry as well. Film thickness increases with increasing cavitation pressure. This is due to the contribution of cavitation pressure to the integrated pressure although the maximum pressure decreases (Figure 6.14). As a result of the increase in film thickness, the cavitation area ratio decreases with increasing cavitation pressure. This also leads to less or no additional cavitation outside of the structure.

a) Ideal geometry – pressure buildup with isobars
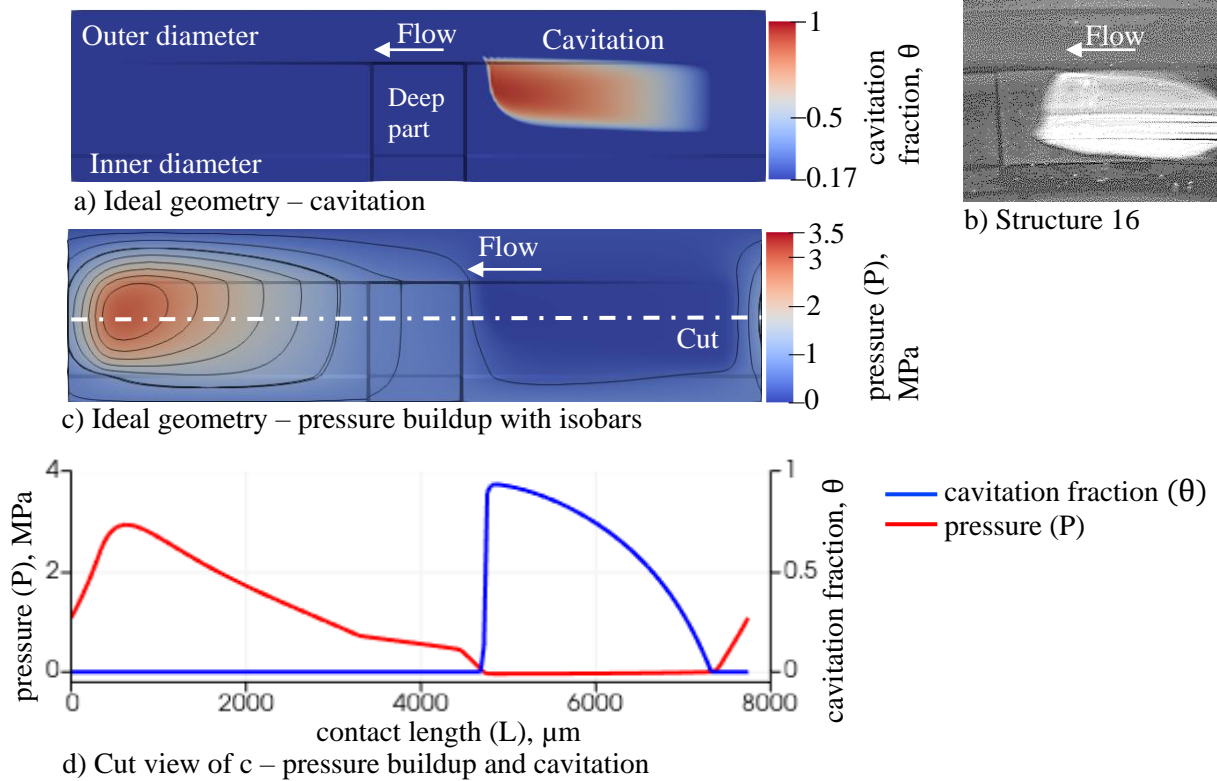
b) Cut view of a – pressure buildup and cavitation
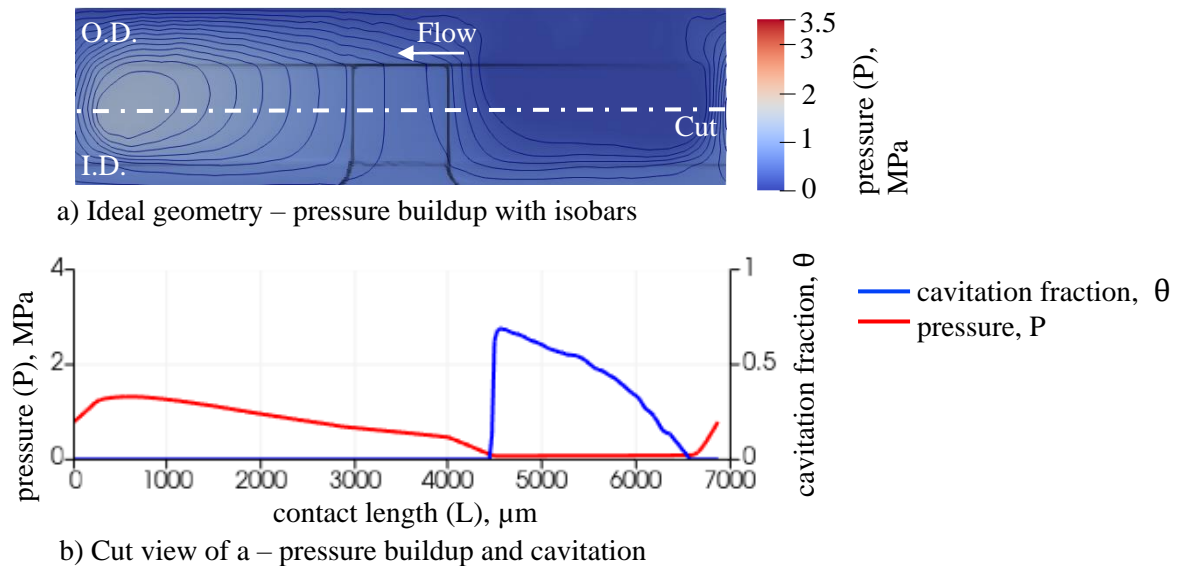
Figure 6.14: Cavitation formation and pressure buildup for the ideal geometry of a structured seal at 1250 rpm, 20 °C and 5 bar. Cavitation pressure= 90 kPa. O.D.= outer diameter, I.D.= inner diameter.
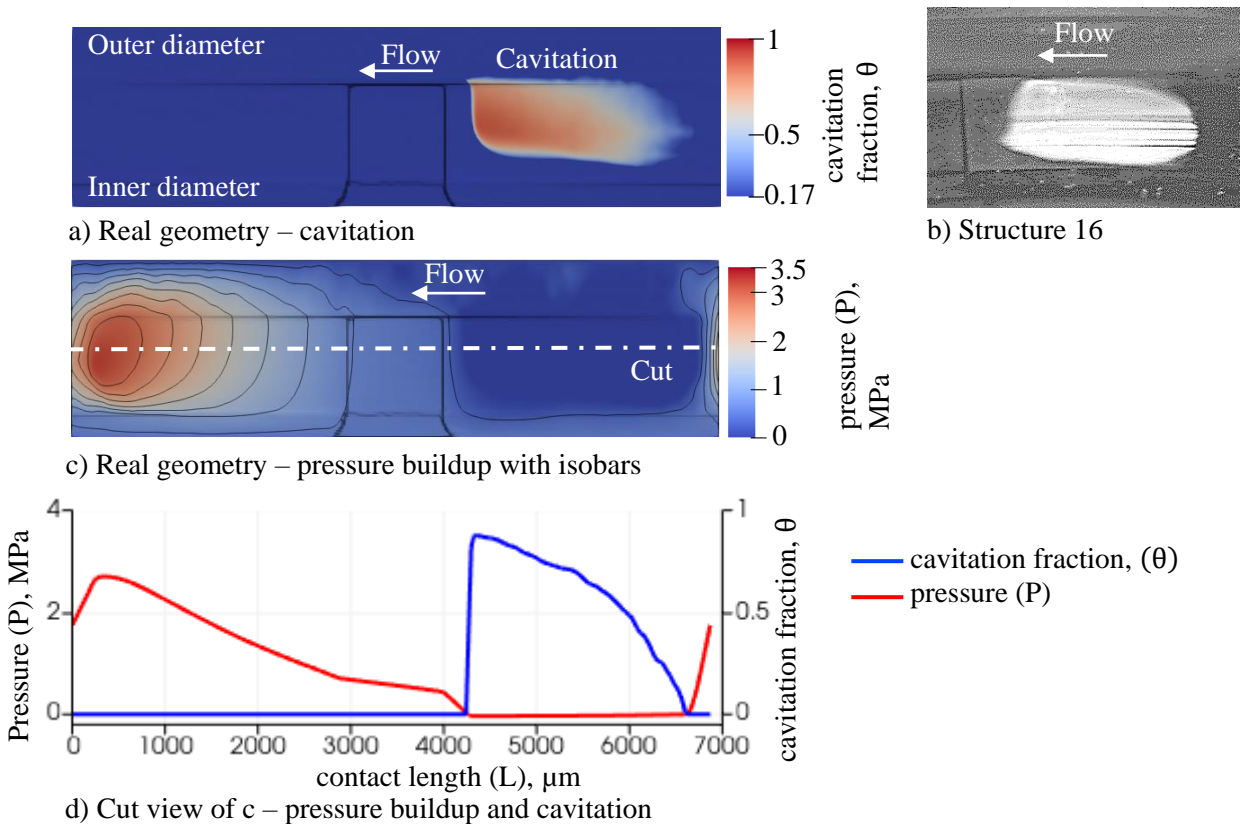
6.2.1.6   INFLUENCE of RADIAL TAPER / TILT

In this section, influence of radial taper is investigated by tilting the ideal geometry of the structured seal with different degrees of tilts. Figure 6.15 shows the convergent and the divergent gaps which are simulated here. Temperature and pressure are set as 20 °C and 5 bar, respectively. Cavitation pressure is set as 0 kPa. The minimum gap height is set as 8.5 µm for a parallel gap. Figure 6.16 shows the change in cavitation area ratio when the gap is tilted. When the gap is tilted to be convergent, a smaller cavitation area ratio is obtained. With increasing tilting degree, the cavitation area ratio decreases for the convergent gap. Because more pressurized oil enters to the gap. The opposite effect occurs for the divergent gap. It should be noted that no cavitation occurs at 50 rpm and 100 rpm due to the selected film thickness.
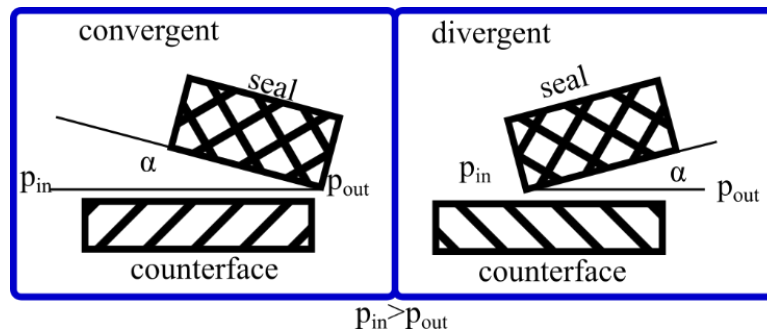
Figure 6.15: A convergent and a divergent gap.

Figure 6.17 shows the calculated film thicknesses via the force balance method for various tilts. The corresponding cavitation area ratios are shown as well. The minimum film thickness is slightly lower for the tilted gaps. In addition, the minimum film thickness decreases with increasing tilting degree for both the convergent and the divergent gaps. This can be due to the higher initial gap heights in the tilted gaps. On the other hand, cavitation area ratio has a similar trend as for the constant gap height. The results show that the influence of radial taper is low up to a tilting degree of 1000 µrad. For the current application, higher magnitude of tilting degrees seems unrealistic.
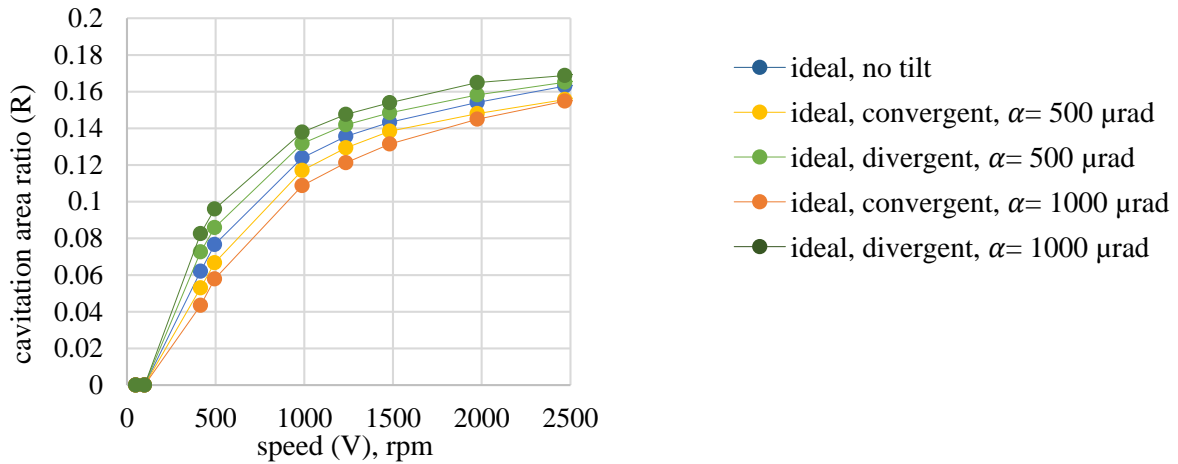
Figure 6.16: Influence of radial taper on cavitation area ratio for the ideal geometry of a structured seal at 20 °C and 5 bar. The minimum film thickness is set as 8.5 μm for the parallel gap. Cavitation pressure is set as 0 kPa.
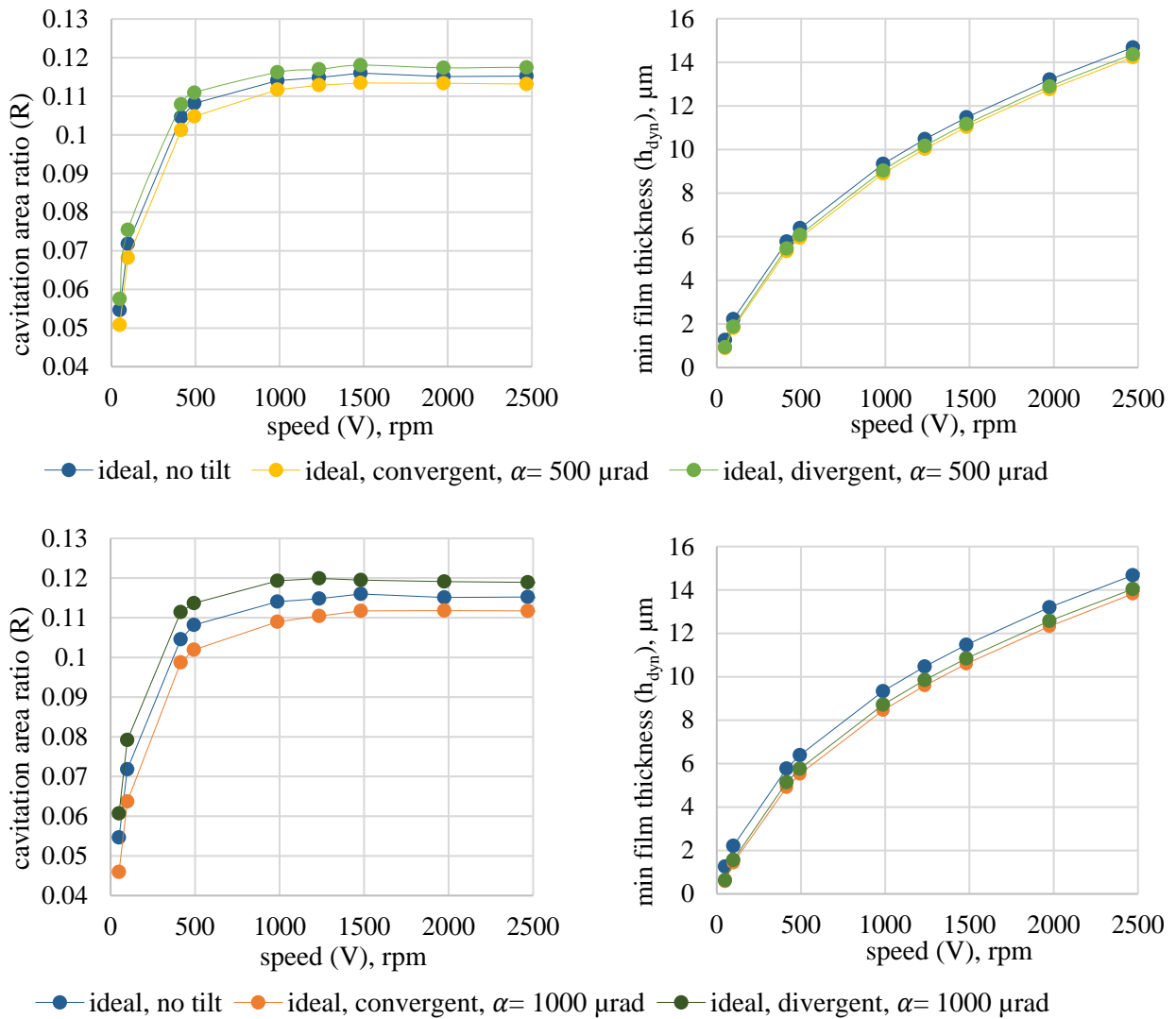
Figure 6.17: Influence of radial taper / tilt on cavitation area ratio and film thickness for the ideal geometry of a structured seal at 20°C, 5 bar. Cavitation pressure= 0 kPa.

Both convergent and divergent gaps influence the hydrodynamic effects negatively. However, a convergent radial taper can provide a hydrostatic load support which can decrease friction in mixed

lubrication regime. The hydrostatic lifting force related to radial Poiseuille flow is 5.79 N at 0 rpm, 20 °C and 5 bar for the ideal geometry with a parallel gap. This hydrostatic lifting force increases to 5.92 N for a convergent gap with a tilting degree of 500 µrad. On the other hand, the divergent gap with tilting degree of 500 µrad leads to a lower lifting force which is 5.61 N.

The morphology of cavitation changes with tilting as shown in Figure 6.18. For a divergent gap, the cavitation is less pushed outwards. This is similar to the behavior of the cavitation in the experiments. A divergent gap leads a more realistic reformation boundary as well. The inclination of the reformation boundary is similar to that in the experiments particularly at low speeds. Hence, considering the radial tilt seems to be necessary to predict the boundaries of cavitation and the cavitation morphology accurately.

a) Untilt gap, 50 rpm

b) Convergent gap, tilting degree=500 µrad, 50 rpm

c) Divergent gap, tilting degree=500 µrad, 50 rpm
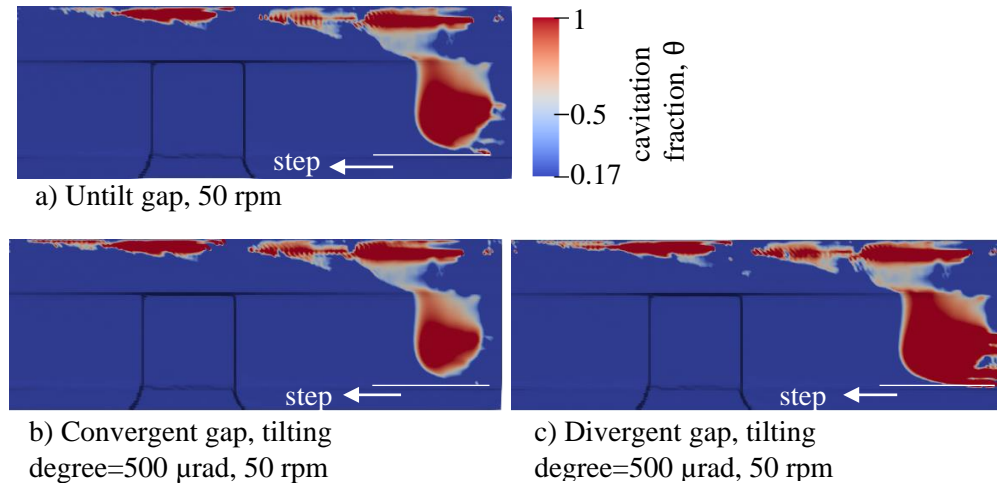
Figure 6.18: Influence of radial taper on cavitation morphology for the real geometry of a structured seal at 20°C, 5 bar. Cavitation pressure is 0 kPa.

6.2.1.7 INFLUENCE of WAVINESS

Influence of waviness is investigated by generating a wavy gap for the ideal geometry. Gap height is set as 2.5 µm for a parallel gap. It is assumed that only one of the friction surfaces is wavy. Here, a harmonic sinusoidal wave with different amplitudes and lengths is applied to the seal. When the wave is applied, the gap height distribution $h_{(x,y)}$ for a parallel gap with a minimum gap height h_{min} becomes:

$$h_{(x,y)} = A sin\big((2\pi\ /\ \lambda)x\big) + z + h_{min} \tag{6.6}$$

Here, the wavelength (λ) is the length from one peak to another. Amplitude (A) is the peak amplitude. Temperature and pressure are set as 20 °C and 5 bar, respectively. Cavitation pressure is set as 0 kPa.

First, the influence of waviness is investigated for a smooth surface without the structure and the surface irregularities. The length of this surface is 30600 µm. Figure 6.19 shows cavitation area ratio and lubricant lifting force for this smooth surface with and without waviness. Here, the lifting force is the combination of hydrostatic and –dynamic effects. For a given wavelength, the lifting force increases as the amplitude increases. For a given amplitude, the lifting force decreases with increasing wavelength. At 1000 rpm, the lifting force is almost 5 times higher for a wavy gap with an amplitude of 1 µm and a wavelength of 7650 µm (four peak wave). Waviness influences the cavitation area ratio similarly to the lifting force as well.
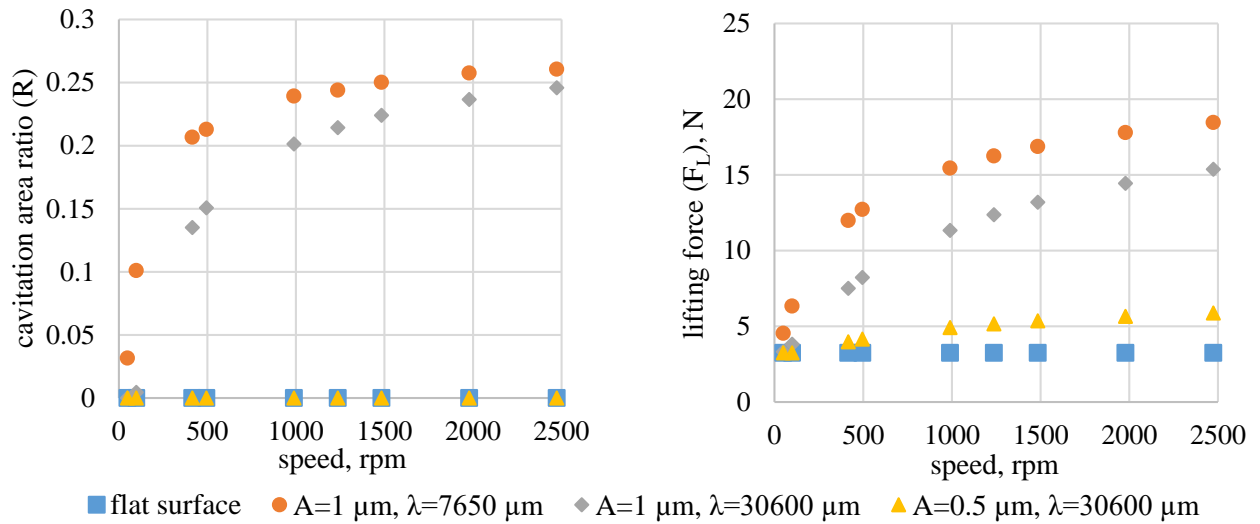
Figure 6.19: Influence of waviness for a smooth surface without the structure at 20 °C, 5 bar. Minimum gap height is set as 2.5 µm for the parallel gap. Cavitation pressure is 0 kPa.

Figure 6.20 shows the influence of a wave with a wavelength of 30600 µm (one peak wave) and different amplitudes for the structured seal section. In contrast to the results for the smooth surface without a structure, the influence of waviness on cavitation area ratio is negligible. The lifting force does not change significantly as well. Increasing amplitudes lead to slightly higher lifting forces with increasing speeds.

The influence of the wavelength is different as well when the surface is structured (Figure 6.21). The selected wavelengths 7650 µm, 15300µm, 22950 µm and 30600 µm are equal to the length of 1, 2, 3 and 4 structured seal sections, respectively. The lifting force decreases when the wavelength is 7650 µm (= length of one structured seal section). This is because the applied wave changes the inclination of the convergent and the divergent planes of the structure unfavorably. Consequently, the film thickness becomes higher in the convergent gap and lower in the divergent gap. The entrainment of less pressurized oil to the divergent gap results in a bigger cavitation zone. On the other hand, the lubricant lifting force decreases. When the flow is changed to the clockwise direction, opposite results are obtained. Because high and low film thickness regions coincide with the divergent and convergent zones, respectively (Figure 6.22).
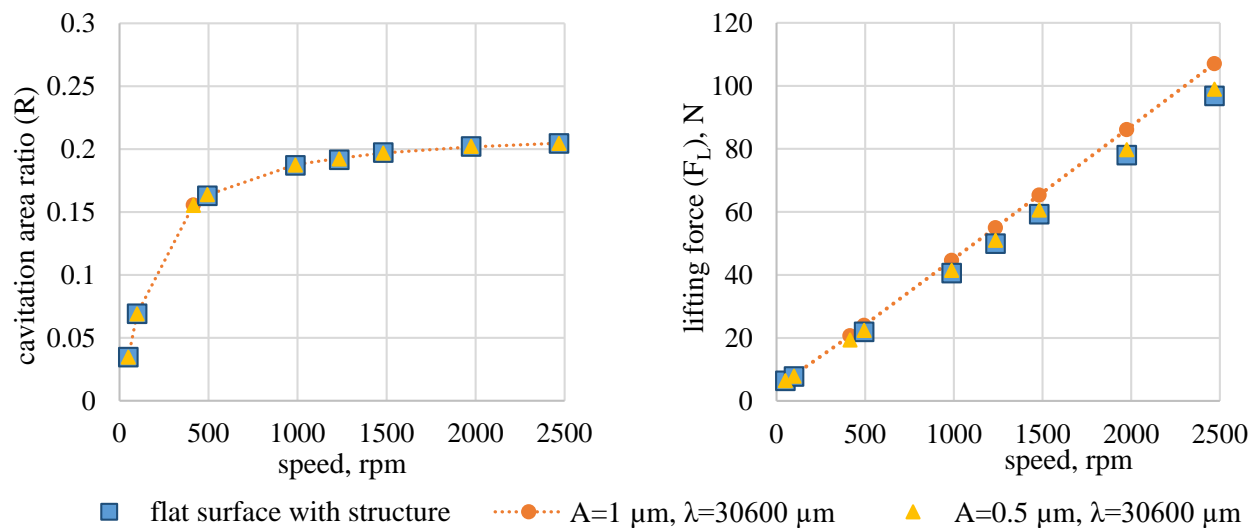
Figure 6.20: Influence of wave amplitude for the ideal geometry of a structured seal at 20 °C and 5 bar. Minimum gap height is set as 2.5 µm for the parallel gap. Cavitation pressure is 0 kPa.

For an amplitude of 1 µm, the highest lifting forces are obtained for the wavelengths of 22950 µm and 30600 µm (3 and 4 structured seal sections, respectively) (Figure 6.21). The wavelength of 30600 results in an increase in cavitation area ratio as well. On the other hand, no significant effect of the waviness is detected when the wavelength is equal to two structured seal section (15300 µm).
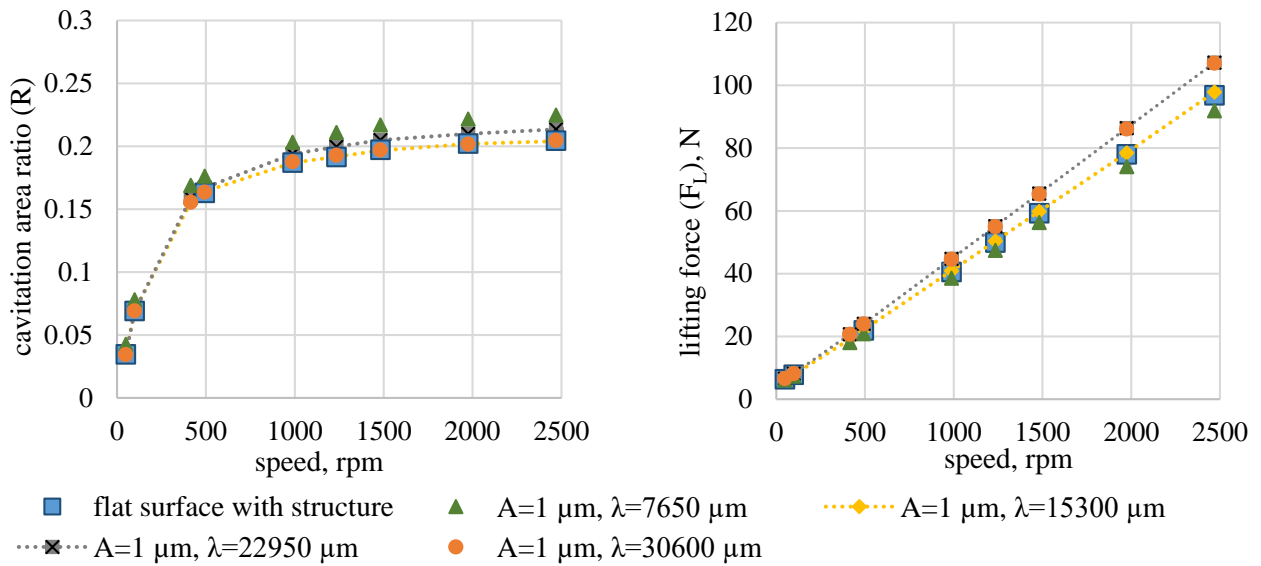
Figure 6.21: Influence of wavelength for the ideal geometry of a structured seal at 20 °C and 5 bar. Minimum gap height is set as 2.5 µm for the parallel gap. Cavitation pressure is 0 kPa.

Non-uniform film distribution due to waviness influences the morphology of the cavitation and the distribution of the lubricant pressure (Figure 6.23). The cavitation and the concentrated pressure zones are smaller in the high gap height regions. Cavitation is pushed outwards. The reformation boundary of the lubricant film is tilted. In the low gap height regions, cavitation and the concentrated pressure zones are bigger. Cavitation zone is less pushed to outwards. The reformation boundary of the lubricant film is less tilted.
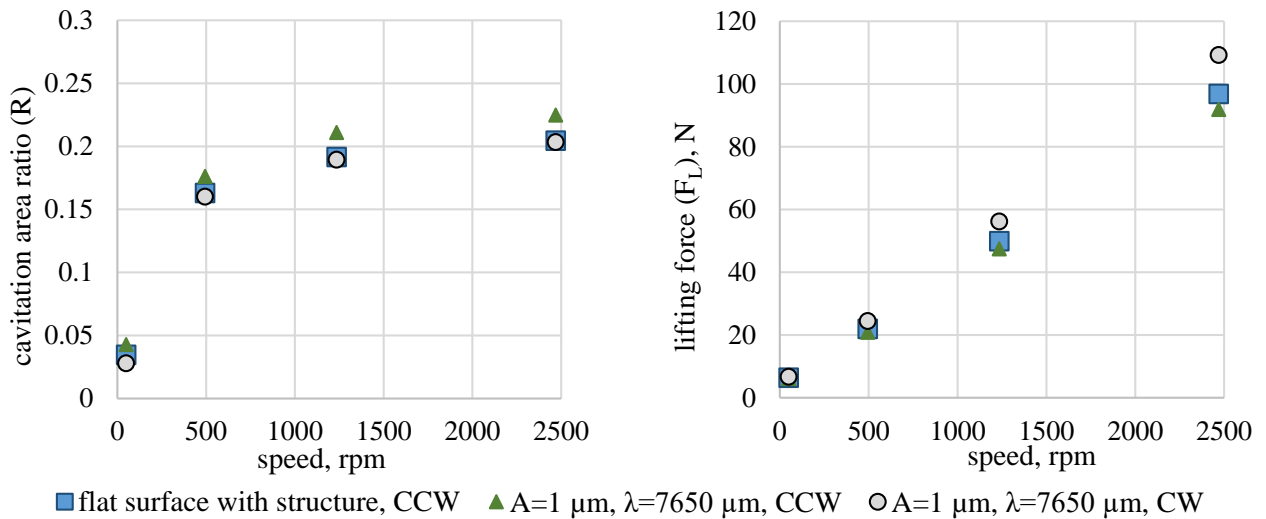
Figure 6.22: Influence of waviness when the wavelength is equal to the length of a structured seal section. Temperature and pressure are 20 °C and 5 bar, respectively. The model is the ideal geometry. Minimum gap height is set as 2.5 µm for the parallel gap. CCW and CW represent the flow direction.

Due to waviness, the unstructured surface over the structures becomes diverging and converging at some regions. This influences the pressure distribution over the unstructured surface. In the second structured section in Figure 6.23b, a low pressure zone crawls over the flat surface and pushes the concentrated high pressure zone. This is due to the diverging form of the gap in this section. Here the distribution of

the low pressure region correlates with the warming regions in the thermography measurements. This shows that waviness can be a reason for the non-uniform temperature distribution over the seal contact. On the other hand, the surface is converging in the first structured section. Therefore, the high pressure zone is distributed over a larger area (Figure 6.23b).

a) Cavitation, A= 1 µm, λ= length of 4 structures

b) Pressure generation with pressure isobars, A= 1 µm, λ= length of 4 structures

c) Film thickness distribution over A-A
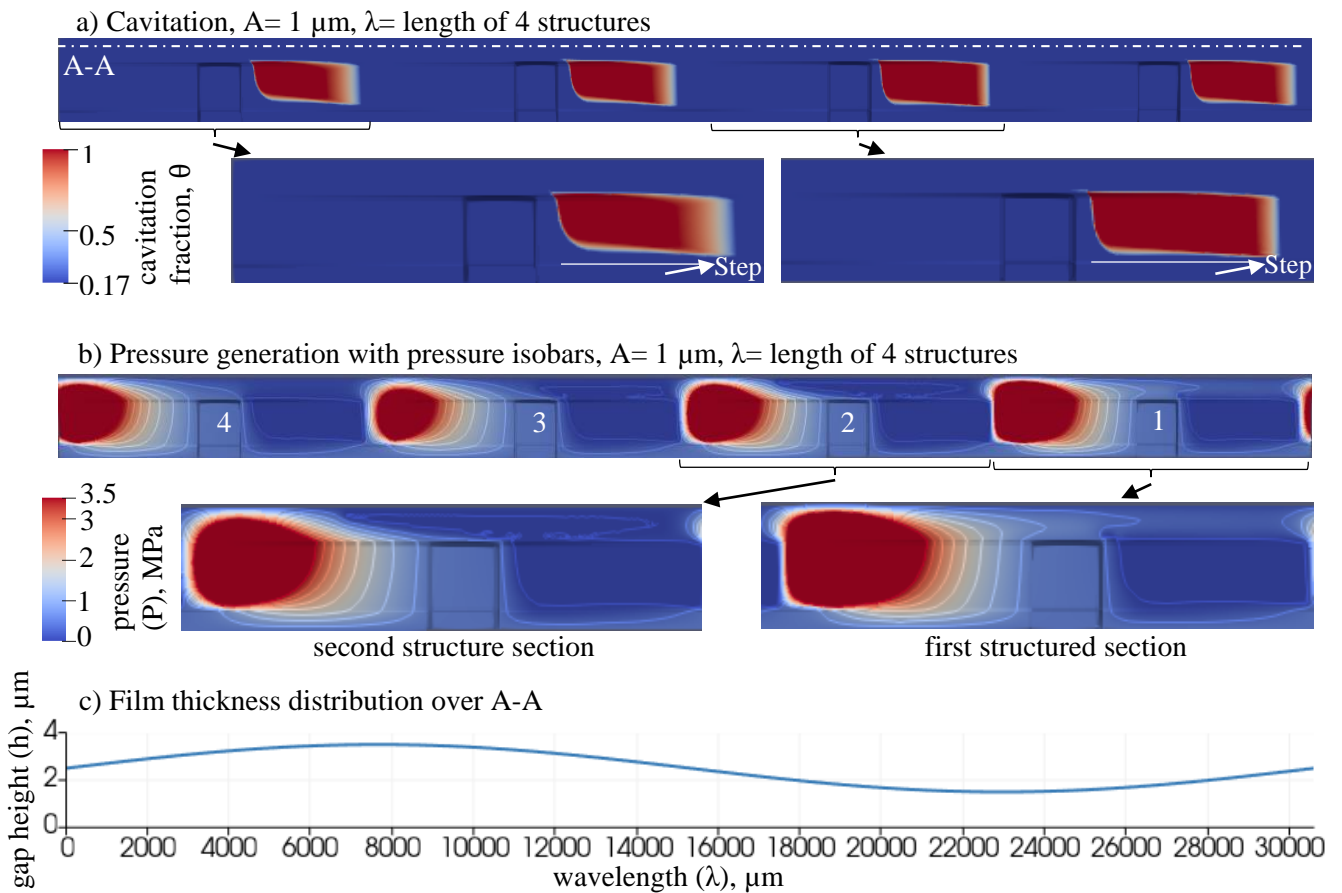
Figure 6.23: Influence of waviness on cavitation morphology for the ideal geometry of a structured seal at 20 °C, 5 bar. Minimum gap height is set as 2.5 µm for the parallel gap. Flow is CCW. Cavitation pressure is 0 kPa.

The results show that waviness can enhance the lubricant lift significantly and generate hydrodynamic effects for macroscopically parallel surfaces. However, when other macro surface features such as structures are present, the influence of the waviness depends on its interaction with these features. Here, the influence of the structures on the film formation is dominant. However, a wave with appropriate features can contribute to the film formation. Here, this can be realized via a wave with a wavelength longer than the length of one structured seal section and high amplitudes. The contribution of the waviness is low when the amplitude is quite low compared to the film thickness.

6.2.1.8   INFLUENCE of WEAR

In this section, the influence of the wear is investigated by comparing the unworn seal with the worn seal from the friction test A of the structured seal. In this test, there was no dramatic change in the initial profile of the structures. The right and the left edges of the structures are changed due to the wear of the flat surfaces between the structures (Figure 6.24). There were also wear tracks at the unstructured surface above the structures.

In the numerical model, temperature and pressure are set as 20 °C and 5 bar, respectively. Cavitation pressure is set as 0 kPa. Figure 6.25 shows the influence of wear. Cavitation are ratio is higher in the worn seal at low speeds, because the wear track at the unstructured surface leads to much more additional cavitation areas. With increasing speed, the additional cavitation areas disappear for both the unworn

and the worn seals. After this, the cavitation area ratio of the worn seal becomes lower than that of the unworn seal. Because the unstructured area between the structures of the worn seal is broader and thus inclined planes of the structures are shorter (Figure 6.24). Therefore, cavitation is restricted to a smaller zone (Figure 6.26).
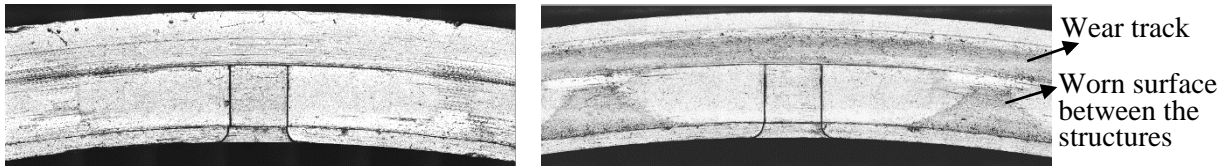
Figure 6.24: A structured seal surface before and after the long term friction tests are shown on the left and the right, respectively.
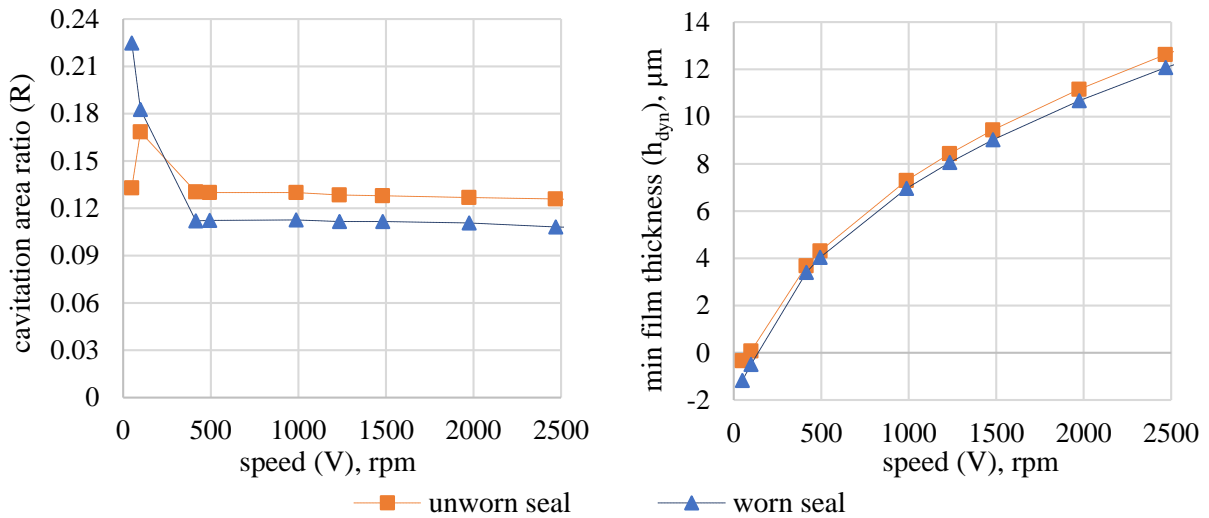
Figure 6.25: Influence of wear on cavitation area ratio and film thickness for the real geometry of a structured seal at 20 °C and 5 bar. Cavitation pressure is set as 0 kPa. Flow is CCW.

The minimum film thickness is slightly lower for the worn seal (Figure 6.25). This becomes more significant at high speeds. In the worn seal, the liquid is compressed in a smaller zone in the converging gap. Therefore the generated pressure is not as high as for the unworn seal (Figure 6.26). The smaller converging gap leads to a lower hydrodynamic film thickness.
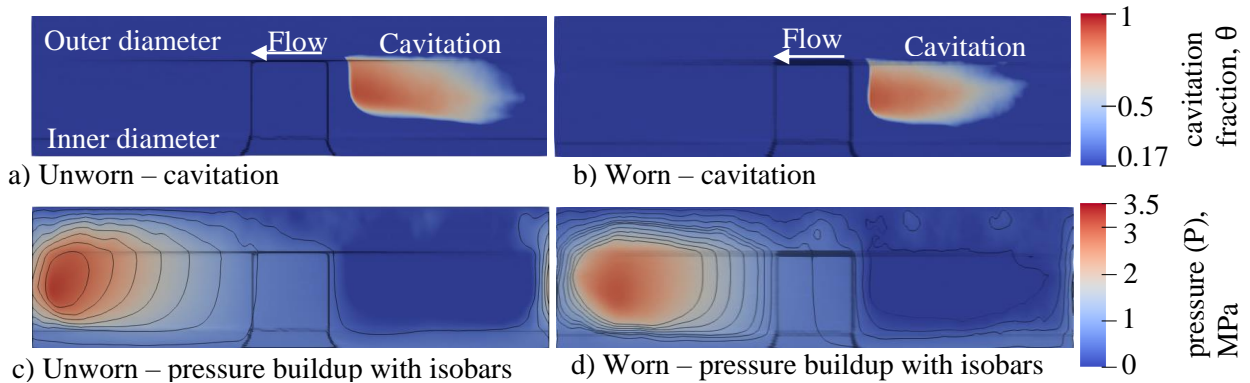
Figure 6.26: Influence of wear on cavitation morphology and pressure distribution at 1250 rpm, 20 °C and 5 bar. Numerical geometry is the real geometry of a structured seal. Cavitation pressure is set as 0 kPa.

6.2.1.9 INFLUENCE of ROUGHNESS

Figure 6.27 shows the pressure generation for a structured seals with macro (a) and micro irregularities (b) at 1250 rpm, 20°C and 5 bar. Cavitation pressure is set as 0 kPa. The simulations are made for constant gap heights. Overall pressure generation looks similar for both cases. The maximum pressure however seems to be slightly higher when taking micro irregularities into account.
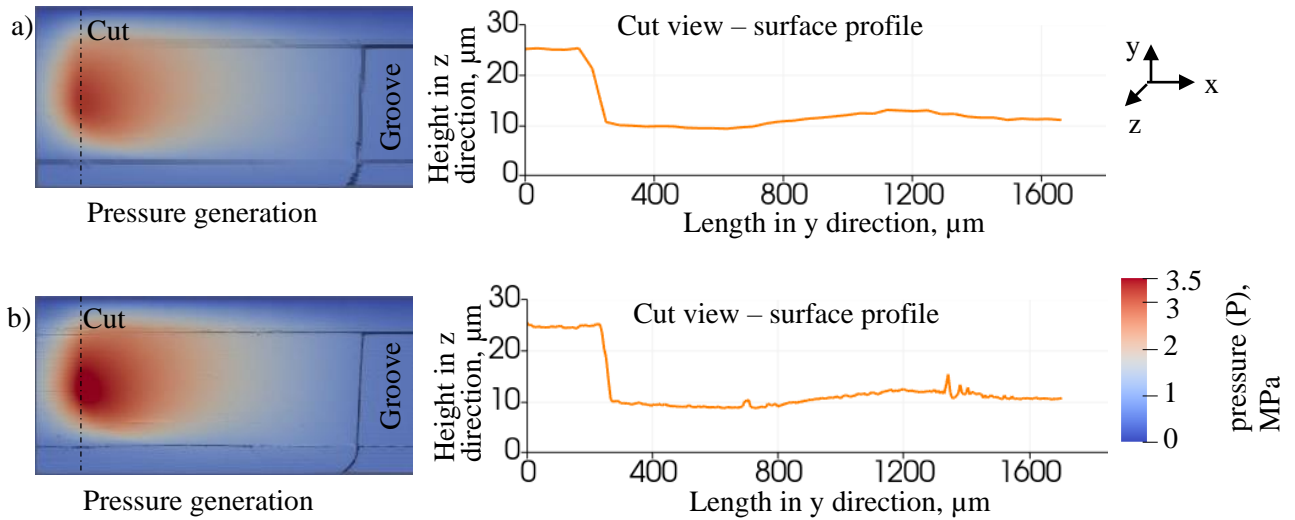
Figure 6.27: Pressure generation for a structured seals with macro (a) and micro irregularities (b) at 1250 rpm, 20°C and 5 bar. Cavitation pressure is set as 0 kPa.

At 1250 rpm, the influence of roughness on the lifting force (integrated pressure generated) is low for a high film thickness (Figure 6.28). However, the influence of roughness of roughness becomes more significant for lower film thicknesses. Here, it is assumed that the asperity peaks form micro sliding bearings leading to better distributed pressure generation.

When considering, thin films with roughness asperities an elastic treatment of the asperities seems necessary as micro-EHL may lead to significantly improved film generation. The first attempt of including roughness to the numerical model shows that further work in this area may explain the film formation in the areas of low film thickness more accurately. It should be noted that the necessary increased mesh sizes lead to a significantly higher computational time.
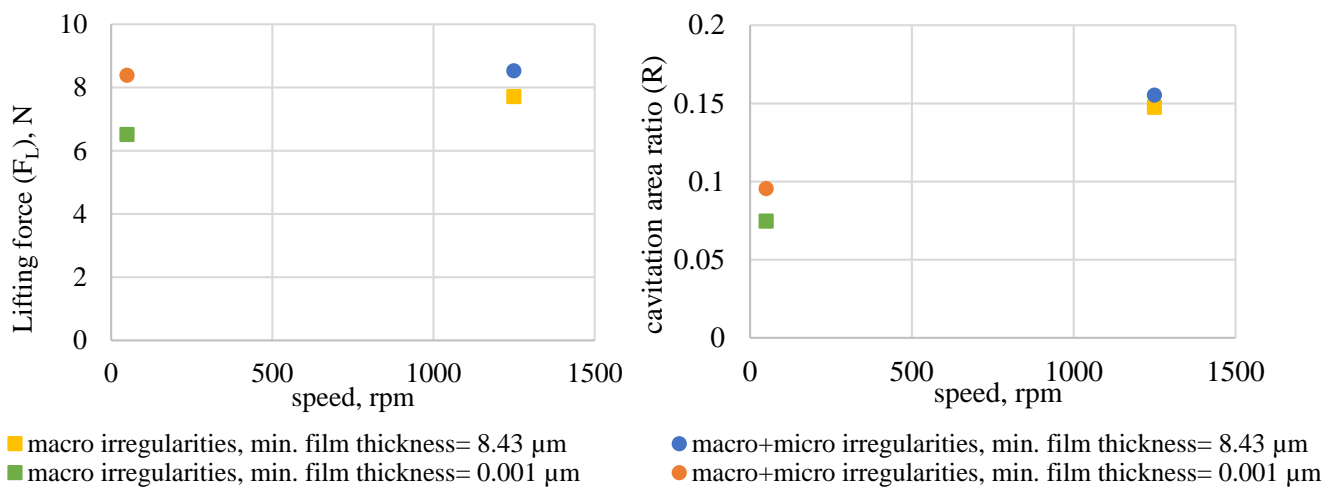
Figure 6.28: Calculated lifting forces and cavitation area ratios for a structured seals with macro and micro irregularities at 50 rpm, 1250 rpm, 20°C and 5 bar. Cavitation pressure is set as 0 kPa.

6.2.2 STANDARD SEALS

Figure 6.29 shows the pressure generation and cavitation formation for an unworn standard seal at 420 rpm, 20 °C and 5 bar. Cavitation pressure is set as 50 kPa since it is shown earlier that this might be the cavitation pressure during the optical tests. Cavitation zones are randomly distributed as in the optical tests. Cavitation seems to occur not because of the pores itself but rather the surface deviations due to the pores and the glass bubbles. Because, only some of the pores result a cavitation zone (Figure 6.30). Such cavitation zones are distributed to a large area and, they cover the pores completely. This fits the cavitation observation in the optical tests.

The cavitation zones are denser in the outer diameter direction. This is also observed in the experiments in a more significant manner and attributed to the radial tilt. The numerical results also show that the pressure is more concentrated in the inner diameter direction. Therefore, Pouseuille flow seems to push the cavitation zones outwards. This is because the surface is carried on the high peaks, which result in some entrainment paths for pressurized oil. This oil pushes the cavitation zones outwards.
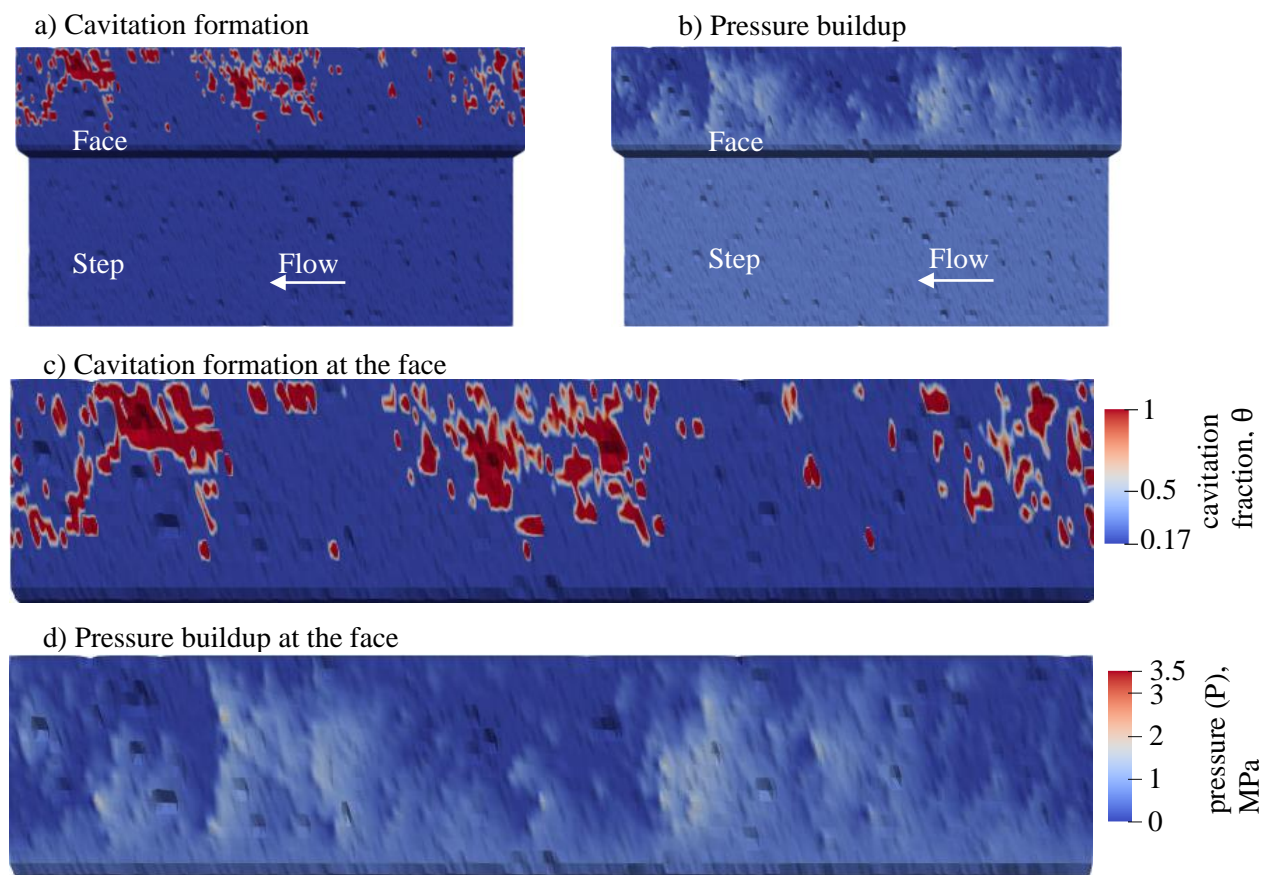
Figure 6.29: Cavitation formation and pressure generation for the standard seal at 420 rpm, 20 °C and 5 bar. Cavitation pressure is set as 50 kPa.
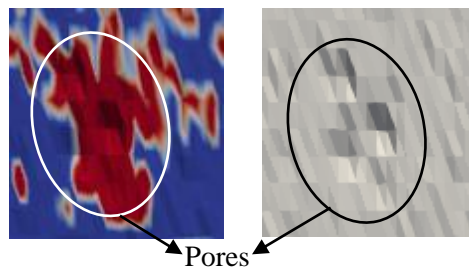
Figure 6.30: A detailed view of the cavitated zones with dimples. Speed, temperature and pressure are set as 420 rpm, 20 °C and 5 bar, respectively. Cavitation pressure is set as 50 kPa.

Figure 6.31 shows the numerically calculated film thicknesses and the cavitation area ratios for the standard seal. Temperature and pressure are set as 20 °C and 5 bar. Cavitation pressure (Pcav) is set as 0 kPa, 50 kPa and 90 kPa. The results show that there is no hydrodynamic film thickness under any conditions. The minimum film thickness has minus values. Because, the generated film pressure is not sufficient to separate the surface completely. Some high peaks are in contact and they should deform.

The selected temperature and pressure values are the lowest values used in the experiments. Therefore, it can be concluded that the micro-pores and other macro surface irregularities are not capable to generate a sufficient hydrodynamic film pressure during the experiments. It should be noted that these pores are not produced on purpose. They result due to the fillers (in this case glass bubbles). Therefore, they do not have an ideal dimple shape. This might influence the lubrication negatively. In addition, some glass bubbles stick out of the surface. They can also rupture the lubricant film. The experimental results also indicate that the standard seals do not operate in the full film lubrication. Therefore, the numerical results seem to be reasonable.
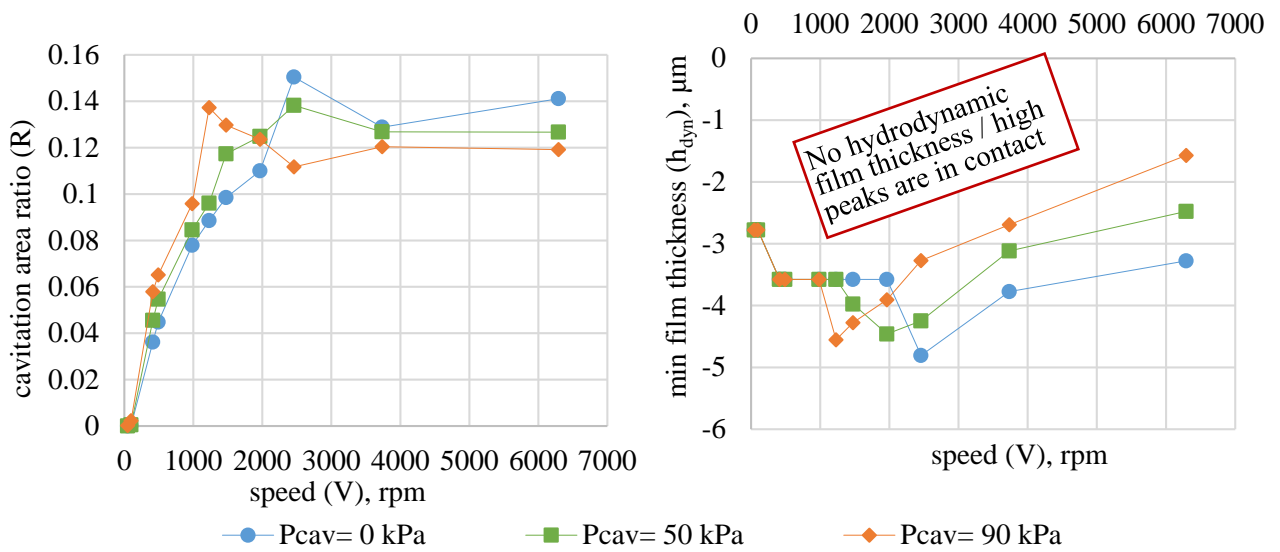
Figure 6.31: Numerically calculated film thickness and cavitation area ratio at various speeds for the standard seals. The model is real geometry of the standard seal. Temperature and pressure are set as 20 °C and 5 bar. Cavitation pressure (Pcav) is set as 0 kPa, 50 kPa and 90 kPa.

The calculated cavitation area ratio is almost 0 at 100 rpm for any cavitation pressure (Figure 6.31- Figure 6.32). For the similar conditions, the very low cavitation area ratio is only observed around the joint in the optical tests. The observed cavitation zones are much more in the region opposite of the joint in the tests. In order to investigate this, the minimum film thickness is increased. However, the cavitation area ratio decreases as the film thickness increases (Figure 6.32). Therefore, the film thickness is not very likely to be the reason of the low cavitation area ratio in the simulation. Another reason can be roughness. The numerical model does not include the roughness. For such thin films, roughness can result inter-asperity cavitation. Therefore, it might be necessary to include the roughness to calculate the cavitation area ratio accurately at thin films.
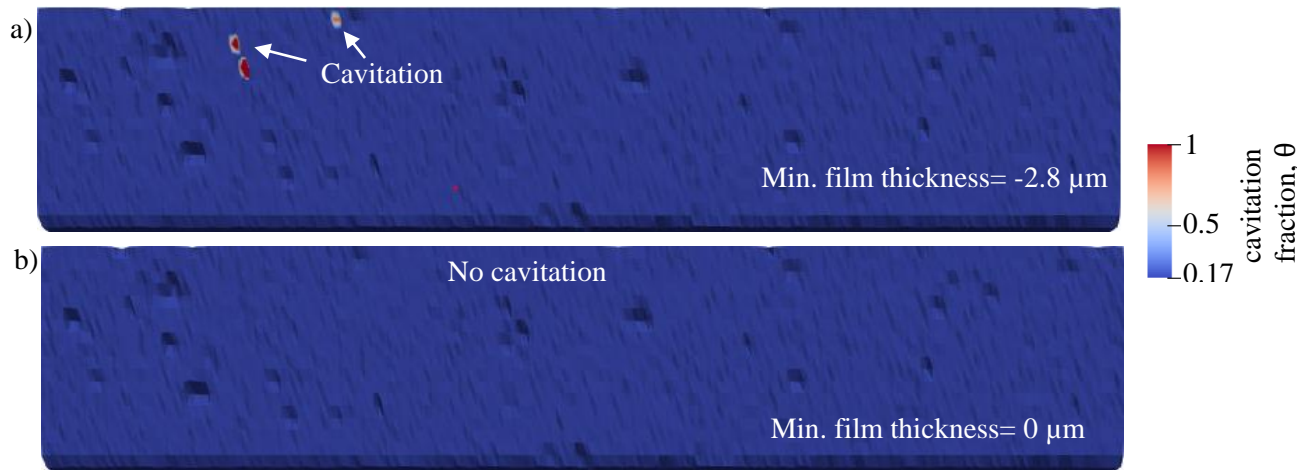
Figure 6.32: a) Cavitation formation for the numerically calculated film thickness via force balance method. b) Cavitation formation when the minimum gap height is set as 0 µm. Speed, temperature and pressure are set as 100 rpm, 20 °C and 5 bar, respectively. The numerical model is the real geometry of a standard seal. Cavitation pressure is set as 50 kPa.

6.2.2.1   *VALIDITY of the RESULTS of the STANDARD SEALS*

As described earlier, the unworn standard seals have some deep micro-pores on their surfaces. Therefore, validity of the Reydnolds equation in standard seals should be considered. Dobrica et al. [168] showed that the validity of the Reynolds equation depends on the Reynolds number (Re) and the texture aspect ratio (λ_{as}):

$$\mathrm{Re} = \frac{\rho\, u\, h_f}{\mu}, \quad \lambda_{as} = \frac{L_d}{h_D} \tag{6.7}$$

Here, h_D is dimple depth and, L_d is dimple length. h_f is land film thickness. When λ_{as} is sufficiently large and Re is sufficiently small, Reynolds equation can be used for the textured sliders (Figure 6.33). When the aspect ratio is smaller 10, the Reynolds model is inapplicable whatever the Reynolds number.

The aspect ratio of the dimples on the standard seal surfaces varies from 1.5 to 15. A considerable amount of pores has an aspect ratio around 2. Therefore, it should be considered that the Reynolds equation might be invalid for the standard seals. Although the simulation results seem to be plausible, further investigations are necessary.
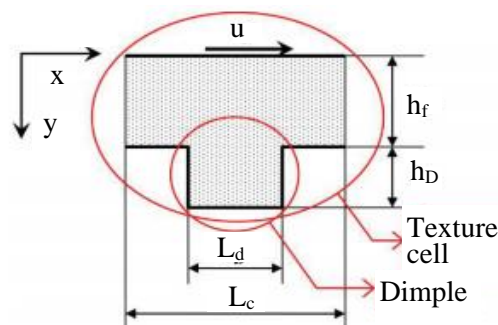
Figure 6.33: Elementary texture cell [168].

The worn standard seals have non-exploded glass bubbles protruding of the surface. The elevation of the glass bubbles is above the surface up to 16 µm. The simulation of such a surface is complex. Firstly, the seal will operate on the surfaces of the glass bubbles. The elastic properties of the standard seals might be different than the bulk material. Thus, the seal might be riding on the glass bubbles which in turn are in direct contact to the counterface, while the lubricant does not provide a real lifting effect. Modelling systems with greatly differing elastic moduli and solid contacts needs further investigations as well.

7 DISCUSSION and OUTLOOK

The film formation mechanism in parallel sliding contacts was investigated by considering cavitation. Therefore, a group of experiments and simulations were performed. Friction torque and contact temperatures were measured. Local contact temperatures were detected via thermography. Cavitation formation in the structured and the non-structured rectangular face seals was observed. The film thickness was measured via the LIF method. Hydrodynamic lubrication was modelled by implementing the mass conservative JFO cavitation model via an FBN algorithm. Modelling was performed by two methods; (1) by assuming the seal surface was smooth with a structure, (2) by directly using the manufactured seal surface with macro surface irregularities. Pressure generation, cavitation, and film thickness were calculated numerically for different operating conditions. The influences of structuring, macro and micro surface irregularities, waviness, radial taper, operating parameters and cavitation pressure were investigated. The main conclusions are:

- The experiments show that appropriate surface structuring can lead to reduction in friction and contact temperature. In the current project, the selected structures provide reduction in friction up to 30 %. Contact temperatures decrease significantly as well.
- The behavior of the non-textured seals seems to be dominated by surface roughness and the stochastically distributed micro-pores. These seals warm in patches on the flat surface.
- Cavitation is randomly distributed over the surface of the non-textured seals. It seems to occur due to surface asperities and fillers.
- For the non-textured seals, no considerable hydrodynamic pressure generation due to micro-pores is detected. Experiments also indicate that there is no sufficient lubricant film during the operation of the non-textured seals. However, elastic deformations and, the combined effect of roughness and the micro-pores should be investigated as well. Also, due to the aspect ratios of the micro-pores, the numerical model may need to be improved.
- The film formation and the thermal behavior of the structured seals is dominated by concentrating cavitation and pressure generation. Structured seals warm concentrated on the unstructured surface close to the cavitation zone. This seems to be mainly due to the design of the structures and cavitation formation.
- Cavitation occurs within the divergent zone of the structures. The cavitation area ratio increases rapidly with speed in the mixed lubrication regime. In the hydrodynamic regime, the change in cavitation becomes small. Both the film thickness and the cavitation area ratio decrease with increasing sump temperature and pressure. There is a strong correlation between lubricant film thickness and cavitation. Cavitation size can be utilized as a hint for the prediction of the lubrication regime.
- Depending on the application, appropriate surface structuring can generate a significant hydrodynamic lift without the support of other surface features such as waviness and roughness. In the present work, asymmetric film pressure due to cavitation formation leads to hydrodynamic pressure generation.
- The manufactured surfaces of the seals influence pressure generation and cavitation and thus, also the load carrying capacity. The consideration of macro surface irregularities is necessary to predict the global cavitation accurately. Surface irregularities result in realistic rupture and reformation boundaries of the cavitation zone. However, it seems that elastic deformation of the seal should be considered as well for a more precise prediction of cavitation morphology.
- For thin films, cavitation forms outside of the structure as well due to surface irregularities. This indicates that inter-asperity cavitation may be an influencing factor for thin films.
- Influence of roughness on lubricant pressure generation is low for thick films, here the macrogeometry dominates film formation. On the other hand, it can provide a contribution in the mixed/thin film lubrication regime. Further investigations seem useful for a better understanding of the mixed regime.

- In the presence of surface textures, the influence of waviness and radial taper may be low depending on the texture design and application. Waviness can still generate more significant effects compared to radial taper. However, these effects can also be negative depending on the influence of waviness on the textures.
- With increasing cavitation pressure, hydrodynamic film thickness increases while the cavitation area ratio decreases. The increase in film thickness is due to the contribution of the increasing cavitation pressure to the integrated pressure generation.
- Experimental and numerical results correlate well in hydrodynamic regime when realistic contact temperatures and realistic cavitation pressures are taken into account. The implemented cavitation algorithm [JFO + FBN] yields good results.

The work can still be improved in many areas. Firstly, some improvements are necessary to detect the elastic deformations of the seals via LIF method. This method has many advantages but also complications. One of the main problems is the light distribution and the laser speckles. In the current work, the influence of the speckles was minimized via calibration. Furthermore, the calibration is performed only for a small contact area to minimize the error in the measurements due to light differences. However, for a reliable determination of the elastic deformations, a bigger area should be investigated. Improvement of the test set-up can lead to a mapping of the bigger contact area. Consequently, elastic deformations can be investigated in more detail. Investigating a broad set of seal surfaces would also provide a better statistics and an understanding in elastic deformations.

The film thickness measurements of the non-textured seals are expected to have higher error since the calibration curve for the structured seals is used for the standard seals too. Due to the fast rotation of these seals, CCD camera might not be completely effective to record the fluorescence emission. An improved calibration method and test set-up can provide more reliable results for the non-textured seals.

Secondly, thermographic experiments provide a good insight for the local temperatures in the contact zone. However, in order to calculate the temperatures of the seal surface, some assumptions are made. One of them is neglecting the emissivity of the lubricant film. Although, a significant influence of the thin lubricant film is not expected, the emissivity of the lubricant film shall be investigated. Furthermore, a detailed work is necessary to detect the error in the measurements. This would provide a better understanding for future work.

Thirdly, although the surface features are tried to be covered as much as possible in the numerical model, the data of the scanned surfaces is always reduced due to computational challenges. Furthermore, the surface scanning tool may generate artificial surface features. These features should always be investigated carefully and removed. In the current work, dramatically high peaks (either artificial or real) were removed before simulations. Otherwise these peaks would initially generate a high gap in the numerical model. In addition, the scanning tool provides the position of the scanned surfaces in an undefined way. Therefore, the position of the scanned surfaces in relation to the counterface should be predicted and adjusted. However, this prediction is complicated.

In the numerical model, only one single structure is simulated. In practice, the sealing surface consists of more than one structures. Each structure would influence the boundary conditions of the next one. This might influence the film formation although it is not expected to be significant. However, it might be necessary to simulate the whole seal ring for the calculation of coefficient of friction. This is due to the non-uniform film distribution and randomly distributed surface features such as burrs and deviations form flatness.

There are some discrepancies between the numerical and the experimental results. This is due to the simulation of one section of the seals without considering waviness and radial tilt. In addition, the cavitation pressure during the operation is not known. The film thickness measurements might contain errors as stated earlier. However, the simulation and the experimental results are also compared via cavitation sizes which is more reliable than the film thicknesses. Waviness and radial tilt are shown to

be important to detect the cavitation morphology accurately. However, they are not influencing the quantitative results substantially. Cavitation pressure does influence the trend of the results in hydrodynamic regime. However, the detection of cavitation pressure experimentally can be an interesting future work.

The influence of surface roughness is investigated by modelling the manufactured surface. On one hand, it may be a reliable method to cover surface features in a realistic manner. On the other hand, it is not a sufficient method to simulate a broad range of operating conditions due to computational time. It is possible to apply mesh partitioning and simulate these sections simultaneously for time saving. However, this method causes more challenges. For instance, the gap height should be equal at the edges of a mesh where the periodic boundary conditions are applied leading to more complex pre-processing routines.

8 OTHER APPLICATIONS and FUTURE WORK

The experimental and the numerical approaches described in this thesis provide reliable results. Thus they can be used in different applications. Friction behaviour optimization of different machine elements can be done by optimizing the design, structuring or improving the micro surface features. It is possible to improve the current numerical method to implement it for EHL lubrication. In this final chapter, a different application which was analysed in the Institute of Machine Design and Tribology is described. Following, a future work which will enable an improvement of the numerical method is explained.

8.1 OPTIMIZATION of a ROTARY VANE PUMP via SURFACE TEXTURING

Rotary vane pumps are widely used in engineering applications such as supplying the oil to the internal combustion engine parts, refrigeration heating and air conditioning. These pumps basically have a cam, rotor and vanes (Figure 8.1). Vanes are capable to slide into and out of the rotor. They seal on all edges and generate fluid chambers. The rotor and the cam are designed in a way that the fluid chamber has different volumes. The increasing volume chambers are filled with the fluid which is driven by the inlet pressure (system pressure). With rotation the fluid is carried. As the volume of the chamber decreases, the fluid is driven out of the pump on the discharge side. In this project, the aim is to reduce the friction losses in this pumps via surface structuring. Structures are planned to be manufactured on the cam surface.
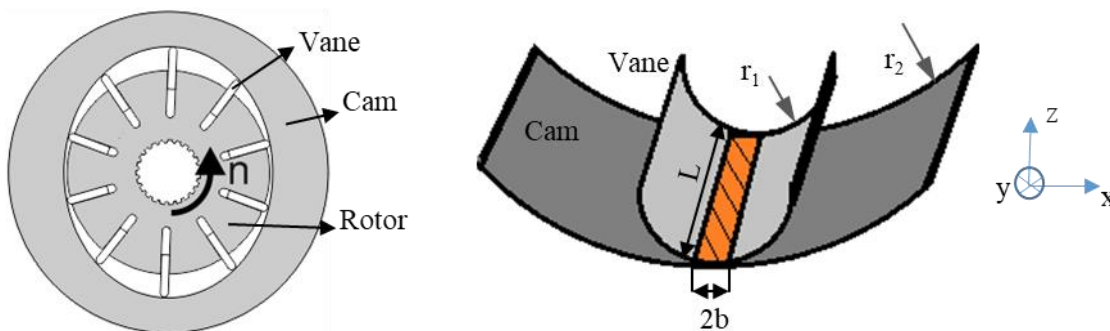

Figure 8.1: Left: a rotary vane pump. Right: the contact area between the vane and the cam.

The contact between the vane and the cam is a non-conformal contact. This is different than the macroscopically parallel contact concept. However, the selection of the structures can be performed via the simulation tools described in the current thesis.
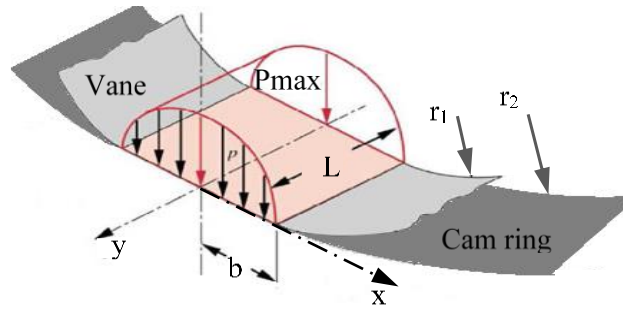
Figure 8.2: The cylindrical Hertzian contact and the pressure distribution between a vane and a cam [176].

8.1.1 CALCULATION of the CONTACT AREA

The contact area between the vane and the cam can be calculated by using the formulas for cylindrical Hertzian contacts (Figure 8.2):

$$b = 2\sqrt{\frac{2Fr}{\pi L E'}}, \qquad \frac{2}{E^1} = 1 - \frac{v_1^2}{E_1} + \frac{v_2^2}{E_2}, \qquad \frac{1}{r} = \frac{1}{r_1} + \frac{1}{r_2} \tag{8.1}$$

Here, F is the load acting on the contact. r_1, r_2 and r are the radiuses of the vane and the cam and the equivalent radius, respectively. E_1 and E_2 are the elastic modulus of the vane and the cam. E is the reduced elastic modulus. v_1 and v_2 are the Poisson's ratios of the vane and the cam. Here, the contact area is calculated as 42 µm for the maximum load conditions (22 bar and 9000 rpm).

8.1.2 SELECTION of the STRUCTURES

Dimple like structures are considered for the sake of manufacturing (Figure 8.3). The width of the structures (a) should be smaller than 42 µm to prevent the internal leakage. On the other hand, the length of the structures (l) can be longer. The pressure distribution can be manipulated by manufacturing asymmetrical structures. The density of the structures should not be too high as high density might cause a rupture of the lubricant film.
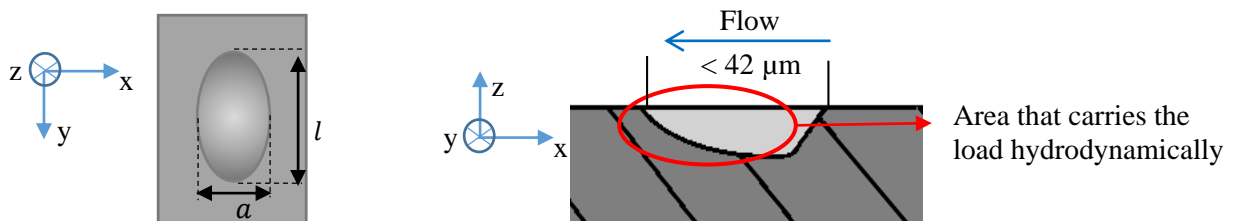
Figure 8.3: Features of the structures.

Figure 8.5 shows the numerically calculated pressure generation and cavitation for a dimple at 9000 rpm, 70 °C and 22 bar. The film thickness is set as 0.16 µm since it is the expected minimum film thickness under the given operating conditions. Cavitation pressure is set as 0 kPa. Pressure concentrates at the converging edge of the dimple. Cavitation covers more than half of the dimple. The structure features are varied and it is found that:

- The suggested structure depth is ≤ 5 µm.
- Elliptical structures lead to higher pressure generation than the circular structures.
- Hexagonally arranged structures (Figure 8.4) result in a higher pressure generation than the cubically arranged structures.
- Increasing the number of structures yields a rise in pressure generation.
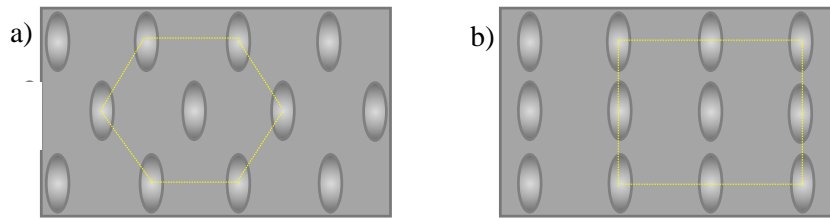
Figure 8.4: a) Hexagonally arranged structures. b) Cubically arranged structures.

The investigation of the distance between the structures, asymmetrical structures and the influence of the boundary conditions are still in process.
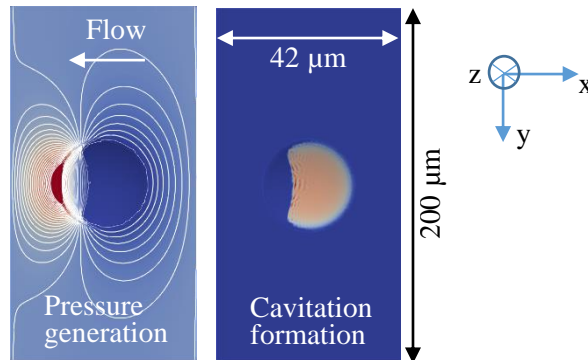
Figure 8.5: Pressure generation and cavitation in a dimple at 9000 rpm, 70 °C, 22 bar. The film thickness is set as 0.16 μm. Cavitation pressure is set as 0 kPa.

8.1.3 SIMULATION of a MANUFACTURED SURFACE with STRUCTURES

According to the first results, a structured cam is manufactured. One structure of the manufactured surface is scanned and modelled. Macro surface irregularities are included to the model. Roughness is not taken into account. Figure 8.6 shows the pressure generation at 9000 rpm, 70 °C and 22 bar. The film thickness is set as 0.1 μm. Cavitation pressure is set as 0 kPa (This is unrealistic as discussed earlier. However, an investigation is necessary to determine cavitation pressure for the system in this project.). Pressure concentrates at the edge of the converging half of the structure as in the dimple. There are randomly distributed high and low pressure zones over the unstructured areas due to the surface irregularities. However, there is no visible cavitation within the structure under these operating conditions. This seems to be due the properties of the manufactured surface.

The manufactured structure is not capable to produce sufficient lifting force at 9000 rpm, 70 °C and 22 bar (Figure 8.7) for 0 kPa cavitation pressure. However, the pressure generation starts to support a thin film at low pressures. This film may not be sufficient to separate the surfaces completely but the partial film lubrication can provide a decrease in friction. Higher cavitation pressures can generate higher load support. However, a cavitation pressure close to ambient pressure seems to be necessary to generate a considerable load support (see Chapter 6.2.1.5) when the ambient pressure is 22 bar. According to these results, structuring the cam at high pressure regions might not be useful. Instead, structuring the low pressure zones might provide benefits in the current application.
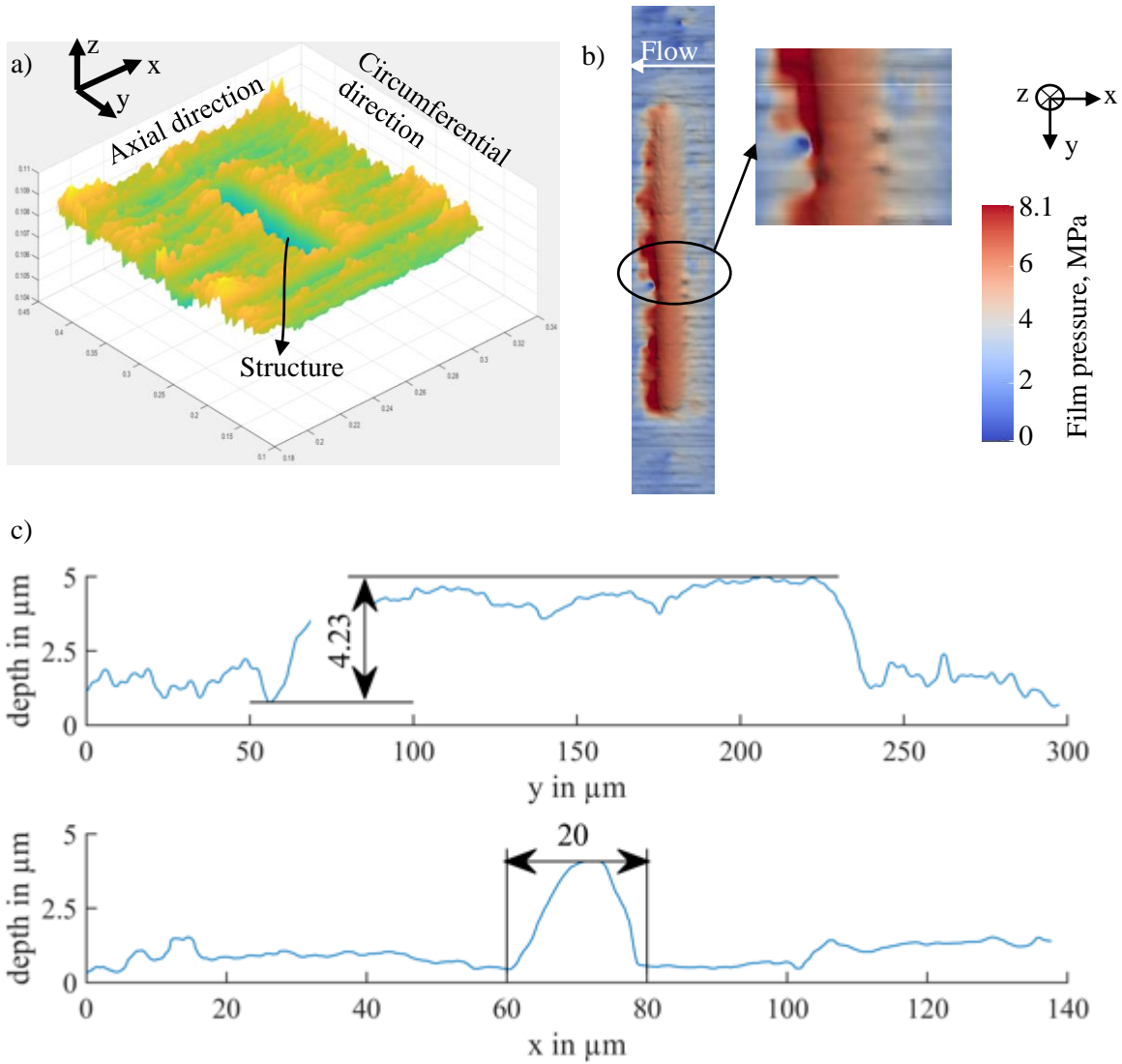
Figure 8.6: a) Manufactured cam surface with a structure. b) Pressure generation for a manufactured surface section with a structure at 9000 rpm, 70 °C and 22 bar. Film thickness is set as 0.1 μm. Cavitation pressure is set as 0 kPa. c) Profile of the manufactured structure.
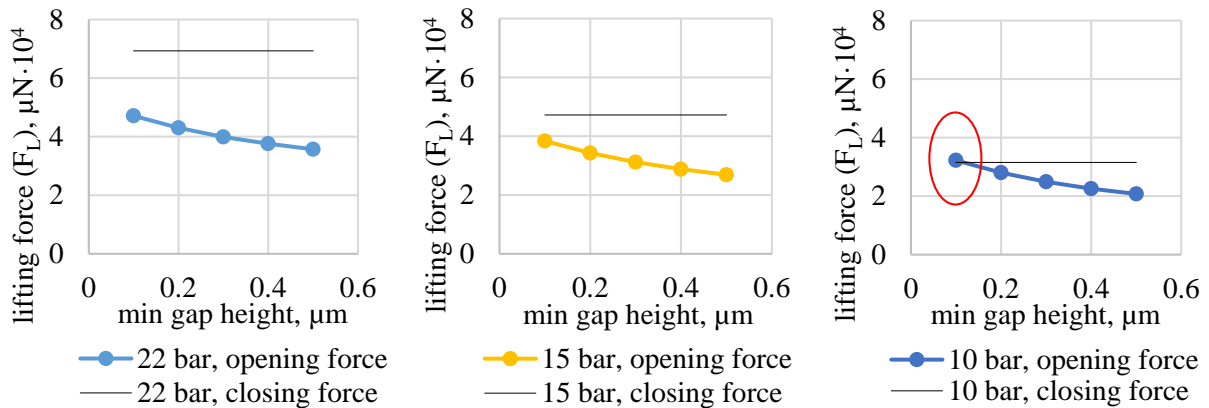

Figure 8.7: Pressure generation for a manufactured surface section with a structure at 9000 rpm, 70 °C and various operating pressures. Cavitation pressure is set as 0 kPa.

8.2 INFLUENCE of MICROSURFACE FEATURES on LUBRICATION of PARALLEL SLIDERS

A large number of tribologically stressed components are currently being manufactured from thermoplastics by injection moulding. The trend is increasing. The motivations are low manufacturing costs for large quantities, free design, low weight, and good damping properties that reduce vibrations and noise emissions. In addition, dry running without lubrication is possible within certain limits, which reduces the corresponding design effort. When selecting and developing thermoplastics, the filler and the process play an essential role. The primary aim is to increase strength, and secondarily to increase heat conduction and reduce friction when running dry. The possibilities of tribological optimization have not yet been fully utilised. In particular, the possibilities for the interaction of fillers and topography with regard to the tribology of lubricated systems have not yet been developed. Plain bearings, gears, seals, cages or joints with minimized or direction-dependent friction could be produced.

In the case of dry running, the mechanical properties of the thermoplastic and the counter-body play a dominant role. In the case of the presence of lubricant, in addition to the mechanical properties, macro-geometry and kinematics, the micro-geometry (roughness) and the lubricant properties determine whether, when and in what order of magnitude a lubricant film is built up. In the Institute of Machine Design and Tribology, it is planned to make and exploratory project to investigate the lubrication of the thermoplastics by focusing the micro surface features. For this reason, a preliminary work is performed with the injection moulded sample washers. These washers are made of PAI and contain fillers. Figure 8.8 shows the scanned surface of a washer. The randomly distributed fillers are visible. These fillers stick out of the surface and some dents are visible around the fillers.
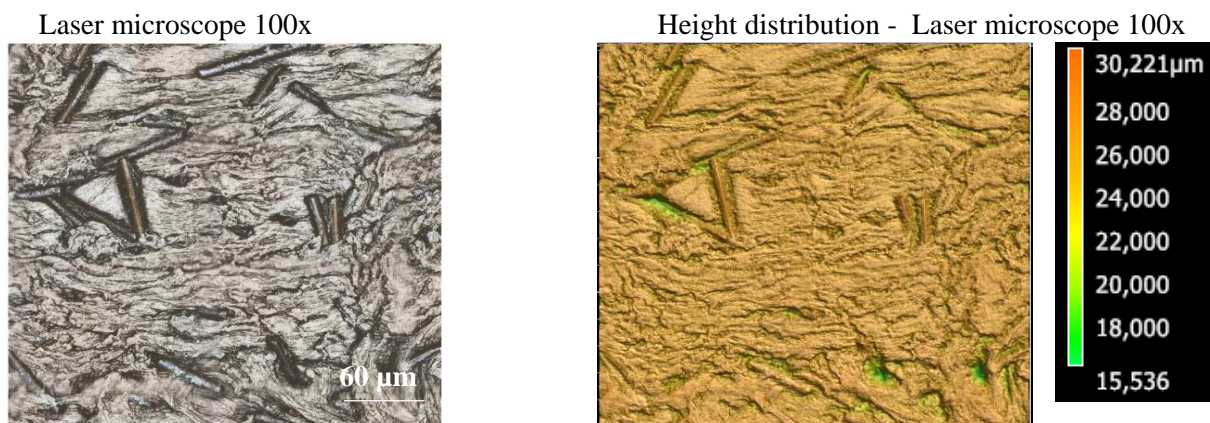
Figure 8.8: Left; scanned real surface of a washer made of PAI and fillers. Right; height distribution of the scanned surface.

For the preliminary work, a small piece from the scanned surface was selected to be meshed and simulated (Figure 8.9). The model has 4 boundary conditions. The boundary conditions 1 and 2 have application pressures. The boundary conditions in the flow direction are periodic boundaries. Currently, only the pressure generation and cavitation formation is calculated for a given minimum gap height without considering elastic deformations.
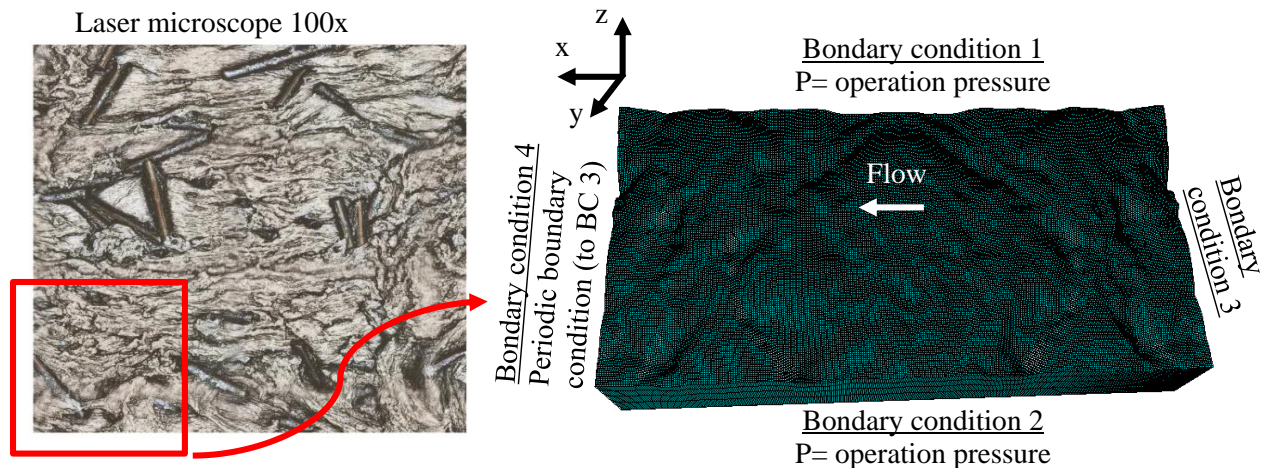
Figure 8.9: Left; the selected area of the scanned surface. Right; the numerical model of the selected area.

Figure 8.10 shows the results for the operational conditions 2,5 m/s, 20 °C and 5 bar. The minimum gap height is set as 0.5 µm. Pressure increases and makes peaks around the fillers. Cavitation is randomly distributed. It also forms generally around the fillers. The opening force which tries to separate the friction partners is calculated as 4340 µN while the closing force is 3164 µN. Since the opening force is bigger than the closing force, it is possible to say that the generated pressure at the contact by the fillers and the roughness is capable to generate a lift.
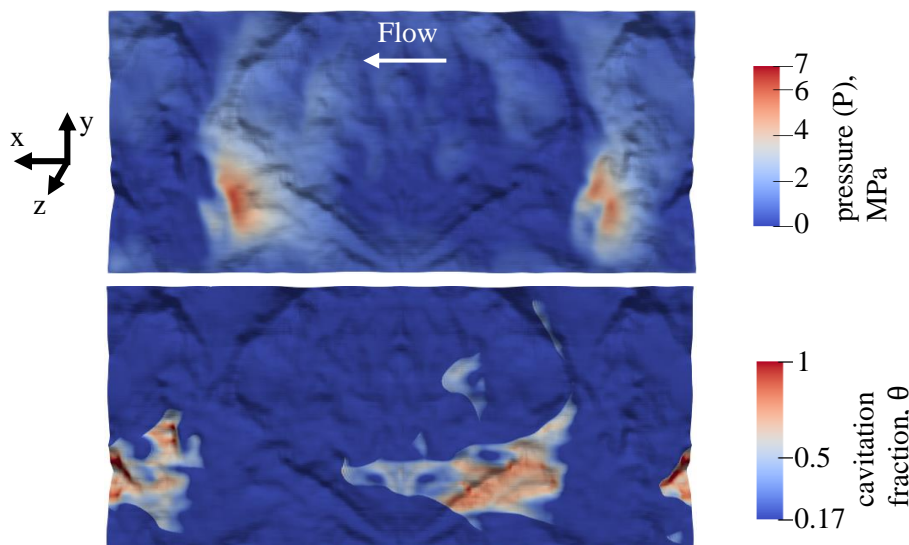
Figure 8.10: Pressure generation and cavitation formation due to micro surface irregularities.

Table 8.1 shows the generated opening forces under different conditions. Even though the elastic deformations are not included in the numerical model, the surface features are capable to produce a load support under many conditions. This load support might not separate the friction surfaces completely. However, it can generate a significant improvement on the friction behaviour.

The preliminary work raises some interesting questions such as:

- Can the scanned machine element surface be used in the simulations? Due to the scanning and the numerical limitations, just a section of the machine element can be scanned and simulated. Many researchers prefer to implement flow factors [177,178]. Is it possible to correlate the numerical results with the experimentally detected coefficient of friction behaviour of the friction pairs without implementing flow factors? If yes, what is the representative surface size?

- The bulk material and the fillers have different elastic properties. Can they be assumed as one body in the numerical approach for the simplicity?
- Do the micro surface features wear off to generate a self-optimization?

The aim in this work is to investigate these questions by using the numerical and the experimental approaches described in this thesis. By doing this, the numerical method in the current work will be extended to the elastohydrodynamic lubrication based on the work of Wennehorst [153]. He investigated soft-EHL contacts by assuming that the peaks of a soft material deform and a very thin film occurs between the peaks of the friction pair instead of pure solid-solid contact.

Table 8.1: The generated lift under different conditions. Green rows show the conditions at which the hydrodynamic lift is sufficient to separate the friction pairs while the red row shows the vice versa.

Speed, m/s	Pressure, bar	Temperature, °C	Viscosity, Pa·s	Min. gap height, µm	Opening force, µN	Closing force, µN
2,5	5	20	0,07	0,5	4340	3164
2,5	5	20	0,07	1	3550	3164
2,5	5	90	0,00734	0,5	3190	3164
2,5	15	20	0,07	0,5	7960	9492
2,5	15	20	0,07	0,1	10700	9492

9 BIBLIOGRAPHY

[1] Björling, M., 2014, "Friction in Elastohydrodynamic Lubrication," Doctoral Thesis, Luleå University of Technology, Department of Engineering Sciences and Mathematics.

[2] Sadeghi, F., 2010, "Elastohydrodynamic lubrication," Tribology and Dynamics of Engine and Powertrain, pp. 171e–226e. https://doi.org/10.1533/9781845699932.1.171

[3] Bader, N., 2018, "Traction in EHL-contacts - the influence of local fluid rheology and temperatures," Doctoral Thesis, IMKT, Hannover. https://doi.org/10.15488/4459

[4] Lyashenko, I.A., 2011, "Tribological properties of dry, fluid, and boundary friction," Tech. Phys. 56, 701. https://doi.org/10.1134/S1063784211050227

[5] Popova, E., Popov, V.L., 2015, "The research works of Coulomb and Amontons and generalized laws of friction," Friction 3, 183–190. https://doi.org/10.1007/s40544-015-0074-6

[6] Liu, H.C., 2020, "Traction prediction in rolling/sliding EHL contacts with reference fluids," Doctoral Thesis, IMKT, Hannover. https://doi.org/10.15488/10206

[7] Sayfidinov, K., Cezan, S.D., Baytekin, B., Baytekin, H.T., 2018, "Minimizing friction, wear, and energy losses by eliminating contact charging," Science Advances, vol. 4, no. 11, eaau3808 DOI: 10.1126/sciadv.aau3808

[8] Stribeck R. (1902) *Die wesentlischen Eigenschaften der Gleit- und Rollenlager*, Zeitschrift des Vereines deutscher Ingenieure; 46(37):1341-1348 (pt I) & 46(38):1432-1438 (pt II) & 46(39) 1463-1470 (pt III).

[9] Woydt, M., Wäsche, R., 2010, "The history of the Stribeck curve and ball bearing steels: The role of Adolf Martens," Wear; 268(11-12):1542-1546. https://doi.org/10.1016/j.wear.2010.02.015

[10]   Eklund, S., 2013, "Roughness effect on friction and wear of lubricated plain bearings," Master's Thesis, Luleå University of Technology, Department of Engineering Sciences and Mathematics.

[11]   Hersey, M.D., 1914, "The Laws of Lubrication of Horizontal Journal Bearings," Journal of the Washington Academy of Sciences, vol. 4, no. 19, pp. 542–552. JSTOR, www.jstor.org/stable/24520857.

[12]   Spikes, H.A., 1997, "Mixed lubrication – an overview," Lubrication Science, vol. 9, no:3, pp221-253. https://doi.org/10.1002/ls.3010090302

[13]   Zhang, Y., Biboulet, N., Venner, C.H., Lubrecht, A.A., 2020, "Prediction of the Stribeck curve under full-film Elastohydrodynamic Lubrication," Tribol. Int., vol. 149, 105569. https://doi.org/10.1016/j.triboint.2019.01.028

[14]   Cann, P., Ioannides, E., Jacobson, B., Lubrecht A.A., 1994, "The lambda ratio – a critical reexamination," Wear;175(1–2):177–88. https://doi.org/10.1016/0043-1648(94)90181-3

[15]   Venner, C.H., Lubrecht A.A., 1999, "Amplitude reduction of non-isotropic harmonic patterns in circular EHL contacts, under pure rolling," Tribol;36:151–62. https://doi.org/10.1016/S0167-8922(99)80037-6

[16]   Schipper, D.J., 1988, "Transitions in the lubrication of concentrated contacts," PhD Thesis, University of Twente.

[17]   Halling J. (1978) Hydrodynamic Lubrication. In: Halling J. (eds) Principles of Tribology. Palgrave, London. https://doi.org/10.1007/978-1-349-04138-1_10

[18]   Khonsari MM. (2008) Applied tribology: bearing design and lubrication. 2nd ed. Chicester, England: Wiley. DOI:10.1002/9781118700280

[19]   Dadouche A., DeCamillo S.M., Fillon M. (2013) Hydrodynamic Tilting-Pad Thrust Bearings. In: Wang Q.J., Chung YW. (eds) Encyclopedia of Tribology. Springer, Boston, MA. https://doi.org/10.1007/978-0-387-92897-5_49

[20]   Yun L., Bliault A., Doo J., (2010) WIG Craft and Ekranoplan: Ground Effect Craft Technology. Springer-Verlag US. DOI: 10.1007/978-1-4419-0042-5

[21]   Reynolds, O., 1886, "On the theory of lubrication and its application to Mr. Beauchamp Tower's experiments, including an experimental determination of the viscosity of olive oil, " Philos. Trans. R. Soc. London 177, 157-234. http://doi.org/10.1098/rstl.1886.0005

[22]   Wen S., Huang P., (2017) Basic Theories of Hydrodynamic Lubrication. Principles of Tribology, 2nd ed. https://doi.org/10.1002/9781119214908.ch2

[23]   Profito, F.J., 2015, "On the development of advanced techniques for mixed-elastohydrodynamic lubrication modelling of journal and sliding bearing systems," Doctoral Thesis, University of Sao Paulo. DOI: 10.13140/RG.2.1.2383.6249

[24]   Hamrock B.J., Schmid S. R. (1991) Fundamentals of Fluid Film. CRC Press, 2nd ed.

[25]   Concli, F., 2016, "Pressure distribution in small hydrodynamic journal bearings considering cavitation: a numerical approach based on the open-source CFD code OpenFOAM®," John Wiley & Sons, Ltd., vol. 28, no 6, pp 329-347. https://doi.org/10.1002/ls.1334

[26]   Braun, M.J., Hannon, W.M., 2013, "Cavitation Formation and Modeling," In: Wang Q.J., Chung YW. (eds) Encyclopedia of Tribology. Springer, Boston, MA. https://doi.org/10.1007/978-0-387-92897-5_29

[27]   Dowson, D. and Taylor, C.M., 1979, "Cavitation in bearings," Ann. Rev. of Fluid Mech., 11, 35-66. DOI: 10.1146/annurev.fl.11.010179.000343

[28]   Sun, D.C., Brewe, D.E., and Abel, P.B., 1993, "Simultaneous Pressure Measurement and High-Speed Photography Study of Cavitation in a Dynamically Loaded Journal Bearing," ASME. J. Tribol. 115(1): 88-95. https://doi.org/10.1115/1.2920991

[29]   Heshmat, H., 1991, "The Mechanism of Cavitation in Hydrodynamic Lubrication," Tribol. Trans., 34, No. 2, pp. 177–186. https://doi.org/10.1080/10402009108982025

[30]   Braun, M.J. and Hendricks, R.C., 1984, "An Experimental Investigation of the Vaporous/Gaseous Cavity Characteristics of an Eccentric Journal Bearing," ASLE Transactions, 27:1, 1-14. https://doi.org/10.1080/05698198408981539

[31]   Findlay, J.A., 1968, "Cavitation in Mechanical Face Seals," ASME. J. of Lubrication Tech., 356–364. https://doi.org/10.1115/1.3601569

[32]   Harp, S.R. and Salant, R.F., 2002, "Inter-asperity Cavitation and Global Cavitation in Seals: An Average Flow Analysis," Tribol. Int., 35, pp 113-121. https://doi.org/10.1016/S0301-679X(01)00103-7

[33]   Brunetière, N., Tournerie, B., 2012, "Numerical analysis of a surface-textured mechanical seal operating in mixed lubrication regime," Tribology International, 49, pp. 80-89. https://doi.org/10.1016/j.triboint.2012.01.003

[34]   Liu, T., Chen, H.l., Liu, Y.H., Wang, Q., Liu, Z.B. and Hou, D.H., 2012, "Study on cavitation effect of mechanical seals with laser-textured porous surface," IOP Conf. Ser.: Earth Environ. Sci. 15 072021. https://doi.org/10.1088/1755-1315/15/7/072021

[35]   Hirayama, T., Sakurai, T., and Yabe, H., 2004, "A Theoretical Analysis Considering Cavitation Occurrence in Oil-Lubricated Spiral-Grooved Journal Bearings with Experimental Verification," ASME. J. Tribol., 126(3): 490-498. https://doi.org/10.1115/1.1691436

[36]   Yagi, K., Sato, H., Sugimura J., 2015, "On the Magnitude of Load Carrying Capacity of Textured Surfaces in Hydrodynamic Lubrication," Tribology Online, vol. 10, No. 3, pp 232-245. https://doi.org/10.2474/trol.10.232

[37]   Gumbel L., 1914, "Monatsblatter Berlin Bezirksver," Verein Deutscher Ingenieure, p5.

[38]   Stieber, W., 1933, "Des Schwimmlager: hydrodinamische Theorie des Gleitlagers, " VDI-Verlag, GmbH.

[39]   Swift, H.W., 1932, "The stability of lubricating films in journal bearings," in: Minutes of the Proceedings of the Institution of Civil Engineers, vol. 233, Thomas Telford-ICE Virtual Library, pp. 267-288. https://doi.org/10.1680/imotp.1932.13239

[40]   Floberg, L., 1973, "On journal bearing lubrication considering the tensile strength of the liquid lubricant," in Transactions of the Machine Elements Division, Lund Technical University, Lund, Sweden, 1973, p. 1–26.

[41]   Brewe, D.E., 1986, "Theoretical Modeling of the Vapor Cavitation in Dynamically Loaded Journal Bearings," ASME. J. Tribol.; 108(4): 628–637. https://doi.org/10.1115/1.3261288

[42]   Brewe, D.E., Ball, J.H., and Khonsari, M.M., 1988, "Current research in cavitating fluid films," in Proceedings of the Cavitation Symposium, STLE Annual Meeting, NASA TM-103184, pp. 25–26.

[43]   Jakobsson, B., and Floberg, L., 1957, "The Finite Journal Bearing Considering Vaporization," Transactions of Chalmers University of Technology, Gothenburg, Sweden, Report No. 190.

[44]   Olsson, K. O., 1965, "Cavitation in Dynamically Loaded Bearing," Transactions of Chalmers University of Technology, Gothenburg, Sweden, Report No. 380.

[45]   Vaidyanathan, K., and Keith Jr. T.G., 1991, "Performance Characteristics of Cavitated Noncircular Journal Bearings in the Turbulent Flow Regime," Tribology Transactions, 34:1, 35-44, DOI: 10.1080/10402009108982006

[46]   Qiu, Y., and Khonsari, M.M., 2009, "On the Prediction of Cavitation in Dimples Using a Mass-Conservative Algorithm," ASME. J. Tribol., 131(4): 041702. https://doi.org/10.1115/1.3176994.

[47]   Zhang, J., Meng, Y., 2012, "Direct Observation of Cavitation Phenomenon and Hydrodynamic Lubrication Analysis of Textured Surfaces," Tribol Lett 46, 147-158. https://doi.org/10.1007/s11249-012-9935-6

[48]   Elrod, H.G., 1981, "A Cavitation Algorithm," ASME. J. of Lubrication Tech. July 1981; 103(3): 350–354. https://doi.org/10.1115/1.3251669

[49]   Elrod, H. G., Adams, M. L., 1974, "A computer program for cavitation and starvation problems," in Cavitation and related phenomena in lubrication, Mechanical Engineering Publications Ltd, London, UK.

[50]   San Andres, Luis (2009). Notes 06. Liquid cavitation in fluid film bearings. Available electronically from https : / /hdl .handle .net /1969 .1 /93246

[51]   Bara, R.J., 2004, "Rupture point movement in journal bearings," Doctoral Thesis, Worcester Polytechnic Institute.

[52]   Bayada, G., Chambat, M., and El Alaoui, M., 1990, "Variational Formulations and Finite Element Algorithms for Cavitation Problems." ASME. J. Tribol. April 1990; 112(2): 398–403. https://doi.org/10.1115/1.2920270

[53]   Vijayaraghavan, D. and Keith, T.G., Jr., 1990 "An Efficient, Robust, and Time Accurate Numerical Scheme to a Cavitation Algorithm," Journal of Lubrication Technology, vol. 112, pp. 44-51. https://doi.org/10.1115/1.2920229

[54]   Giacopini, M., Fowell, M.T., Dini, D., Strozzi, A., 2010, "A mass-conserving complementarity formulation to study lubricant films in the presence of cavitation," J. Tribol. T. ASME 132. https://doi.org/10.1115/1.4002215

[55]   Bertocchi, L., Dini, D., Giacopini, M., Fowell, M.T., Baldini, A., 2013, "Fluid film lubrication in the presence of cavitation: a mass-conserving two-dimensional formulation for compressible, piezoviscous and non-Newtonian fluids," Tribol. Int. 67, 61-71. https://doi.org/10.1016/j.triboint.2013.05.018

[56]   Biancofiore, L., Giacopini, M., Dini, D., 2019, "Interplay between wall slip and cavitation: A complementary variable approach," Tribology International, vol. 137, pp 324-339. https://doi.org/10.1016/j.triboint.2019.04.040

[57]   Woloszynski, T., Podsiadlo, P., Stachowiak, G. W., 2015, "Efficient Solution to the Cavitation Problem in Hydrodynamic Lubrication," Tribol Lett 58, 18. https://doi.org/10.1007/s11249-015-0487-4

[58]   Biboulet N, Lubrecht A.A., 2018, "Efficient solver implementation for Reynolds equation with mass-conserving cavitation," Tribology International; 118: 295-300. https://doi.org/10.1016/j.triboint.2017.10.008

[59]   Gu, C., Meng, X., Zhang, D., Xie, Y., 2017, "A transient analysis of the textured journal bearing considering micro and macro cavitation during an engine cycle," Proceedings of the Institution of Mechanical Engineers, Part J: Journal of Engineering Tribology, 231(10), 1289–1306. https://doi.org/10.1177/1350650117692721

[60]   Hu, Y., Meng, X., Xie, Y., 2017, "A computationally efficient mass-conservation-based, two-scale approach to modeling cylinder liner topography changes during running-in," Wear, vol. 386-387, pp 139-156. https://doi.org/10.1016/j.wear.2017.06.014

[61]   Hu, Y., Meng, X., Xie, Y., 2018, "A new efficient flow continuity lubrication model for the piston ring-pack with consideration of oil storage of the cross-hatched texture," Tribology International, vol. 119, pp 443-463. https://doi.org/10.1016/j.triboint.2017.11.027

[62]   Gu, Y., Meng, X., Xie, Y., Zhang, D., 2016, "Mixed lubrication problems in the presence of textures: An efficient solution to the cavitation problem with consideration of roughness effects," Tribology International, vol. 103, pp 516-528. https://doi.org/10.1016/j.triboint.2016.08.005

[63]   Fogg, A., 1946, "Fluid Film Lubrication of Parallel Thrust Surfaces," Proceedings of the Institution of Mechanical Engineers, 155(1), pp. 49–67. doi:10.1243/PIME_PROC_1946_155_011_02.

[64]   Summers-Smith, D., 1961, "Laboratory investigation of the performance of a radial face seal," in: BHRA (ed.) 1st International Conference on Fluid Sealing, paper D1. BHRA, Ashford, UK.

[65]   Henry Y., Bouyer J., Fillon M., 2014, "An experimental analysis of the hydrodynamic contribution of textured thrust bearings during steady-state operation: A comparison with the untextured parallel surface configuration", Journal of Engineering Tribology, vol 229, pp 362-375. https://doi.org/10.1177/1350650114537484

[66]   Charitopoulos, A., Fillon, M., Papadopoulos, C. I., 2020, "Numerical investigation of parallel and quasi-parallel slider bearings operating under ThermoElastoHydroDynamic (TEHD) regime", Tribology International, 149, pp.105517. https://doi.org/10.1016/j.triboint.2018.12.017

[67]   Hailing, J., (1975) Principles of Tribology. Macmillan Press Ltd., London and Basingstoke.

[68]   Yang P., Kaneta M., 2013, "Thermal Wedge in Lubrication," in: Wang Q.J., Chung YW. (eds) Encyclopedia of Tribology. Springer, Boston, MA. https://doi.org/10.1007/978-0-387-92897-5_161

[69]   Cameron, A., (1966) The principles of lubrication. Longman, London, pp. 144–149.

[70]   Lebeck, A., 1987, "Parallel sliding load support in the mixed friction regime. part 2 – evaluations of the mechanisms," Journal of Tribology109(1), 196–205. https://doi.org/10.1115/1.3261319

[71]   Kneizys, F.X., Anderson, G.P., Shettle, E. P., Gallery, W.O., Abreu, L.W., Selby, J.E.A., Chetwynd, J.H. and Clough S.A. (1988) Users Guide to LOWTRAN 7. Environmental Research Papers, No. 1010 AFGL-TR-88-04 77. Air Force Geophysics Laboratory.

[72]   Orcutt, F.K., Bell, J. C, Glaeser, W.A., and Allen, C.M., 1962, "Summary Report on the Dynamic Behavior of High Speed Liquid Lubricated Face Seals to the Rotary Shaft Seal Research Group," Battelle Memorial Institute, Columbus, Ohio.

[73]   N.B., Naduvinamani, N.B, Siddangouda, A., 2007, "Effect of surface roughness on the hydrodynamic lubrication of porous step-slider bearings with couple stress fluids," Tribology International, vol. 40, no 5, 780-793. https://doi.org/10.1016/j.triboint.2006.07.003

[74]   Sahlin, F., 2005, "Hydrodynamic lubrication of rough surfaces," Doctoral Thesis, Luleå University of Technology, Department of Applied Physics and Mechanical Engineering.

[75]   Minet, C., Brunetière, N., and Tournerie, B., 2011, "A Deterministic Mixed Lubrication Model for Mechanical Seals," ASME. J. Tribol. October 2011; 133(4): 042203. https://doi.org/10.1115/1.4005068

[76]   Brunetière, N., Francisco, A., 2019, "Lubrication mechanisms between parallel rough surfaces," Tribology Letters 67(4):116. DOI: 10.1007/s11249-019-1228-xT

[77]   Wennehorst, B., and Poll, G., 2017, "Soft micro-elastohydrodynamic lubrication and friction at rough conformal contacts," Proceedings of the Institution of Mechanical Engineers, Part J: Journal of Engineering Tribology, 231(3), 302–315. https://doi.org/10.1177/1350650114558322

[78]   Kashinath, B., 2012, "Squeeze Film Lubrication between Parallel Stepped Plates with Couplestress Fluids," International Journal of Statistika and Mathematika, Vol. 3, no:2, pp 65-69.

[79]   Shin, JH., Kim, KW., 2013, "Effect of surface non-flatness on the lubrication characteristics in the valve part of a swash-plate teype axial piston pump," Meccanica 49, 1275–1295 (2014). https://doi.org/10.1007/s11012-014-9893-1

[80]   Gronitzki, M., 2006, "Untersuchungen zur Funktion und Auslegung von Rechteckdichtringen für Drehdurchführungen," Doctoral Thesis, Universität Hannover.

[81]   Schüller, M., 2017, "Optimierung und Reibungsreduzierung von Drehdurchführungen," Forschungsheft 1207 der Forschungsvereinigung Antriebstechnik e.V.

[82]   Kuroki, T., Abe, Y., and Sowa, M. 1992, "Durability Upgrading and frictional torque lowering of the seal ring used for automatic transmissions," SAE paper 920720. https://doi.org/10.4271/920720.

[83]   Gronitzki, M., Poll, G.W.G., 2007, "Optimization of the tribological performance of rectangular seals in automotive transmissions," in: Proceedings of the Institution of Mechanical Engineers, Part J: Journal of Engineering Tribology 221 (2007), Nr. 3, S. 259-270. https://doi.org/10.1243/13506501JET247

[84]   Lubbinge H., 1999, "On the lubrication of mechanical face seals," PhD Thesis, University of Twente, Twente, The Netherlands.

[85]   Young, L.A., and Lebeck, A.O., 1982, "Experimental Evaluation of a Mixed Friction Hydrostatic Mechanical Face Seal Model Considering Radial Taper, Thermal Taper, and Wear," ASME. J. of Lubrication Tech. October 1982; 104(4): 439-447. https://doi.org/10.1115/1.3253244

[86]   Etsion, I., 1978, "Nonaxisymmetric Incompressible Hydrostatic Pressure Effects in Radial Face Seals," ASME. J. of Lubrication Tech. July 1978; 100(3): 379-383. https://doi.org/10.1115/1.3453190

[87]   Lebeck, A.O. (1991) Principles and Design of Mechanical Face Seals. Wiley-Interscience Publication.

[88]   Minet, C., Brunetiere, N., Tournerie B., Fribourg, D., 2010, "Analysis and Modeling of the Topography of Mechanical Seal Faces," Tribology Transactions, 53:6, 799-815. https://doi.org/10.1080/10402004.2010.487294

[89]   Ruddy, A. V., Dowson, D. and Taylor, C. M, 1982, "The Prediction of Film Thickness in a Mechanical Face Seal with Circumferential Waviness on both the Face and the Seat," Journal Mechanical Engineering Science, Vol. 24, No. 1, pp. 37–43. https://doi.org/10.1243/JMES_JOUR_1982_024_008_02

[90]   Liu, W., Liu, L., Wang Y., Peng, X., 2011, "Parametric Study on a Wavy-Tilt-Dam Mechanical Face Seal in Reactor Coolant Pumps," Tribology Transactions, 54:6, 878-886. https://doi.org/10.1080/10402004.2011.611325

[91]   Stanghan-Batch, B., Iny, E.H., 1973, "A Hydrodynamic Theory of Radial-Face Mechanical Seals," Journal of Mechanical Engineering Science, 15(1), 17-24. https://doi.org/10.1243/JMES_JOUR_1973_015_005_02

[92]   Cochain, J., Brunetière, N., Parry, A., Denoix, H., & Maoui, A., 2020, "Experimental and numerical study of wavy mechanical face seals operating under pressure inversions," Proceedings of the Institution of Mechanical Engineers, Part J: Journal of Engineering Tribology, 234(2), 247-260. https://doi.org/10.1177/1350650119862696

[93]   Lebeck, A.O., Teale, J.L., and Pierce, R.E., 1978, "Hydrodynamic Lubrication and Wear in Wavy Contacting Face Seals," ASME. J. of Lubrication Tech. January 1978; 100(1): 81–90. https://doi.org/10.1115/1.3453120

[94]   Etsion, I., Burstein, L., 1996, "A Model for Mechanical Seals with Regular Microsurface Structure," Tribology Transactions 39(3):677-683. https://doi.org/10.1080/10402009608983582

[95]   Tala-Ighil, N. and Fillon, M., 2015, "Surface texturing effect comparative analysis in the hydrodynamic journal bearings," Mechanics & Industry, vol. 16, no 3. https://doi.org/10.1051/meca/2015001

[96]   Watanabe, K., Seki, K., Tadano, H., Kaiser, F., 2017, "A Study on the Friction Reduction of Seal Ring for Automatic Transmission by Applying Surface Texture," Tribology Online 12(3):151-154. https://doi.org/10.2474/trol.12.151

[97]   Brizmer, V., Kligerman, Y., Etsion, I., 2003, "A Laser Surface Textured Parallel Thrust Bearing," Tribology Transactions, 46:3, 397-403. https://doi.org/10.1080/10402000308982643

[98]   Qiu, Y., Khonsari, M., 2011, "Investigation of tribological behaviors of annular rings with spiral groove," Tribology International, 44, 1610-1619. https://doi.org/10.1016/j.triboint.2011.05.008

[99]   Kakehi, K., Kondou, T., Ishii, T., Yoshino, M., 2013, "Development of Low Torque Seal Ring for Automotive Transmission," NTN Technical Review No.81.

[100]   Tønder, K., 2001, "Inlet Roughness Tribodevices: Dynamic Coefficients and Leakage," Tribol. Int., 37, pp. 137 – 142. https://doi.org/10.1016/S0301-679X(01)00084-6

[101]   Fowell, M., Olver, A. V., Gosman, A. D., Spikes, H. A., and Pegg, I., 2006, "Entrainment and Inlet Suction: Two Mechanisms of Hydrodynamic Lubrication in Textured Bearings," ASME. J. Tribol. April 2007; 129(2): 336–347. https://doi.org/10.1115/1.254008

[102]   Vladescu, S.C., Olver, A.V., Pegg, I.G., Reddyhoff, T., 2015, "The effects of surface texture in reciprocating contacts – An experimental study," Tribol. Int., 82, Part A, pp. 28-42. https://doi.org/10.1016/j.triboint.2014.09.015

[103]   Dwyer-Joyce R.S., Drinkwater B.W. and Donohoe C.J., 2003, "The measurement of lubricant–film thickness using ultrasound," Proc. R. Soc. Lond. A.459957–976. http://doi.org/10.1098/rspa.2002.1018

[104]   Dorinson, A., Ludema, K.C., 1985, "Measurement of Fluid Film Thickness and Detection of Film Failure," in Tribology Series, vol. 9, 109-133. https://doi.org/10.1016/S0167-8922(08)70845-9

[105]   Clarke, A., Weeks, I.J.J., Evans, H.P., and Snidle, R.W., 2016, "An Investigation into Mixed Lubrication Conditions Using Electrical Contact Resistance Techniques," Tribology International, 93, pp 709–716. DOI: 10.1016/j.triboint.2014.10.010

[106]   Furey, M.J., 1961, "Metallic Contact and Friction between Sliding Surfaces, A S L E Transactions," 4:1, 1-11. DOI: 10.1080/05698196108972414

[107]   Lane, T.B. and Hughes, J.R., 1952, "A study of the oil-film formation in gears by electrical resistance measurements," Br. J. Appl. Phys. **3** 315. DOI: 10.1088/0508-3443/3/10/305

[108]   Crook, A.W., 1957 "Simulated Gear-Tooth Contacts: Some Experiments upon Their Lubrication and Subsurface Deformations," Proceedings of the Institution of Mechanical Engineers, 171(1), 187–214. https://doi.org/10.1243/PIME_PROC_1957_171_025_02

[109]   Lugt, P.M., Severt, R.W.M., Fogelströ, J., and Tripp, J.H., 2001, "Influence of Surface Topography on Friction, Film Breakdown and Running-In in the Mixed Lubrication Regime," Proceedings of the IMechE Part J: Journal of Engineering Tribology, 215, pp 519–533. doi:10.1243/1350650011543772

[110]   Lord, J., and Larsson, R., 2008, "Film-Forming Capability in Rough Surface EHL Investigated Using Contact Resistance," Tribology International, 41, pp 831–838. https://doi.org/10.1016/j.triboint.2007.11.006

[111]   Zhang, X., Glovnea, R., 2020, "Grease film thickness measurement in rolling bearing contacts," Proceedings of the Institution of Mechanical Engineers, Part J: Journal of Engineering Tribology. https://doi.org/10.1177/1350650120961278

[112]   Cann P.M., Willianson B.P., Coy R.C., Spikes, H.A., 1992, "The behaviour of greases in elastohydrodynamic contacts," J. Phys. D: Appl. Phys. 25: 124–132.

[113]   Jablonka, K., Glovnea, R., Bongaerts, J., 2018, "Quantitative measurements of film thickness in a radially loaded deep-groove ball bearing," Tribology International, vol. 119, pp 239-249. https://doi.org/10.1016/j.triboint.2017.11.001

[114]   N. Bader, A. Furtmann, H. Tischmacher and G. Poll, 2017, "Capacitances and Lubricant Film Thicknesses of Grease and Oil Lubricated Bearings," STLE Annual Meeting & Exhibition, Atlanta, Georgia (US), Volume: 72nd.

[115]   Prashad H., 1992, "An approach to evaluate capacitance, capacitive reactance and resistance of pivoted pads of a thrust bearing," Tribology Trans; 35: 435–440. https://doi.org/10.1080/10402009208982140

[116]   New, N.H., 1974, "Experimental comparison of flooded, directed, and inlet orifice type of lubrication for a tilting pad thrust bearing," J. of Lubrication Tech., 96(1): 22-26. https://doi.org/10.1115/1.3451900

[117]   Hamilton, G.M., Moore, S.L., 1974, "Measurement of the oil film thickness between the piston rings and liner of a small diesel engine," Proc. Inst. Mech. Engrs., vol 188, p 253-261. https://doi.org/10.1243/PIME_PROC_1974_188_028_02

[118]   Ducu D.O., Donahue R.J., Ghandhi J.B., 2001 "Design of capacitance probes for oil film thickness measurements between the piston ring and linear in internal combustion engines," ASME J Eng Gas Turbines Power 2001; 123: 633–643. https://doi.org/10.1115/1.1368116

[119]   Hamilton G.M., 1980, "The hydrodynamic of a cam follower," Tribology Int; 13: 113–119. https://doi.org/10.1016/0301-679X(80)90054-7

[120]   Van Leeuwen, H. Meijer, H., Schouten, M., 1987, "Elastohydrodynamic film thickness and temperature measurements in dynamically loaded concentrated contacts: eccentric cam-flat follower," Tribology Series, vol. 11, pp 611-625. https://doi.org/10.1016/S0167-8922(08)70995-7

[121]   Furtmann, A., Poll, G., 2016, "Evaluation of oil-film thickness along the path of contact in a gear mesh by capacitance measurement," Tribology Online; 11: 189–194. https://doi.org/10.2474/trol.11.189

[122]   Maruyama, T., Nakano, K., 2018, "In Situ Quantification of Oil Film Formation and Breakdown in EHD Contacts," Tribology Transactions, 61:6, 1057-1066. DOI:10.1080/10402004.2018.1468519

[123]   lrani, K, Pekkari, M., and Angstrom, H-E., 1997), "Oil filin thickness measurement in the middle main bearing of a six-cylinder supercharged 9 litre diesel engine using capacitive transducer," Wear. 207: 29-33. https://doi.org/10.1016/S0043-1648(96)07470-4

[124]   Harper, P., 2008, "Measurement of Film Thickness in Lubricated Components using Ultrasonic Reflection," Doctoral Thesis, Department of Mechanical Engineering, University of Sheffield.

[125]   Attia, F.S., Whomes, T.L., 1979, "Further developments in the inductive measurement of ehl film thickness," Tribology International; 12: 215-217. https://doi.org/10.1016/0301-679X(79)90191-9

[126]   Glavatskikh, S.B., Uusitalo, Ö., Spohn, D.J., 2001, "Simultaneous monitoring of oil thickness and temperature in fluid film bearings," Tribol Int; 34:853-857. DOI: 10.1016/S0301-679X(01)00086-X

[127]   Read, L.J., Flack, R.D., 1987, "Temperature, pressure and fllm thickness measurements for an offset half bearing," Wear 117:197-210. https://doi.org/10.1016/0043-1648(87)90255-9

[128]   Bai, Q., Guo, F., Wong, P.L. et al., 2017, "Online Measurement of Lubricating Film Thickness in Slider-on-Disc Contact Based on Dichromatic Optical Interferometry," Tribol Lett 65, 145. https://doi.org/10.1007/s11249-017-0928-3

[129]   Liu, H.C., Guo, F., Guo, L., Wong, P.L., 2015, "A dichromatic interference intensity modulation approach to measurement of lubricating film thickness," Tribol. Lett.58(1), 1–11. https://doi.org/10.1007/s11249-015-0480-y

[130]   Michelson A., Morley E., 1887, "On the Relative Motion of the Earth and the Luminiferous Ether". American Journal of Science, 34 (203): 333–345. doi:10.2475/ajs.s3-34.203.333.

[131]   Higginson, G. R., Reed, S. 1967, "Report 5: An Optical Method of Measuring Film Thickness," Proceedings of the Institution of Mechanical Engineers, Conference Proceedings, 182(7), 56–58. https://doi.org/10.1243/PIME_CONF_1967_182_180_02

[132]   Myant, C., Reddyhoff, T., Spikes, H.A., 2010, "Laser-induced fluorescence for film thickness mapping in pure sliding lubricated, compliant, contacts," Tribology Int; 43(11): 1960-1969. https://doi.org/10.1016/j.triboint.2010.03.013

[133]   Fowell, M.T., Myant, C., Spikes, H.A., Kadiric, A., 2014, "A study of lubricant film thickness in compliant contacts of elastomeric seal materials using a laser induced fluorescence technique, " Tribology Int; 80, 76-89. https://doi.org/10.1016/j.triboint.2014.05.028

[134]   Necas, D., Sperka, P., Vrbka, M., Krupka, I., Hartl, M., 2015, "Film thickness mapping in lubricated contacts using fluorescence," MM Science Journal,821-824. DOI: 10.17973/MMSJ.2015_12_201524

[135]   Petrova, D., Weber, B., Cleménce, A., Audebert, P., Venner, C.H., Brouwer, A.M., Bonn, D., 2019, "Fluorescence microscopy visualization of the roughness-induced transition between lubrication regimes," Science Advances, vol. 5, no. 12, eaaw4761. DOI: 10.1126/sciadv.aaw4761

[136]   Hidrovo, C.H., Hart D.P., 2001, "Emission reabsorption laser induced fluorescence (ERLIF) film thickness measurement," Measurement Science and Technology, vol. 12, no 4.

[137]   Zhang, K., Meng, Q., Geng, T., Wang, N., 2015, "Ultrasonic measurement of lubricant film thickness in sliding Bearings with overlapped echoes," Tribology Int; 88: 89-94. https://doi.org/10.1016/j.triboint.2015.03.017

[138]   Dwyer-Joyce, R.S., Drinkwater, B.W. and Donohoe, C.J., 2003, "The measurement of lubricant-film thickness using ultrasound," Proc. R. Soc. Lond. A.459957–976. http://doi.org/10.1098/rspa.2002.1018.

[139]   Li, M., Jing, M., Chen, Z., Liu, H., 2013, "Ultrasound measurement of lubricant-film thickness distribution in cylindrical roller bearings," IEEE International Symposium on Assembly and Manufacturing (ISAM), Xi'an, China, pp. 304-306. doi: 10.1109/ISAM.2013.6643464

[140]   Ouyang, W., Zhou, Z., Jin, Y., Yan, X., Liu, Y., 2020, "Ultrasonic measurement of lubricant film thickness distribution of journal bearing," Review of Scientific Instruments 91, 065111. https://doi.org/10.1063/5.0007481

[141]   Reddyhoff, T., Dwyer-Joyce, R., Harper, P., 2006, "Ultrasonic measurement of film thickness in mechanical seals," Sealing Technology, vol. 2006, issue 7, pp 7-11. https://doi.org/10.1016/S1350-4789(06)71260-0

[142]   Brunetière, N., Modolo, B., 2009, "Heat transfer in a mechanical face seal," International Journal of Thermal Sciences, vol. 48, issue 4, pp 781-794. https://doi.org/10.1016/j.ijthermalsci.2008.05.014

[143]   Dingui, K., Brunetière, N., Bouyer, J., Adjemout, M., 2020, "Surface texturing to reduce temperature in mechanical seals," Tribology Online, 15 (4), pp.222-229. https://doi.org/10.2474/trol.15.222

[144]   Omasta, M., Adam, J., Sperka, P., Krupka, I., Hartl, M., 2018, "On the Temperature and Lubricant Film Thickness Distribution in EHL Contacts with Arbitrary Entrainment," Lubricants 6, no. 4: 101. https://doi.org/10.3390/lubricants6040101

[145]   Lu, J., Reddyhoff, T., Dini, D., 2018, "3D Measurements of Lubricant and Surface Temperatures Within an Elastohydrodynamic Contact," Tribol Lett 66, 7. https://doi.org/10.1007/s11249-017-0953-2

[146]   Hidrovo, C.H., Hart, D.P., 2002, "2D thickness and temperature mapping of fluids by means of a two-dye laser induced fluorescence radiometric scheme," J. Flow Vis. Image process 9 171-191.

[147]   Bruchhausen, M., Delconte, A., Blondel, D., Lemoine, F., 2006, "Temperature measurements in polydisperse sprays by means of laser-induced fluorescence (LIF) on three spectral bands," Atomization and Sprays, vol. 16, issue 6, 599-614. DOI: 10.1615/AtomizSpr.v16.i6.10

[148]   Banks, D., Robles, V., Zhang, B., Devia-Cruz, L.F., Camacho-Lopez, S., Aguilar, G., 2019, "Planar laser inducedfluorescence for temperature measurement of optical thermocavitation," Experimental Thermal and Fluid Science, 103, 385-393. https://doi.org/10.1016/j.expthermflusci.2019.01.030

[149]   Jaszczur, M., Pyrda, L., 2016, "Application of Laser Induced Fluorescence in experimental analysis of convection phenomena" J. Phys.: Conf. Ser. 745 032038. DOI: 10.1088/1742-6596/745/3/032038

[150]   Tournerie, B., Reungoat, D., Frene, J. 1991, "Temperature Measurements by Infrared Thermography in the Interface of a Radial Face Seal," ASME. J. Tribol. July 1991; 113(3): 571–576. https://doi.org/10.1115/1.2920661

[151]   Cox G. (2019) Fundamentals of Fluorescence Imaging. CRS Press, 1351129392, 9781351129398,

[152]   French A.P., Taylor E.F. (1978), Introduction to Quantum Physics. M.I.T. Introductory Physics Series) 1st Edition, pp. 24, 55.

[153]   Wennehorst, B., 2016, "On Lubrication and Friction in Soft Rough Conformal Sliding Contacts - Experimental and theoretical contributions to the discussion on elastomer shaft seal tribology," Doctoral Thesis, IMKT, Hannover.

[154]   Skubacz, T., 2020, "Experimentelle Untersuchungen zur Schmierstoff-Oberflächen-Wechselwirkung in nasslaufenden Reibsystemen am Beispiel von Synchronisierungen," Doctoral Thesis, Gottfried Wilhelm Leibniz Universität. https://doi.org/10.15488/10313

[155]   Lambert, J.H., (1760) Photometria sive de mensura et gradibus luminis, colorum et umbrae [Photometry, or, On the measure and gradations of light intensity, colors, and shade] (in Latin). Augsburg, (Germany): Eberhardt Klett.

[156]   Beer, A., 1852, "Bestimmung der Absorption des rothen Lichts in farbigen Flüssigkeiten" [Determination of the absorption of red light in colored liquids]. Ann. der Phys, 162(5), pp. 78-88. https://doi.org/10.1002/andp.18521620505

[157]   Poll G., Gabelli A., Binnington P.G., Qu J.,1992, "Dynamic Mapping of Rotary Lip Seal Lubricant Films by Fluorescent Image Processing," in: Nau B.S. (eds) Fluid Sealing. Fluid Mechanics and its Applications, vol 8. Springer, Dordrecht. https://doi.org/10.1007/978-94-011-2412-6_5

[158]   Wennehorst, B., Poll, G., 2009, "Untersuchung zur Tribologie von RWDR – Ergebnisse von Schmierfilmhöhen– und Reibungsmessungen," VII. Hamburger Dichtungstechnisches Kolloquium, Hamburg.

[159]   Lakowicz J.R. (2006) Quenching of Fluorescence. In: Principles of Fluorescence Spectroscopy. Springer, Boston, MA. https://doi.org/10.1007/978-0-387-46312-4_8

[160]   Vollmer, M., Möllmann K.P, (2011) Infrared Thermal Imaging: Fundamentals, Research, and Applications. second. Weinheim: Wiley VHC.

[161]   Fouad, N.A., Richter T. (2012) Leitfaden Thermografie im Bauwesen. 4th ed. Fraunhofer IRB Verlag.

[162]   Reungoat, D., Tournerie, B. 1994, "Temperature Measurement by Infrared Thermography in a Lubricated Contact: Radiometric Analysis," Proceedings of the Eurotherm Seminar 42: Quantitative InfraRed Thermography, Editions Européennes Thermique et Industrie pp 30–36, Paris. DOI: 10.21611/qirt.1994.006

[163]   Adjemout, M., Brunetière, N., Bouyer J., 2018, "Friction and Temperature Reduction in a Mechanical Face Seal by a Surface Texturing: Comparison between TEHD Simulations and Experiments," Tribology Transactions, 61:6, 1084-1093. DOI: 10.1080/10402004.2018.1478053

[164]   Sedlaček, M., Gregorčič, P., Podgornik, B., 2016, "Use of the Roughness Parameters Ssk and Sku to Control Friction—A Method for Designing Surface Texturing," Tribology Transactions, 60:2, 260-266, DOI: 10.1080/10402004.2016.1159358

[165]   Jeng, Y., 1996, "Impact of Plateaued Surfaces on Tribological Performance," Tribology Transactions, 39, pp 354–361. DOI: 10.1007/s11249-017-0953-2

[166]   Gropper, D., Wang, L., Harvey, T., 2015, "Hydrodynamic lubrication of textured surfaces: A review of modeling techniques and key findings," Tribol. Int., 94:509 – 529. DOI: 10.1016/j.triboint.2015.10.009

[167]   Sahlin, F., Glavatskih, S., Almqvist, T., Larsson, R., 2005 "Two-dimensional CFD-analysis of micro-patterned surfaces in hydrodynamic lubrication," J Tribol; 127:96–102. https://doi.org/10.1115/1.1828067

[168]   Dobrica, M.B., Fillon, M., 2009, "About the validity of Reynolds equation and inertia effects in textured sliders of infinite width," Proc Inst Mech Eng Part J: J Eng Tribol; 223:69–78. DOI: 10.1243/13506501JET433

[169]   de Kraker, A., van Ostayen, R.A.J., Rixen, D.J., 2010, "Development of a texture averaged Reynolds equation," Tribol Int; 43:2100–9. https://doi.org/10.1016/j.triboint.2010.06.001

[170]   Etsion, I., Halperin, G., 2002, "A laser surface textured hydrostatic mechanical seal," Tribol Trans; 45:430–4. https://doi.org/10.1080/10402000208982570

[171]   Tønder, K., 1996, "Dynamics of rough slider bearings: effects of one-sided roughness/waviness," Tribol Int; 29:117–22. https://doi.org/10.1016/0301-679X(95)00095-L

[172]   Scaraggi, M., 2014, "Partial surface texturing: A mechanism for local flow reconditioning in lubricated contacts," Proceedings of the Institution of Mechanical Engineers, Part J: Journal of Engineering Tribology, 229(4), 493–504. https://doi.org/10.1177/1350650114539935

[173]   Mezzadri, F., Galligani, E., 2018, "An inexact Newton method for solving complementarity problems in hydrodynamic lubrication," Calcolo 55, 1. https://doi.org/10.1007/s10092-018-0244-9

[174]   Råback, P., 2020, "ElmerGrid Manual." http://www.nic.funet.fi ›, CSC – IT Center for Science.

[175]   Ghattas, O., 1996, "Mesh partitioning." http://www.cs.cmu.edu

[176]   Muraro, M.A., Koda, F., Reisdorfer Jr., U., Silva, C., 2012, "The Influence of Contact Stress Distribution and Specific Film Thickness on the Wear of Spur Gears During Pitting Tests," Journal of the Brazilian Society of Mechanical Sciences and Engineering 34(2):135-144. DOI: 10.1590/S1678-58782012000200005

[177]   Wang Q.J., Cheng H.S., 2013, "Flow Factors for Average Reynolds Equation," in: Wang Q.J., Chung YW. (eds) Encyclopedia of Tribology. Springer, Boston, MA. https://doi.org/10.1007/978-0-387-92897-5_155

[178]   Patir, N., Cheng, H.S., 1978, "An Average Flow Model for Determining Effects of Three-Dimensional Roughness on Partial Hydrodynamic Lubrication," ASME. J. of Lubrication Tech.; 100(1): 12–17. https://doi.org/10.1115/1.3453103

[179]   Bowen, E.J., Sahu, J., 1959, "The effect of temperature on fluorescence of solutions," J. Phys. Chem. 63, 1, 4-7. https://doi.org/10.1021/j150571a003

[180]   Giri, R., 1992, "Temperature effect study upon the fluorescence emission of substituted coumarins," Spectrochimica Acta Part A: Molecular Spectroscopy, vol. 48, issue 6, pp 843-848. https://doi.org/10.1016/0584-8539(92)80080-G

[181]   Råback, P., Malinen, M., Ruokolainen, J., Pursula, A., Zwinger, T., 2015, "Elmer – Finite Element Solver for Multiphysical Problems." http://www.csc.fi/elmer, CSC – IT Center for Science.

[182]   Råback, P., Malinen, M., Ruokolainen, J., Pursula, A., Zwinger, T., 2015, "Elmer – Finite Element Solver for Multiphysical Problems. Elmer Models Manual" http://www.csc.fi/elmer, CSC – IT Center

[183]   Kudlaty, K., 2004 "Attenuated Total Reflection technique for on-line oil monitoring by means of a FTIR fiber-optic probe," Doctor Thesis, Institute for Measurement Systems and Sensor Technology, Technischen Universität München.

[184]   Holmberg, K., Erdemir, A., 2015, "Global impact of friction on energy consumption, economy and environment," FME Transactions, vol. 43, no. 3, pp 181-185.

[185]   Holmberg, K., Andersson, P., Erdemir, A., 2012, "Global energy consumption due to friction in passenger cars," Tribol. Int., Vol. 47, pp 221-234. https://doi.org/10.1016/j.triboint.2011.11.022

[186]   Holmberg, K., Erdemir, A., 2017, "Influence of tribology on global energy consumption, costs and emissions," Friction 5, 263–284. https://doi.org/10.1007/s40544-017-0183-5

[187]   Kulkarni, P.D., Phalle, V.M., 2018, "Influence of Turbulent Flow on Performance of Fluid Film Journal Bearing – Overview," Proceedings of TRIBOINDIA-2018 An International Conference on Tribology, Available at SSRN: https://ssrn.com/abstract=3347085 or http://dx.doi.org/10.2139/ssrn.3347085.

APPENDIX A
Calibration curve for the fluorescence measurements

The calibration curve which shows the relationship between the fluorescence intensity and the film thickness is shown in Figure A-1. The calibration curve shows that the fluorescence intensity increases linearly with the film thickness up to a film thickness of 40 µm. Therefore, the calibration curve can be used for the structured seals except the deep areas of the structures.
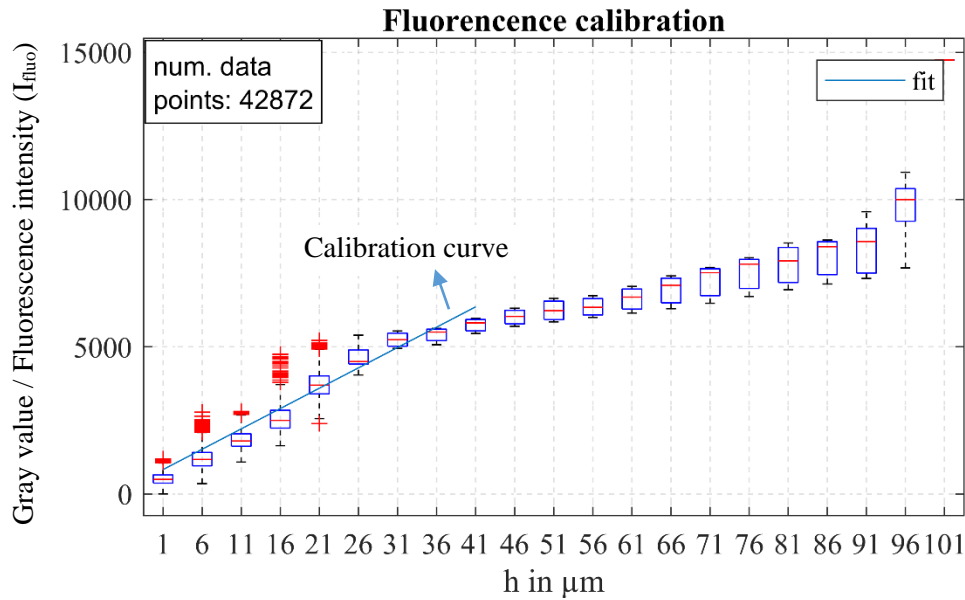

Figure A-1: The calibration curve which is used in the fluorescence methods. The curve is obtained for 0 rpm, 20 °C and 5 bar.

Reproducibility of the film thickness measurements

Table A-1: Reproducibility of the film thickness measurements

Median value of the fluorescence intensity at 0 rpm, 20 °C and 5 bar. Seal type: structured, measurement region: flat surface over the structure		
first measurement	second measurement	third measurement
1067.862	1068.138	1072
1076.43491	1079.89122	1078.20023

Film thickness values according to the measurement location

Here, the film thickness values shown in Figure 5.34 and Figure 5.35 are compared. It should be noted that the comparison is not performed for 2500 rpm since the film thickness shown in Figure 5.34 was not measured at 2500 rpm for the whole selected area.

The film thickness values shown in Figure 5.34 are measured within the calibration area (see Figure A-2). The film thickness values shown in Figure 5.35 are measured within the film thickness measurement area. However, for both the film thickness and the calibration areas, the film thickness measurement values are similar (Figure A-2). This shows that the method which is used to measure the film thickness provides consistent results. In addition, the calibration seems to be valid for a bigger area.
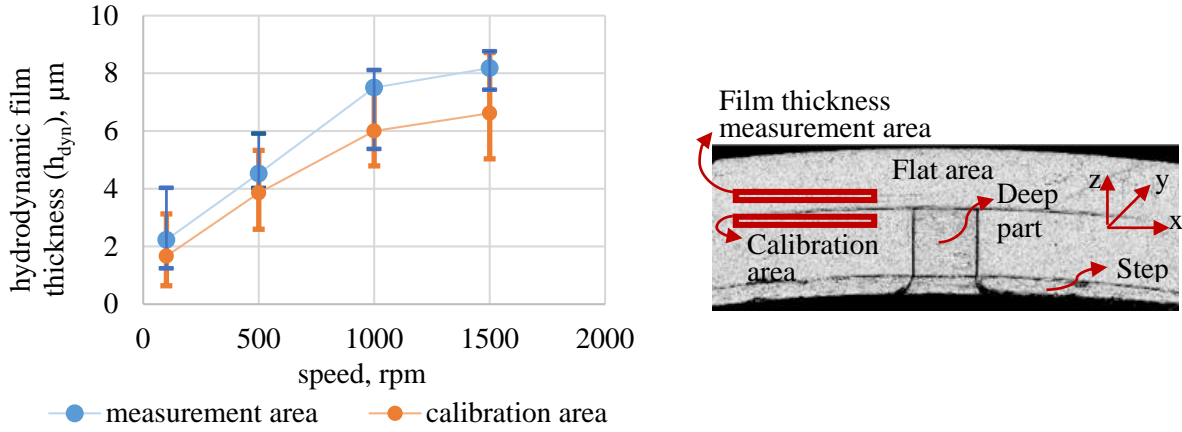
Figure A-2: The calculated film thicknesses for the calibration and the film thickness measurement areas. Pressure is 5 bar. Sump temperature is 20 °C.

APPENDIX B
Infrared thermography

$$B = B^+ = B^- = \left(\frac{(1 - \rho_{air,1})\left((1 - \rho_{1,2})\right)\tau}{1 - \rho_{air,1}\rho_{1,2}\tau^2} \right)$$

$$R^+ = \left(\frac{\rho_{1,2} + \tau^2\rho_{1,2}(1 - 2\rho_{1,2})}{1 - \rho_{air,1}\rho_{1,2}\tau^2} \right); \; R^- = \left(\frac{\rho_{air,1} + \tau^2\rho_{1,2}(1 - 2\rho_{air,1})}{1 - \rho_{air,1}\rho_{1,2}\tau^2} \right)$$

$$E^+ = \left(\frac{(1 - \tau)(1 - \rho_{1,2})(1 - \tau\rho_{air,1})}{1 - \rho_{air,1}\rho_{1,2}\tau^2} \right); \; E^- = \left(\frac{(1 - \tau)(1 - \rho_{air,1})(1 - \tau\rho_{1,2})}{1 - \rho_{air,1}\rho_{1,2}\tau^2} \right)$$

$$\rho_3 = 1 - \varepsilon_3; \; \rho_{air,1} = \left(\frac{n_{air} - n_1}{n_{air} + n_1} \right)^2; \; \rho_{1,2} = \left(\frac{n_1 - n_2}{n_1 + n_2} \right)^2$$

Coefficient of emissivity of the seal is denoted by ε_3. Coefficient of transmissivity of the sapphire disc is denoted by τ. Coefficient of reflectivity of the interfaces environment/sapphire and sapphire/oil are denoted by $\rho_{air,1}$ and $\rho_{1,2}$, respectively. Other optical parameters are shown in Table B-1. Emissivity of the seal ε_3 is measured by heating the structured seal to different temperatures and measuring those temperatures via the thermal camera. The temperature of the seal ring is controlled via a thermocouple which is placed on the seal surface. The seal material and the surface properties have a good emissivity (almost equal to 1). Since the material and the surface properties are similar for the standard seal, it is assumed that it has the similar emissivity to that of the structured seal.

Table B-1: Optical parameters

Optical parameter	Value
ε_3, seal emissivity	0.96
τ, sapphire disc transmissivity	0.577
ε_1, sapphire emissivity	0.48
n_{air}, air refraction index	1.0029
n_1, sapphire refraction index	1.762-1.778
n_2, oil refraction index	1.479

The transmissivity of the sapphire is measured by placing a black body behind the sapphire disc. The black body is heated and the radiative flux is measured through the sapphire disc. A mean value for the transmissivity is obtained for the measured temperature range. Other parameters given in Table B-1 are

based on the literature. It should be noted that the oil refraction index is based on the hydraulic oil measurement in the work of [183].
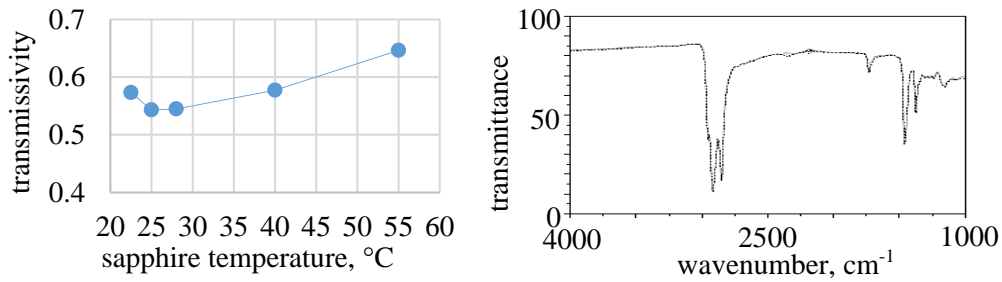
Figure B-1: Left: Transmissivity τ of the sapphire disc. Right: ATR-fiber spectra of ATF oil from Bruker FTIR spectometer (resolution: $\Delta\bar{v} = 6$ cm^{-1}) [183].

APPENDIX C
Friction torque measurements including leakage and temperature
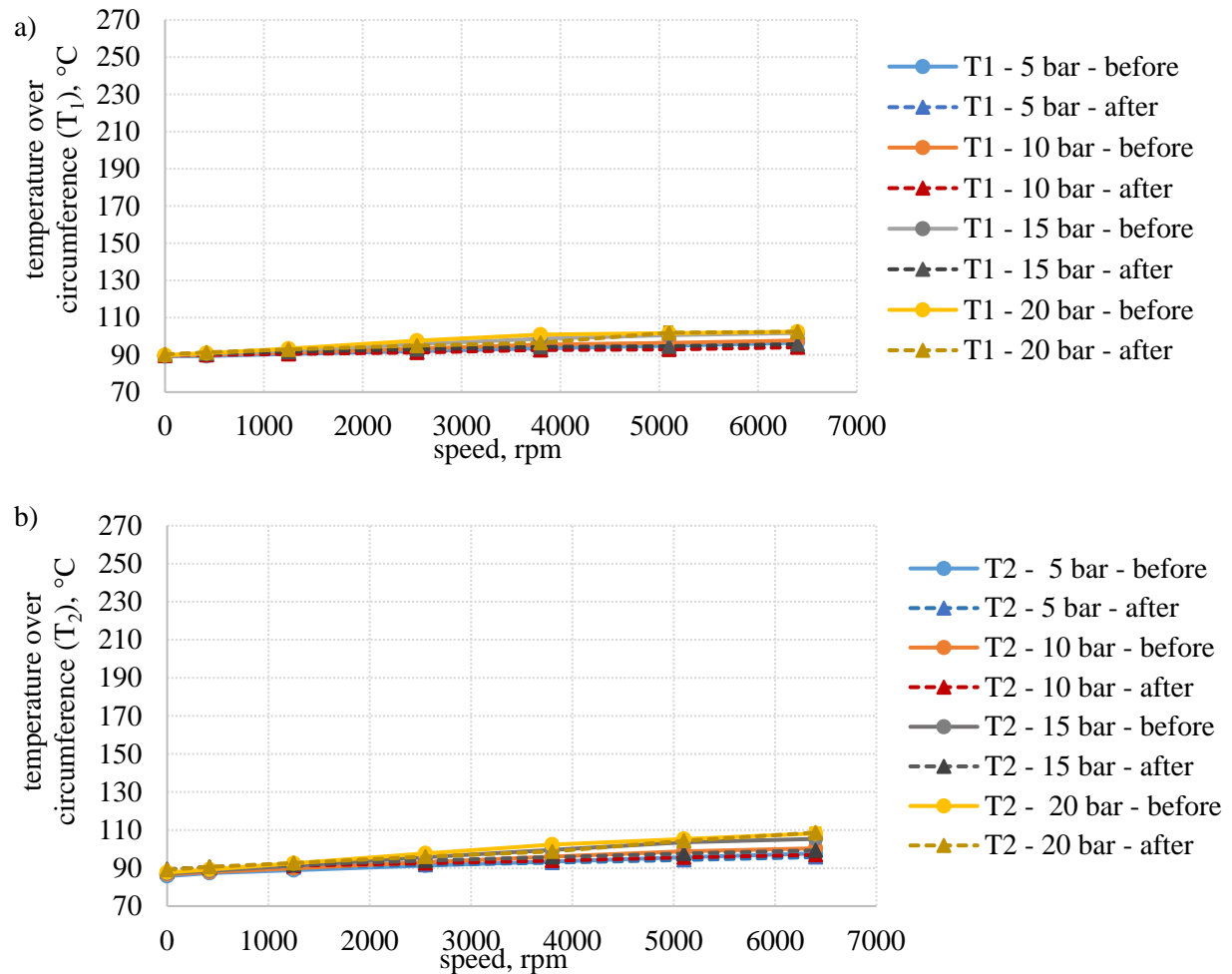## Structured seals – test A

Figure C-1: Temperatures over the circumferences of (a) structured seal 1 and (b) structured seal 2. 'before' and 'after' represent the function tests 1 and 2, respectively.
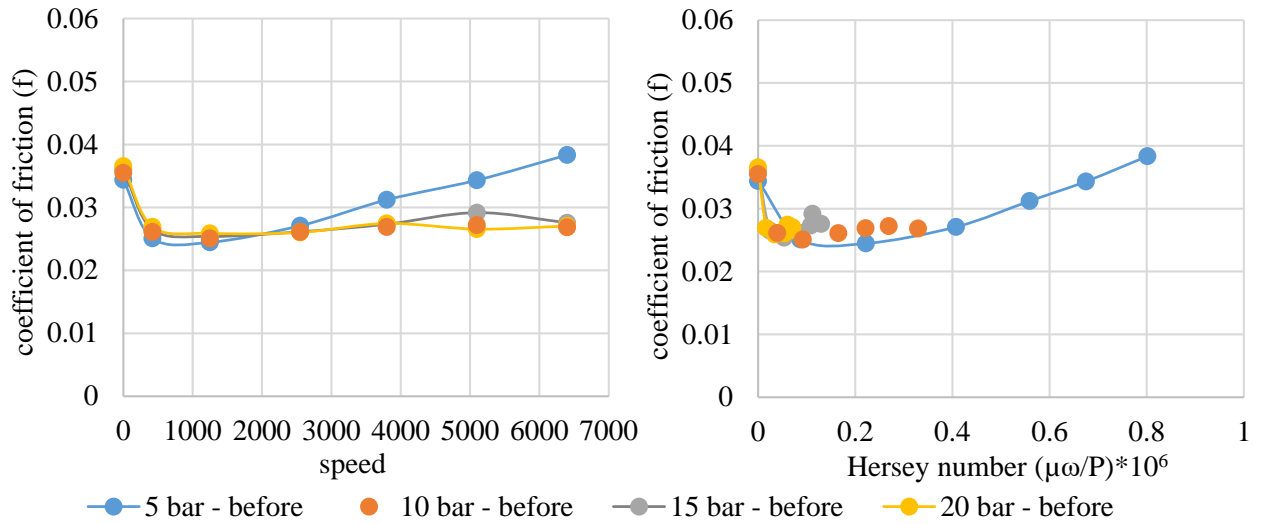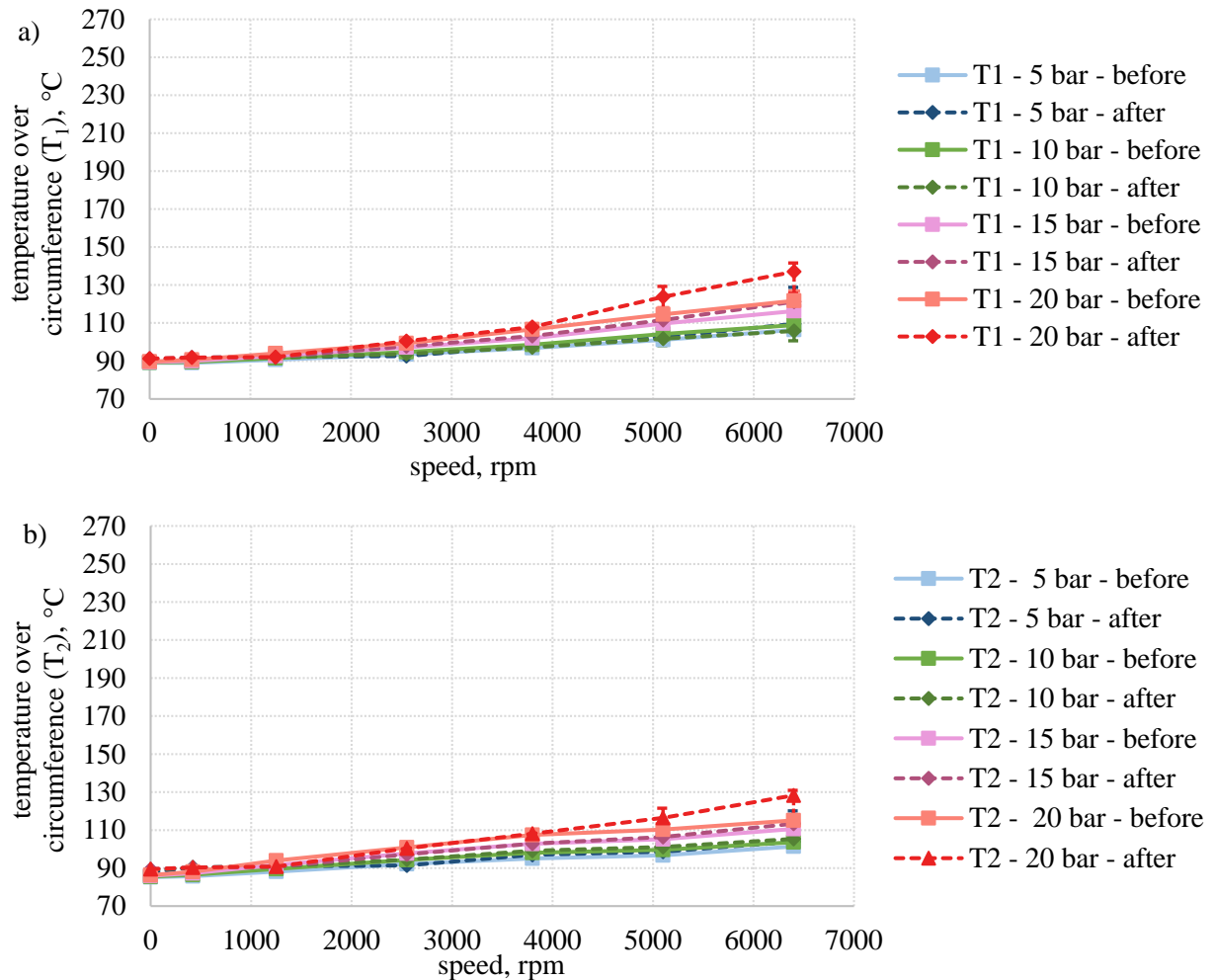
Figure C-2: Coefficient of friction vs speed and Hersey number for the structured seals. 'before' represents the function test 1 of test A.

Structured seals – test B
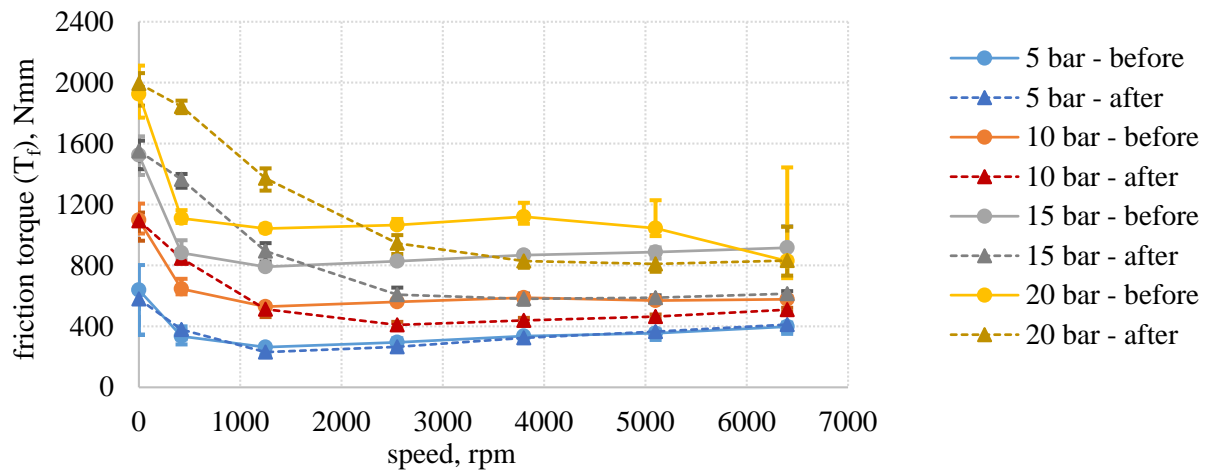
Figure C-3: Friction torque (resulted from two structured seals) in Test B. 'before' and 'after' represent the function tests 1 and 2, respectively.
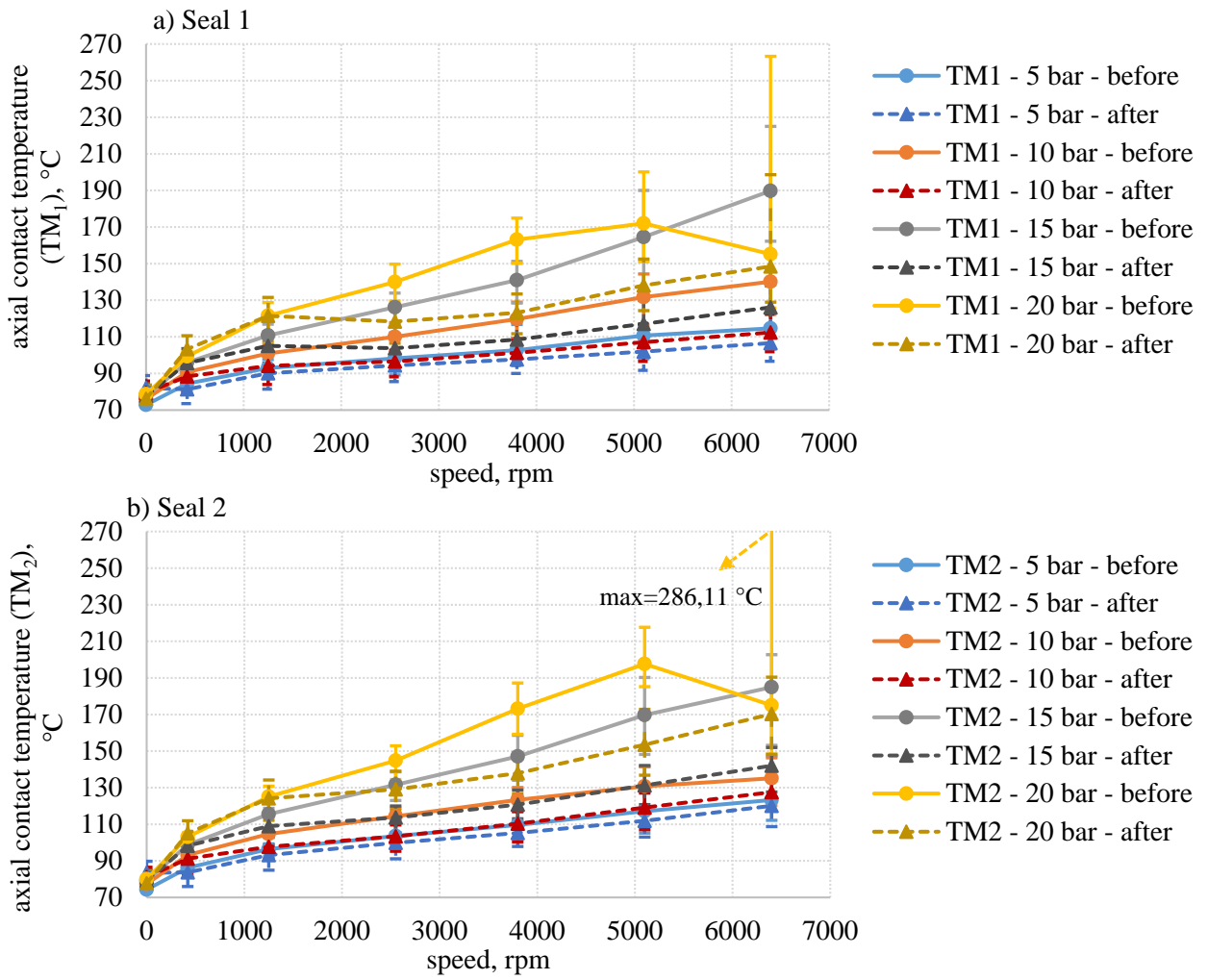
Figure C-4: Axial contact temperatures for the structured seals 1 and 2. 'before' and 'after' represent the function tests 1 and 2, respectively.
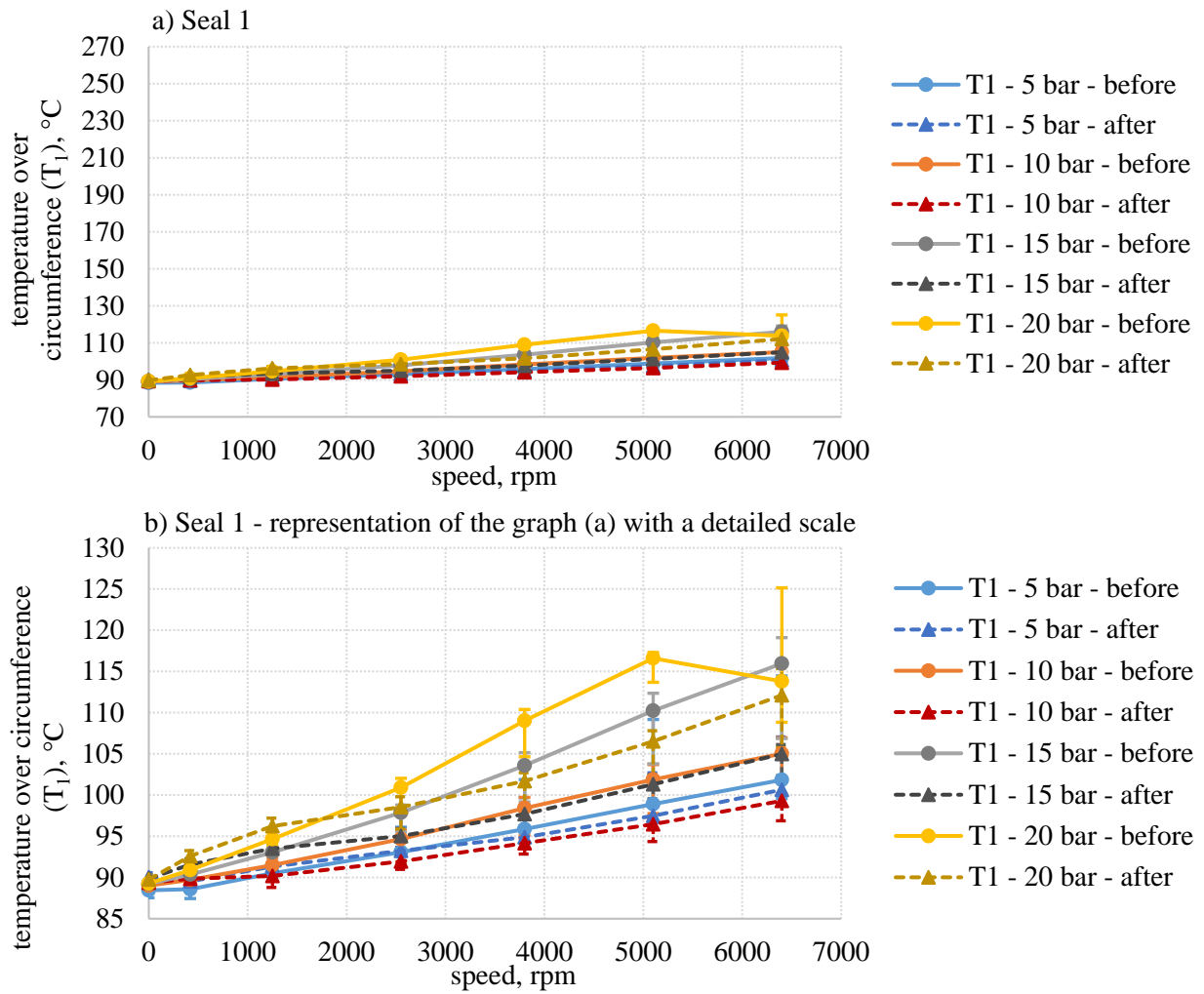
Figure C-5: Temperatures over the circumference of structured seal 1. 'before' and 'after' represent the function tests 1 and 2, respectively.
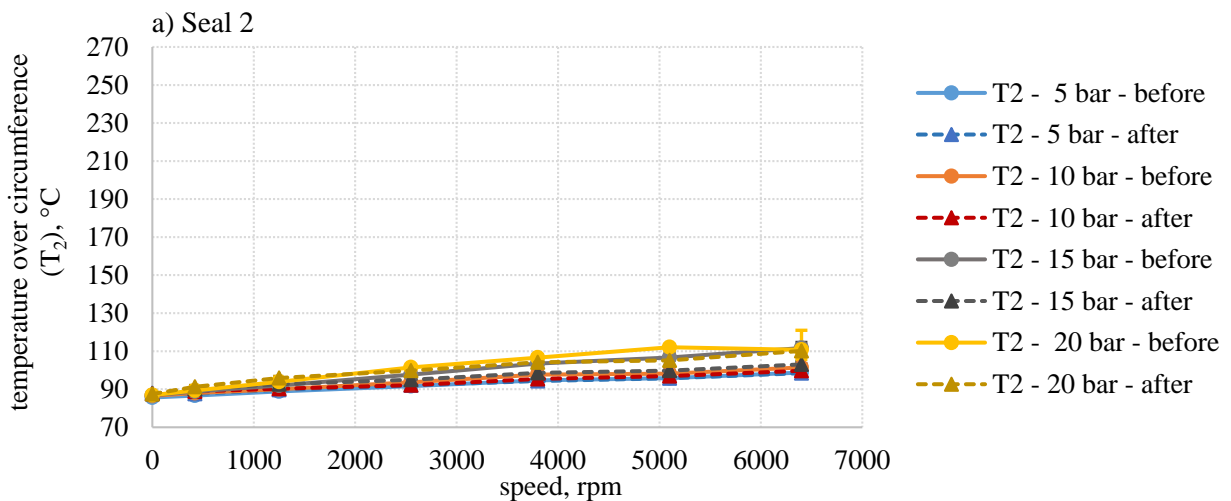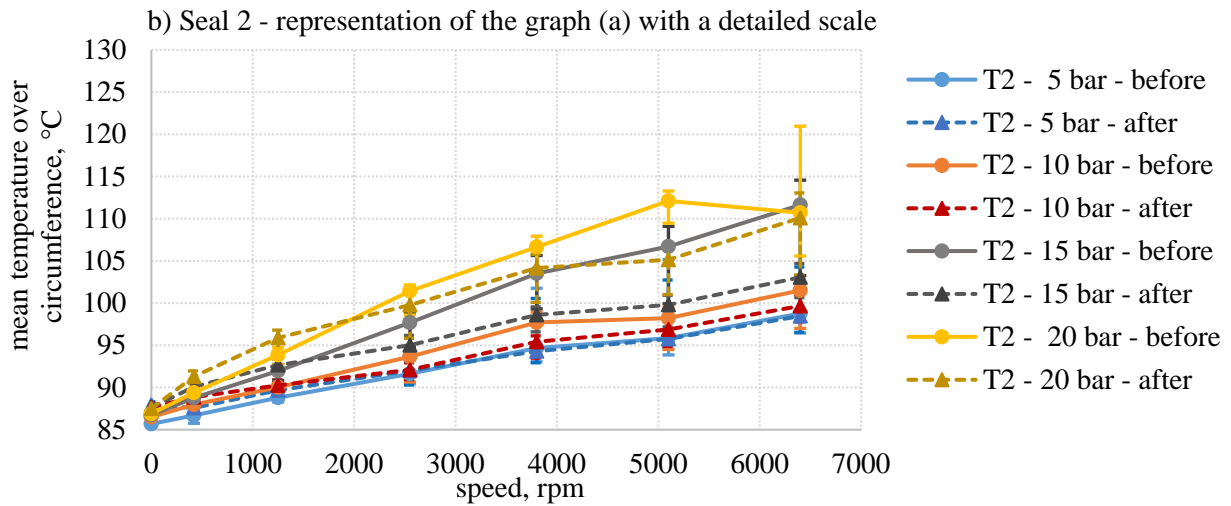
Figure C-6: Temperatures over the circumference of structured seal 2. 'before' and 'after' represent the function tests 1 and 2, respectively.
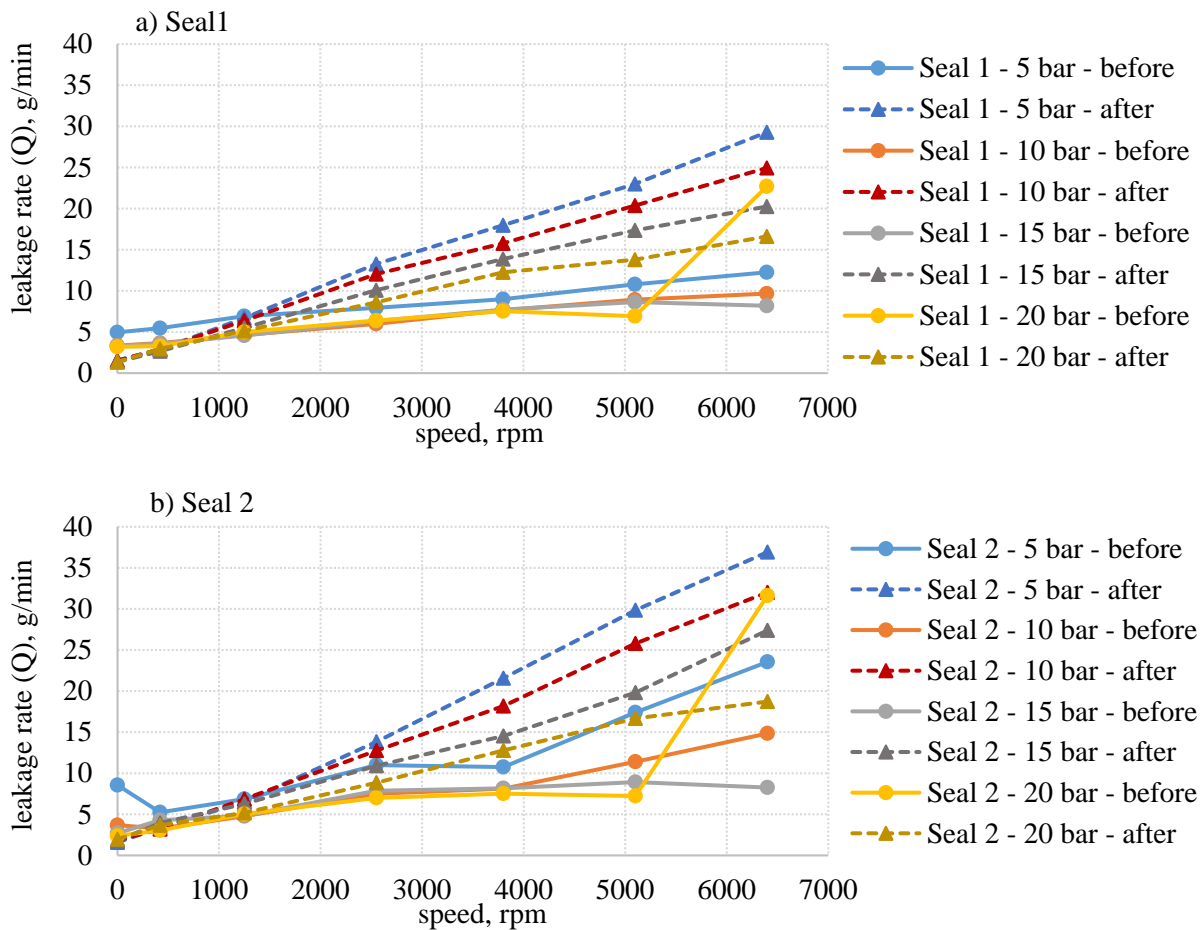

Figure C-7: Leakage rates for the structured seals 1 and 2 in Test B. 'before' and 'after' represent the function tests 1 and 2, respectively.
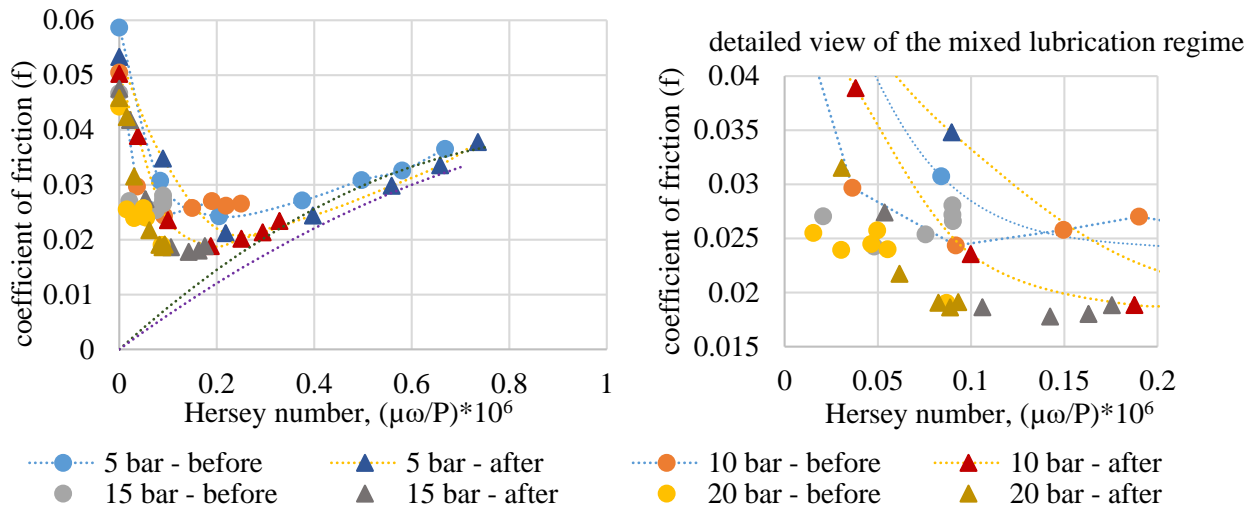
Figure C-8: Comparison of the coefficient of friction values for the function tests 1 and 2 of the structured seals. 'before' and 'after' represent the function tests 1 and 2, respectively. The curves which represent the behaviour of the smooth surfaces are taken from Test A.
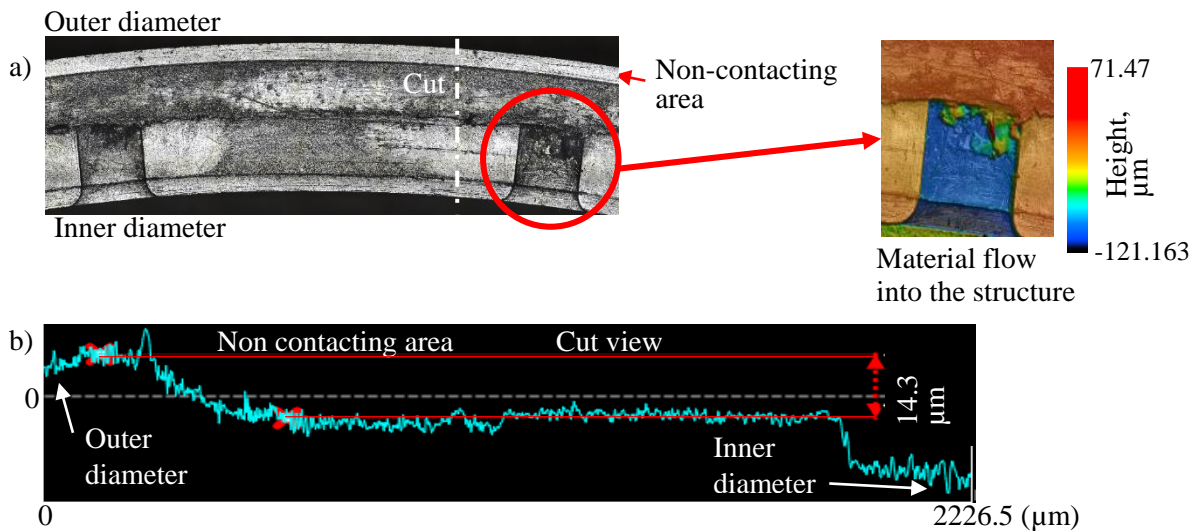
Figure C-9: The wear pattern and the radial profile of structured seal 2 after the tests.
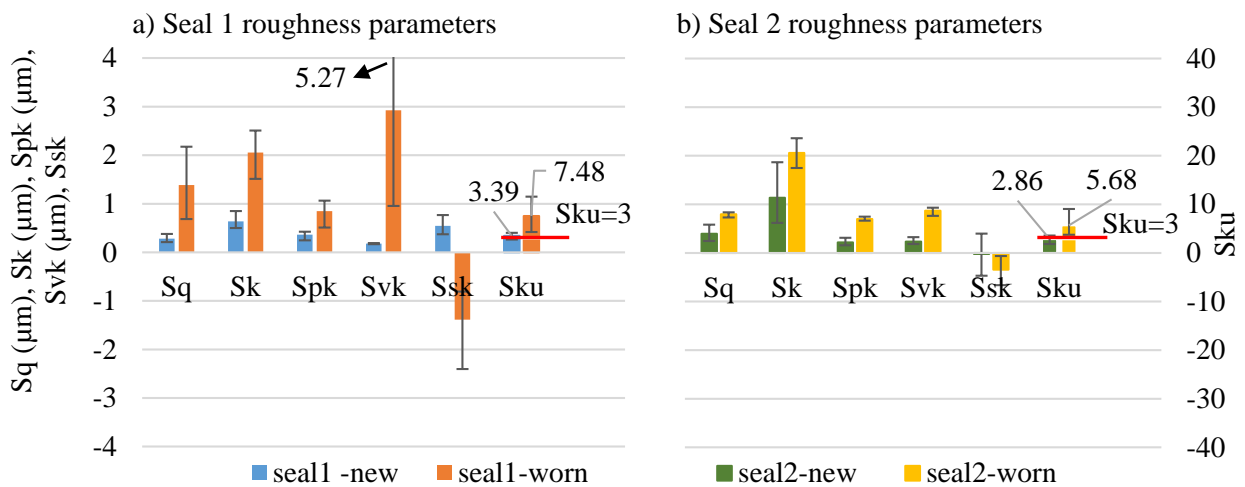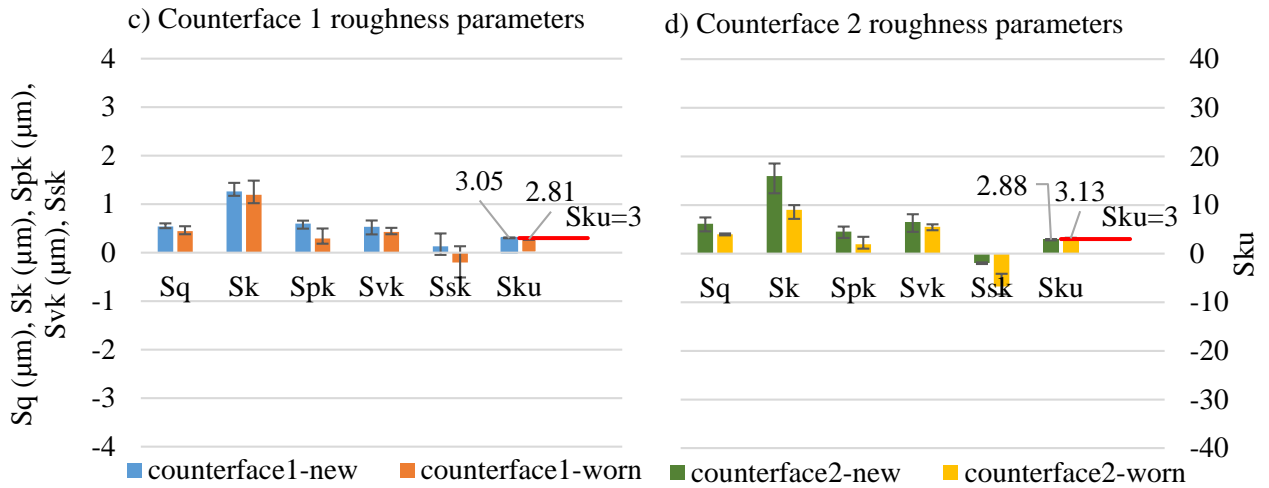
Figure C-10: a) Surface roughness parameters of the structured seals and the counterfaces before and after the tests.

Standard seals – test C

Figure C-11: Temperatures over the circumferences of (a) standard seal 1 and (b) standard seal 2. 'before' and 'after' represent the function tests 1 and 2, respectively.
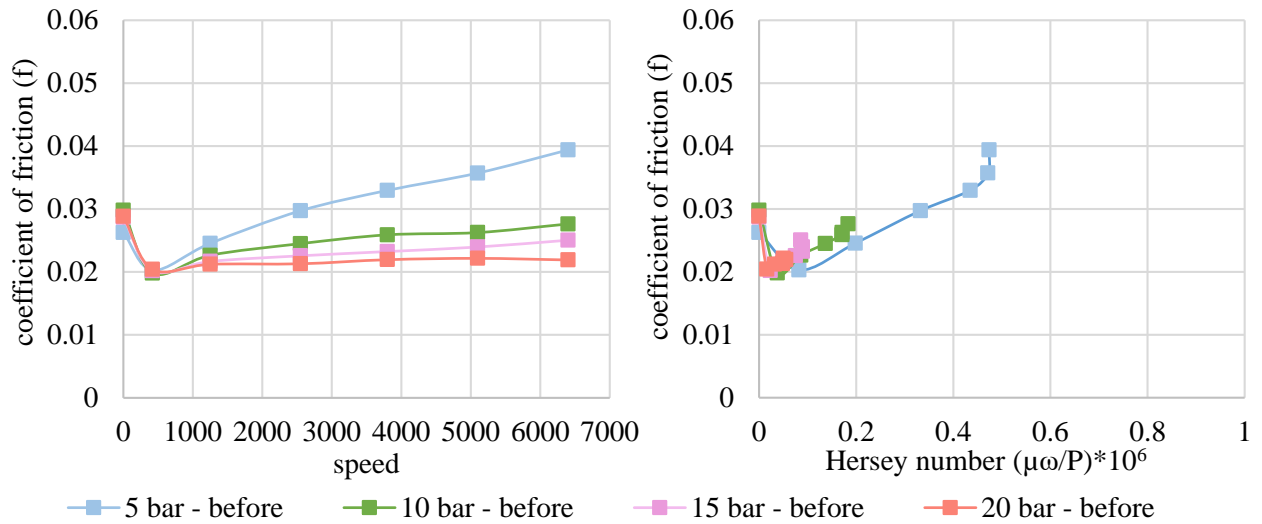
Figure C-12: Coefficient of friction vs speed and Hersey number for the standard seals. 'before' represents the function test 1 of test C.

Standard seals – test D
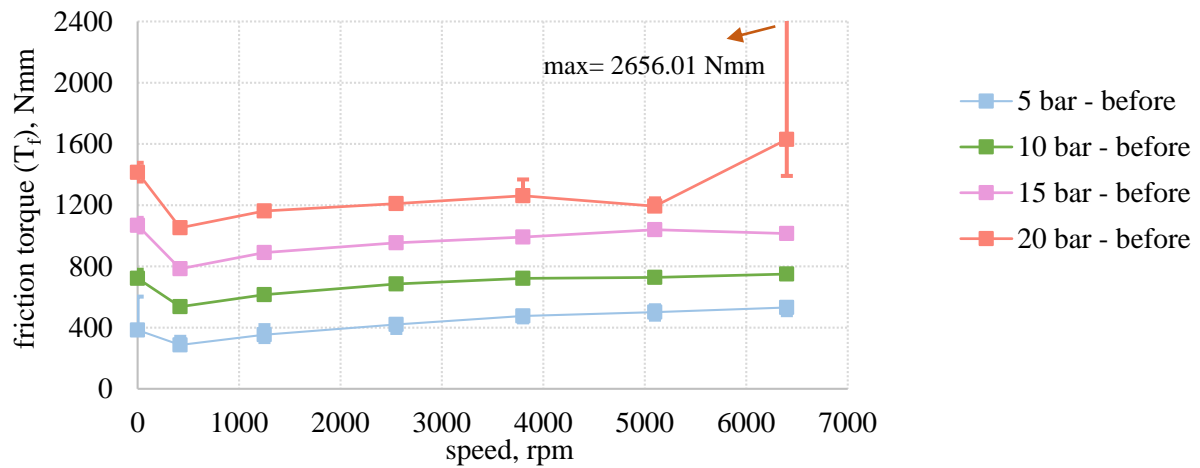
Figure C-13: Friction torque (resulted from two standard seals) in Test D. 'before' represents the function tests 1 and 2, respectively.
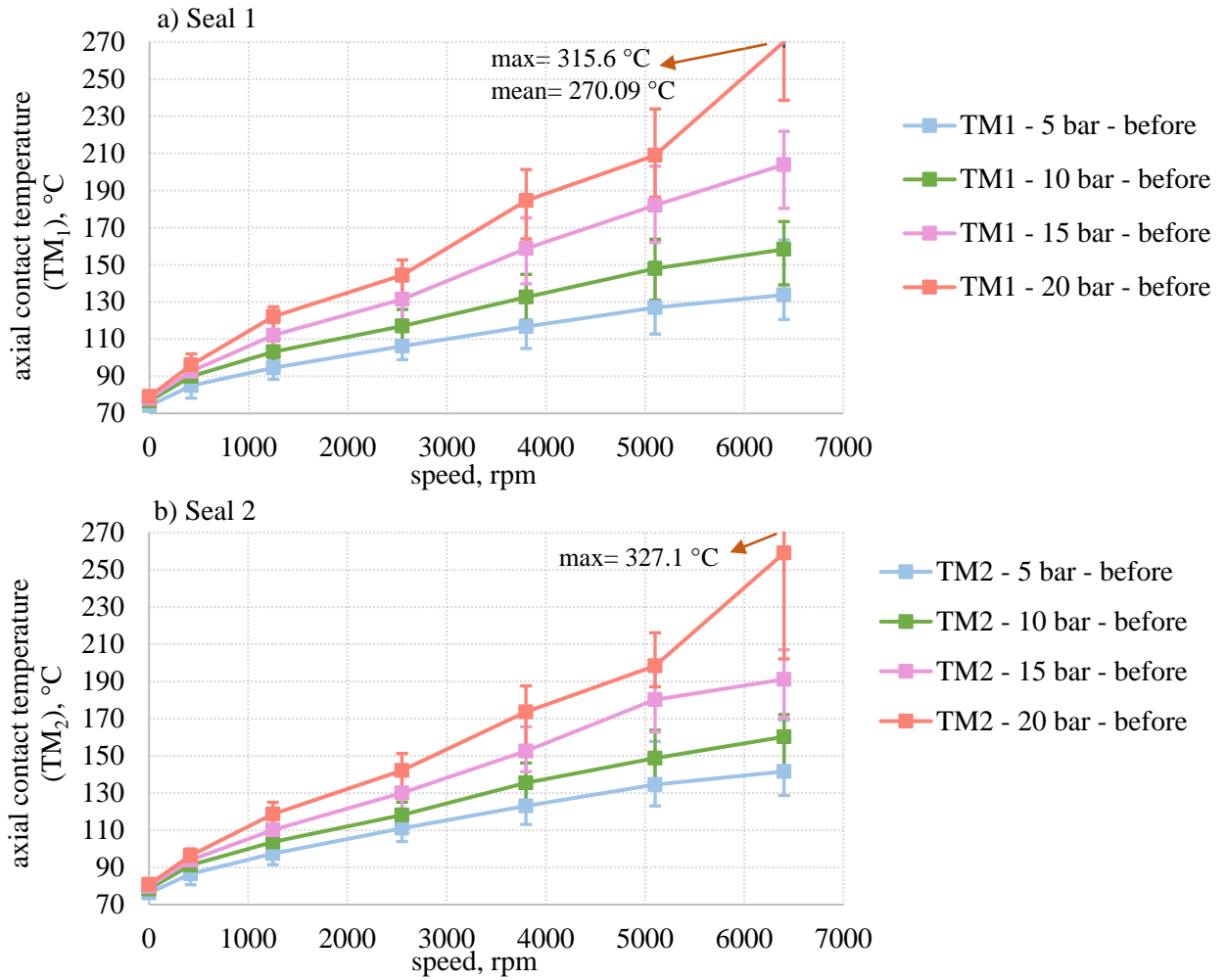
Figure C-14: Axial contact temperatures for the standard seals 1 and 2. 'before' represents the function test 1.
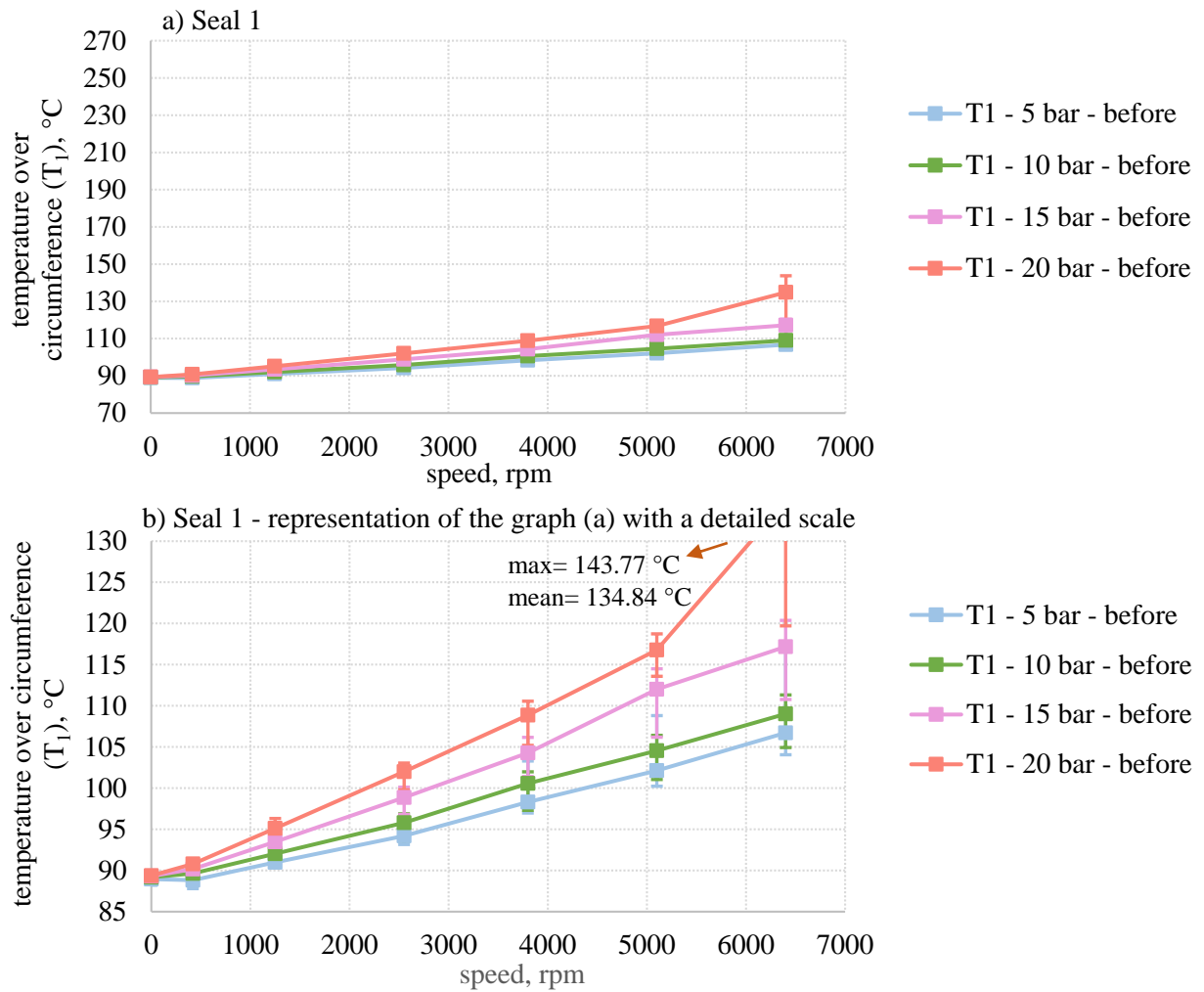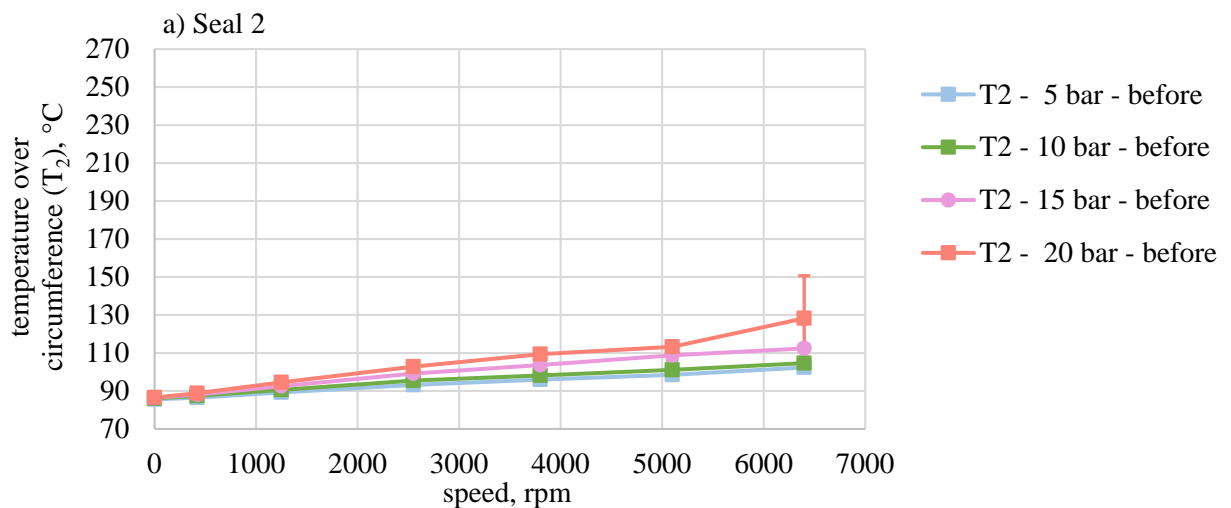
a) Seal 1

b) Seal 1 - representation of the graph (a) with a detailed scale

max= 143.77 °C
mean= 134.84 °C

Figure C-15: Temperatures over the circumference of standard seal 1. 'before' represents the function test 1.

a) Seal 2

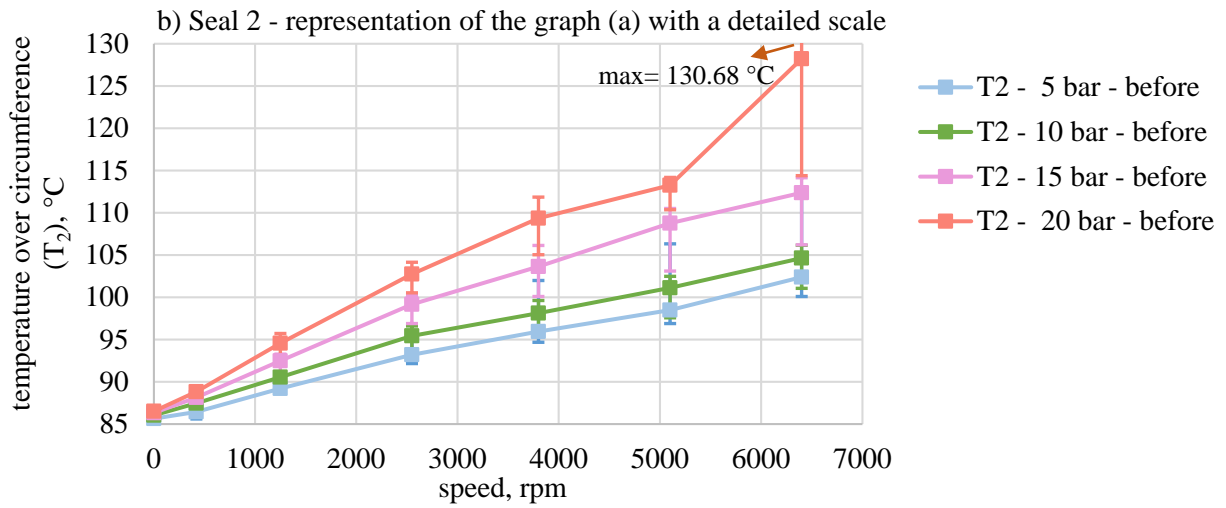Figure C-16: Temperatures over the circumference of standard seal 2. 'before' represents the function test 1.
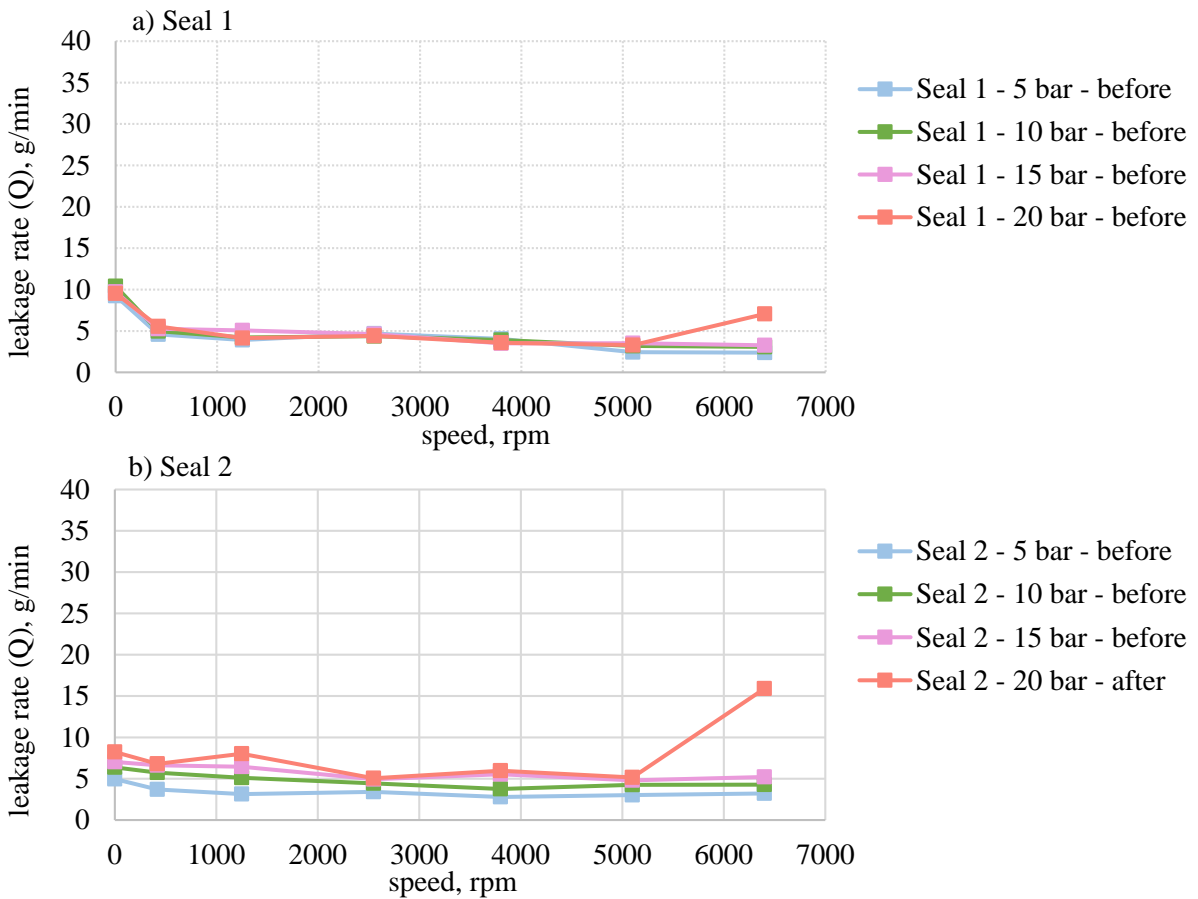

Figure C-17: Leakage rates for the standard seals 1 and 2 in Test D. 'before' represents the function test 1.
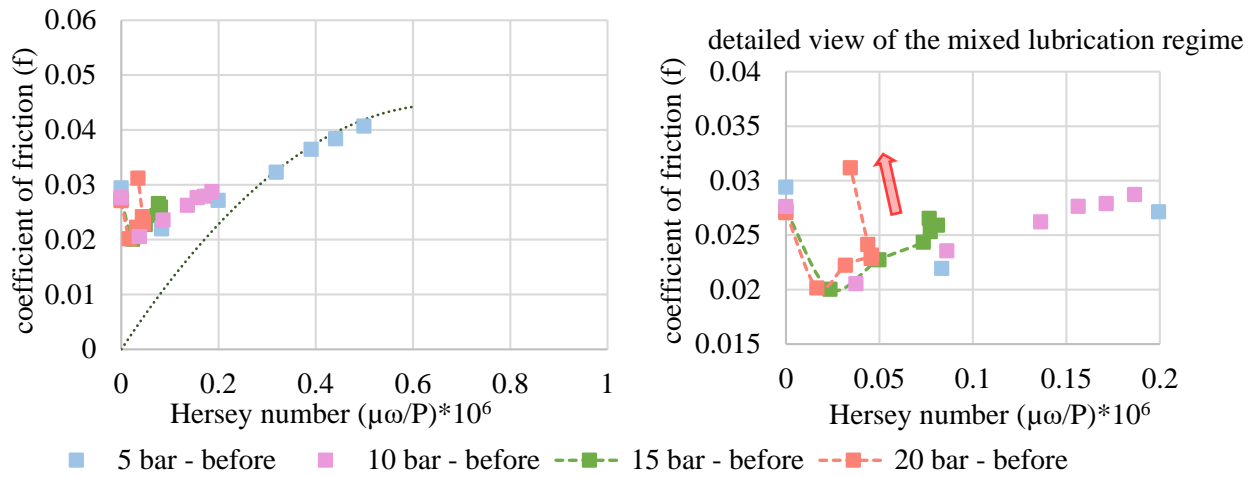
Figure C-18: The coefficient of friction values for the function test 1 of the standard seals. 'before' represents the function test 1.
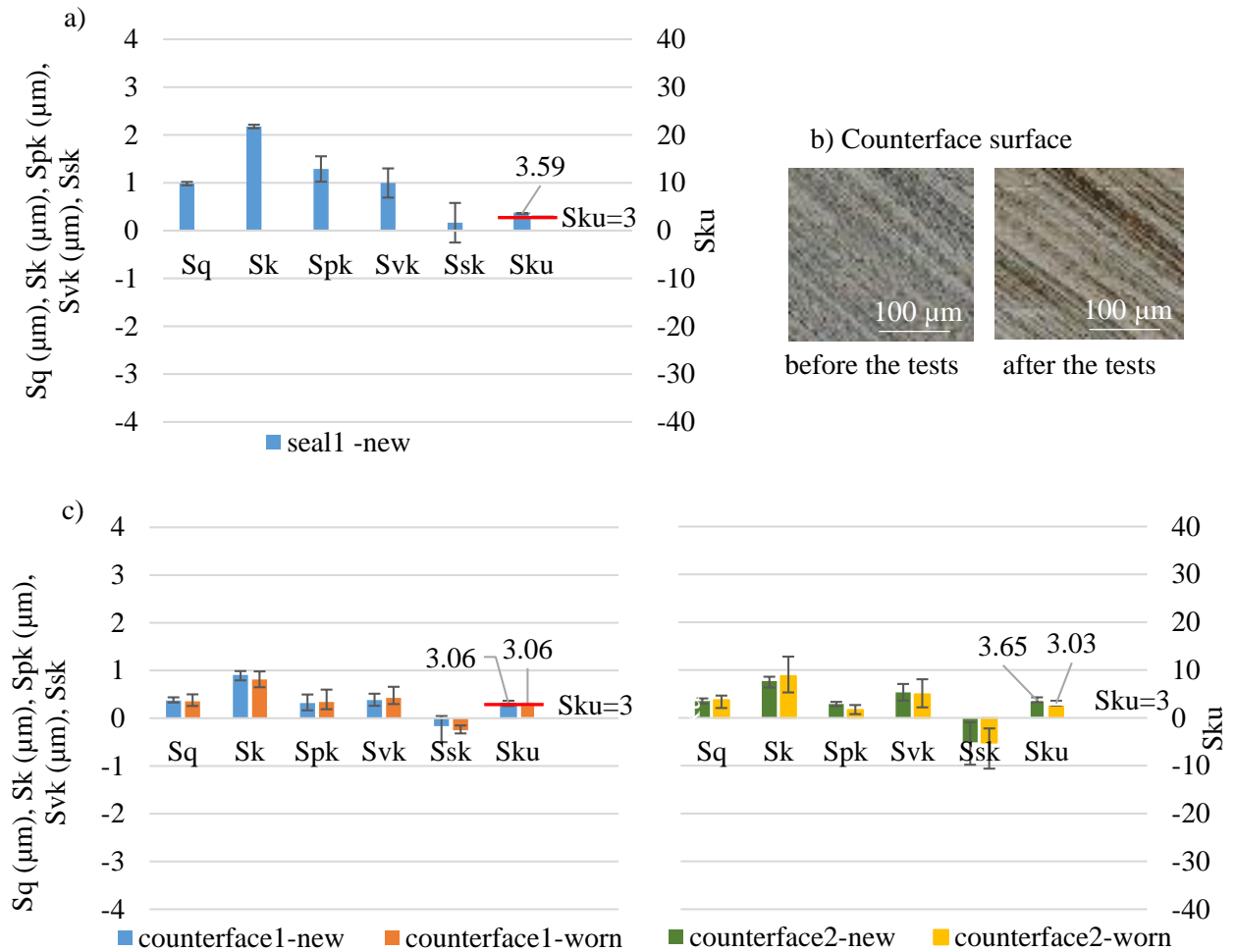

Figure C-19: a) Roughness parameters of the standard seals. c) Surface of a counterface before and after the tests. c) Roughness parameters of the counterfaces.
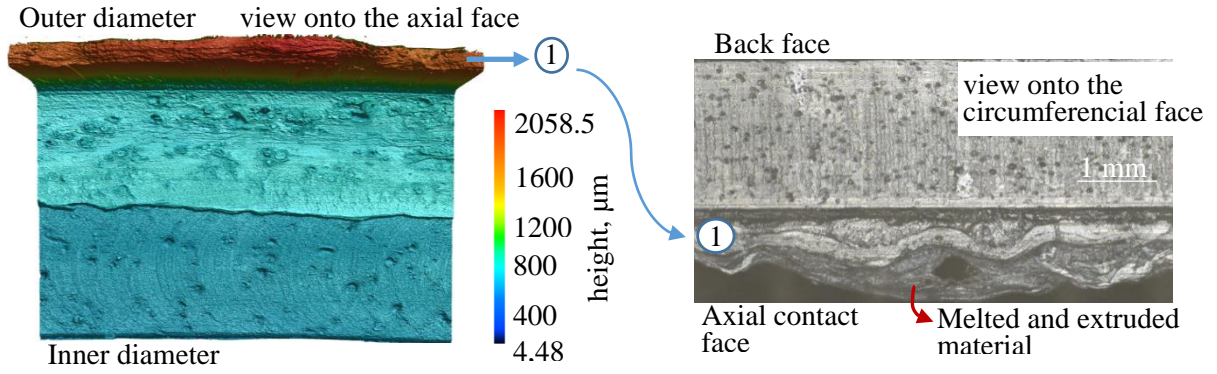
Figure C-20: A standard seal surface after the tests.

APPENDIX D
Derivation of p-θ formulation of Reynolds equation

Consider Reynolds equation in 2D for the face seal problem described in this thesis:

$$\frac{\partial}{\partial x}\left(\frac{\rho_{avg}}{\mu}h^3\frac{\partial p}{\partial x}\right) + \frac{\partial}{\partial y}\left(\frac{\rho_{avg}}{\mu}h^3\frac{\partial p}{\partial y}\right) = 6U\frac{\partial(\rho_{avg}h)}{\partial x} \tag{1}$$

Here, the problem is steady state and there is no Couette flow in the y direction. The lubricant is weakly compressible. The lubricant has the density ρ for a given pressure. ρ_{avg} is the average density of the lubricant and cavitation pockets across the film [85]. In the non-cavitated region, ρ_{avg} is constant and equal to ρ. Pressure is higher than cavitation pressure. In the cavitated region fluid is a mixture of lubricant, gas and vapour. The fluid density ρ_{avg} is lower than or equal to ρ and it varies both in time and space. Pressure is equal to cavitation pressure in the cavitating region. These conditions can be written as below [85]:

$$(p - p_{cav})\theta = 0, \qquad p - p_{cav} \geq 0, \qquad \theta = 1 - \rho_{avg}/\rho \geq 0$$
$$\theta = 0, \quad p > p_{cav} \rightarrow \text{no cavitation} \tag{2}$$
$$\theta > 0, \quad p = p_{cav} \rightarrow \text{cavitation}$$

In order to find the functional relationship between p and θ, the term θ should be extracted from eq. (1). For this, the density parameter in eq. (1) is rewritten as [88]:

$$\rho_{avg} = \rho - \rho\theta \tag{3}$$

Substituting eq. (3) in eq. (1) gives:

$$\frac{\partial}{\partial x}\left(\frac{(\rho - \rho\theta)}{\mu}h^3\frac{\partial p}{\partial x}\right) + \frac{\partial}{\partial y}\left(\frac{(\rho - \rho\theta)}{\mu}h^3\frac{\partial p}{\partial y}\right)$$
$$= 6U\frac{\partial[(\rho - \rho\theta)h]}{\partial x} \tag{4}$$

Finally, it is possible to obtain:

$$-\frac{\partial}{\partial x}\left(\frac{\rho\theta}{\mu}h^3\frac{\partial p}{\partial x}\right) + \frac{\partial}{\partial x}\left(\frac{\rho h^3}{\mu}\frac{\partial p}{\partial x}\right) - \frac{\partial}{\partial y}\left(\frac{\rho\theta}{\mu}h^3\frac{\partial p}{\partial y}\right) + \frac{\partial}{\partial y}\left(\frac{\rho h^3}{\mu}\frac{\partial p}{\partial y}\right)$$
$$= -6U\frac{\partial(\rho\theta h)}{\partial x} + 6U\frac{\partial(h\rho)}{\partial x} \tag{5}$$

In eq.(5), the first and the third terms include both the variables p and θ. This results a non-linearity in the functional connection between the variables [88]. According to the eq. (2), p is constant and equal to p_{cav} inside the cavitation zone. Also, $\frac{\partial p}{\partial x}$ and $\frac{\partial p}{\partial y}$ are equal to 0 while θ is greater than 0. On the other hand, p is greater than 0 and θ is equal to 0. Therefore, it is possible to conclude that almost everywhere within the lubricant film (except at the interfaces between cavitated and non-cavitated zones) [88]:

$$\theta \frac{\partial p}{\partial x} = 0, \qquad \theta \frac{\partial p}{\partial y} = 0 \tag{6}$$

With eq. (6), the first term of the eq.(5) may be neglected in terms of Lebesgue integration without any loss of generality and when performing the above integrations, reference may be made to the following equation:

$$\frac{\partial}{\partial x}\left(\frac{\rho h^3}{\mu}\frac{\partial p}{\partial x}\right) + \frac{\partial}{\partial y}\left(\frac{\rho h^3}{\mu}\frac{\partial p}{\partial y}\right) = 6U\frac{\partial[(1-\theta)\rho h]}{\partial x} \tag{7}$$

By integrating the eq.(7), the functional relationship can be obtained p and θ.
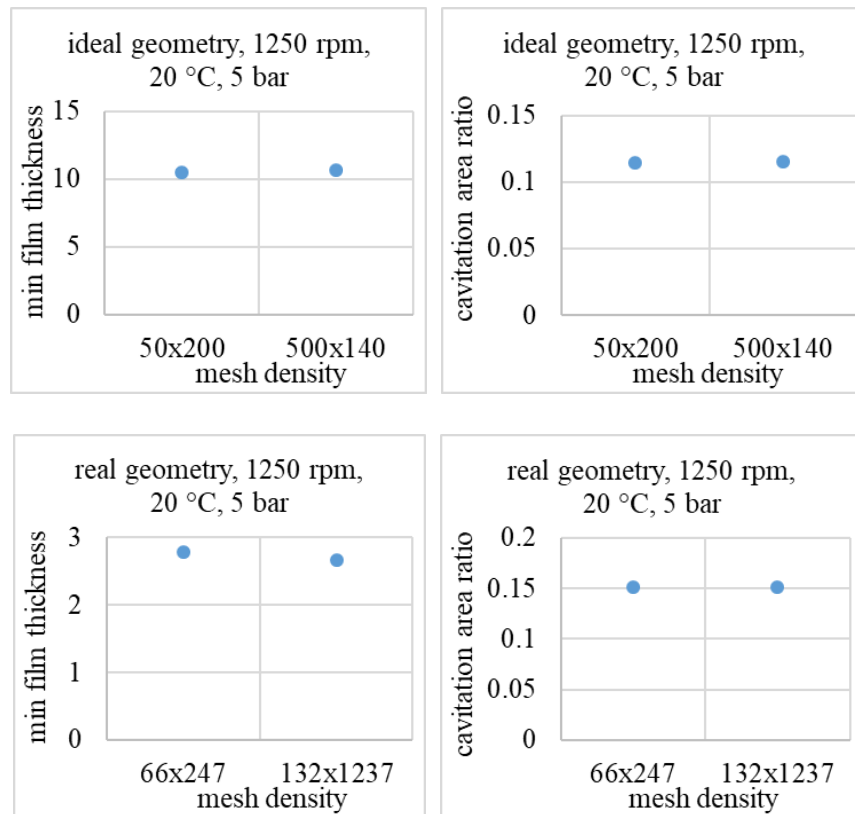
APPENDIX E
Mesh study

Figure E-1: Mesh study for the unworn structured seal surface.
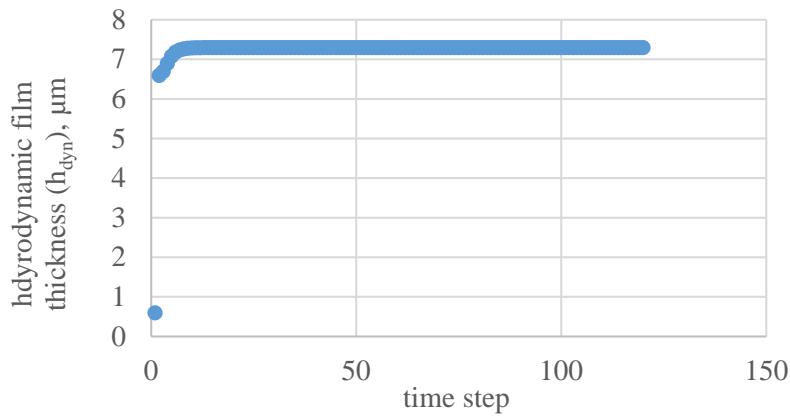
Numerical convergence study

Figure E-2: Convergence study for real geometry. Speed, temperature and pressure are set as 1000 rpm, 20 °C and 5 bar, respectively. Cavitation pressure is set as 0 kPa.

APPENDIX F

Validation of the numerically calculated shear forces

Figure F-1 shows the analytically and numerically calculated shear forces for a parallel and ideally smooth gap. The calculations are performed for various gap heights. The analytically calculated shear forces are determined according to eq. (6.5).
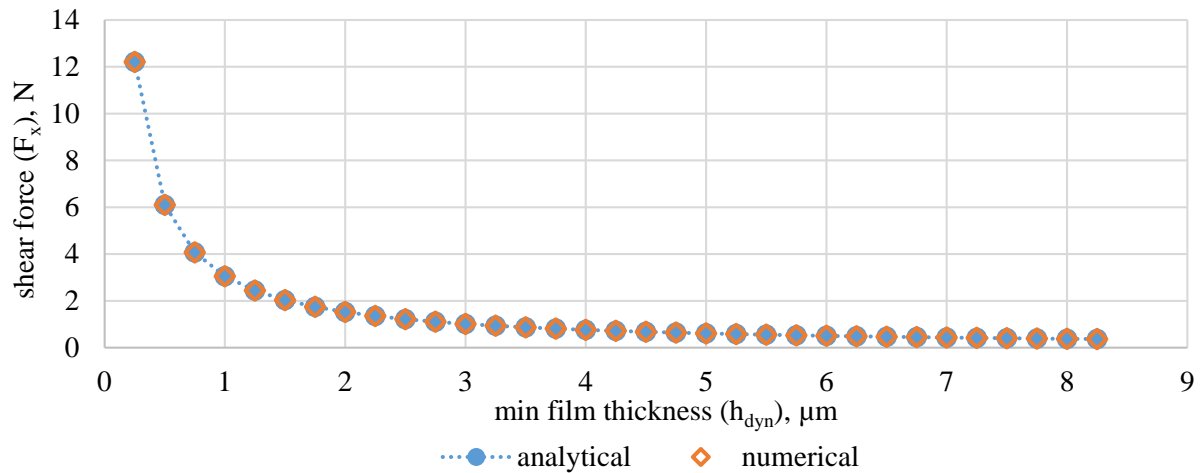

Figure F-1: Analytically and numerically calculated shear forces for a parallel and ideally smooth gap.

CURRICULUM VITAE

Persönliche Daten

Name	Dilek Bulut
Geburtsdatum	13.02.1989
Geburtsort	Istanbul, Türkei
Staatsangehörigkeit	Türkei
Status	Ledig

Berufliche Tätigkeit

seit 2016	Wissenschaftliche Mitarbeiterin am Institut für Maschinenkonstruktion und Tribologie (IMKT), Fakultät für Maschinenbau, Leibniz Universität Hannover
2013 - 2015	Wissenschaftlicher Mitarbeiter, Fakultät für Maschinenbau, Technische Universität Istanbul

Ausbildung und Schule

2013 - 2015	Masterstudium Maschinenbau an der Technische Universität Istanbul
2008 - 2012	Bachelorstudium Maschinenbau an der Istanbul Universität
2003 - 2007	Adile Mermerci Anatolian High School

CURRICULUM VITAE